Realization of Planar and SIW Filters with the Focus on Transmission Zero (TZ) and Evanescent-Mode Pole

by

Mehdi Nosrati

A thesis submitted in partial fulfillment of the requirements for the degree of

Doctor of Philosiphy

in

ELECTROMAGNETICS AND MICROWAVES

Department of Electrical and Computer Engineering
University of Alberta

Abstract

With the recent progress in wireless and satellite communication and the 5G requirements for increased multi-band structures, integrated platforms with simple configurations are in need to offer flexibility in the design, selective pass-bands generation and/or unwanted frequencies suppression. In this connection, transmission zero realization is one of the most interesting concepts in the design of high frequency filters responsible for increasing attenuation and suppressing parasitic EM signals at specific frequencies. On the other hand, evanescent-mode technique is an alternative for miniaturization. Here, planar and 3D (waveguides) filters are studied with the focus on creating transmission zero and evanescent-mode pole. This thesis creates a bridge between the planar and 3D structures by expanding a comprehensive lumped element circuit modeling of distributed-element structures. The results have enhanced flexibility in the filter design with multiple notch-band realization, stop-band expansion and multi-band functionality using evanescent and ordinary modes excitation.

For planar structures, the application of transmission zero is narrowed to notch-band realization to suppress the signal at some specific frequencies avoiding interference between local communication networks. Adopting the wave's cancellation theory, multiple notches are realized in UWB BPFs using the higher spurious resonance frequencies of a resonator. In this connection, single-layer platforms are proposed to design UWB BPFs with multiple notch-band frequencies. In addition, the concept is further studied to develop tunable multiple notch-band UWB BPFs where a new configuration of coplanar waveguide multi-mode resonator integrated with MEMS capacitor is developed for single/double notch-band realization.

Moreover, the importance of such analysis is highlighted in 3D structures integrated with new L-shaped irises and open side walls. The proposed integration is more studied using lumped element equivalent circuits to conceptually discuss the behavior of distributed-element structures resulting in the complete analysis and control of these components. Furthermore, a prescribed filtering function is demonstrated using the lumped element analysis including not only evanescent-mode pole, but also close-in transmission zero.

Preface

This thesis is an original work by Mehdi Nosrati submitted in partial fulfillment of the requirements for the degree of doctor of philisiphy in electromagnetics and microwaves. The subject mainly includes transmission zeros and evanescent-mode poles realization in both planar and 3D structures.

The thesis is written in paper-based format with the details as follows:

Chapters 3 has been published as M. Nosrati and M. Daneshmand, "Compact microstrip ultra wideband double/single notch-band band-pass filter based on wave's cancellation theory," *IET Microw. Antennas Propag.*, vol.6, no.8, pp. 862-868, Jun. 2012.

Chapter 4 has been published as M. Nosrati and M. Daneshmand, "Developing single-layer ultra-wideband band-pass filter with multiple (triple and quadruple) notches," *IET Microw. Antennas Propag.*, vol.7, no.8, pp. 612-620, Jun. 2013.

Chapter 5 has been published as M. Nosrati, N. Vahabisani and M. Daneshmand, "Compact MEMS-based ultrawide-band CPW band-pass filters with single/double tunable notch-bands," *IEEE Trans. Compon. Packag. Manuf. Tech.*, vol.4, no.9, pp.1451-1460, Aug. 2014.

Chapter 6 has been accepted, as M. Nosrati and M. Daneshmand, **"**Substrate integrated waveguide L-shaped iris for realization of transmission zero and evanescent-mode pole," in *IEEE Trans. Microw. Theory and Tech.,* Feb. 2017**.**

Chapter 7 will be submitted as M. Nosrati, N. Vahabisani and M. Daneshmand, "Dual-band evanescent-mode BPFs using open-sidewall substrate integrated waveguide,".

In all these publications, Mehdi Nosrati is responsibble for the design, fabrication, data collections and analysis. Nahid vahabisani would take a helping and advising role and Dr. Mojgan Daneshmand was the supervisory author and involved in concept formation and manuscript composition.

Dedicated to

Those who have been profoundly looking for perception, knowledge and understanding

and to my Family.

Acknowledgments

Firstly, I would like to express my sincere gratitude to my supervisor, Prof. Mojgan Daneshmand, for her persistent supports, discussions and guidance. Without doubt, this work could not be successfully accomplished without her knowledge, experience and patience. I must confess that she is more than a supervisor for me who taught me how to broadly think and research.

I would like to thank my friend Dr. Nahid Vahabisani for her continuous discussions on some parts of this study and her insightful comments and help. I would also like to thank M2M group members for their help and discussion during my Ph.D, Mohammad Abdolrazzaghi, Tom Jones, Sabreen Khan, Sameir Deif, Mohammad Hossein Zarifi, Zahra Abassi, Hamid Moghadass, Aaron Seilis, Amirali Toossi and my roommates Mahmood Reza Yassin and Saeed Hojjati.

I am also grateful to financially support from CMC for fabrication of some of the designs.

I also acknowledge my candidacy and Ph. D exam committee members.

Last but not the least; I would like to thank my lovely family for spiritually supporting me throughout my life.

Table of Contents

List of Tables

List of Figures

Chapter 1 Introduction

1.1 Synopsis

Filter is one of the main components in communication systems. This device is used to partially pass a signal at some specific frequencies and simultaneously suppress the signal in the other frequencies. An ideal filter has zero insertion loss and linear phase response in its pass-band as well as infinite attenuation in the stop-band. However, practical limitations cause deviations in the actual performance of the filter.

Apart from the efforts to design a near-ideal performance filter, the size and complexity of a structure are also considered as the main design concerns. Available filter structures are mainly categorized into two classes; planar and 3D structures. The former mitigates the size and complexity concerns over the deviation from near-ideal performance, while the latter lowers that deviation (high Q-factor, less radiation loss in higher frequencies, more selectivity) at the expense of more complexity and larger volume size.

Depending on the application, the need arises to design and utilize complicated structures that include the advantages of both classes, regarding near-ideal performance (low loss and high isolation), small size and less complexity. Up to date, filters have developed with variety of characteristics mainly with the focus on optimized bandpass behavior. Suppression and stopband behavior however, has not been adequately investigated.

In the literature, lumped element equivalent circuit proved to be an effective approach to model the performance of distributed-element structures via behavioral analysis. However, it has only been used for narrow-band applications, i.e. at their resonance frequency and pass band. The problem becomes more pronounced noting that the narrow band circuits have been vastly studied in the pass bands, neglecting the importance of suppression in stopbands.

This thesis aims to cover these shortcomings and generate the knowledge required to design filters in planar and substrate integrated structures and highlight the importance of considering stopband and transmission zeros. Comprehensive circuit analysis is included to accurately perceive the behavior of distributed elements and optimally take advantage of these structures.

1.2 Thesis Objectives

The main objective of this thesis is to investigate wideband circuit modeling and develop new techniques for flexible transmission zeros in both planar and SIW based filters. Although our focus is mostly on TZ realization, pass band performance (transmission pole) is also of significance importance in this work. Achieving low loss performance in small size compared to wavelength has been always considered throughout the thesis. This work aims on creating flexibility in the design of the number of pass bands and TZs.

To achieve the objective, a comprehensive and wideband circuit modeling of a transmission line is studied. The results are then used for:

- Developing a ***more complete equivalent lumped element circuit*** for distributed elements in ***transverse direction*** (Chapter 2).
- Developing a new technique based on wave's cancellation theory to create ***single and double*** transmission zeros and notch bands in ultra-wideband (UWB) filters (Chapter 3).
- Developing a new technique based on waves cancellation theory to create ***triple and quadruple*** transmission zeros and notch bands in ultra-wideband (UWB) filters (Chapter 4)
- Developing UWB BPFs with single/double ***tunable*** transmission zeros and notch bands by integration of MEMS capacitors with coplanar waveguide (CPW) (Chapter 5)
- Developing new structures for ***flexible realization of transmission zero and evanescent-mode pole*** at the same structure achieving miniature single/double band filters with ultra-wide stop-band (Chapter 6).

- Developing new technique and structure for ***flexible*** realization of transmission zeros by integration of substrate integrated waveguides (SIW) with planar resonators (Chapter 7).

1.3 Thesis Overview

To achieve a lumped element equivalent circuit that can accurately model the behavior of a distributed-element structure in a wider frequency band, we expand the conventional lumped element equivalent circuit for the integrated substrate integrated waveguide. We will elaborate more on the details of this proposal in Chapter 2.

It should be noted that this model studies the behavior of distributed-element structures in the transverse direction. However, more future research work can be done to include the propagation direction.

This thesis investigates the behavioral analysis of distributed elements for both planar and 3D structures on one hand and for the integration of these two structures on the other hand.

Ultra wide-band band-pass filters (UWB BPFs) with single notch-band are realized on a single-layer structure with no via-hole or short-circuited stub. Since, the increase of notch-band entails more complicated structures, either with multi-layered structures or via-holes [3]-[6], complexity minimization with near-ideal performance is required in the design of planar UWB BPFs with multi notch-bands.

In this study, we aim to design planar UWB BPFs with multi notch-band and simultaneously minimize complexity. Thus, we propose the use of wave's cancelation theory in the development of single/double/triple and quadruple notch-band UWB BPFs on a single-layer structure with no via-hole or short-circuited stub (Chapter 3 and Chapter 4).

Moreover, UWB BPFs with tunable single/multi notch-band are capturing the interests of researchers [7]-[9]. As a result, our goal in Chapter 5 is to develop such filters with tuning capabilities.

Another aim in this study is to investigate L-shaped iris embedded in 3D structures (Chapter 6). A lumped element equivalent circuit is utilized to thoroughly discuss the iris behavior in a wide frequency band. This structure has one more degree of freedom and design parameter compared to the conventional iris structures; therefore, it enables design flexibility with enhanced performance. The L-shaped iris is utilized to realize a two-pole evanescent-mode filter with an enhanced stop-band and a dual-band filter combining evanescent and ordinary modes excitation. Moreover, a prescribed filtering function is demonstrated using the lumped element analysis not only including evanescent-mode pole, but also close-in transmission zero.

It is well-known that a filter structure consists of a resonator and two coupling sections where discontinuities including gap-coupled TLs and coupling aperture are employed to realize coupling sections in planar and 3D structures, respectively. In this study, we propose to partially integrate these two structures to make a trade-off between their advantages and disadvantages resulting in size and complexity reduction.

To accomplish this, planar stepped-impedance resonator (SIR) is integrated with 3D coupling structure and presented in Chapter 7. Moreover, reduced-height open-circuited stubs are added to mitigate radiation loss of the resonator. The structure demonstrates a small BPF with wide upper stop-band.

Furthermore, the capability of this integration is also studied to design dual-band BPFs by adding the least complexity to the structure (one reduced-height open-circuited stub). Note that the structure is realized in low frequencies and the design procedure can be further studied for the higher frequencies in the future work.

1.3.1 Organization

This thesis has been written in paper-based format. The entire thesis is presented in eight chapters.

Chapter 1 provides a brief background and motivation on this research. It includes detailed literature review on transmission zero's realization and also provides comparison between the existing technologies.

Chapter 2 presents a thorough review of the literature and theories related to transmission zero (TZ) and evanescent pole realization.

Chapter 3 presents a new technique to realize flexible single and double TZs in UWB BPFs based on the wave's cancellation theory. The technique is studied in detail involving the first spurious resonance frequency of the resonator to generate notch-band.

Chapter 4 presents another study on TZ's realization in UWB BPFs by further developing the idea of the wave's cancellation theory to increase the number of notch-bands in this type of filters. In this Chapter, the structure in Chapter 3 is further developed by integrating double notch-band filters with µ-strip gap coupled transmission lines resulting in triple and quadruple notch-band UWB BPFs.

Chapter 5 presents a further development on the use of wave's cancellation theory to realize ultra-wideband band-pass filters with tunable single/double notch-bands. To develop the structure, multi-mode resonators (MMRs) are integrated with MEMS actuators resulting in independently tunable single and double notch-band UWB BPFs.

Chapter 6 investigates L-shaped iris embedded in substrate integrated waveguide structures. A lumped element equivalent circuit is utilized to thoroughly discuss the iris behavior in a wide frequency band. This structure has one more degree of freedom and design parameter compared to the conventional iris structures; therefore, it enables design flexibility with enhanced performance. The L-shaped iris is utilized to realize a two-pole evanescent-mode filter with an enhanced stop-band and a dual-band filter combining evanescent and ordinary modes excitation. Moreover, a prescribed filtering function is demonstrated using the lumped element analysis not only including evanescent-mode pole, but also close-in transmission zero. The proposed L-shaped iris promises to substitute the conventional posts in substrate integrated waveguide filter design.

Chapter 7 presents a new technique to realize flexible multi-band band-pass filters based on integration of open side-wall substrate integrated waveguide (SIW) and planar stepped-impedance resonators (SIRs). Partially open side-wall SIWs are employed as evanescent feeding for SIRs to develop single/dual-band BPFs with arbitrarily tunable resonance frequencies and ultra-wide stop-band. Furthermore, a novel technique is developed to realize TZs between the bands by using vertically integrated open and short-circuited stubs.

Finally, Chapter 8 summarizes the main conclusion and contributions from this study and provides some recommendations for future studies.

1.4 References

[1] N. Marcuvitz, *Waveguide Handbook*, New York, NY, USA: McGraw-Hill, 1951.

[2] D. M. Pozar, Microwave Engineering, 3rd Ed. New York: Wiley, 2005.

[3] Z-C. Hao, J-S. Hong, J. P. Parry, and D. P. Hand, "Ultra-wideband bandpass filter with multiple notch bands using nonuniform periodical slotted ground structure," *IEEE Trans. Microw. Theory and Tech*., vol. 57, no.12, pp.3080-3088, Dec. 2009.

[4] S. G. Mao, Y.Z. Chueh, C.H. Chen, and M. C. Hsieh, "Compact ultra-wideband conductor–backed coplanar waveguide bandpass filter with a dual band-notched response," *IEEE Microw. Wireless Compon. Lett.*, vol.19, no.3, pp.149-151, Mar. 2009.

[5] Z. C. Hao and J-S. Hong, "Compact UWB filter with double notch bands using multilayer LCP technology," *IEEE Microw. Wireless Compon. Lett.*, vol.19, no.8 pp. 149-151, Aug. 2009.

[6] Z.-C. Hao, J.-S. Hong, S. K. Alotabi, J.P. Parry, and D.P. Hand, "Ultra-wideband bandpass filter with multiple notch-bands on multilayer liquid crystal polymer substrate," *IET Microw. Antennas Propag*., vol.3, no.5, pp.749-756, Aug. 2009.

[7] F. Wei, L. Chen, X.-W. Shi, and B. Liu, "Compact UWB band-pass filter with tunable notch-band based on folded SIR," *Electronic Lett*., vol. 47, no. 22, pp.1229-1230, Oct. 2011.

[8] F. Wei, L. Chen, X.-W. Shi, and C.-J. Gao, "UWB band-pass filter with one tunable notch-band based on DGS," *J. of Electromagn. Waves and Appl*., vol.26, no.5-6, pp.673-680, Jul. 2012.

[9] Z. Wu, Y. Shim, and M. Rais-Zadeh, "Miniaturized UWB filters integrated with tunable notch filters using a silicon-based integrated passive device technology," *IEEE Trans. Microw. Theory and Tech*., vol.60, no.3, pp.518-527, Mar. 2012.

Chapter 2 Background and Principles

This chapter is divided into two main parts. In the first part, literature is initially reviewed for the conventional techniques of transmission zero and evanescent pole realization. In the second part, the conventional lumped element equivalent circuit of transmission lines is critically discussed and a comprehensive wideband equivalent circuit is proposed as a principle of operation in our designs and circuit modelling.

2.1 Literature review

This section is divided into two main parts where the literature is reviewed for the conventional techniques of transmission zeros and evanescent pole's realization, respectively.

2.1.1 Transmission zero

This section is also divided into some sub-sections to review the proposed structures to realize TZs for different applications such as notch-band realization or upper stop-band extension in high-frequency filter design. Additionally, the proposed techniques are separately discussed for both planar and 3D waveguide structures.

2.1.1.1 Single-multiple notch-band UWB BPF

The use of ultra-wide-band (UWB) technology has been dramatically increased since the U.S. federal communication commission (FCC) authorized UWB for the unlicensed use in short-distance communication in early 2002 [1].

A wide-band filter generally requires a large design area or complicated structure such as a three-dimensional coupling structure utilizing either wire-bonding connections or via-holes. In addition, since the 3.1GHz to 10.6 GHz UWB covers various existing wireless communication frequency bands, such as the 3.5-GHz WiMax band, 5.0 GHz WLAN band, 5.9GHz DSRC, 8.0-GHz military and satellite-communication bands, it is desirable to introduce multiple notch bands to avoid these interferences. In addition, it is expected that the rapid growth of communication systems will entail the need for UWB band pass filters with multiple notches even further.

As the number of the required notches increases, the number of transmission zeros of the filter should be enhanced which makes the design more challenging. In general, many different designs have been introduced to realize UWB BPFs utilizing multi-mode resonators (MMRs), defected ground structures and left/right-handed technique [2]-[10]. While these models offer effective techniques to design UWB BPFs, they still suffer from a long list of drawbacks such as: incapable of realizing more than one notch-band [2]-[4], lack of transmission zeroes for high selectivity [5]-[8], narrow upper stop-band [9]-[10], complicated and expensive fabrication procedure including multi-layer structure [7], [8] and [10] , high cost from the use of via holes [8]-[9], incompatibility with monolithic microwave integrated circuits (MMICs) [7]-[9]. Although these filters provide double notch bands, there is still a need to design multi notch bands including triple (TNBs) or quadruple notch-bands (QNBs). Aligned with this need, two not quite different models have been recently reported to demonstrate TNBs in [8]-[9]; but at the expense of multi-layer LCP technology including short-circuited stubs or via-holes. Ref [10] has recently reported the only quadruple notch-band filter (based on our knowledge) and yet requires multi-layer patterning. Generally, three important characteristics are considered in the priority of the notch-band filters including the size, complexity in the structure and the number of the notch-bands. Table 2.1 summarizes several recently proposed single and multiple notch-band UWB BPFs.

As provided in Table 2.1, each filter has its own advantages and disadvantages for instance; the first two ones can provide a single notch-band, the ones proposed in [5] and [7] are realized by a complicated multi-layer substrate without any transmission zero accompanied by using via-holes and short-circuited stubs.

Moreover, the triple notch band BPF in [8] requires a three-layer substrate with via-holes and short circuits, it also occupies a large area on the substrate. Eventually, the quadruple notch-band UWB BPF developed in [10] also needs a multi-layer patterning and the notches are not able to be arbitrarily tuned.

Table 2.1. Comparison between the conventional single/multiple notch-band UWB BPFs.

Ref.	Pic. Of Filter	Structure	Size ($\lambda_g \times \lambda_g$)	Notch. Num
[3]	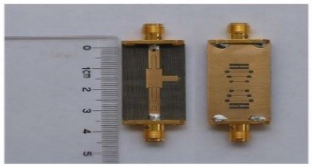	µ-strip +DGS	1.0 ×0.2	Single-notch
[4]	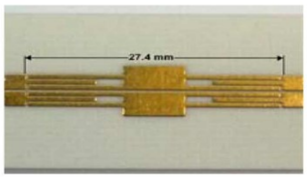	µ-strip	0.86 ×0.1	Single-notch
[5]	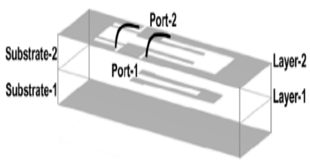	Multi-layer µ-strip	0.46 ×0.1	Dual-notch
[7]	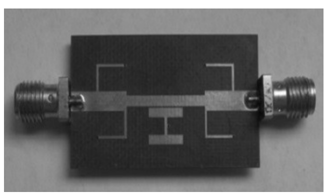	µ-strip + via hole	0.84 ×0.5	Dual-notch
[8]	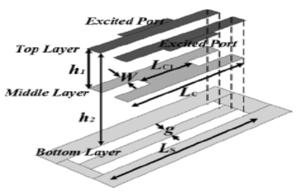	Multi-layer µ-strip + via hole	1.1 ×0.6	Triple-notch
[10]	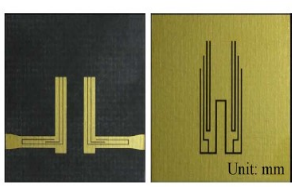	µ-strip	0.46 ×0.35	Quadruple-notch

2.1.1.2 Tunable notch- band UWB BPF

As presented in the previous section, several studies have focused to realize single and multiple notch-band filters [2]-[10]; however, they are limited to fixed notches. It is well known that the existing parasitic signals change from place to place and from time to time.

Therefore, recent investigations have attempted to design tunable notch-bands for UWB filters to suppress these tunable signals [11]-[15]. A single tunable notch-band UWB BPF has been reported in [11] based on harmonic characteristics of a half wavelength transmission line integrated with varactor diodes. Another tunable notch-band filter has been investigated using open-circuited μ-strip structure integrated with varactor diodes [12]. An electronically reconfigurable notch-band UWB BPF on liquid crystal polymer (LCP) substrate has been reported in the literature [13]. The same technology has been used to develop tunable single notch-band UWB BPF.

However, these filters have been designed by incorporating varactor diodes and via holes which require hybrid integration with associated complexity. Besides, they consume power and show poor RF performance [13]. Figure 2.1 shows the structure as well as the performance of the proposed tunable notch-band UWB BPFs discussed in [14]-[15].

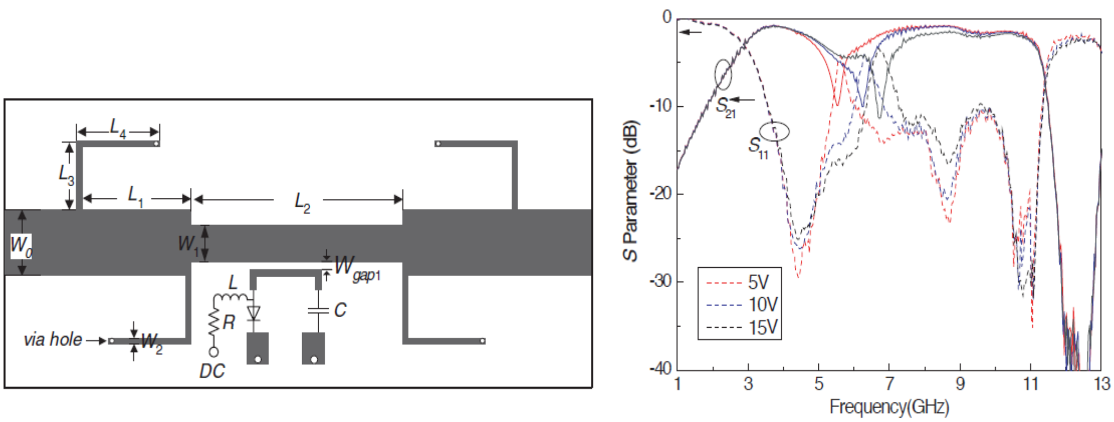

(a) (b)

Figure 2.1. (a) The structure and (b) the performance of the tunable notch-band UWB BPF proposed in [14]-[15].

Active filters have also been employed in several studies to meet these requirements but at the expense of increased CMOS chip area, cost and power consumption [16]-[17]. MEMS filter technology has been widely studied during the last decade due to the superior characteristics that it offers low DC power consumption and low RF loss [18]. To capture such benefits, a miniaturized tunable notch-band UWB BPF integrated with MEMS actuators has been recently investigated shown in Figure 2.2 [19].

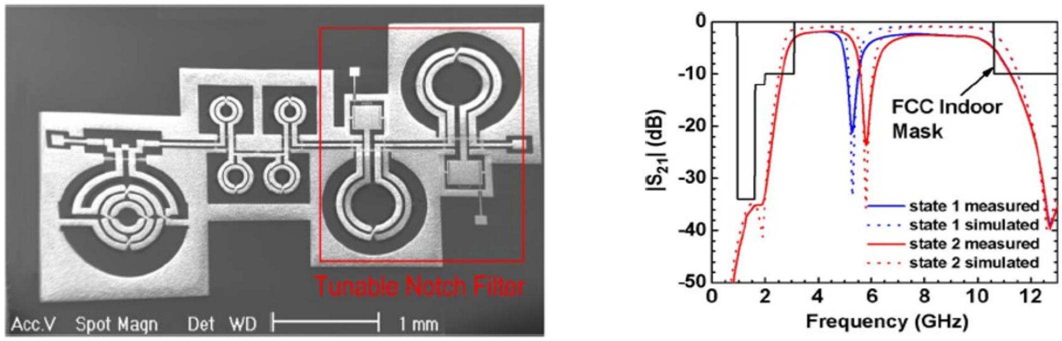

(a) (b)

Figure 2.2. (a) The structure and (b) the performance of the tunable notch-band UWB BPF proposed in [19].

This filter provides a tunable single notch-band on a silicon-based substrate; however, the structure is limited to a tunable single notch-band. Table 2.2 summarizes the performances of the main reported tunable notch-band UWB BPFs in the literature.

Table 2.2 Comparison between the conventional tunable notch-band UWB BPFs.

BPF	Structure	Size (mm^2)	Notch-No	Rejection (dB)
Wei [14]	μ-strip + varactor diode	35×20	One	10
Wei [15]	μ-strip + varactor diode	35×17	One	11
Wu [19]	Silicon + MEMS	4.8 × 2.9	One	21

2.1.2 Transmission zero realization in 3-D waveguide

Transmission zeroes (TZs) or attenuation poles are required in the design of microwave and millimeter-wave components to improve the performance of the structure in terms of high selectivity, sharp skirts, and wide-band upper stop-band. The techniques of realizing TZs can be initially reviewed in two categories including planar and 3D waveguide structures. In the previous section, several techniques have been discussed to demonstrate a TZ in the planar structures for notch-band UWB applications [2]-[23]. Here, the other application of this concept is reviewed for both planar and 3D structures.

Some studies have proposed several different techniques to realize TZs for upper stop-band extension in both planar and 3D structures [24]-[47]. For planar structures, the TZ is mainly tuned by changing the length of one open or short-circuited stub involved in the attenuation pole resonance [24]. Figure 2.3 shows two types of planar structures to realize tunable TZs [24]-[25]. As shown in the left-handed picture, two TZs have been demonstrated and tuned using open-circuited stubs integrated with varactor diodes [24]. In a similar way, a tunable TZ has been realized using the integration of complementary split ring resonator (CSRR) integrated with varactor diodes [25].

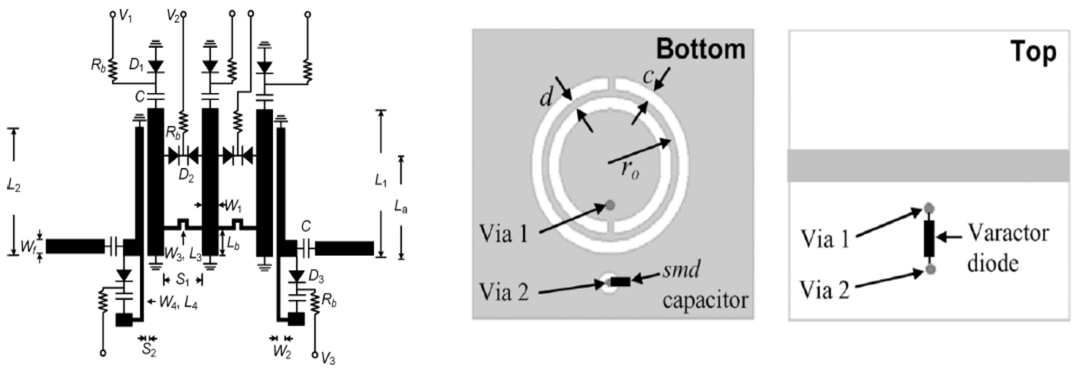

(a) (b)

Figure 2.3. The proposed structure for tunable TZs realization: (a) using combination of open- and short-circuited stubs integrated with varactor diodes [24] (b) CSRR integrated with varactor diodes [25].

TZs realization and tuning in 3D waveguide are reported to be a challenge where totally two different techniques have been proposed to establish that in the literature. The first technique is reported to be cross coupling between nonadjacent cavities or higher order excitation which can provide controllable TZs; however, at the expense of complicated 3-D structures. Figure 2.4 shows the concept behind this technique [28]-[39]. As shown in Figure 2.4(a), the non-resonating TE_{10} bypasses the resonance mode TM_{110} [29] and in the other model, coupling between nonadjacent cavities is realized to demonstrate a TZ. It should be noted that these two techniques realize TZs based on the wave cancellation theory [45]. In the other technique, the TZ realization is reported by means of multi metallic posts and irises inside 3D structure [42]-[47].

Table 2.3 Comparison between the conventional techniques of TZ realization in 3D structures.

Ref.	Resonator	Structure	TZ	Ref.	Resonator	Structure	TZ
[28]	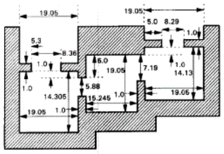	Waveguide	1-2	[38]	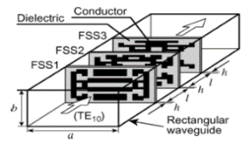	Waveguide	1-6
[29]	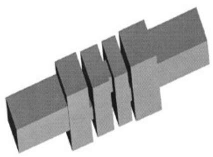	Waveguide	1-4	[39]	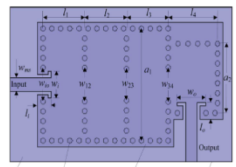	SIW	1-2
[30]	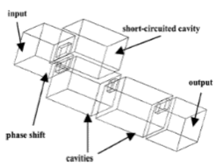	Waveguide	1-2	[42]	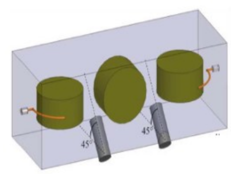	Waveguide	1-6
[33]	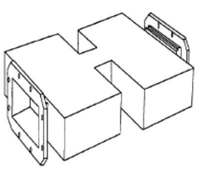	Waveguide	1-2	[44]	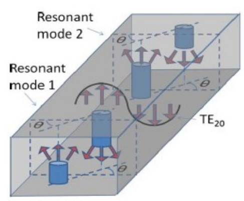	Waveguide	#NOP
[34]	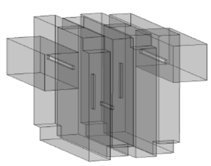	Waveguide	*NOC	[45]	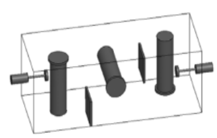	Waveguide	1-2
[36]	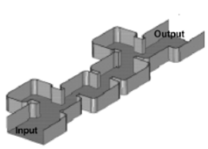	Waveguide	*NOC	[46]	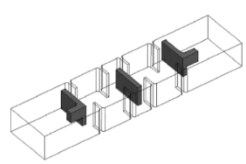	Waveguide	1-4
[37]	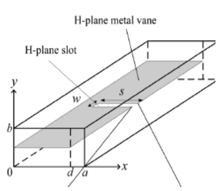	Waveguide	Multiple	[47]	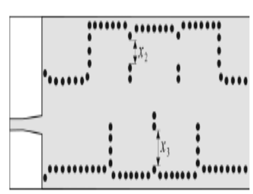	SIW	1 or 2

*NOC : Depending on the number of cavities #NOP: Depending on the number of posts

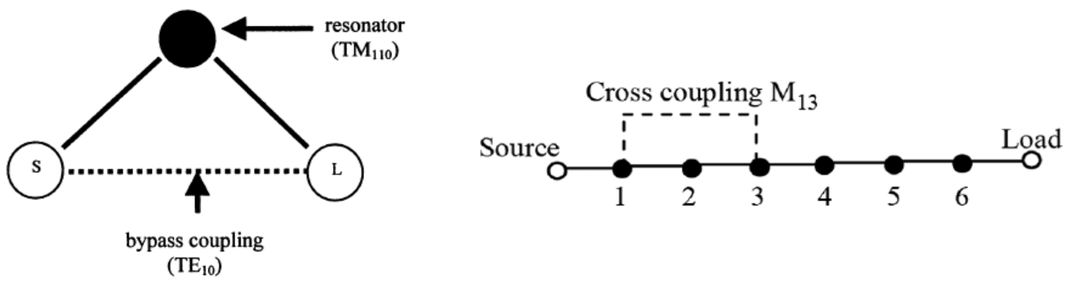

(a) (b)

Figure 2.4. The diagram schematic of TZ realization: (a) singlet with bypass coupling [29] (b) non-adjacent cavity coupling [45].

Table 2.3 summarizes the proposed structures using the conventional techniques of TZ realization in both 3D waveguides and SIWs. Inspecting the proposed structures, the techniques result in complicated and bulky 3D structures. Another limitation imposed by these structures is that at least one cavity or post is needed for each TZ.

2.1.3 Evanescent-mode band-pass filters

It can be said that the main advantage of the evanescent-mode resonators in comparison to those operating in ordinary modes is their small size with high-Q but at the expense of a higher in-band insertion loss.

Historically, the evanescent-mode resonator has been discovered and discussed for the first time in [50]. Afterwards, this concept has been further discussed in other studies [51]-[53]. Since operating in this mode was still unknown, it was called as “ghost mode” [50]-[51]. Later, the concept has been analyzed based on a lumped element equivalent circuit model as given in Figure 2.5 [51]-[53].

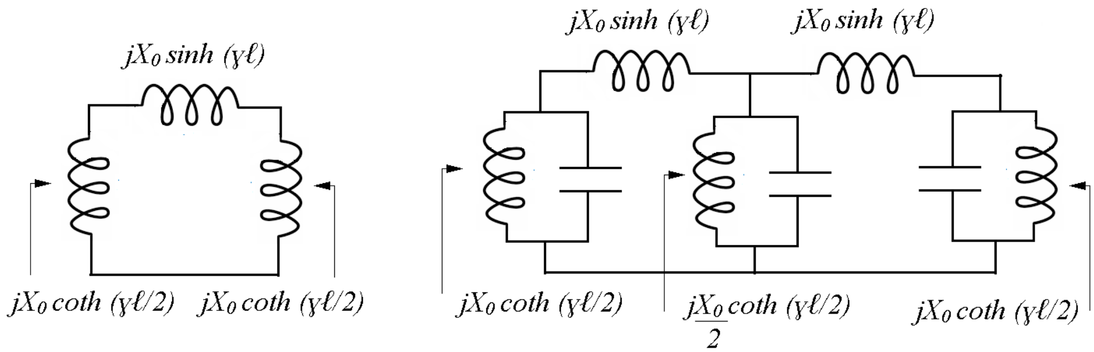

Figure 2.5. The conventional lumped element equivalent circuit of a waveguide operating in evanescent mode [53].

As shown in Figure 2.5(a), the waveguide operating in evanescent-mode can be represented by two parallel inductors connected to each other by means of another series inductor. Based on the model in Figure 2.5(b), an evanescent-mode resonance is realized by adding some capacitors to the circuit [53].

The conventional lumped element equivalent circuits proposed in [53]-[54] have been reported with some limitations where these circuits have been further expanded in some other research studies [55]-[56]. Moreover, evanescent-mode filters have been realized using double-step waveguide junction [57]-[58].

All the structures proposed in these studies have been reported to comply with the original equivalent circuit presented in [53] where the waveguide is modeled with an inductor under the 3D structure cut-off frequency and an evanescent-mode BPF is realized by adding a parallel capacitor to the circuit.

2.1.3.1 Evanescent-mode BPF based on micro-machined technology

After a decade, the design of this kind of resonator has been resumed again in different investigations [59]-[67]. In these studies, the original technique of evanescent-mode realization has been applied to other technologies where two evanescent-mode BPFs have been developed using micro-machined technology [60]-[61]. Table 2.4 compares these two evanescent-mode microwave components in terms of size, fractional bandwidth and in-band insertion loss.

Table 2.4. Comparison between the conventional two μ-machined evanescent-mode BPFs.

Ref.	Micro-machined Resonator	Size ($\lambda_g \times \lambda_g$)	FBW%	IL(dB)
[60]	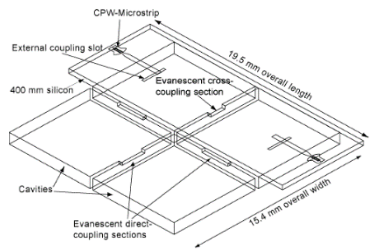	1.79 ×1.4	1.9	1.6
[61]	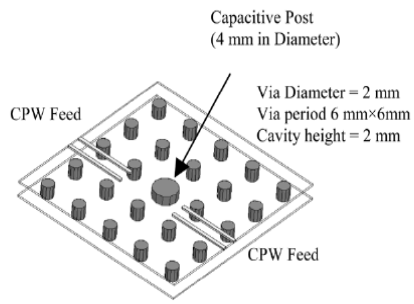	0.23×0.23	1.69	0.83

Inspecting the two evanescent-mode filters developed based on the micro-machined technology, we observe that the second effort in [61] has significantly improved the performance and the size of the first one in [60].

Generally, the evanescent-mode BPFs can be categorized in two different classes. The first class includes the BPFs designed by adding a parallel plate or post inside the waveguide [47]-[67]. The second class is those developed based on metamaterials, specifically complementary split ring resonators (CSRRs) placed either vertically inside the waveguide or on the broad side of the waveguide [72]-[76]. Here, the proposed evanescent-mode BPFs based on these two techniques are reviewed and compared in terms of their size, fractional bandwidth and in-band insertion loss.

2.1.3.2 First class: evanescent-mode BPF based on embedded parallel capacitor

In some research studies, tunable evanescent-mode high-Q BPFs have been developed based on the original technique integrated with MEMS actuators. It should be noted that no significant changes have been reported in the original structure except incorporating tunable capacitors in the structure. In these structures, the parallel capacitor for resonance has been realized by placing an iris between the ground and the top layer of the waveguide integrated with tunable actuators. Depending on structure, metallic waveguide or substrate integrated waveguides (SIW), these structures can demonstrate evanescent-mode BPFs with different quality factors. Table 2.5 compares three types of these evanescent-mode BPFs.

Inspecting the reported three evanescent-mode BPFs in Table 2.5, we observe that each filter has its own advantages and disadvantages, e.g., the one proposed in [62] is the better candidate for moderate bandwidth and good insertion loss. The filter in [65] is a better choice for integration with other components and the one in [67] for higher unloaded-Q applications, but at the expense of higher in-band insertion loss [90].

2.1.3.3 Second class: evanescent-mode BPF based on complementary split ring resonator (CSRR)

As presented, several studies have recently proposed some techniques to tune the evanescent-mode resonance using the conventional mechanism of evanescent-mode realization below the 3D structure cut-off frequency.

In addition to the proposed works, some studies have been also reported to develop different 3D structures to operate below the cut-off frequency of the 3D structures. These studies have developed the evanescent-mode realization based on the metamaterial concept, specifically the integration of waveguide cavity with complementary split ring resonators (CSRRs). Depending on the configuration of this integration, these studies can be categorized in two sub-classes.

In the first class, the CSRR unit cells are placed in the propagation direction while the CSRR unit cells are etched on the broadside wall, top layer, of cavity in the other category. Figure 2.6 shows the proposed configurations for these two classes [68]-[72].

Table 2.5. Comparison between the new generation of evanescent-mode BPFs based on the original structure.

Ref.	Resonator	Structure	Size ($\lambda_g \times \lambda_g$)	FBW%	IL (dB)
[62]	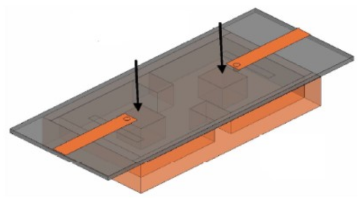	Metallic Waveguide	0.17 ×0.08	2.25	1.3
[65]	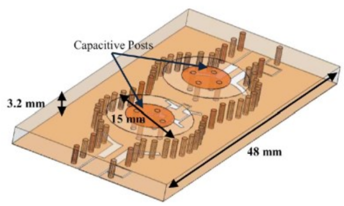	SIW	0.23×0.1	3.1	3.1
[67]	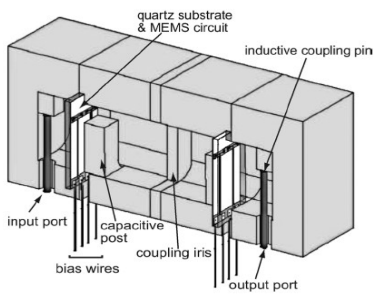	Metallic Waveguide	0.15×0.12	0.78	4.9

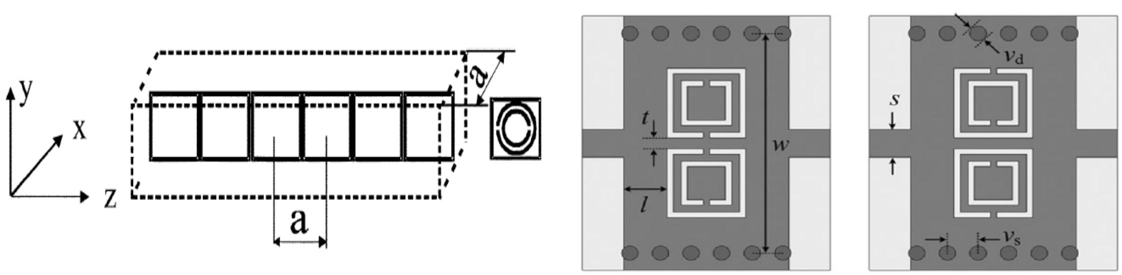

(a) (b)

Figure 2.6. Evanescent-mode realization using CSRRs integrated with waveguide cavity (a) oriented in the propagation direction [68] (b) on the broadside wall [72].

Different structures have been developed by means of CSRRs integrated with waveguide cavities where Table 2.6 summarizes the recent studies based on this technique.

Table 2.6. Comparison between evanescent-mode BPFs based on the integration of CSRRs and 3D SIW structures.

Ref.	CSRR Configuration	Size ($\lambda_g \times \lambda_g$)	FBW%	IL (dB)
[68]	Propag. Direction	3.7×0.52	5.0	25
[69]	Propag. Direction	0.68×0.21	6.2	3.5
[70]	Propag. Direction	1.90×0.40	Not Given	15
[71]	Propag. Direction	1.21×0.58	20	20
[72]	Broadside Wall	0.79×0.32	11	2.63
[73]	Broadside Wall	0.45×0.24	15-20	1.75
[74]	Broadside Wall	0.10×0.14	5.4	3.30
[76]	Both	0.49×0.40	8.7	1.20

The data presented in Table 2.6 reveal that the first configuration cannot be roughly considered as a band-pass filter [68]-[71]. As pointed out in [68], this technique can be only considered as a technique to realize the backward waves.

In contrast to the first configuration, the studies presented in [72] to [74] show that an evanescent-mode BPF can be demonstrated by placing CSRRs on the top layer of waveguide cavity. The data presented in Table 2.6 show that this configuration can realize an evanescent-mode BPF with typical fractional bandwidth (FBW) of 10%. Discussed in [74], the FBW can be decreased by sacrificing the insertion loss. In another effort, an evanescent-mode BPF has been designed and proposed using multi-layer SIW integrated with two CSRRs placing in both propagation direction and top layer of the waveguide [76]. As provided in Table 2.6, this filter provides the lowest in-band insertion loss.

2.1.3.4 Dual-band evanescent-mode band-pass filter

As discussed in the previous sections, evanescent-mode filters have become an interesting alternative to further reduce the size of 3D structure filters. However, they are mostly limited to a single frequency band and research studies on dual band BPFs are very limited [77]-[78]. These two dual-band evanescent-mode BPFs have been reported based on etching the multiple CSRRs on the top layer of the waveguide. The second band is realized using the coupling between the CSRRs unit cells on the broadside walls of the waveguide.

2.2 Principle circuit modelling: Enhanced wideband lumped element equivalent circuit of a transmission line

In filter design, the electrical length of transmission lines (TLs), employed in the coupling sections of the structure, determines not only the resonance frequency of the main resonator but also that of the coupling sections. Inspecting the structure of a basic planar band-pass filter for instance, the electrical length of the coupling sections and the main resonator are equal to $\lambda/4$ and $\lambda/2$, respectively. Therefore, as it is well-known, $\lambda/4$ electrical length plays a crucial role in determination of the main resonance frequency of the entire structure.

At the same time, lumped element-based analysis, due to its simplicity and easy-digestive characteristics, is a crucial technique to predict and model the EM behavior of transmission lines or distributed-element structures [79]-[84]. Inspecting the conventional lumped element equivalent circuits in the literature, we observe that there are different lumped element equivalent circuits corresponding to the different electrical lengths of a TL. For example, the Richard's transformation presents the lumped element equivalent circuit of an open-circuited TL as a capacitor at the frequency corresponding to $\lambda/8$ [80], and S.B. Cohn has proposed four possible L-C networks to demonstrate the inversion properties of a $\lambda/4$ transformer [79]. Although these circuits are fundamental and regularly used in filter design, they are limited to narrow band applications. Four possible L-C networks are proposed by S.B. Cohn to demonstrate the inversion properties of a quarter wavelength transformer in terms of these networks. While these models are perfect in a mathematical point of view at resonance, mathematically demonstrating the inversion property of a quarter-wavelength TL, they are unable to model and predict the behavior of a TL for the frequencies below and above the resonance frequency. More importantly, they not only exclude the impact of frequency, but also add some ambiguities to lumped element *L*-*C* equivalent circuits of a quarter-wavelength TL from a circuit point of view by including negative *C* or *L* components.

Here, we aim to investigate a wideband circuit modelling to not only include frequency dependence, but also exclude negative *L*-*C* components. Moreover, the developed *L*-*C* circuit not only meets the inversion properties of a TL at the frequency corresponding to $\lambda/4$, it but also reduces to the Richard's transformation at the frequency corresponding to $\lambda/8$. More importantly, the proposed lumped element equivalent circuit models both planar, TEM-supporting, and 3D waveguide, TE/TM-supporting, structures.

To develop the complete lumped element equivalent circuit, the conventional lumped element equivalent circuit of a TL at the critical frequency corresponding to $\lambda/4$, known as impedance-admittance inverter [79], [82]-[89], is initially discussed.

Here, due to the importance of the electrical length of $\lambda/4$, a comprehensive *L*-*C* network with no negative *L*-*C* components is advocated to not only mathematically meet the inversion properties of a TL at the critical frequency corresponding to $\lambda/4$, but also model and predict the behavior of the TL for the frequencies below and above this critical frequency.

To do this, following steps are taken in the next section.

- A simple and comprehensive, lumped element equivalent circuit is developed for a quarter-wavelength TL to model the line for a wider frequency band.
- The deficiency of Richard's transformation in the conventional lumped element models of distributed elements is discussed as a comparative example of the proposed lumped element equivalent circuit showing that the conventional models miss the impacts of TZs out of the band.

It is shown that the proposed lumped element equivalent circuit reduces to Richard's transformation at the frequency corresponding to $\lambda/8$.

2.2.1 The proposed lumped element equivalent circuit of a quarter-wavelength TL

For narrow-band applications, a discontinuity in waveguides or some types of transmission lines (TLs) (e.g., admittance or impedance inverters) is usually modeled using lumped element equivalent circuits [81]-[84]. For example, the changes in the cross section of a waveguide (H-plane) are modeled using an inductor for the frequencies below the waveguide cut-off frequency [81]. Also, an open-circuited stub is modeled using a series *L*-*C* at the frequency corresponding to $\lambda/4$ [82]. Although, these models efficiently predict their behaviors for narrow-band applications, but they are not sufficient at wide-band applications. This scenario becomes more critical when two structures with different resonance frequencies (or different electrical lengths) are analyzed (for our case, the LSI integrated with the SIW in the transverse direction). In such scenarios, the behavioral model of integrated structure is predicted only at a specific frequency by considering the resonance effect of one sub-structure at a time.

However, we believe all the details should be considered for obtaining a thorough and complete circuit model.

To develop a complete lumped element equivalent circuit modeling a TL within a wider frequency band, the circuit model in Figure 2.7(b) is used. It includes both inductive and capacitive impacts. In the transverse direction, the input impedance of a loaded TL ($Z_{in\text{-TL}}$) and its corresponding *L*-*C* components are calculated in terms of the characteristic impedance and the electrical length of the transmission line (TL). In the general case, the analysis of TL loaded with Z_L is performed in the transverse direction by considering Z_L to be either zero (short- circuited load) or infinity (open-circuited load).

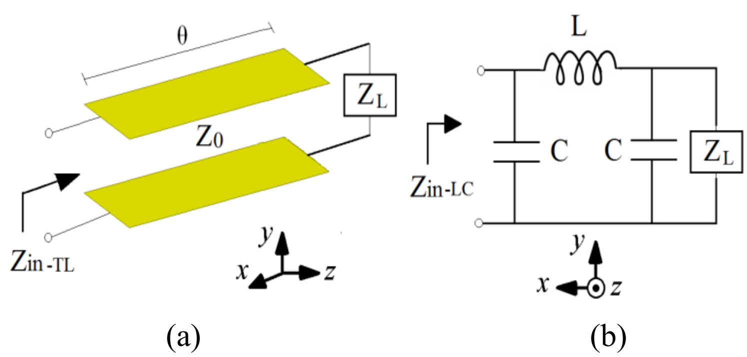

Figure 2.7. (a) Loaded TL with the electrical length of θ and the characteristic impedance of Z_0 (b) the corresponding lumped element equivalent circuit.

The equivalency between the loaded TL and its corresponding lumped element equivalent circuit in Figure 2.7 is mathematically analyzed using their input impedances. The well-known input impedance of a loaded TL with the characteristic impedance of Z_0 and the electrical length of θ can be considered as in (2-1) [82]:

$$Z_{in-TL} = Z_0 \frac{Z_L + jZ_0 \tan(\theta)}{Z_0 + jZ_L \tan(\theta)} \tag{2-1}$$

By expanding the term of tan (θ) to $2\tan(\theta/2)/(1 - tan^2(\theta/2))$, (2-1) can be considered as (2-2).

$$Z_{in-TL} = \frac{Z_L\left(1 - tan^2(\frac{\theta}{2})\right) + j2Z_0 \tan(\frac{\theta}{2})}{\left(1 - tan^2(\frac{\theta}{2})\right) + j2\frac{Z_L}{Z_0}\tan(\frac{\theta}{2})} \tag{2-2}$$

On the other hand, the input impedance of the lumped element equivalent circuit given in Figure 2.7(b) can be calculated as follows:

$$Z_{in-LC} = \frac{Z_L(1 - \omega^2 LC) + j\omega L}{(1 - \omega^2 LC) + j\omega C Z_L (2 - \omega^2 LC)} \tag{2-3}$$

To map the numerator and denominator of equation (2-2) to those of the corresponding lumped element equivalent circuit in (2-3), two well-known short- and open-circuited stubs are considered. In the short-circuited analysis of the TL and its corresponding *L-C* circuit (Z_L=0), we get the following equations:

$$Z_L = 0 \rightarrow Z_{in-TL} = jZ_0 \tan(\theta) = \frac{j2Z_0 \tan(\frac{\theta}{2})}{1 - tan^2(\frac{\theta}{2})} \tag{2-4}$$

$$Z_L = 0 \rightarrow Z_{in-LC} = \frac{j\omega L}{1 - \omega^2 LC} \tag{2-5}$$

The values of the *L* and *C* components can be calculated in terms of the Z_0 and θ parameters by equating the denominator and the numerator of (2-4) to those of (2-5).

$$X_L = \omega L = 2Z_0 \tan(\frac{\theta}{2}) \tag{2-6}$$

$$X_C = \omega C = \frac{1}{2Z_0} \tan(\frac{\theta}{2}) \tag{2-7}$$

Similarly, in the open-circuited analysis of the TL and its corresponding *L*-*C* circuit (Z_L=∞), we get the following equations:

$$Z_L = \infty \rightarrow Z_{in-TL} = \frac{Z_0}{j\,tan(\theta)} = \frac{Z_0(1-tan^2(\frac{\theta}{2}))}{j2tan(\frac{\theta}{2})} \tag{2-8}$$

$$Z_L = \infty \rightarrow Z_{in-LC} = \frac{1-\omega^2 LC}{j\omega C(2-\omega^2 LC)} \tag{2-9}$$

The following simplification is done in the denominator of (2-9) for the frequency corresponding to $\lambda/4$ or $\theta=\pi/2$.

$$P(\omega) = 2 - \omega^2 LC = 1 + \left[1 - \tan\left(\frac{\theta}{2}\right)^2\right] \leftrightarrow at\,\frac{\lambda}{4}\,or\;\theta = \pi/2, P(\omega) = 1 \tag{2-10}$$

Note that the lumped element equivalent circuit of the open-circuited stub (Z_L=∞) will be a *C*-*L*-*C* π-network circuit shown in Figure 2.8. This circuit consists of two parts in parallel; a series *L*-*C* circuit and a capacitor where the series *L*-*C* circuit represents the behavior of the line at the resonance (at the frequency corresponded to $\lambda/4$), otherwise, the capacitor *C* represents the behavior of the line at the other frequencies. Therefore, (2-10) is derived based on the assumption of the narrowband behavior of the series *L*-*C* circuit at $\theta=\pi/2$ and the entire circuit (the series *L*-*C* circuit parallel with *C*) models the line for wider frequency band.

Now, the corresponding lumped element *L* and *C* components can be calculated for the open-circuited case in terms of characteristic impedance and electrical length as follows:

$$X_C = \omega C = \frac{2}{Z_0} \tan(\frac{\theta}{2}) \tag{2-11}$$

$$X_L = \omega L = \frac{Z_0}{2} \tan(\frac{\theta}{2}) \tag{2-12}$$

As a conclusion for the analysis, the lumped element equivalent circuits of the short- and open-circuited stubs can be derived in a complete way as provided in Figure 2.8.

It should be noted that the main objective of this analysis, in comparison to the conventional ones, is to study the lumped element equivalent circuit of distributed element in a comprehensive way to include the different behaviors of distributed elements in different situations. For example, a short-circuited stub or a slice of SIW waveguide in the transverse direction is modeled with an inductor for frequencies below cut-off frequency of the structure [81]; while it can be shown that its complete lumped element equivalent circuit can be considered as a parallel *L*-*C* circuit. The *L* and *C* components stand for the lumped element equivalent circuit of the structure below and above its cut-off frequency, respectively. Similarly, an open-circuited stub is usually modeled with a series *L*-*C* circuit at the resonance [84]; while the Richard's transformation [80] models the stub with a capacitor. Later, it is shown that the proposed lumped element equivalent circuit is beneficial to include both transmission poles and transmission zeros in the design of a filter in comparison to Richard's transformation technique.

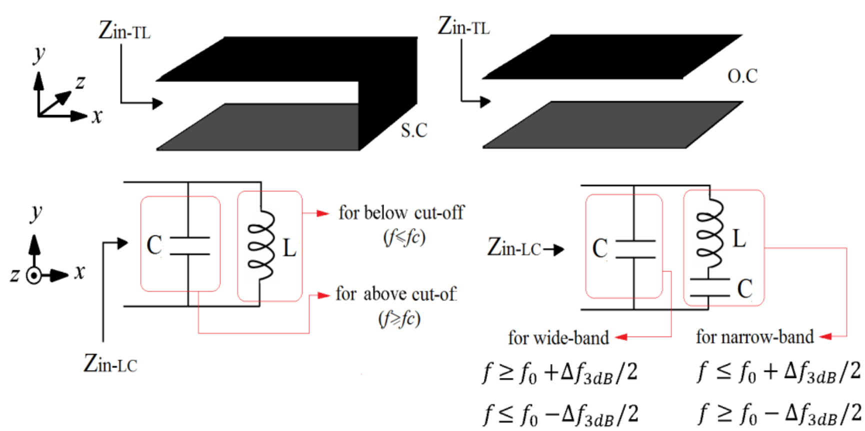

(a) (b)

Figure 2.8. (a) Short- and (b) open-circuited distributed elements and their lumped elements equivalent circuits for wide-band applications.

Note that this lumped element circuit analysis will be extensively used in the design of integrated structures specifically L-shaped irises integrated with SIW in Chapter 6 to realize either TZs or evanescent poles.

2.2.2 Evaluating the lumped element equivalent circuit of a quarter-wavelength TL as a function of frequency

According to the discussion on the current ambiguities in the conventional lumped element equivalent circuit of a quarter-wavelength TL in Section 2.2.1, here, the suggested *L*-*C* network is discussed and evaluated as a function of frequency.

1- Unlike the conventional models, the proposed *L*-*C* network does not consist of negative lumped elements, as shown in Figure 2.7(b).

2- To show the functionality of the circuit in terms of frequency, the proposed network is similarly inspected using a short-circuited load or $Y_L=\infty$ ($Z_L=0$) as shown in Figure 2.9(b). The short-circuited load is parallel with one of the capacitors where it bypasses this capacitor. As the result, the circuit in Figure 2.9(b) is reduced to the one in Figure 2.9(c). In this case, the calculated input admittance will be equal to $Y_{in} = (1-\omega^2 LC)/j\omega L$. Comparing the two calculated input admittances of the conventional and the proposed lumped element networks reveals that the conventional one inverts the load of $Y_{in}=\infty$ to $Y_{in}=0$ regardless of frequency; while the proposed one inverts the load of $Y_{in}=\infty$ to $Y_{in}=0$ when the condition of $\lambda/4$ is met or $1-\omega^2 LC = 0$ which corresponding to $\left(1-tan^2(\frac{\theta}{2})\right) = 0$ resulting $\theta = \frac{\pi}{2}$ or $\ell=\lambda/4$.

3- Inspecting the proposed equivalent *L*-*C* network of a TL at the frequency corresponding to $\lambda/4$ with an open-circuited load or $Z_L=\infty$, the input impedance of the TL in (2-1) reduces to the one in (2-8). This reduced input impedance inverts the load of $Z_L=\infty$ to the load of $Z_L=0$ at $\ell=\lambda/4$ or $\theta=\pi/2$.

4- It can be shown that at the critical frequency corresponding to $\lambda/4$ or $\theta=\pi/2$, the condition of resonance is met by which $1-\omega^2 LC = 1-tan^2\left(\frac{\theta}{2}\right) = 0$ results. Therefore, using these conditions, the equations (2-2) and (2-3) are reduced to the following:

$$Z_{in-TL} = \frac{Z_0^2}{Z_L}, Z_{in-LC} = \frac{L}{CZ_L} \rightarrow Z_0 = \sqrt{\frac{L}{C}} \tag{2-14}$$

Inspecting the calculated characteristic impedance in (2-14), we observe that it includes both the inductive (magnetic) and capacitive (electric) properties of the material.

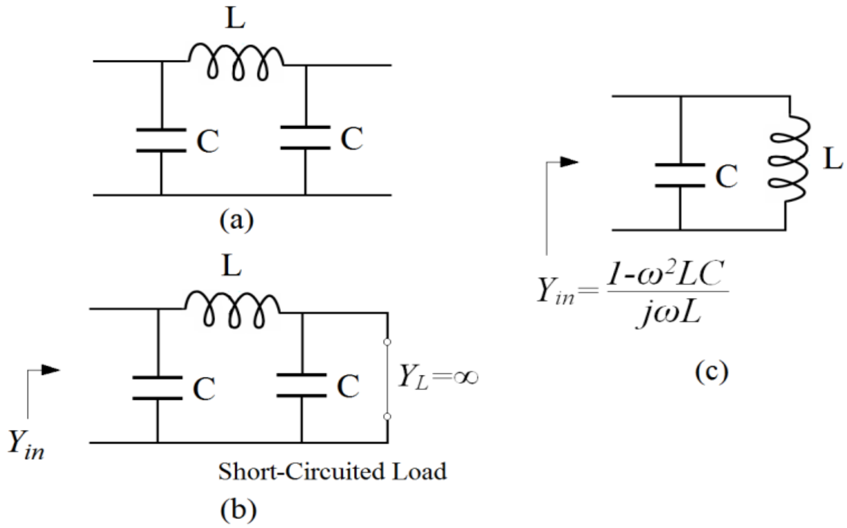

Figure 2.9. (a)The proposed Lumped element network of a TL at the frequency corresponding to $\lambda/4$ (b) the network with short-circuited load (c) input admittance of this inverter with short-circuited load or $Y_L=\infty$.

2.2.3 Filter design using lumped and distributed elements

2.2.3.1 Richard's transformation

Richard's transformation [80] accompanied by Kuroda's identities are some of the most useful tools in filter design at microwave frequencies by which lumped elements are converted to distributed elements or transmission line (TL) sections [84]. In this section, the objective is to show while these techniques are significantly effective in the design of microwave components, they are not still able to provide a comprehensive modeling in transforming lumped elements to distributed ones or TLs.

To address the deficiency of the Richard's transformation, the distributed-element and lumped-element performances of a low-pass filter, presented in [84], is exemplified. A filter is a device to partially pass a signal at some specific frequencies and simultaneously suppress the signal at other frequencies. Transmission poles and zeros are responsible to filter the signal, therefore, transmission zeros (TZs) are as crucial as transmission poles in in filter design. Referring to the lumped element equivalent circuit provided by Richard's transformation reveals that it merely models the transmission poles or the pass-band of the distributed elements [84]. Figure 2.10 shows the performance of a distributed-element filter in comparison to that of a corresponded lumped element circuit derived by Richard's transformation. Inspecting the results, we observe that the performance of the lumped-element filter is in a good agreement with that of distributed elements only up to the cut-off frequency or in the pass-band region, while it is not matched outside of the pass-band, ignoring the TL realized by distributed-element circuit.

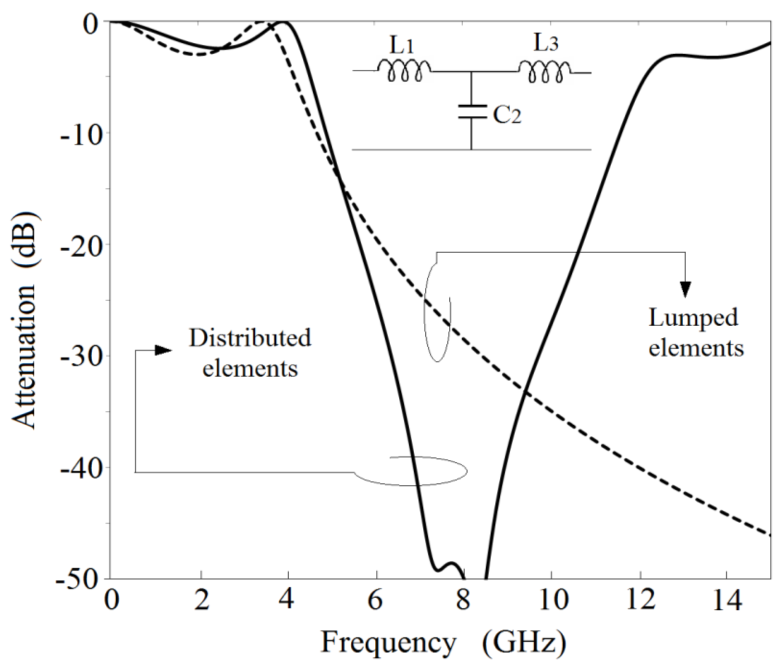

Figure 2.10. "Amplitude responses of lumped-element and distributed low-pass filter" [84], EM simulation in ADS on a 50-mil- thickness substrate with dielectric constant of 2.2 with normalized L_1=L_3=3.3487 and C_2=0.7117 provided in [84].

2.2.3.2 The proposed transformation

In this study, the efficiency of Richard's transformation in filter design is studied in more detail and complete equivalent lumped element circuits are discussed to include not only transmission poles in pass-band but also transmission zeros out of the pass-band. It is shown that the new lumped element equivalent circuit models not only the transmission poles but also the transmission zeros of the distributed-element structure. To address the deficiency of the conventional techniques, an example of a low-pass filter (LPF) presented in [84] is discussed. Discussed in [84] and Figure 2.10, the conventional lumped element equivalent circuit of the LPF in Figure 2.11 has been presented as a combination of two inductors and one shunt capacitor. However, as shown in Figure 2.11(a), the complete *L*-*C* equivalent circuit of the filter is derived using the circuits in Figure 2.7 and Figure 2.8. In this modeling, each section of the layout is considered as an individual quarter wavelength TL and. For example, the open-circuited stub with characteristic impedance of 64.9 Ω is modeled with a capacitor (C_{65}) integrated with a series L_{65}-C_{65} circuit (analyzed in the transverse direction) while the TL with characteristic impedance of 217.5 Ω is modeled with two shunt capacitors (C_{217}) integrated with an inductor (L_{217}) in the propagation direction. The lumped-element values are then calculated using the equations in (2-11)-(2-12). Table 2-7 gives the calculated values for the lumped element equivalent circuit of the LPF in Figure 2.11(a).

Table 2.7 Calculated lumped elements of the LPF in Figure 2.11

Inductor	L_{50}	L_{65}	L_{70}	L_{217}
Value (nH)	1.00	0.64	0.70	2.15
Capacitor	C_{50}	C_{65}	C_{70}	C_{217}
Value (pF)	0.40	0.61	0.57	0.18

With no optimization, the calculated lumped elements in Table 2-7 are simulated and compared to the EM performance of the distributed elements. Figure 2.11(b) compares the lumped-element and distributed-element performances of the LPF derived using the Richard's transformation and the proposed technique.

Inspecting the results in Figure 2.11(b), we observe that the proposed lumped element equivalent circuit models not only the transmission poles but also the transmission zeros of the distributed-element structure.

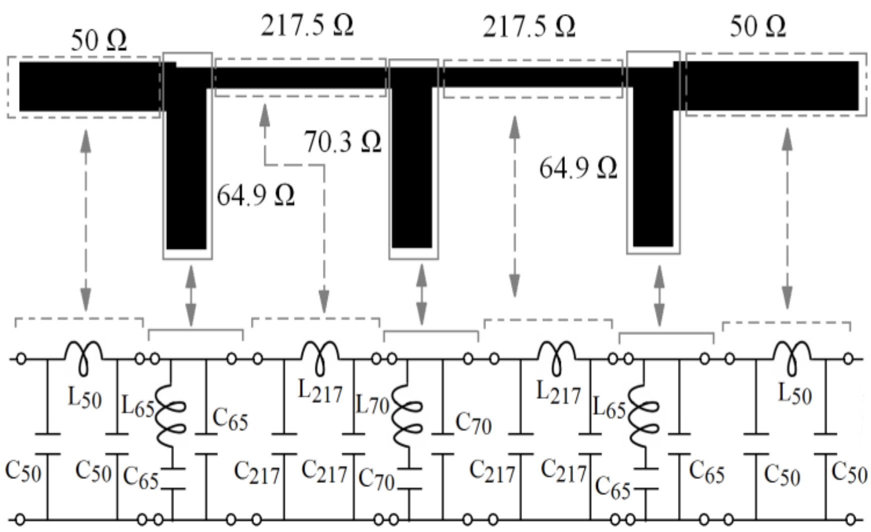

(a)

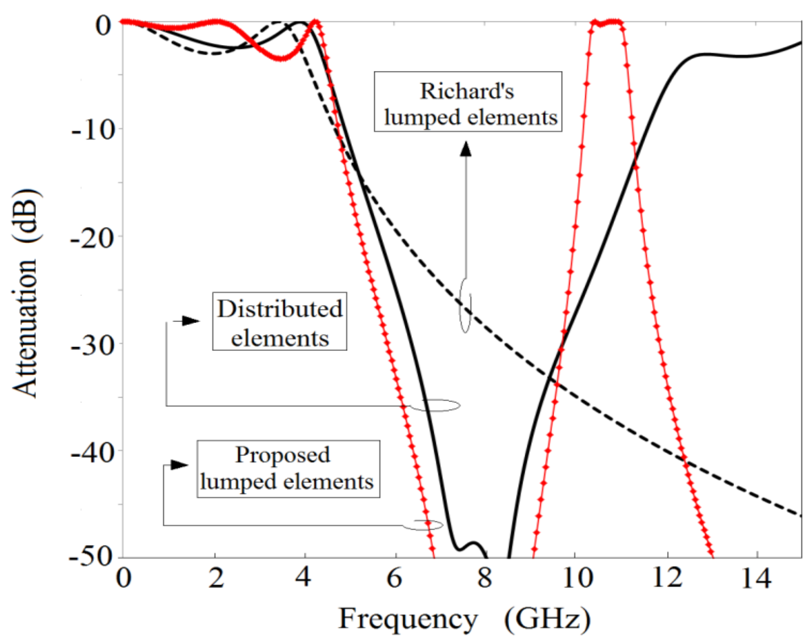

(b)

Figure 2.11. (a) Layout of low-pass filter in [84] and its complete lumped element equivalent circuit (b) comparison between the *L-C* performance of the filter using Richard's transformation (dashed black lines) and the proposed technique (marked red lines) based on new lumped elements' circuit of quarter-wavelength TL and distributed elements (solid black lines).

2.3 References

[1] FCC Code of Federal Register (CFR), Title 47, pt. 15, United States.

[2] M. Mokhtari, J. Bornemann, "Ultra-wideband and notched wideband filters with grounded vias in microstrip technology," *Asia Pacific Microw., Conf.*, pp.1-4, Dec. 2008.

[3] G-M. Yang, et al., "Small ultra-wideband (UWB) bandpass filter with notched band," *IEEE Microw. Wireless Compon. Lett*., vol.18, no.3, pp. 176-178, Mar. 2008.

[4] P. Mondal and Y. L. Guan, "A coplanar stripline ultra-wideband bandpass filter with notch-band*," IEEE Microw. Wireless Compon Lett*., vol.20, no.1, pp.22-24, Jan. 2010.

[5] S.G. Mao, et al., "Compact ultra-wideband conductor–backed coplanar waveguide bandpass filter with a dual band-notched response," *IEEE Microw. Wireless Compon Lett*., vol.19, no.3, pp.149-151, Mar. 2009.

[6] M. Nosrati and M. Daneshmand, "Compact microstrip UWB double/single notch-band BPF based on wave's cancellation theory," *IET Microw. Antennas Propag*, vol.6, no.8 pp.862-868, Jun. 2012.

[7] F. Wei, Q. Yi Wu, X. W. Shi, and L. Chen "Compact UWB bandpass filter with dual notched bands based on SCRLH resonator," *IEEE Microw. Wireless Compon Lett.*, vol. 21, no.1, pp.28-30, Jan. 2011.

[8] Z-C. Hao, J-S. Hong, J. P. Parry, and D. P. Hand, "Ultra-wideband bandpass filter with multiple notch-bands using nonuniform periodical slotted ground structure," *IEEE Trans. Microw. Theory and Tech.*, vol.57, no.12, pp.3080-3088, Dec. 2009.

[9] Z.-C. Hao, et al., "Ultra-wideband bandpass filter with multiple notch-bands on multilayer liquid crystal polymer substrate," *IET Microw. Antennas Propag*., vol.3, no.5, pp.749-756, Aug. 2009.

[10] X. Luo, J.-G. Ma, K. S. Yeo, and E. P. Li, "Compact ultra-wideband (UWB) bandpass filter with ultra-narrow dual- and quad-notched bands," *IEEE Trans. Microw. Theory and Tech*., vol.59, no.6, pp.1509-1519, Jun. 2011.

[11] M. Mokhtaari and J. Bornemann, "Tunable notch characteristics in microstrip ultra-wideband filters," *Asia Pacific Microw., Conf.*, pp. 937-940, Dec. 2009.

[12] Y. Yamamoto, K. Li, and O. Hashimoto, "Tunable sharp notch filter for UWB application," *Microw. Opt. Tech. Lett*., vol.50, no.10, pp.2712-2715, Oct. 2008.

[13] H. R. Arachchige, J. S. Hong, and Z. C. Hao, "UWB bandpass filter with tunable notch on liquid crystal polymer substrate," *Asia-Pacific Microw. Conf.*, pp.1-4, Dec. 2008.

[14] F. Wei, L. Chen, X.-W. Shi, and B. Liu, "Compact UWB bandpass filter with tunable notch-band based on folded SIR," *Electronic Lett.*, vol.47, no.22, pp.1229-1230, Oct. 2011.

[15] F. Wei, L. Chen, X.-W. Shi, and C.-J. Gao, "UWB bandpass filter with one tunable notch-band based on DGS," *J. of Electromagn. Waves and Appl.*, vol.26, pp.673-680, Jul. 2012.

[16] G. Cusmai, M. Brandolini, P. Rossi, and F. Svelto, "A 0.18-μm CMOS selective receiver front-end for UWB applications," *IEEE J. Solid- State Circuits*, vol.41, no.8, pp.1764-1771, Aug. 2006.

[17] A. Vallese, A. Bevilacqua, C. Sandner, M. Tiebout, A. Gerosa, and A. Neviani, "Analysis and design of an integrated notch filter for the rejection of interference in UWB systems," *IEEE J. Solid-State Circuits*, vol.44, no.2, pp.331-343, Feb. 2009.

[18] G. M. Rebeiz, *RF MEMS: Theory, Design, and Technology*, Hoboken, NJ: Wiley, 2003.

[19] Z. Wu, Y. Shim, and M. Rais-Zadeh, "Miniaturized UWB filters integrated with tunable notch filters using a silicon-based integrated passive device technology," *IEEE Trans. Microw. Theory and Tech.*, vol.60, no.3, pp.518-527, Mar. 2012.

[20] M. Nosrati and M. Daneshmand, "Compact microstrip UWB double/single notch-band BPF based on wave's cancellation theory," *IET Microw. Antennas Propag*, vol.6, no.8, pp 862-868, Jun. 2012.

[21] M. Nosrati and M. Daneshmand, "Developing single layer ultra-wide band band-pass filter with multiple (triple and quadruple) notches," *IET Microw. Antennas Propag.*, vol.7, no.8 pp.612-620. Jun. 2013.

[22] M. Nosrati, N. Vahabisani, and M. Daneshmand, "A novel tunable double notch-band UWB BPF using MEMS capacitors," *IEEE/MTT-S Int. Microw. Symp,* Jun. 2013.

[23] M. Nosrati, N. Vahabisani, and M. Daneshmand, "Compact MEMS-based ultra wideband CPW band-pass filters with single/double tunable notch-bands," *IEEE Trans. Compon., Pack. Manufac Tech.*, vol.4, no.9, pp.1451-1460, Aug. 2014.

[24] Y.C. Chiou and G.M. Rebeiz, “A tunable three-pole 1.5-2.2-GHz bandpass filter with bandwidth and transmission zero control,” *IEEE Trans. Microw. Theory and Tech*., vol.59, no.11, pp.2872-2878, Nov. 2011.

[25] A. Velez, J. Bonache, and F. Martin, “Varactor-loaded complementary split ring resonators (VLCSRR) and their application to tunable metamaterial transmission lines,” *IEEE Microw. Wireless Compon. Lett*., vol.18, no.1, pp.28-30, Jan. 2008.

[26] J. Long, C. Li, W. Chi, J. Huangfu, and L. Ran, “A tunable microstrip bandpass filter with two independently adjustable transmission zeros,” *IEEE Microw. Wireless Compon. Lett*., vol.21, no.2, pp.74-76, Feb. 2011.

[27] W.H. Tu, “Compact double-mode cross-coupled microstrip bandpass filter with tunable transmission zeros,” *IET Microw Antennas Propag*., vol.2, no.4, pp.373-377, Jun. 2008.

[28] M. Guglielmi, F. Montuati, L. Pellegrini, and P. Arcioni, “Implementing transmission zeroes in inductive-window bandpass filters,” *IEEE Trans. Microw. Theory and Tech*., vol.43, no.8, pp.1911-1915, Aug. 1995.

[29] U. Rosenberg, S. Amari, and J. Bornemann, “Inline TM_{110}-mode filters with high-design flexibility by utilizing bypass coupling of nonresonating $TE_{10/01}$ modes,” *IEEE Trans. Microw. Theory and Tech*., vol.51, no.6, pp.1735-1742, Jun. 2003.

[30] S. Amari and U. Rosenberg, “Synthesis and design of novel in-line filters with one or two real transmission zeros,” *IEEE Trans. Microw. Theory and Tech*., vol.52, no.5, pp.1464-1478, May 2004.

[31] I. Ohira, H. Deguchi, M. Tsuji, and H. Shigesawa, “Novel waveguide filters with multiple attenuation poles using dual-behavior resonance of frequency-selective surfaces,” *IEEE Trans. Microw. Theory and Tech*., vol.53, no.11, pp.3320-3326, Nov. 2005.

[32] Amari and U. Rosenberg, “Characteristics of cross (bypass) coupling through higher/lower order modes and their applications in elliptic filter design,” *IEEE Trans. Microw. Theory and Tech*., vol.53, no.10, pp.3135-3141, Oct. 2005.

[33] M. Guglielmi, P. Jarry, E. Kerherve, O. Requebrm, and D. Schmitt, “A new family of all-inductive dual-mode filters,” *IEEE Trans. Microw. Theory*, vol.49, no.10, pp. 1764-1769, Oct. 2001.

[34] S. Bastioli, C. Tomassoni, and R. Sorrentino, “A new class of waveguide dual-mode filters using TM and nonresonating modes,” *IEEE Trans. Microw. Theory and Tech*., vol.58, no.12, pp.3909-3917, Dec. 2010.

[35] K. Gong, W. Hong, Y. Zhang, P. Chen, and C.J. You, “Substrate integrated waveguide quasi-elliptic filters with controllable electyric and magnetic mixed coupling,” *IEEE Trans. Microw. Theory and Tech*., vol.60, no.10, pp.3071-3077, Oct. 2012.

[36] M. Garai, J. A. R. Cruz, J. M. Rebollar, M. J. P. Cruz, A. O. Navarro, and I. H. Carpintero, “Synthesis and design of in-line N-order filters with N real transmission zeros by means of extracted poles implemented in low-cost rectangular H-plane waveguide,” *IEEE Trans. Microw. Theory and Tech*., vol.53, no.5, pp.1636-1642, May 2005.

[37] D.J. Kim and J.-H. Lee, “Partial H-plane filters with multiple transmission zeros,” *IEEE Trans. Microw. Theory and Tech*., vol.56, no.7, pp.1693-1698, Jul. 2008.

[38] M. Ohira, H. Deguhi, M. Tsuji, and H. Shigeswa, “Novel waveguide filters with multiple attenuation poles using dual-behavior resonance of frequency-selective surfaces,” *IEEE Trans. Microw. Theory*, vol.53, no.11, pp.3320-3326, Nov. 2005.

[39] X.P. Chen, K. Wu, and D. Drolet, “Substrate integrated waveguide filter with improved stopband performance for satellite ground terminal,” *IEEE Trans. Microw. Theory and Tech*., vol.57, no.3, pp.674-683, Mar. 2009.

[40] W. Shen, W.Y. Yin, and X.W. Sun, “Compact substrate integrated waveguide transversal filter with microstrip dual-mode resonator,” *J. of Electromagn. Waves and Appl*., vol.24, pp.1887-1896, 2010.

[41] H. Shigesawa, M. Tsuji, T. Nakao, and K. Takiayama, “Two-path cutoff waveguide dielectric resonator filters,” *IEEE Trans. Microw. Theory and Tech*., vol.37, no.7, pp. 1105-1112, Jul. 1989.

[42] S. Bastioli and R. Snyder, “Inline pseudoelliptic TE_{01}-mode dielectric resonator filters using multiple evanescent modes to selectively bypass orthogonal resonators,” *IEEE Trans. Microw. Theory and Tech*., vol.60, no.12, pp.3988-4001, Dec. 2012.

[43] O. Glubokov and D. Budimir, “Extraction of generalized coupling coefficients for inline extracted pole filters with nonresonating nodes,” *IEEE Trans. Microw. Theory and Tech*., vol.59, no.12, pp.3023-3029, Dec. 2011.

[44] R. Tomassoni and R. Sorrentino, “A new class of pseudoelliptic waveguide filters using dual-post resonators,” *IEEE Trans. Microw. Theory and Tech*., vol.61, no.6, pp. 2332-2339, Jun. 2013.

[45] Y. Wang and M. Yu, “True inline cross-coupled coaxial cavity filters,” *IEEE Trans. Microw. Theory and Tech*., vol.57, no.12, pp.2958-2965, Dec. 2009.

[46] S. Bastioli, L. Marcaccioli, and R. Sorrentino, “Waveguide psedoelliptic filters using slant and transverse rectangular ridge resonators,” *IEEE Trans. Microw. Theory*, vol.49, no.10, pp.1764-1769, Oct. 2001.

[47] F. Mira, J. Mateu, S. Cogollos, and V. E. Boria, “Design of ultra-wideband substrate integrated waveguide (SIW) filters in zigzag topology,” *IEEE Microw. Wireless Compon. Lett*., vol.19, no.5, pp.281-283, May 2009.

[48] I. V. Lebedev and E. M. Guttsait, “Resonator of the subcritical waveguide type,” *Radiotekh Electron*, Oct.1956.

[49] E. T. Jaynes, “Ghost modes in imperfect waveguides,” *Proceedings of the IRE*, pp.416-418, Feb. 1958.

[50] W.A. Edson, “Microwave filters using ghost-mode resonance,” *IRE Electron Components Conf*., vol.19, p.2, 1961.

[51] G. Craven, “Waveguide below cutoff: a new type of microwave integrated circuit,” *Microwave J*., vol.13, pp.51, Aug.1970.

[52] G. Craven, “Waveguide bandpass filters using evanescent modes,” *Electron Lett*., vol.2. no.7, pp.251-252, Jul. 1966.

[53] G. F. Craven and C. K. Mok, “The design of evanescent mode waveguide bandpass filters for a prescribed insertion loss characteristic,” *IEEE Trans. Microw. Theory and Tech*, vol.19, no.3, pp.295-308, Mar. 1971.

[54] R. Levy, “Theory of direct-coupled-cavity filters,” *IEEE Trans. Microw. Theory and Tech*., vol.15, no.6, pp.340-348, Jun. 1967.

[55] R.V. Snyder, “New application of evanescent mode waveguide to filter design,” *IEEE Trans. Microw. Theory and Tech*, vol.25, no.12, pp.1013-1021, Dec. 1977.

[56] R.V. Snyder, “Broadband waveguide or coaxial filters with wide stopbands, using a stepped-wall evanescent mode approach,” *Microwave J.*, vol.26, pp.53-58, Dec. 1983.

[57] Q. Zhang and T. Itoh, “Computer-aided design of evanescent-mode waveguide filter with nontouching E-plane fins,” *IEEE Trans. Microw. Theory and Tech*., vol.36, no.2, pp.404-412, Feb. 1988.

[58] H.C. Chang and K.A. Zaki, “Evanescent-mode coupling of dual-mode rectangular waveguide filters,” *IEEE Trans. Microw. Theory and Tech*., vol.39, no.8, pp.1307-1312, Aug. 1991.

[59] T. Shen and K.A. Zaki, “Length reduction of evanescent-mode ridge waveguide bandpass filters,” *Prog. In Electromag. Res.,* PIER 40, pp.71-90, 2003.

[60] L. Harle and L. P. B. Katehi, “A silicon micromachined four-pole linear phase filter,” *IEEE Trans. Microw. Theory and Tech*, vol.52, no.6, pp.1598-1607, Jun. 2004.

[61] X. Gong, A. Margomenos, B. Liu, S. Hajela, L. P.B. Katehi, and W. J. Chappell, “Precision fabrication techniques and analysis on high-Q evanescent-mode resonators and filters of different geometries,” *IEEE Trans. Microw. Theory and Tech*, vol.52, no.11, pp.2557-2566, Nov. 2004.

[62] H. Joshi, H. H. Sigmarsson, D. Peroulis, and W. Chappell, “Highly loaded evanescent cavities for widely tunable high-Q filters,” *IEEE/MTT-S Int. Microw. Symp*., pp.2133-2136, Jun. 2007.

[63] S. J. Park, I. Reines, and G. Rebeiz, “High-Q RF-MEMS tunable evanescent-mode cavity filter,” *IEEE/MTT-S Int. Microw. Symp.,* pp.1145-1148, Jun. 2009.

[64] X. Liu, L.P.B. Katehi, W.J. Chappell, and D. Peroulis, “A 3.4-6.2GHz continuously tunable electrostatic MEMS resonator with quality factor of 460-530,” *IEEE/MTT-S Int. Microw. Symp*., Jun. 2009.

[65] H. Joshi, H.H. Sigmarsson S. Moon, D. Peroulis, and W. J. Chappell, “High –Q fully reconfigurable tunable bandpass filters,” *IEEE Trans. Microw. Theory and Tech*., vol.57, no.12, pp.3525-3533, Dec. 2009.

[66] S. Moon, H. H. Sigmarsson, H. Joshi, and W.J. Chappell, “Substrate integrated evanescent-mode cavity filter with a 3.5 to 1 tuning ration,” *IEEE Microw. Wireless Compon. Lett*. vol.20, no.8, pp.450-452, Aug. 2010.

[67] S. J. Park, I. Reines, C. Patel and G. Rebeiz, “High-Q RF-MEMS 4-6 GHz tunable evanescent-mode cavity filter,” *IEEE Trans. Microw. Theory and Tech*., vol.58, no.2, pp.381-389, Feb. 2010.

[68] S. Hrabar, J. Bartolic and Z. Sipus, “Waveguide miniaturization using uniaxial negative permeability metamaterial," *IEEE Trans. Antenn*as *Propag*., vol.53, no.1, pp.110-119, Jan. 2005.

[69] T. Yang, P.L. Chi, R. Xu, and W. Lin, “Folded substrate integrated waveguide based composite right/left-handed transmission line and its application to partial H-plane filters,” *IEEE Trans. Microw. Theory and Tech*., vol.61, no.2, pp.789-799, Feb. 2013.

[70] F. Farzami, K. Forooraghi, and M. Norooziarab, “Design and modeling of a miniaturized substrate integrated waveguide using embedded SRRs,” *IEEE Anten. Wireless. Propag. Lett.,* vol.10, pp.713-716, 2011.

[71] F. Farzami and M. Norooziarab, “Experimental realization of tunable transmission lines based on single-layer SIWs loaded by embedded SRRs,” *IEEE Trans. Microw. Theory and Tech*., vol.61, no.8, pp.2848-2857, Aug. 2013.

[72] Y.D. Dong, T. Yang, and T. Itoh, “Substrate integrated waveguide loaded by complementary split-ring resonators and its application to miniaturized waveguide filters,” *IEEE Trans. Microw. Theory and Tech*., vol.57, no.9, pp.2211-2223, Sep. 2009.

[73] Q.L. Zhang, W.Y. Yin, and S. He, “Evanescent-mode substrate integrated waveguide (SIW) filters implemented with complementary split ring resonators,” *Prog. Electromag. Res.,* vol.111, pp.419-432, 2011.

[74] Y. Zheng, M. Sazegar, H. Maune, X. Zhou, J. R. Binder, and R. Jakoby, “Compact substrate integrated waveguide tunable filter based on ferroelectric ceramics,” *IEEE Microw. Wireless Compon. Lett*. vol.21, no.9, pp.477-479, Sep. 2011.

[75] D. E. Senior, X. Cheng, and Y.K. Yoon, “Electrically tunable evanescent mode half-mode substrate-integrated-waveguide resonators,” *IEEE Microw. Wireless Compon. Lett*, vol.22, no.3, pp.123-125, Mar. 2012.

[76] L.S. Wu, X.L. Zhou, W.Y. Yin, L. Zhou, and J.F. Mao, “A substrate-integrated evanescent-mode waveguide filter with nonresonating node in low-temperature co-

fired ceramic," *IEEE Trans. Microw. Theory and Tech*., vol.58, no.10, pp.2654-2662, Oct. 2010.

[77] Y. Dong and T. Itoh, "Miniaturized dual-band substrate integrated waveguide filters using complementary split-ring resonators," *IEEE/MTT-S, Int. Microw. Symp*., 2011.

[78] D.E. Senior, X. Cheng, and Y.K. Yoon, "Dual-band filters using complementary split-ring resonator and capacitive loaded half-mode substrate-integrated-waveguide," *IEEE/MTT-S, Int. Microw. Symp*., pp.1-2, Jul. 2012.

[79] S.B. Cohn, "Direct-coupled-resonator filters," *Proc. IRE*, vol. 45, no.2, pp.187-196, Feb. 1957.

[80] P. I. Richard, "Resistor-transmission line circuits," *Proceedings of the IRE*, vol.36, no.2, pp.217-220, Feb. 1948.

[81] N. Marcuvitz, *Waveguide Handbook*, New York, NY, USA: McGraw-Hill, 1951.

[82] G.L. Matthaei, L. Young, E.M.T. Jones, *Microwave Filters, Impedance-Matching Networks, and Coupling Structures*, McGraw-Hill, 1964.

[83] J. A. G. Malherbe, *Microwave Transmission Line Filters*, Artech House, Dedham, Mass., 1979.

[84] D. M. Pozar, *Microwave Engineering*, 3rd Ed. New York: Wiley, 2005.

[85] L. Young, "Table for cascaded homogeneous quarter-wave transformers," *IRE Trans. Microw. Theory and Tech*., vol.7, no.2, pp.233-237, Apr. 1959.

[86] L. Young, "Direct-coupled cavity filters for wide and narrow band-widths," *IEEE Trans. Microw. Theory and Tech*., vol.11, no.3, pp.162-178, May 1963.

[87] R. Levy, "Theory of direct-coupled-cavity filters," *IEEE Trans. Microw. Theory and Tech*., vol.15, no.6, pp.340-348, Jun. 1967.

[88] J. D. Rhodes, "The generalized direct-coupled cavity linear phase filter," *IEEE Trans. Microw. Theory and Tech*., vol.18, no.6, pp.308-313, Jun. 1970.

[89] J.-S. Hong and M. J. Lancaster, *Microstrip Filters for RF/Microwave Applications*, John Wiley & Sons, 2001.

[90] D. Kajfez, *Q-Factor-Encyclopedia of RF and Microwave Engineering,* John Wiley & Sons, Inc, 2005.

Chapter 3 Compact microstrip UWB double/single notch-band BPF based on wave's cancellation theory

3.1 Introduction

Ultra-wideband band-pass filters are highly demanded since the U.S. FCC authorized the unlicensed use of the ultra-wide frequency spectrum range for commercial purposes. In the recent years, many different models have been introduced to realize wide and ultra-wide BPFs mainly designed by means of multi-mode resonators (MMR) [1]–[6] and defected ground structures [7]. While these models offer effective techniques to design UWB BPFs with or without a notch-band BPF, they still suffer from a long list of deficiencies such as:

A large electrical size [1]-[2], employing via-holes or short-circuited stubs [1]-[4] and [6], lack of transmission zeroes for high selectivity resulting in narrow upper stop-bands [5], ultra-narrow-band notch-band [6], incompatible with Monolithic Microwave Integrated Circuits (MMIC) [7].

Despite these drawbacks, there is an ever-increasing need for multi-notches UWB band-pass. The need to avoid interference from existing wireless communication signals makes the design of multi notch-band UWB BPFs a subject of interest. No doubt, the rapid growth of communication systems will increase the need for notch bands even further. To date, several UWB BPFs have been reported realizing double/multi notch-bands; however, these UWB BPFs suffer from a series of drawbacks including a large CPW periodical structure with SIW and SIR [8], a large size based on a dual-line coupling structure [9], the need for a multilayer non-uniformed periodical structure including short-circuited stub resonators [10], the use of a complicated structure including the multilayer conductor-backed coplanar waveguide [11] or the multilayer LCP technology [12]-[13].

While the proposed BPF in [12] provides dual notch-bands, its notches are still very narrow-band and incapable of being tuned to an arbitrary notch-band. The double notch-band BPFs introduced in [12]-[13] are reported to realize notches with wider bandwidth, though at the expense of a complicated 11-layered structure. Additionally, in [14], another approach has been proposed to design a dual notch-band BPF based on left/right-handed technique embraced by using many via-holes. Additionally, another single notch-band UWB BPF has been proposed in [15]; however, it is not capable of realizing more than one notch-band. Moreover, a direct analysis has not been presented to establish the notch-band in this study.

In this Chapter, a novel approach is introduced to design an ultra-wideband (UWB) band-pass filter (BPF) that demonstrates double/single notch-bands using a simple micro-strip transmission line. Two different UWB BPFs are designed and proposed using two parallel T-shaped and tri-section stepped-impedance resonators (TSSIRs) with better performance and smaller size compared to other existing counterparts. The design procedure of these UWB BPFs is established based on the waves' cancellation theory conventionally utilized in rat race hybrid analysis.

The structure of the Chapter is as follows. Next section will explain the design procedure of single notch-band BPF, simulated results and measured data. A model for the T-shaped SIR is presented that improves the performance of the filter. The concept will be further expanded to implement a double notch-band UWB BPF accompanied by the design procedure of the filter. The proposed structure offers tuning flexibility of the frequency as well as the bandwidths of the notches.

3.2 Proposed single notch UWB BPF

Here, waves' cancellation theory is adopted to design UWB BPFs with single and double notch-bands which were previously demonstrated using a multi-layer non-uniform periodical structure [10] or a multilayer LCP structure [12]-[13].

3.2.1 The operation principles of the proposed single notch-band UWB BPF

Inspecting the structure in Figure 3.1(a), we can substitute the two black boxes by two tri- or dual-section stepped-impedance resonators. Considering the given graph in Figure

3.1(b), the grey solid lines represent the S_{21}-parameter of a wide-band BPF (1) with a center frequency of f_{r1}, and the black dashed lines represent that of another wide-band BPF (2) with a center frequency of f_{r2} whose S_{21} parameter is crossed by that of the first filter at the frequency of f_{n1} (region R_1).

Based on the waves' cancellation theory, extensively used in the rat race analysis [16], when two traveling signals arrive to an output port with a 180° phase shift and equal amplitude, they cancel each other out and the port is isolated. Here, we are utilizing a similar concept to generate the notch. Therefore, the two signal paths through the BPFs should satisfy the following condition.

$$|\beta_1\ell_1 - \beta_2\ell_2| \cong (2n+1)\pi \tag{3-1}$$

where β_1, β_2 ℓ_1 and ℓ_2 are the phase constants and the physical lengths of the two BPFs given in Figure 3.1(a), respectively. It is well known that a transmission zero will establish in this region due to the waves' cancellation, indicated on the graph. The outcome of these two integrated wide-band BPFs is another UWB BPF realizing a notch-band at the frequency of f_{n1}.

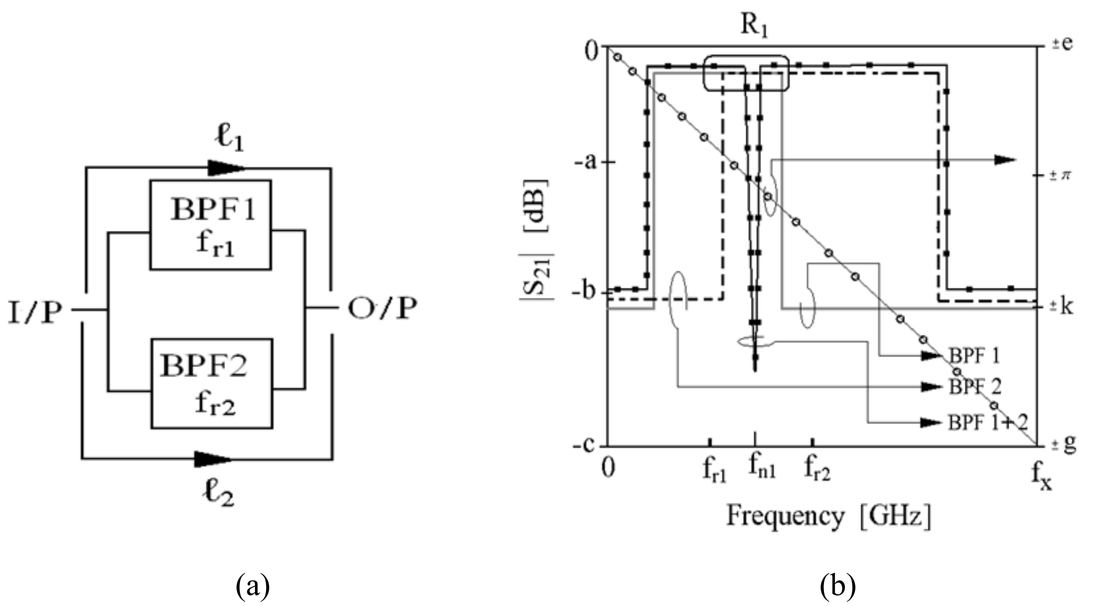

Figure 3.1. (a) The parallel configuration of two wide-band BPFs (b) the proposed concept to realize a single notch-band UWB BPF.

To develop the BPF1 and BPF2, we propose to incorporate tri-section stepped-impedance resonators shown in Figure 3.2 which have been well detailed in some research studies in the literature [17]-[18].

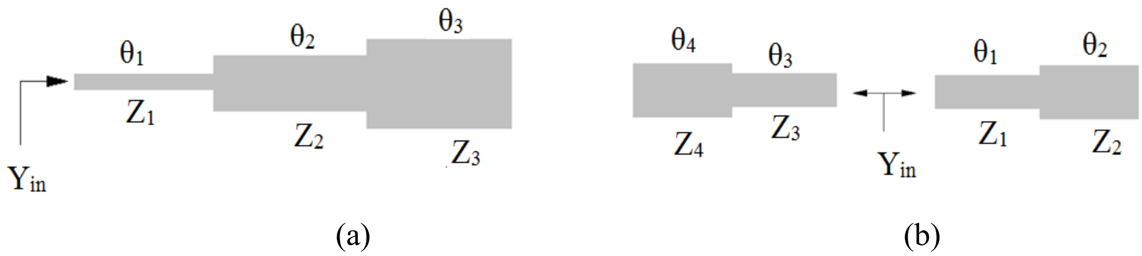

Figure 3.2. (a) The layout of a tri-section stepped-impedance resonator (b) simplified two parallel dual-section SIRs.

With the geometry of the TSSIR depicted in Figure 3.2 and the corresponding analysis in [17]-[18], as well as by assuming the same electrical length for the three sections of the TSSIR (i.e. $\theta_1 = \theta_2 = \theta_3 = \theta_0$), the electrical lengths of the first two resonance modes of the TSSIR can be derived as follows:

$$\theta_{01} = tan^{-1}\left(\sqrt{\frac{K_1K_2}{K_1+K_2+1}}\right) \tag{3-2}$$

$$\theta_{02} = tan^{-1}\left(\sqrt{\frac{K_1+K_1K_2+1}{K_2}}\right) \tag{3-3}$$

where K_1 ($=Z_3/Z_2$) and K_2 ($=Z_2/Z_1$) are the impedance ratios of the given SIR in Figure 3.2.

Based on (3-2)-(3-3), the fundamental and the first resonance frequencies of this kind of resonators are located close to each other. If we design an UWB filter using these resonators, as will be explained in the next section, it realizes double notch-bands. However, to design a single notch UWB filter, the first spurious resonance frequency of the TSSIR should be properly suppressed.

Referring to the given equations in (3-2)-(3-3) that express the relation between K_1 and K_2 for the conventional SIR, the smallest K_1 is desired to further increase the frequency ratio (r_f) of the fundamental (f_{01}) and the first spurious resonance (f_{02}) frequencies [3]. However, since only an impedance of 20-120 Ohm can be practically realized using the µ-strip fabrication process, the realization of a K_1 smaller than 0.15 is not possible [19]. To further decrease K_1 and subsequently increase r_f, a T-shaped SIR, shown in Figure 3.3(a), is proposed to develop the same frequency ratio with more realizable impedance values.

Similar to the conventional case, the relationship between K_1, K_2 and r_f can be calculated for the T-shaped SIR as depicted in Figure 3.3(b). Comparing the given graphs of the proposed T-shaped SIR with those of the conventional ones presented in [3], it is found that $K_1 = 0.2$ provides an exact frequency ratio (r_f) as $K_1 = 0.1$ for the conventional one which is difficult to realize in practice. Therefore, the proposed model is superior to design the single notch-band BPF based on the principle given in Figure 3.3.

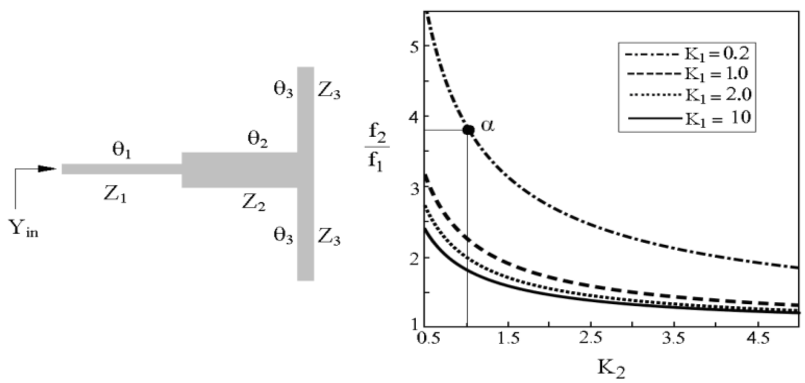

(a) (b)

Figure 3.3. (a) The T-shaped tri-section SIR (b) fundamental and the first spurious resonance frequencies ratio versus impedance ratios of K_2 for several different values of K_1.

3.2.2 Simulated and measured results of the proposed single notch-band UWB BPF

As discussion in the previous section, an UWB notch-band BPF is designed employing the proposed T-shaped SIR. To design this filter, two wide-band BPFs are arranged in parallel with two different resonance frequencies using the parallel topology in Figure 3.1(a). The resonance frequencies of the two filters are adjusted in such a way that their accumulative bandwidths exhibit an ultra-wide bandwidth and their S-parameters cross each other only at one point.

Consulting the impedance ratios of the proposed T-shaped SIR presented in Figure 3.3(b), K_2 is initially chosen to be 1 and the other impedance ratio, K_1, is chosen to be 0.1 to realize a frequency ratio bigger than three. Figure 3.4 shows the final layout of the proposed single notch-band BPF with the optimized parameters, using an EM simulator tools (Agilent ADS Momentum).

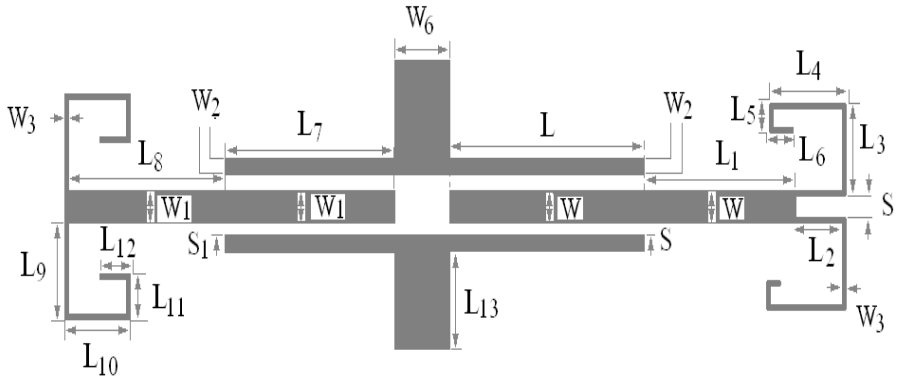

Figure 3.4. The proposed parallel BPF with L= 12 mm, L_1=3.4 mm, L_2 = 1.2 mm, L_3 = 1.4 mm, L_4 = 1.6 mm, L_5 = 0.5 mm, L_6 = 0.4 mm, L_7 = 6 mm, L_8 = 2.3 mm, L_9 = 2.4 mm, L_{10} =1.4 mm, L_{11}= 0.9 mm, L_{12} = 0.5 mm, L_{13} = 2.2 mm, W= 0.3 mm, W_1 = W_3= 0.2 mm, W_2 =0.28 mm, S = 0.1 mm and S_1= 0.12 mm.

The ultra-wideband single notch-band BPF is then fabricated on a Duroid 5880 substrate with a 0.787 mm thickness and a dielectric constant of ε_r =2.2. The size of the entire layout is reported to be an area of 26 × 5.5 mm^2 including two extra transitions at the input/output ports to avoid unwanted coupling between them shown in Figure 3.5(a).

Figure 3.5(b) and (c) present comparisons between the EM simulated and measured results of the proposed single band-notched UWB BPF. The measured S-parameters are in a good agreement with those of simulations. The slight discrepancy between the simulated and measured S_{11} is attributed to the fabrication tolerance problems where a tolerance analysis is performed to show the changes in this parameter, shown in Figure 3.5(d). As shown in the results, S_{11} is changed when the length of the I/O transmissions is changed. Note that the same analysis can be done for the other parameters in the structure. The 3-dB bandwidth of the measured filter is reported to be about 7.657 GHz from 3.87 GHz to 11.527 GHz which is within the BW authorized by the FCC. The measured in-band insertion losses are 0.215 dB and 0.43 dB at the center frequencies of the two pass-bands. The measured and simulated $d\varphi/d\omega$, the rate of change in transmission phase (S_{21} phase derivative) with respect to frequency, are also presented where the results indicate that they are almost flat except at the notched-band. Note that this parameter is stated in [28] is defined as group delay in the pass-band of the filter.

(a)

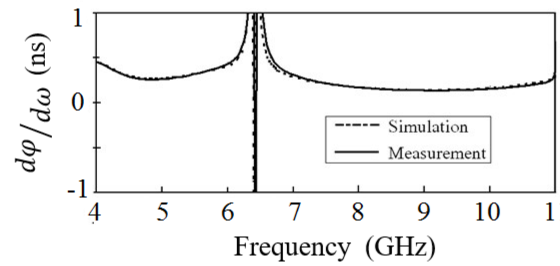

(b)

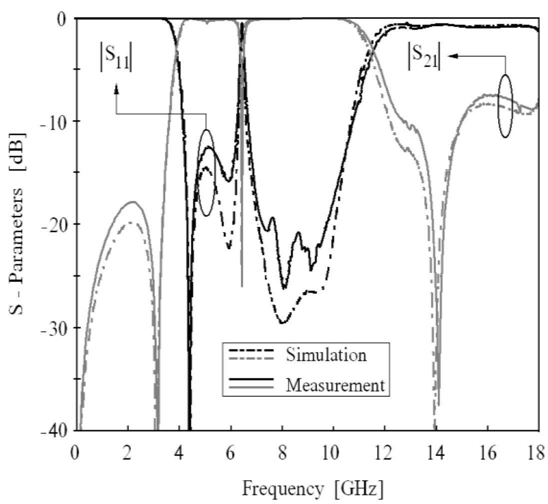

(c)

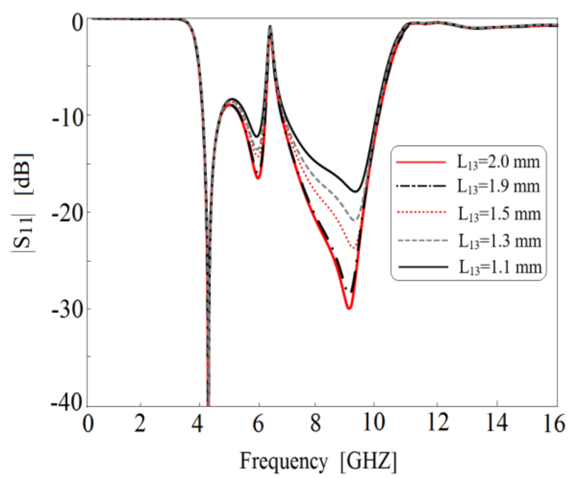

(d)

Figure 3.5. (a) A digital photograph of the proposed single notch-band UWB BPF (b) and (c) comparison between the simulated and the measured performances of the filter in terms of the group delay as well as insertion and return losses (d) tolerance analysis for the length of L_{13} in the filter layout.

The proposed filter is much smaller than the previously published microstrip filters while it avoids via holes and complicated multilayer fabrication. As comparison, the conventional one introduced in [1] has an overall size of 575 mm^2 and the proposed one has an overall size of 143 mm^2 where a size reduction of around 75% has been demonstrated.

Note that the structure demonstrates two TZs at the lower and upper stop-band (f_{tz1}~ 3.1 GHz and f_{tz2}~14 GHz) which are typical of this type of structure [21].

3.3 Proposed double notch (DNB) UWB BPF

3.3.1 Operation principles of the proposed UWB notch-band BPF

Similar to the UWB BPF with single notch-band, another double notch-band BPF can be realized based on the waves' cancellation theory provided in Figure 3.1(b); however, unlike the previous case, the first spurious resonance frequency of the SIR is deliberately supported to generate the second notch in the pass-band of the filter. Based on the proposed concept given in Figure 3.1 as well as the TSSIR, provided in Figure 3.2, two TSSIRs are chosen and arranged in parallel to realize a double notch-band UWB BPF given in Figure 3.6. In this design, the first spurious resonance frequency of BPF1 is utilized to produce the second notch as will be explained in more detail.

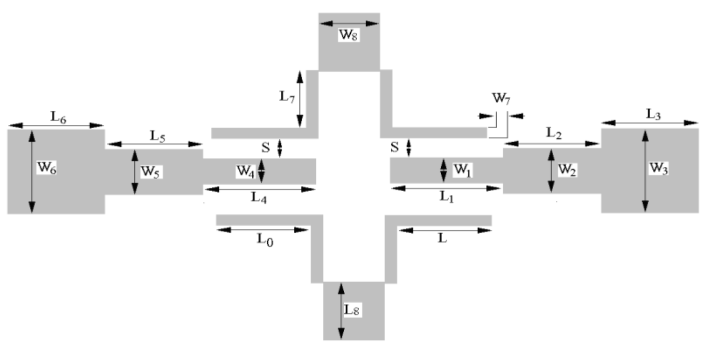

Figure 3.6. Layout of the proposed double notch-band UWB BPF with optimized parameters: L_0 = 3 mm, L = 9 mm, L_1 9.4 mm, L_2 = 10.4 mm, L_3 = 4 mm, L_4 = 3.4 mm, L_5 = 3.7 mm, L_6 = 4 mm, L_7 = 1.7 mm, L_8 = 1.7 mm, S = 0.075 mm, W_1 = 0.2 mm, W_2 = 3 mm, W_3 = 5 mm, W_4 = 0.2 mm, W_5 = 2.4 mm, W_6 = 5 mm, W_7 = 0.2 mm *and* W_8 = 1 mm.

Figure 3.7(a) presents the simulated frequency responses of the two wide-band BPFs building blocks indicated with BPF1 and BPF2 and the resultant double notch-band UWB

BPF indicated with BPF1+BPF2. At the frequencies of the desired transmission zeros, signals flowing through these two paths must have almost the same magnitude and a phase difference of about 180° based on (3.1). The results indicate that the signal-cancellation phenomenon results in the realization of two notch-bands. The simulated phase difference of the two filters is provided in Figure 3.7(b) presenting a phase difference of about 180-200 degrees between the two filters with equal amplitudes at both notch bands confirming the proposed concept. It should be noted that we have zoomed on the phase difference at the notches for clear observation.

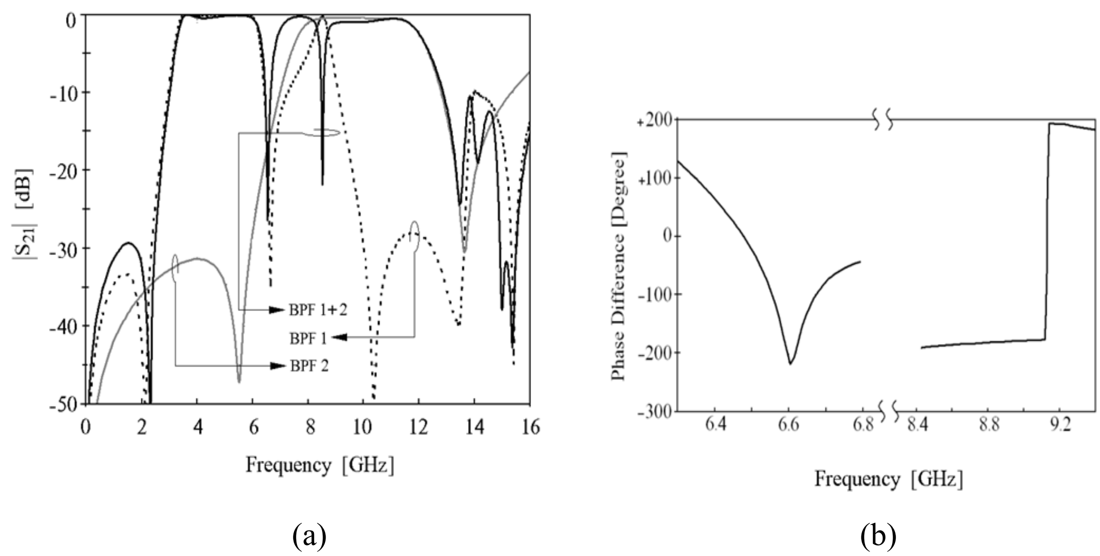

Figure 3.7. (a)The simulated performances of the two BPF1 & 2 as well as DNB UWB BPF (b) the phase difference between the insertion losses of the two BPF1 & BPF2.

One of the main advantages of the proposed filters is its flexible notch frequency design. Previously presented filters in [10]-[13] with complicated LCP technology are not capable of providing an adequate control to arbitrary tune the first notch-band with no information for the second notch-band tuning. Similarly, the notch-band BPF proposed in [12] provides a narrow range to tune the frequencies of notches typically around 0.1-0.2 GHz. To compare as well as present the priority of the proposed prototype filter, the capability of this model is fully investigated in terms of tuning flexibility of the two notches in a much wider frequency range in comparison with the conventional filters.

3.3.2 The first notch- band realization and tuning

As demonstrated, the first notch-band is established at the crossing point of the S_{21}-parameters of the two parallel filters due to the waves' cancellation, thus this point can be freely tuned as long as the crossing point exists. To illustrate this tuning characteristic, the resonance frequency of the first BPF can be kept constant while that of the other BPF can be varied as long as the S-parameters of the two filters cross each other. Figure 3.8 provides the performances of the two filters at the frequency their S-parameters cross each other. The simulation is performed by the optimized parameters of the two filters given in the caption of Figure 3.6 with changing L_1 from 5mm to 13mm.

One may simulate these frequency responses by changing either the length of the coupling sections of the second BPF (L_4) or the value of this length for both filters. Note that the other parameters can also be changed, e.g., L_2, L_3 in the first BPF or L_5 or L_6 in the second filter, where the correlation between these parameters and the resonance frequency of the designed filters have been well researched in several studies [17]-[18], [20]-[24].

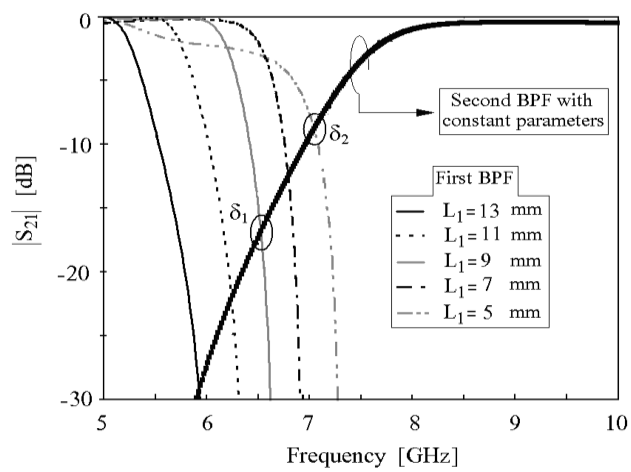

Figure 3.8. The simulated performances of both BPF1 and BPF2 with different values of L_1.

Inspecting the simulated results in Figure 3.8, the crossing point of the two BPFs' S_{21} parameters can be tuned by changing the resonance frequency of the first BPF. Therefore, different resonance frequencies are realized for the first notch-band, for instance, the 9-mm length of coupling section of the first BPF is expected to establish the first notch-band at

6.56 GHz indicated by δ_1. If this length is changed to 5 mm, the notch-band frequency is shifted to 7.38 GHz. Comparing these initial simulations with the recent studies based on LCP technology, the tuning range of the first notched frequency is found to be around 1.8 GHz in the proposed model versus 0.2 GHz for those presented in [12] and [13].

3.3.3 The second notch-band realization and tuning

As demonstrated in the previous section, the second notched frequency of the DNB UWB BPF is realized when the BPF1's first spurious resonance frequency crosses the BPF2's S-parameter as shown in Figure 3.7(a).

As discussed in [22], the spurious resonance frequency of a SIR can be tuned by changing the impedance ratio of the resonator (K). Equation (3-4) presents the relation between f_0 and f_{s1}, the fundamental and the first spurious frequencies of the SIR, and K.

$$f_{s1} = \frac{\pi}{2tan^{-1}(\sqrt{K})} f_0 \tag{3-4}$$

Based on the prototype double notch-band BPF, the first spurious resonance frequency of the SIR is not suppressed, but it is tuned to demonstrate the second notch-band at different frequencies. Since the first spurious resonance frequency of the first BPF contributes in the second notch-band realization, we only consider the first BPF in this section. The relation between the two impedance ratios, K_1 and K_2, and the ratio of the first spurious and the fundamental frequencies in the first BPF1 is evaluated.

Figure 3.9 provides the simulated performance of the BPF1 for the six different values of W_2 with no changes in the other parameters of the structure. The simulated results show that a tuning frequency range of around 2 GHz can be demonstrated for the first spurious resonance frequency.

3.4 Fabricated prototype and measured results of the proposed double notch-band (DNB) UWB BPF

The proposed UWB DNB BPF is fabricated and tested with two notch-bands according to the graphs in given Figures 3.8 and 3.9.

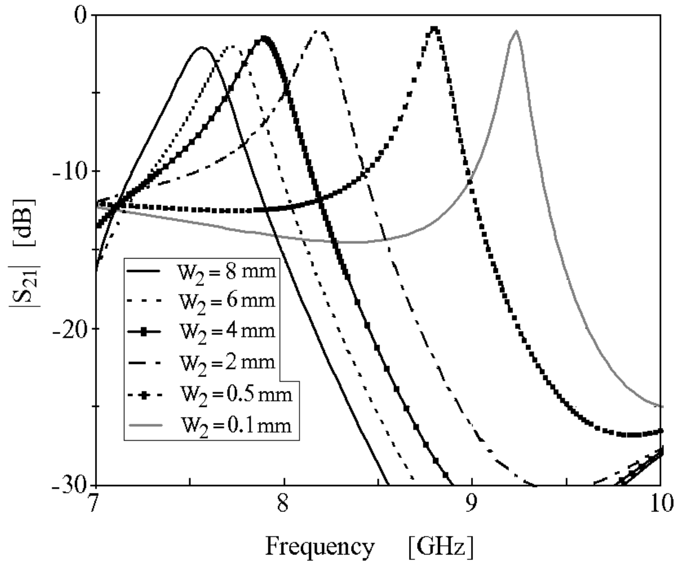

Figure 3.9. S_{21} performance of the first spurious resonance frequency of BPF1 with different values of W_2.

To realize this filter, the first and the second notched frequencies are chosen to be around 6.55 GHz, 9 GHz, respectively. Table 3.1 provides the parameters of both filters to realize the double notch-band UWB BPF.

Table 3.1. The initial and optimized impedance and length ratios of the wide-band BPFs (BPF1 and BPF2).

Filter	$\theta/Z/f$	U_1	U_2	K_1	K_2	f_0/f_{s1}
BPF1	Initial Value	1.00	0.500	1.00	0.50	2.70
BPF1	Opt. Value	1.15	0.398	0.69	0.29	3.89
BPF2	Initial Value	1.00	0.500	1.00	0.50	2.70
BPF2	Opt. Value	1.15	1.100	0.59	0.32	1.83

Before choosing the appropriate parameters, the length ratios of the TSSIR are defined as free variables as $U_1 = \theta_2/\theta_1$ and $U_2 = \theta_3/\theta_2$. These parameters are initially assumed to be 1 and 0.5, respectively. K_1 is initially chosen to be equal to 1 and K_2 is then chosen to be 0.5 based on (3-2) - (3-3).

Based on the initial impedance and length ratios in Table 3.1, the initial parameters of the tri-section SIR in Figure 3.2, are chosen to be $\theta_1 = \theta_2 = 70°$, $\theta_3 = 35°$, $Z_1 = 90\ \Omega$, $Z_2 =$

Z_3 = 45 Ω at f_{r1} for the first BPF. This is according to the basic correlation between the fundamental frequencies, first spurious frequencies, characteristic impedances and electrical lengths in (3-2) - (3-4). Similarly, the initial parameters are adapted for the second BPF at f_{r2} = *10 GHz* based on the values given in Table 3.1. To evaluate the analysis, the performance of the proposed double notch-band UWB BPF is simulated with initial and optimized values given in Table 3-1. Figure 3.10 shows the EM simulated results for the filter.

Inspecting the EM simulated results in Figure 3-10, we observe that the structure demonstrates double notches within the UWB pass-band with the initial values; however, these values are optimized to improve the loss and required BW.

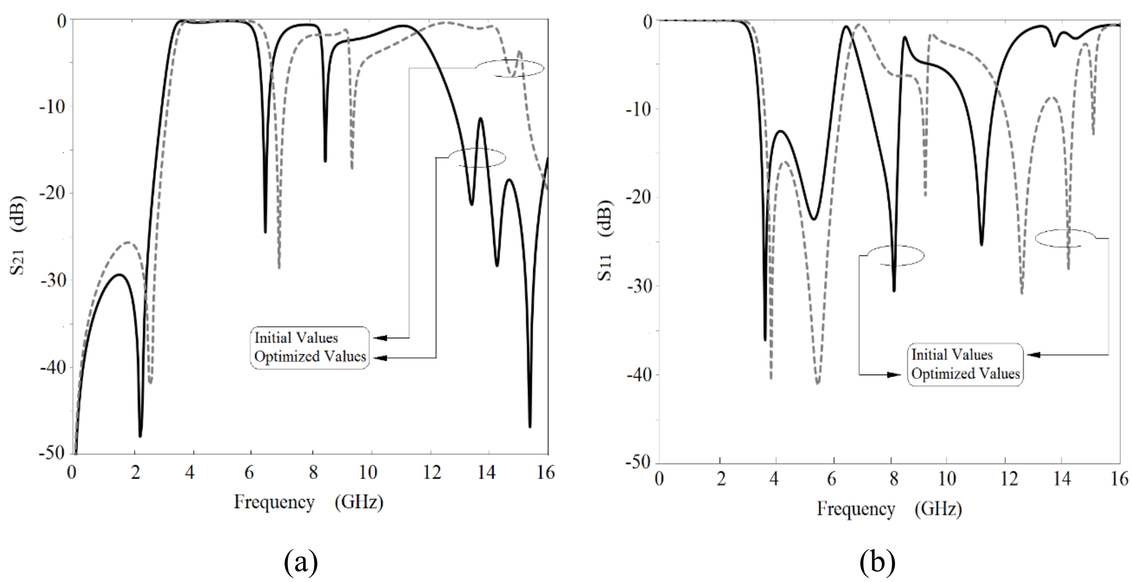

Figure 3.10. EM simulated performance of the proposed dual-notch-band UWB BPF with initial and optimized values given in Table 3-1.

The UWB double notch-band BPF is fabricated on a Duroid 5880 substrate with a 0.787 mm thickness and a dielectric constant of ε_r= 2.2. Two extra transitions are used at the input/output ports to increase isolation between them. As provided in the digital photograph of the fabricated filter in Figure 3.11(a), the actual size of the entire layout is reported to be an area about 36 × 7.3 mm^2. The scattering parameters of the proposed BPF are measured by an Agilent 8722ES network analyzer over the frequency range from 1 GHz to 16 GHz. Figure 3.11(b) and (c) provide a comparison between the simulated and measured performances of the filter.

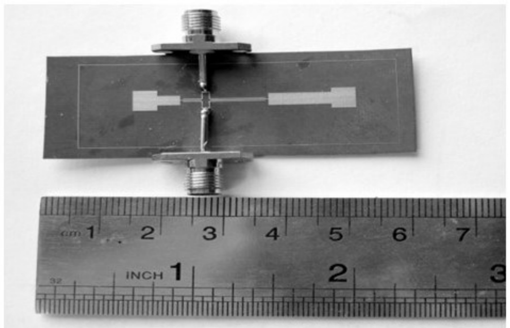

(a)

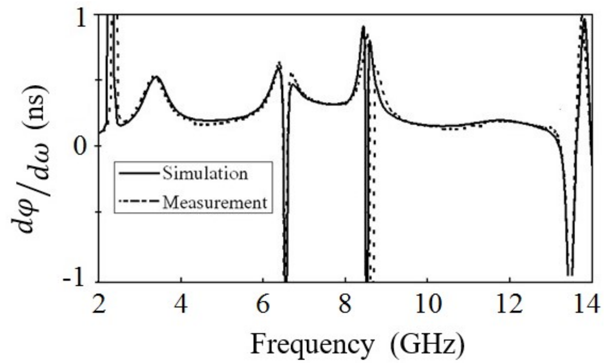

(b)

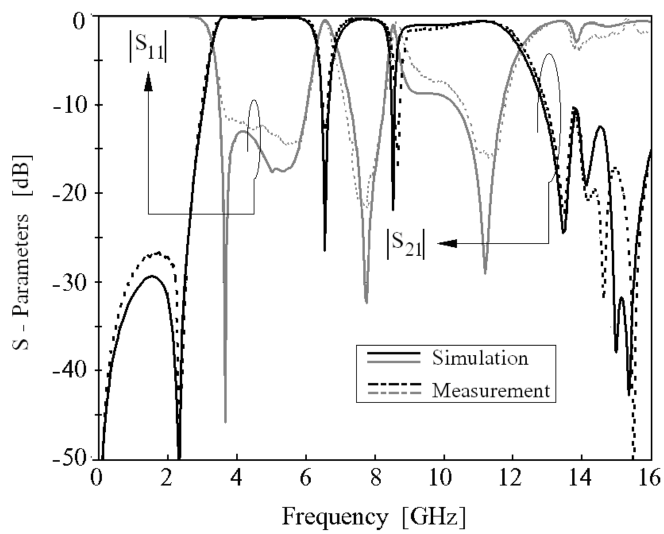

(c)

Figure 3.11. (a) A digital photograph of the proposed double notch-band UWB BPF (b) and (c) comparison between the simulated and the measured performances of the double band-notch UWB BPF in terms of phase variation as well as S-parameters.

The three pass-bands of the fabricated BPF are reported to be centered at 4.77, 7.62, and 10.525 GHz with 3-dB fractional bandwidths (FBWs) of 3.1 GHz (3.22 - 6.32 GHz), 1.66 GHz (6.79-8.45 GHz), and 3.31 GHz (8.87-12.18GHz), respectively. The two notch bands centered at 6.55 and 8.62 GHz have a 10 dB FBW of about 7.2% and 4.87%, respectively.

The attenuations at the two notch bands are measured to be around 24 dB and 19 dB, respectively. Furthermore, shown in Figure 3.11, the measured $d\varphi/d\omega$ within the three pass-bands are flat except at two notch frequencies. In addition, the upper stop-band of the filter is extended to 16 GHz with a suppression level of around 15 dB.

Table 3.2 compares the performance of the novel band-notched UWB BPF to its recent counterparts indicating that the proposed filter is more suitable than the conventional filters for UWB systems due to its smaller size, wider bandwidth and simplicity in design and ease in implementation. It should be noted that the upper stop-band of the proposed filter is wider than that of the conventional filter in [9].

Table 3.2. Comparison between the proposed and the conventional DNB UWB BPFs.

DNB UWB BPF	Size(mm^2)	TZ Up/Low	BW(GHz)	Structure
The Filter in [8]	3150	upper side	5.50	CPW + SIW + SIR
The Filter in [9]	450.0	None	7	μ-Strip Lines
The Filter in [10]	405.7	upper side	N-given	Multilayer + via
The Filter in [12]	300.8	Two	8	11-Layered LCP
The Filter in [14]	680.0	None	8.10	L/R- Hand Via-Holes
New Filter	262.8	Two	8.96	μ-Strip SIRs

Note that the rate of change in transmission phase with respect to frequency, $d\varphi/d\omega$, for both filters with single and double notch-band presented in Figure 3.5 and Figure 3.11 takes negative values at notch frequencies. While some studies have presented group delay with negative value at notch frequencies [9], [13] and [25]-[26], some other works have considered group delay with negative values doubtful [27]-[28]. Discussed in [28], group delay at stop-band should be calculated from the phase of reflection coefficient using lossless symmetrical two-port devices.

3.5 Discussion on the lumped element equivalent circuit of stepped-impedance resonator

In this section, the stepped-impedance resonator (SIR) given in Figure 3.2 is briefly analyzed based on lumped element circuit presented in Chapter 2. Figure 3.13(a) shows a pair coupled µ-strip coupled line. Based on the analysis presented in Section 2.2, Chapter 2, each line can be modeled with a π-network *C*-*L*-*C* lumped element circuit at $\lambda/4$. Figure 3.13(b) shows the equivalent lumped element circuit of the coupled line where capacitor C_c stands for the coupling between the two lines.

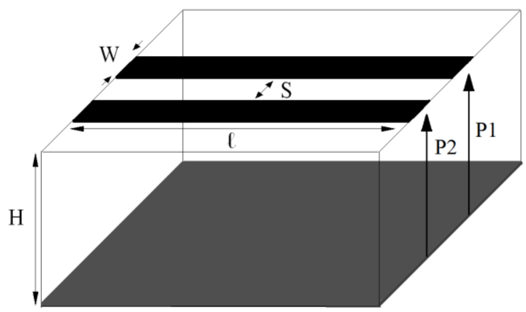

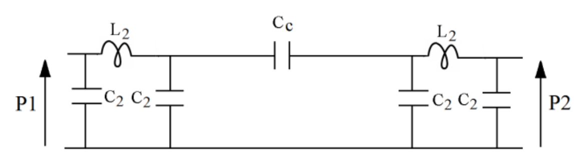

(a) (b)

Figure 3.12. (a) Coupled µ-strip line (b) equivalent circuit based on Figure 2.8.

Generally, a planar resonator is coupled to I/O ports with gap-coupled structure given in Figure 3.14(a) [29]. Therefore, the equivalent lumped element circuit of the entire structure can be derived by incorporating that of the main resonator in the lumped element circuit of the coupled line in Figure 3.13(b).

Since, the electrical length of resonator is $\lambda/2$ at resonance [16]; the resonator is modeled with two cascaded π-network *C*-*L*-*C* circuits shown in Figure 3.14(b). Note that each π-network *C*-*L*-*C* circuit represents the half of resonator at $\lambda/4$, details in Section 2.2, Chapter 2.

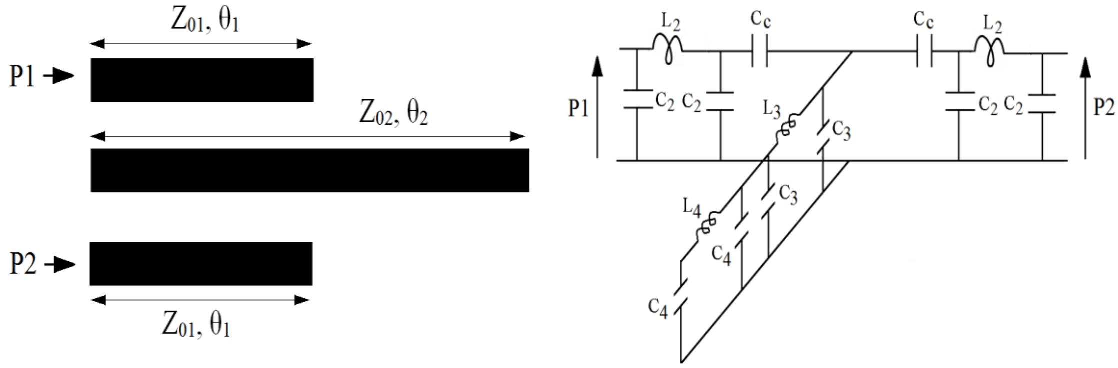

(a) (b)

Figure 3.13. (a) The structure of coupled line resonator (b) its equivalent lumped element circuit.

To evaluate the perfoamnce of the equivalent lumped element circuit, the EM perfonace of the distributed-elemeent structure given in Figure 3.14(a) is simulated and comapred to the *L*-*C* performance of its equivalent circuit given in Figure 3.14(b).

Figure 3.15 shows the comaprison between EM and *L*-*C* performances of the structure with the given valuses in the caption of the figure.

Note that the *L*-*C* values of the circuit are calculated using equations (2-11) and (2-12) at f_0=5.4 GHz corresponding to the electrical length of $\lambda/4$ with charactristics impedance of 150 Ω. This charactristic impedance is calculated for a transmission line with width of 0.23mm on a 0.787-mm-substrate with dielectric constant of 2.2 [30].

Inspecting the EM and *L*-*C* performances given in Figure 3.15, the *L*-*C* circuit models the distributed-element structure at its transmission zeros as well as pass-band. However, there is a discrepancy between these two results where one of the *L*-*C* circuit poles is out of the pass-band. This discrepancy can be attributed to the following reasons:

- The calculated *L*-*C* circuit values have been directly used for simulation without optimization.
- The equivalent lumped element circuits of the I/O transition lines (ℓ_3, the structure given in Figure 3.15(a)) have not taken into consideration in the circuit.

- The value of coupling capacitor C_c has been approximately calculated [16] whose value mostly impacts the discrepancy between S_{21} out of the pass-band (it can be shown by simulation).

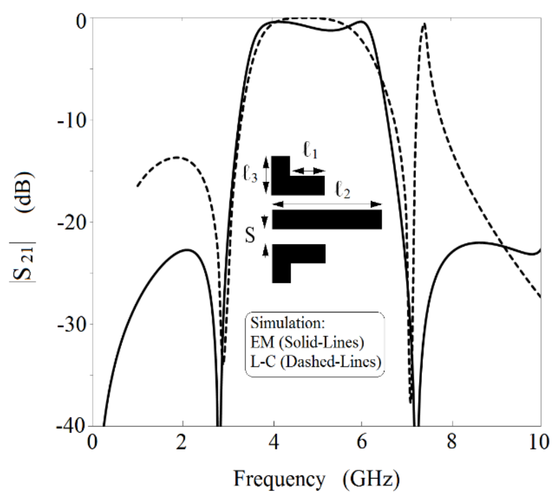

(a)

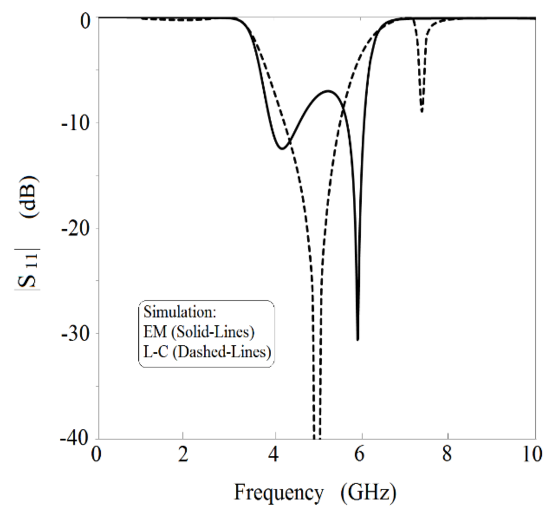

(b)

Figure 3.14. Comparison between EM and *L-C* performances of the structure (a) S_{21} (b) S_{11} with ℓ_1=11mm, ℓ_2=22.5mm, ℓ_3=1.9mm, S=0.075mm and for all lines W=0.23mm for the distributed-element structure and L_2=L_3=L_4=2.2 nH, C_2=C_3=C_4=0.39 pF and C_c=1 pF for the lumped element equivalent circuit.

Similarly, the equivalent lumped element circuits of the stepped-impedance resonators given in Figure 3.2 can be considered as the circuit provided in Figure 3.14(b); however, the following points should be taken into consideration:

- For dual-section SIR with the same electrical lengths but different characteristic impedances (different widths), the values of π-network C_4-L_4-C_4 circuit will be different from those of π-network C_3-L_3-C_3 circuit due to different characteristic impedances (equations (2-11)-(2-12)).
- For dual-section SIR with different electrical lengths and characteristic impedances (different widths), the values of π-network C_4-L_4-C_4 circuit will be different from those of π-network C_3-L_3-C_3 circuit due to different characteristic impedances as

well as different frequencies corresponding to different $\lambda/4$ (equations (2-11)-(2-12)).

- For tri-section SIR, another π-network C_5-L_5-C_5 circuit is cascaded to the π-network circuits and so on.

Note that the equivalent lumped element circuit of the UWB BPFs with single and double notch-band given in Figure 3.4 and Figure 3.6 can be derived and discussed in the same way.

3.6 Conclusion

A novel approach has been introduced and investigated to realize compact ultra-wide-band (UWB) band-pass filters (BPFs) with double/single notch-band using μ-strip TLs and avoiding via-holes. The proposed approach has been realized using two parallel stepped-impedance resonators (SIRs) providing two paths with different electrical lengths.

Adjusting the lengths of these paths according to the wave cancellation theory provides the required notch bands for the filter. The conventional tri-section SIR has been adopted where its fundamental and first spurious resonance frequencies have been pointed to be either suppressed or supported to realize an UWB BPF with single or double notch-bands. The first and the second cases have been ascertained by the proposed parallel dual-section T-shaped and tri-section stepped-impedance resonators, respectively. Two UWB BPFs have been designed, analyzed and fabricated demonstrating single and double notch-bands. Besides, the theoretical data have been verified by the measurements. Additionally, a size reduction of around 75% has been achieved in comparison to the conventional BPFs with single notch-band accompanied by two transmission zeroes at the lower and upper stop-bands.

Moreover, the proposed double notch-band BPF has been reported to demonstrate a similar performance to that of the recent filters designed by complicated multilayer LCP technology, though with a size reduction of around 12.6%.

3.7 References

[1] G-M. Yang, R. Jin, C. Vittoria, V. G. Harris,and X. Sun, “Small ultra-wideband (UWB) bandpass filter with notched band,” *IEEE Microw. Wireless Compon. Lett.,* vol.18, no.3, pp.176-178, Mar. 2008.

[2] P. Mondal and L. Guan, “A coplanar stripline ultra-wideband bandpass filter with notch band,” *IEEE Microw. Wireless Compon. Lett.,* vol.20, no.1, pp.22-24, Jan. 2010.

[3] C. H. Lee, C. I. G. Hsu, and L.Y. Chen, “Notch-bands ultra-wideband bandpass filter design using combined modified quarter-wavelength tri-section stepped-impedance resonators,” *IET Microw. Antennas. Propag*., vol.3, no.8, pp.1232-1236, Dec. 2009.

[4] S. W. Wong and L. Zhu, “Implementation of compact UWB bandpass filter with a notch-band,” *IEEE Microw. Wireless Compon. Lett.,* vol.18, no.1 pp.10-12, Jan. 2008.

[5] S. Pirani, J. Nournia, and C. Ghobadi, “Band-notched UWB BPF design using parasitic coupled line,” *IEEE Microw. Wireless Compon. Lett.,* vol.20, no.8, pp.444-446, Aug. 2010.

[6] X. Luo, J-G. Ma, K. Ma, and K. S. Yeo, “Compact UWB bandpass filter with ultra-narrow notched band,” *IEEE Microw. Wireless Compon. Lett.,* vol.20, no.3, pp.145-147, Mar. 2010.

[7] L. Chen, Y. Shang, and Y.L. Zhang, “Design of a UWB bandpass filter with a notched band and wide stopband,” *Microw. J,* vol.52, no.11, pp.96-105, Nov. 2009.

[8] J. Wang, W. Hong, H. Tang, C. Y. J. Zhang, and J. Zhou, “Ultra-wide band bandpass filter with multiple frequency notched bands based on SIW and SIR technology,” *Proc. of the 39th Europ. Microw. Conf*., pp.268-271, Oct. 2009.

[9] K. Song and Q. Xue, “Asymmetric dual-line coupling structure for multiple-notch implementation in UWB bandpass filters,” *Electron. Lett*., vol.46, no.20, pp.1388-1390, Sept. 2010.

[10] Z-C. Hao, J-S. Hong, J. P. Parry, and D. P. Hand, “Ultra-wideband bandpass filter with multiple notch bands using nonuniform periodical slotted ground structure,” *IEEE Trans. Microw. Theory and Tech*., vol.57, no.12, pp.3080-3088, Dec. 2009.

[11] S. G. Mao, Y. Z. Chueh, C. H. Chen, and M. C. Hsieh, “Compact ultra-wideband conductor–backed coplanar waveguide bandpass filter with a dual band-notched response,” *IEEE Microw. Wireless Compon. Lett.*, vol.19, no.3, pp.149-151, Mar. 2009.

[12] Z. C. Hao and J-S. Hong, “Compact UWB filter with double notch bands using multilayer LCP technology,” *IEEE Microw. Wireless Compon. Lett.*, vol.19, no.8 pp.149-151, Aug. 2009.

[13] Z.-C. Hao, J.-S. Hong, S. K. Alotabi, J. P. Parry, and D. P. Hand, “Ultra-wideband bandpass filter with multiple notch-bands on multilayer liquid crystal polymer substrate,” *IET Microw. Antennas Propag*., vol.3, no.5, pp.749-756, Aug. 2009.

[14] F. Wei, Q. Y. Wu, X. W. Shi, and L. Chen, “Compact UWB bandpass filter with dual notched bands based on SCRLH resonator,” *IEEE Microw. Wireless Compon. Lett.*, vol.21, no.1, pp.28-30, Jan. 2011.

[15] M. Mirzaee, “A novel small ultra-wideband bandpass filter including narrow notched band utilizing folded-T-shaped stepped impedance resonator (SIR),” *Progress In Electromag. Res. C*, vol.22, pp.85-96, 2011.

[16] Pozar D. M.: *Microwave Engineering*, 2nd Ed. New York: Wiley, 1998.

[17] D. Packiaraj, M. Ramesh, and A. T. Kalghatgi, “Design of a tri-section folded SIR filter,” *IEEE Microw. Wireless Compon. Lett.*, vol.16, no.5, pp.317-319, May 2006.

[18] C.-I G. Hsu, C-H. Lee, and Y.-H. Hsieh, “Tri-band bandpass filter with sharp passband skirts designed using tri-section SIRs,” *IEEE Microw. Wireless Compon. Lett.*, vol.18, no.1, pp.19-21, Jan. 2008.

[19] K-S. Chin, K-M. Lin, Y-H. Wei, T-H. Tseng, and Y-J. Yang, “Compact dual-band branch-line and rat race couplers with stepped-impedance stub lines,” *IEEE Trans. Microw. Theory and Tech*, vol.58, no.5, pp.1213-1221, May 2010.

[20] M. Nosrati and M. Mirzaee, “Compact wideband microstrip bandpass filter using quasi-spiral loaded multi-mode resonator,” *IEEE Microw. Wireless Compon. Lett*., vol.20, no.11, pp.607-609, Nov. 2010.

[21] H. Zhang and K. J. Chen, “A tri-section stepped-impedance resonator for cross-coupled bandpass filters,” *IEEE Microw. Wireless Compon. Lett*., vol.15, no.6, pp.401-403, Jun. 2005.

[22] M. Makimoto and S. Yamashita, “Bandpass filters using parallel coupled stripline stepped impedance resonators,” *IEEE Trans. Microw. Theory and Tech*, vol.28, no.12, pp.1413-1417, Dec. 1980.

[23] Y.-C. Chang, C.-H. Kao, and M.-H. Weng, “A compact wideband bandpass filter using asymmetric SIR with low loss and high selectivity,” *Microw. Opt. Tech. Lett*., vol.51, no.1, pp.242-244, Jan. 2009.

[24] Y-C. Chiou, J-T. Kuo, and E. Cheng, “Broadband quasi-chebyshev bandpass filters with multimode stepped-impedance resonators (SIRs),” *IEEE Trans. Microw. Theory and Tech*, vol.54, no.8, pp.3352-3358, Aug. 2006.

[25] F. Wei, L. Chen, Q.-Y. Wu, X.-W. Shi, and C.-J. Gao, “Compact UWB bandpass filter with narrow notch-band and wide stop-band,” *J. of Electromagn. Waves and Appl.,* vol.24, pp.911–920, 2010.

[26] C.-H. Lee, C.-I.G. Hsu, and L.-Y. Chen, “Band-notched ultra-wideband bandpass filter design using combined modified quarter-wavelength tri-section stepped-impedance resonator,” *IET Microw. Antennas Propag*., vol.3, no.8, pp.1232-1236, Dec. 2009.

[27] I. Shapir, “Suggestion for a new formula to calculate group delay from frequency domain measurements,” *Proceedings of the 36th European Microw. Conf.*, pp.1233-1236, Sept. 2006.

[28] M. Mokhtaari and J. Bornemann, “Microstrip ultra-wideband filter with flexible notch characteristics,” *Int. J. Wireless Engr. and Tech*., vol.3, no.1 pp.12-17, Jan. 2012.

[29] J.-S. Hong and M. J. Lancaster, *Microstrip Filters for RF/Microwave Applications*. New York: Wiley, 2001.

[30] Advanced Design System, ADS 2015.

Chapter 4 Developing single layer ultra-wide band band-pass filter with multiple (triple and quadruple) notches

4.1 Introduction

The use of ultra wide-band (UWB) technology has been dramatically increased since the U.S. federal communication commission (FCC) authorized UWB for the unlicensed use in short-distance communication in early 2002.

A wide-band filter generally requires a large design area or complicated structure, such as a three-dimensional coupling structure utilizing either wire-bonding connections or via-holes. In addition, since the 3.1GHz to 10.6 GHz UWB covers various existing wireless communication frequency bands, such as the 3.5-GHz WiMax band, 5.0 GHz WLAN band, 5.9GHz DSRC, 8.0-GHz military and satellite-communication bands, it is desirable to introduce multiple notch bands to avoid these interferences. In addition, it is expected that the rapid growth of communication systems will entail the need of UWB band pass filters with multiple notches even further.

As the number of the required notches increases, the number of transmission zeros of the filter should be enhanced which makes the design more challenging. In general, many different designs have been introduced to realize UWB BPFs employing multi-mode resonators (MMRs), defected ground structures and left/right-handed techniques [1]-[14]. While these models offer effective techniques to design UWB BPFs, they still suffer from a long list of shortcomings such as: incapable of realizing more than one notch-band [1]-[14], lack of transmission zeroes for high selectivity [15]-[18], narrow upper stop-band [17]-[19], complicated and expensive fabrication procedure including multi-layer structure [19]-[21], high cost from the use of via holes [18],[20]-[22], incompatibility with monolithic microwave integrated circuits (MMICs) [19]-[22].

Although these filters provide double notch bands, there is still a need to design multi notch bands including triple (TNBs) or quadruple notch-bands (QNBs). Aligned with this need, two not quite different models have been recently reported to demonstrate DNBs [22] and TNBs in [23]-[24], but at the expense of using multi-layer LCP technology with short-circuited stubs or via-holes. Ref [25] has recently reported the only quadruple notch-band filter (based on our knowledge) requiring multi-layer patterning.

To avoid the expensive and complicated fabrication process and at the same time developing triple and quadruple notches, we propose a new solution using parallel integration of stepped impedance resonators (SIRs) and gap coupled μ-strip resonators.

On the other hand, parallel connection of two resonators has been previously reported to realize dual-band BPFs [26]-[30], UWB BPFs and stop-band filters [31]-[32]; However, they have not been studied to realize UWB BPFs with multiple notches (three and four).

In this Chapter, we propose to use two parallel SIRs as a platform integrated with gap coupled μ-strip resonators to develop several transmission zeros (multiple notches). Here, we demonstrate that this technique offers the capability of designing a compact easy-to-fabricate single layer UWB BPF demonstrating triple notch bands (TNBs) and quadruple notch bands (QNBs). The proposed approach uses only μ-strip transmission lines without any via hole.

The arrangement of this Chapter is as follows. First, the proposed integration of SIRs and gap coupled μ-strip resonators is discussed. Then a detailed design procedure is explained to demonstrate triple and quadruple notch filter. Two prototype units are fabricated and their measured results are illustrated. The proposed notch-band filters are much smaller in size compared to their previously published multi-layer counterparts and provide low cost single layer patterning option. There are few abbreviations used in the Chapter, which are defined in Table 4.1.

Table 4.1. Abbreviations and their definition.

Abbreviation	TSSIR	DNBs	TNBs	QNBs	MNBs	GCMR
Definition	Tri-Section Stepped-Impedance Resonator	Dual Notch-Bands	Triple Notch-Bands	Quadruple Notch-Bands	Multi Notch-Bands	Gap Coupled Microstrip Resonator

4.2 The proposed principles of operation

Source/load coupling is one of the recent techniques for transmission zero realization in 3D waveguide structures [36]. Here the same idea but on planar structure is developed to realize multi transmission zeros. Figure 4.1(a) shows the proposed configuration of UWB BPF with multiple notch bands, while Figure 4.1(b) depicts the circuit model of the filter. To produce multiple notches, we propose to use a double notch BPF as starting platform (two parallel TSSIRs as a DNB BPF [33]) and integrated with GCMR to realize the third and the fourth notches.

Figure 4.2 conceptually shows the expected performance of the proposed filter. The red solid line represents insertion loss of a DNB UWB BPF and the blue dashed line stands for that of the GCMR. The black dotted line shows the overall performance of the integrated filter with the notches at the frequencies of f_{nb1}, f_{nb2} and f_{nb3}.

The diagram in Figure 4.2 indicates that the response of the integrated filter tracks the performance of the DNB filter across the band except at the additional notch frequency (f_{nb3}) where it follows the GCMR performance. The concept can be explained based on simple circuit theory. It is well known that when an RF signal is applied to a circuit including two parallel paths with different impedances, the signal is mostly passed through the path with the lower impedance. Inspecting the simulated input impedance of the GCMR in Figure 4.2(b), we observe that the input impedance is large (open circuit) across the band except at the resonant frequency where it approaches zero. Thus, the signal ideally follows the GCMR behavior only at its resonances. In another word, notch-bands are realized at the resonances of the GCMR.

Moreover, the forth notch-band can be realized by adding another parallel GCMR path with different resonant frequency. Alternatively, it is shown in this paper that this can be established by the higher order resonant frequencies of distributed GCMR resonators. In the next sections, the design procedure of UWB BPFs with multi notch-bands is explained in detail.

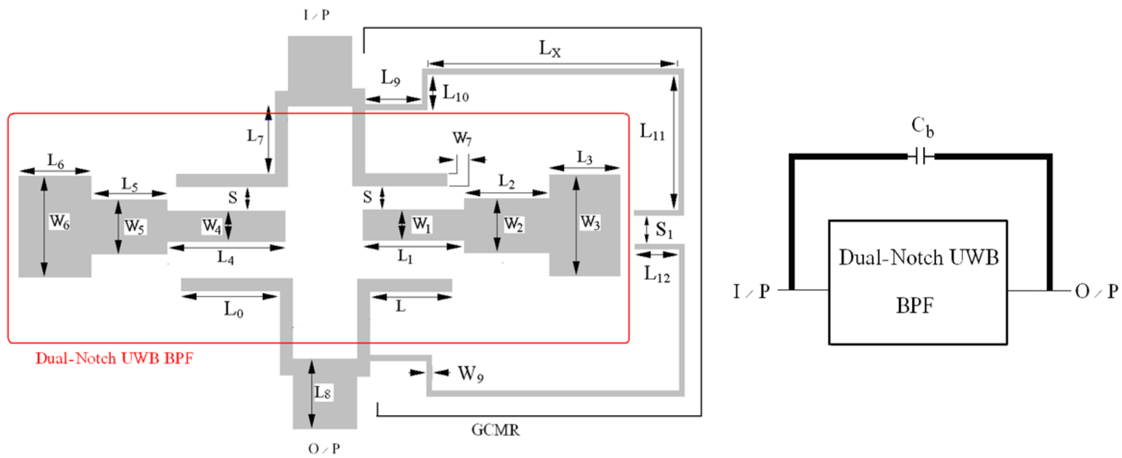

(a) (b)

Figure 4.1. (a) The layout and (b) circuit model of the proposed multi notch band UWB filter.

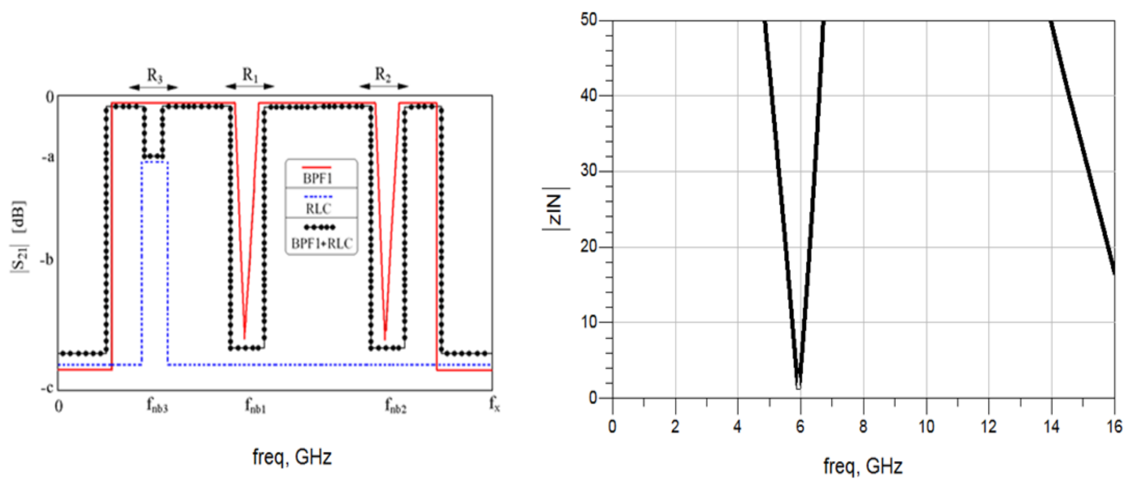

(a) (b)

Figure 4.2. (a) The principle operation of the proposed concept for triple notch-band UWB BPF realization (b) simulated input impedance of a GCMR.

4.3 Proposed multi notch-band UWB BPFs

4.3.1 Characteristics of the GCMR at resonance

As previously discussed, the response of the proposed filter in Figure 4.1 follows the GCMR characteristics only at its resonances where the notch bands are realized. Thus, we characterize the GCMR at its resonance frequencies using lumped element equivalent circuit and transmission line (TL) theory to understand the notch behavior in the proposed filter.

Figure 4.3 shows the GCMR with the characteristic impedance and electrical length of Z_1 and θ_1 as well as its lumped element equivalent circuit. In the given lumped element equivalent circuit, two *C-L-C* π-networks and a coupling capacitor represent the two TLs and the gap between them, respectively (Figure 2.7 and Figure 2.8, Chapter 2, Section 2.2.1).

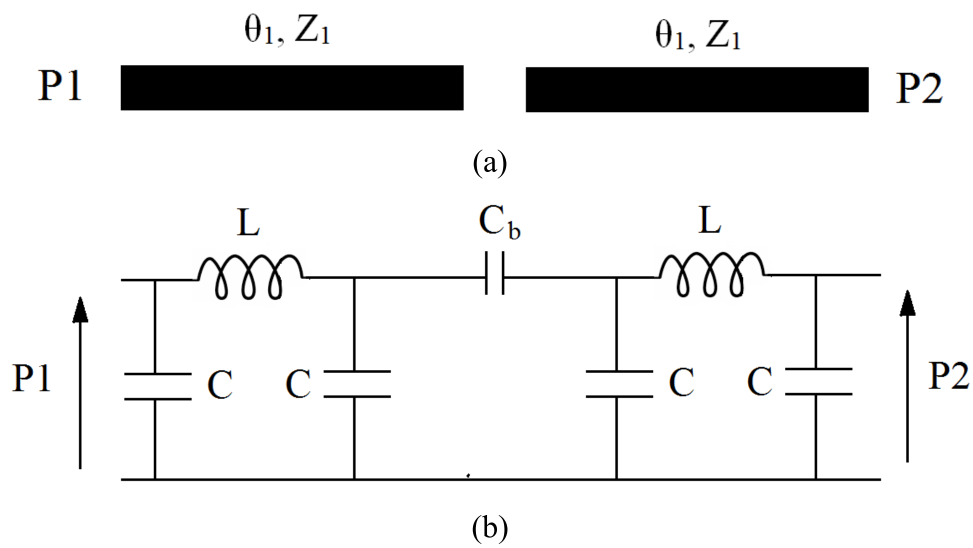

Figure 4.3. (a) Gap-coupled microstrip lines (b) lumped element equivalent circuit.

Based on *ABCD* matrix analysis, the resonance frequencies of the circuit are calculated as follows [34]:

$$\begin{bmatrix} A & B \\ C & D \end{bmatrix}_T = \begin{bmatrix} A & B \\ C & D \end{bmatrix} \begin{bmatrix} 1 & Z \\ 0 & 1 \end{bmatrix} \begin{bmatrix} A & B \\ C & D \end{bmatrix} \tag{4-1}$$

where the first and the third matrixes stand for *C-L-C* π-networks and the second one for the coupling capacitor.

The Z_{21} parameter of the impedance matrix can be calculated using the C component of the total *ABCD* matrix of the circuit as (4-2) [34]:

$$Z_{21} = \frac{1}{C_T} = \frac{1}{2C(A+CZ)} = \frac{1}{j\omega C(2-\omega^2 LC)[2(1-\omega^2 LC)+\frac{C}{C_b}(2-\omega^2 LC)]} \tag{4-2}$$

Moreover, the resonance frequencies of the circuit can be calculated from (4-2) as follows:

$$\omega_{01} = \sqrt{\frac{2(1+{C}/{C_b})}{LC(2+{C}/{C_b})}}, \omega_{02} = \sqrt{\frac{2}{LC}} \tag{4-3}$$

Similarly, the structure can be analyzed using the transmission line theory presented in [34].

The resonance condition of the conventional gap-coupled resonator, loaded by an open-circuited stub, has been well explained using the method of image impedance in [34]. In this structure, the GCMR is somehow different from the conventional one where it is explained using its corresponding circuit model in Figure 4.4(a).

Considering $1/(j\omega C_b)$ for the impedance of the capacitor C, the image impedance of the GCMR in the structure can be expressed as follows [34]:

$$Z_{i1} = \sqrt{Z_1^2 \frac{\sin(2\theta_1) - \alpha cos^2(\theta_1)}{\sin(2\theta_1) + \alpha sin^2(\theta_1)}} \tag{4-4}$$

where α or attenuation is $Z_1/(j\omega C_b)$, for the GCMR. Considering the electrical length of the GCMR in terms of θ, the solutions of (4-4) is schematically derived for different values of θ_1, shown in Figure 4.4(b).

Inspecting the results, the number of the resonance frequencies can be adjusted by increasing the electrical length of the GCMR. For example, for θ_1 equal to θ, there is only one resonance frequency, while four resonance frequencies are demonstrated for θ_1 equal to 4θ.

In addition, based on (4-4) and presented in Figure 4.4(c), the attenuation level and bandwidth of the sub-pass bands of the GCMR can be also controlled by changing the capacitor C_b given by $\alpha = Z_1/(j\omega C_b)$. It is shown that reducing the capacitance leads to higher signal suppression. This is also verified by EM simulated results using ADS Momentum for the different values of C_b in Figure 4.4(d).

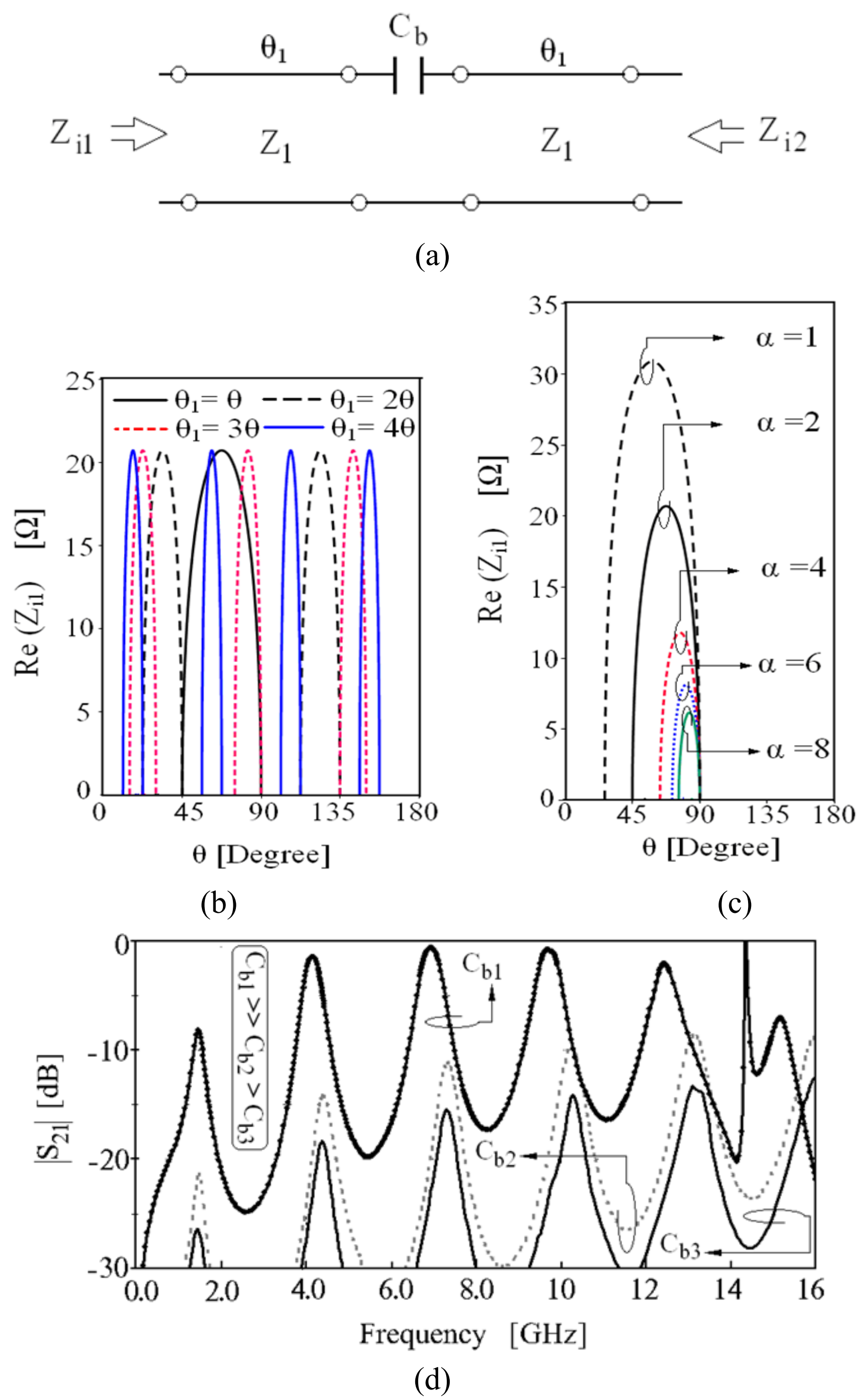

Figure 4.4. (a) The equivalent circuit of GCMR (b) the solutions of (4-4) for the different values of θ_1 in terms of the electrical length (c) bandwidth and attenuation control of the sub-pass-bands of the GCMR with different values of α (d) EM simulated results to control the bandwidth and the attenuation of the GCMR in terms of C_b.

To further understand the GCMR behavior, the performances of the DNB UWB BPF and the GCMR resonators are separately simulated using the EM simulator tool where Figure 4.5(a) shows the results for different values of the L_X parameter. As an example, L_X = 24 mm demonstrates five high-loss quasi pass-bands indicated by δ_1-δ_5 at their resonance frequencies. Three of them, δ_2-δ_4, are realized within the pass-band of the DNB UWB BPF. These points can be adjusted to produce notch bands at the certain frequencies and also improve the selectivity at the lower and upper skirts. Figure 4.5(b) also shows the input impedance of the GCMR. This reconfirms the fact that the input impedance of the GCMR approaches zero at the resonance frequencies, thus, its performance becomes dominant resulting in notches realization.

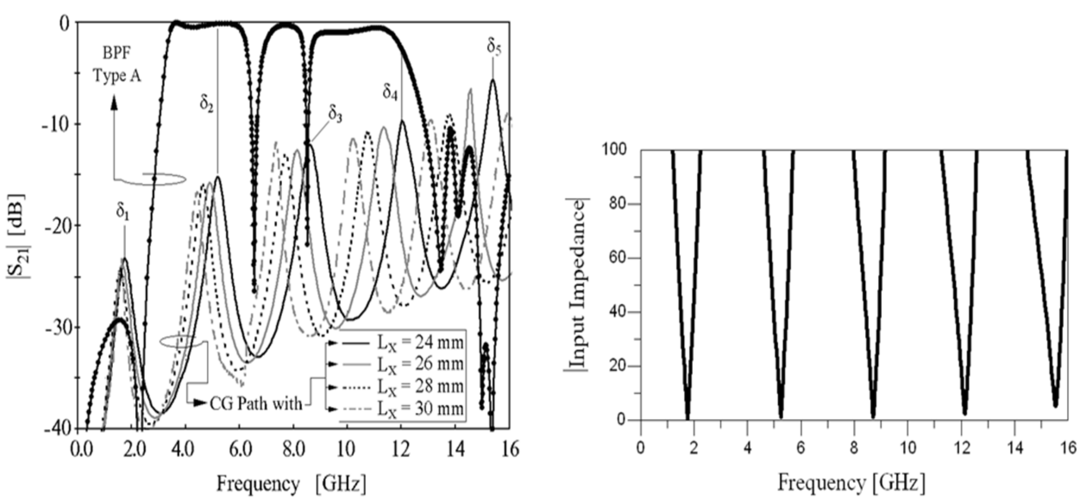

(a) (b)

Figure 4.5. (a) The simulated performance of the DNB BPF (type A) with L_0 = 3 mm, L = 9 mm, L_1 =9.4 mm, L_2 = 10.4 mm, L_3 = 4 mm, L_4 = 3.4 mm, L_5 = 3.7 mm, L_6 = 4 mm, L_7 = 1.7 mm, L_8 = 1.7 mm, S = 0.075 mm, W_1 = 0.2 mm, W_2 = 3 mm, W_3 = 5 mm, W_4 = 0.2 mm, W_5 = 2.4 mm, W_6 = 5 mm, W_7 = 0.2 mm, W_8 = 1 mm and the GCMR with L_9 = 2 mm, L_{10} = 2.1 mm, L_{11} = 3.6 mm, L_{12} = 1 mm, S_1 =0.65 mm, W_9 = 0.1 mm and with the different values of L_X (b) the simulated input impedance of the GCMR.

4.3.2 Triple notch-band (TNB) UWB BPF

In this section, a design procedure is discussed to design a triple notch-band (TNB) UWB BPF. Based on the integration of three resonators in parallel, Figure 4.1, accompanied by the simulated verifications in Figure 4.5, a triple notch UWB BPF is designed by employing the DNB UWB BPF integrated with GCMR.

Inspecting the simulated results in Figure 4.5, we observe that the GCMR can generate five quasi-pass bands from 0 GHz to 16 GHz. On the other hand, since we try to synthesize a TNB UWB BPF, the electrical length of the GCMR should be chosen to add only one transmission zero to the UWB pass-band while the other two notches have already been realized by the DNB BPF. The following considerations should therefore be taken into account in the design of triple notch UWB BPFs:

- δ_1 and δ_5 are determined to be located out of the pass-band to further suppress the unwanted modes of MMRs.
- δ_2 is determined to be located at the operation frequency of the wireless local area network (WLAN) to generate the third notch-band of the TNB BPF.
- δ_3 is determined to be exactly on or in the vicinity of one of the notches realized by the DNB BPF. Note that it adds a degree of freedom to control the bandwidth of the notch.
- δ_4 is determined to be located at the upper side of the pass-band of the DNB BPF to further sharpen its upper skirt.

According to the given considerations, a TNB UWB BPF is synthesized where Figure 4.6 separately presents the simulated performances of the GCMRs, the DNB and the TNB UWB BPFs. The results are simulated using an EM simulator tool (Agilent ADS Momentum) on a 0.787-mm-thick substrate with the dielectric constant of $\varepsilon_r = 2.2$.

Inspecting the simulated results in Figure 4.6, we observe that the resultant performance of the filter follows that of the DNB BPF, except at the resonance frequencies of the GCMR resulting in a TNB UWB BPF.

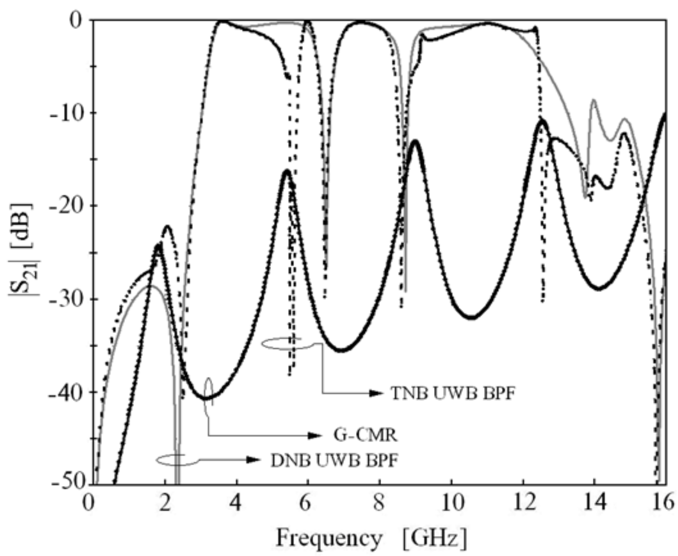

Figure 4.6. The simulated performances of the GCMR, the DNB and the TNB UWB BPFs with L_X = 24 mm, Agilent ADS Momentum.

4.3.3Quadruple notch-band (QNB) UWB BPF

Similar to the previous case, a new quadruple notch UWB BPF can be designed by appropriately choosing the parameters of three sections of the proposed topology in Figure 4.1 and the design curves in Figure 4.6.

Based on the simulated results in Figure 4.5, the central frequencies of the five quasi-pass bands (δ_1-δ_5) can be tuned for the different values of L_X parameter.

It is observed that more harmonics (sub-pass-band) can be demonstrated in the UWB pass-band of the structure by increasing the length of the GCMR. Thus, the electrical length of the GCMR is increased to realize six quasi pass-bands in the frequency range of DC to16 GHz.

In this case, since we try to synthesize a QNB UWB BPF, the electrical length of the GCMR should be somehow chosen to add two transmission zeros within the UWB pass-band while the other two required notches have already been realized by the DNB BPF. The following considerations should be therefore taken into account to design a QNB UWB BPF:

Similar to the TNB case, δ_1 and δ_6 are determined to be located out of the pass-band to further suppress the unwanted modes of MMRs.

- δ_2 is determined to be located between the lower skirt of the DNB BPF and its first notch-band.
- δ_3 is determined to be exactly on or in the vicinity of one of the notches realized by DNB BPF where it adds a degree of freedom to widen the bandwidth of the notch.
- δ_4 is determined to be located between either the first and the second notches of the DNB BPF or the second notch and the upper side of the DNB BPF.
- Similar to the TNB UWB BPF, δ_5 is determined to be exactly located at the upper side of the pass-band to further sharpen its upper skirt.

According to the given considerations, a QNB UWB BPF is developed. To conceptually show the locations of the QNBs within the pass-band of the proposed filter, the EM simulated performances of the GCMR with six quasi pass-bands, the DNB UWB and the QNB UWB BPFs are separately provided in Figure 4.7. The results are simulated using the simulator tool (Agilent ADS Momentum) on a 0.787-mm-thickness substrate with the dielectric constant of ε_r= 2.2.

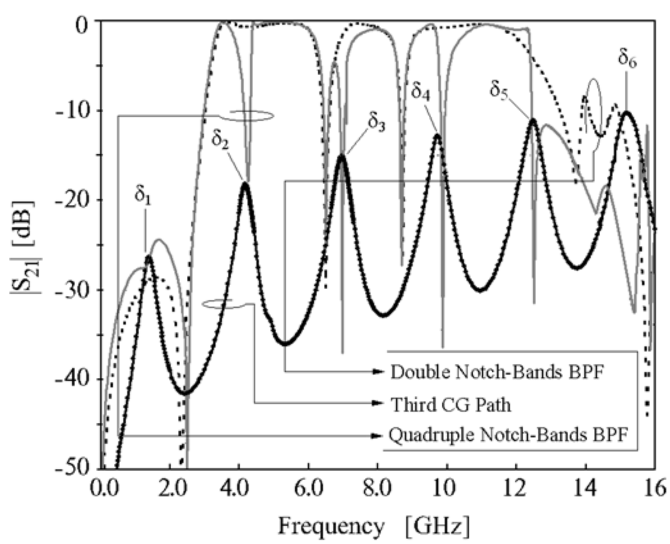

Figure 4.7. The simulated performance of the GCMR, the DNB and the QNB UWB BPFs with L_X = 33 mm, the other required parameters in the caption of Figure 4.5.

Inspecting the simulated performance of the proposed multiple notch-band BPF in Figure 4.7, we realize three quasi pass-bands within the pass-band of the DNB BPF and one transmission zero at its upper skirt resulting in a QNB UWB BPF. Note that the electrical length of L_X in the GCMR is further increased to be around 33 mm in comparison to the previous case. Figure 4.8 provides the current distribution on the layout at different notches. The current distribution indicates that the GCMR contributes to the filter performance only at the first and the fourth notches. This is confirmed by the current distribution presented in Figure 4.8(a) and (b). The results show that the current is mostly conducted through the GCMR at the specified notched frequencies. However, the scenario is different at the other notched frequencies as shown in Figure 4.8(c). Inspecting the simulated results, we observe that the current flow through the SIRs is significantly higher than that through the GCMR at the second notch-band realized by phase cancellation [33].

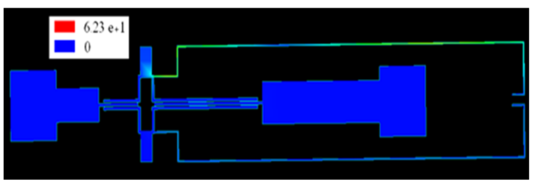

(a)

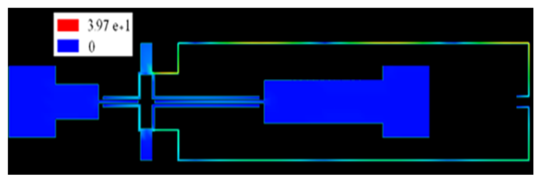

(b)

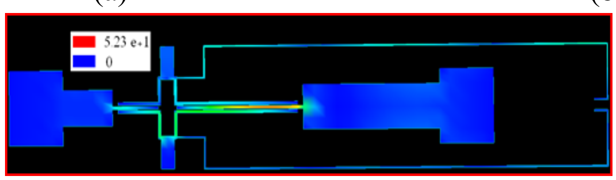

(c)

Figure 4.8. The current distribution on the layout at (a) the first notched (b) the forth notched (c) the third notched frequencies.

4.4 Fabricated prototype and measured results

4.4.1 TNB UWB BPF

According to the given specifications, a TNB UWB BPF is designed using the simulated results in Section 4.3 and the filter is fabricated on a Duroid 5880 0.787-mm-thick substrate with the dielectric constant of ε_r= 2.2. The size of the entire layout is reported to be around 8.2×37.6 mm^2 where Figure 4.9(a) shows the digital photograph of this filter.

To verify the simulated performance of the proposed filter, the S-parameter measurements are performed using an Agilent network analyzer from DC to 16 GHz.

Figure 4.9(b) compares the simulated and measured performances of the TNB UWB BPF in terms of the S-parameters and the group-delay.

The four pass-bands of the fabricated BPF are reported to center at 4.33, 6.02, 7.5 and 10.985 GHz with a 3-dB bandwidth of 2.26 GHz (3.2 – 5.46 GHz), 0.42 GHz (5.81-6.23 GHz), 1.6 GHz (6.7-8.3 GHz) and 2.85 GHz (9.56-12.41 GHz), respectively. The first notch-band is measured at 5.63 GHz with a rejection level of 20 dB and a 3-dB bandwidth of 6.2% (from 5.46 to 5.81 GHz). The measured second notch band is located at 6.47 GHz with a rejection level of 24.3 dB and a 3-dB bandwidth of 7.26% (from 6.23 to 6.7 GHz). The third notch band is measured at 8.93 GHz with a rejection level of 11 dB and a 3-dB bandwidth of 14.1% (from 8.3 to 9.56 GHz). The measured group-delay, $d\varphi/d\omega$ in the pass-band of the filter, response of the filter in Figure 4.9(b) shows the variation of 0.2 nsec to 0.4 nsec in the sub-passbands.

Comparing the measured simulated results, we observe that the pass band deteriorates at the vicinity of the notches which could be considered a drawback of this design.

Table 4.2 compares the performance of the proposed TNB UWB BPF with those of the conventional counterparts designed using complicated multi-layer technologies.

These results show that the proposed filter is superior as it uses a single-layer substrate compatible with MIMIC technology. The proposed filter also has the benefit of two transmission zeros at both sides. Moreover, the notched frequencies in [23] appear to be a constant multiple of each other with a ratio of $\alpha = 1.3$ while in the proposed prototype, the DNB BPF and the GCMR can be designed in such a way that the three notch bands to be tuned in a wider frequency range [23]-[24].

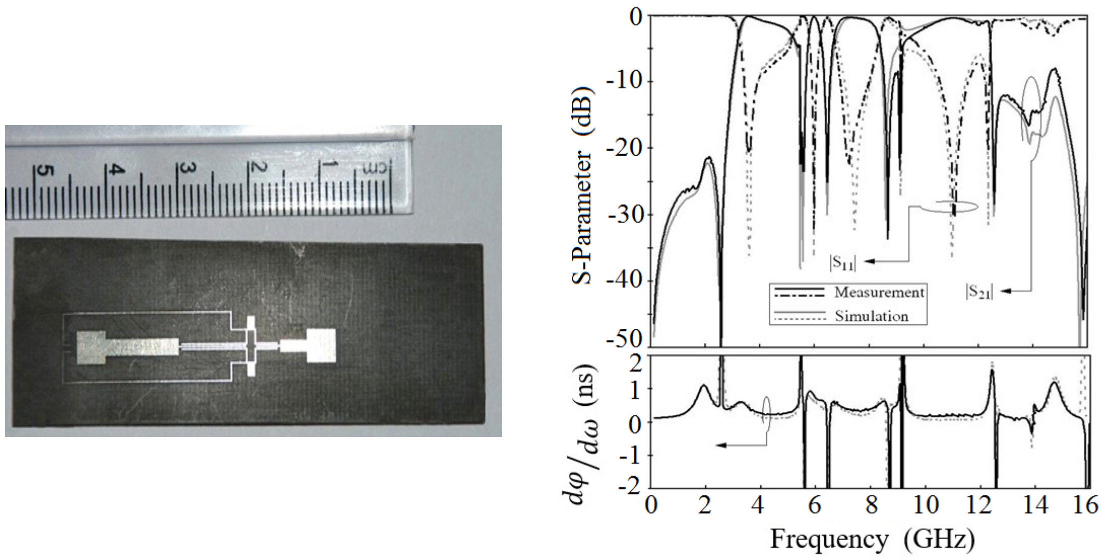

(a) (b)

Figure 4.9. (a) The digital photograph of the proposed TNB UWB BPF (b) simulated and measured results of the filter.

Table 4.2. Comparison between the proposed TNB UWB BPF and the conventional counterparts.

BPF	Structure	Size(mm^2)	TZs	Notched Frequencies (GHz)
[35]	SIW +CPW + 68 Via-Holes	654.0	One Located at Upper Side	6.8/8.35/9.48
[23]	Multi-Layer LCP + Via-Holes	178.6	One Located at Upper Side	4.98/6.85/8.87
[24]	Multilayer + Short-Circuited Stub	405.7	One Located at Upper Side	5.4/5.98/6.76
This Work	μ-strip TSSIR	308.0	Two Located at Both Sides	5.63/6.47/8.93

It should be noted that the main reason of the loss in the pass-bands of the filter, especially at the first and the third sub pass-bands, can be attributed to the very high characteristic impedance of the GCMR.

4.4.2 QNB UWB BPF

Similarly, based on the simulated results in Section 4.3, the proposed QNB UWB BPF is fabricated with the optimized parameters in the Figure 4.5 and L_X=33 mm in Figure 4.7. Figure 4.10(a) shows the digital photograph of the filter whose size is reported to be around 46.5× 8.3 mm^2. Figure 4.10(b) shows the measured and simulated performances of the QNB BPF where a good agreement is observed between them and the little discrepancy is attributed to the fabrication tolerance.

Based on the results in Figure 4.10, the five sub pass-bands of the fabricated QNB UWB BPF are centered at 3.593 GHz, 5.31 GHz, 7.86 GHz, 9.43 and 10.83 GHz with 3- dB bandwidths (FBW) of 0.71 GHz (3.24 – 3.95 GHz), 1.9 GHz (4.36 – 6.26 GHz), 1.33 GHz (7.19 – 8.52GHz), 0.65 GHz (9.1-9.75 GHz) and 1.05 GHz (10.3-11.35), respectively.

The four notched frequencies are centered at 4.26 GHz, 6.8 GHz, 8.78 GHz and 9.9 GHz, respectively. The attenuations at the centers of the four notched bands are measured to be around 16.7 dB, 12.6 dB, 20.9 dB, and 27 dB, respectively. Furthermore, as shown in Figure 4.10, the measured $d\varphi/d\omega$, the group delay in the pass-band of the filter [28], variation is reported to be between 0.2 nsec and 0.4 nsec. In addition, the upper stop-band of the filter is extended up to around 16 GHz with a suppression level of around 10 dB.

The proposed QNB UWB filter demonstrates the capability of rejecting the four unwanted parasitic bands. The design can be further developed to realize more notch-bands. Compared to the only previously reported quadruple notch band filter [25] this filter has a much simpler design procedure and requires only a single layer patterning which can significantly reduce the production cost.

It is worthy to mention that the I/O SMA connectors are connected close to the main resonator of the structure size reduction. This may be responsible for the discrepancy between the simulated and measured results. In summary, the initial two notches are caused by the SIR's dimensions as outlined in [33] and the additional notches (third and higher) can be introduced by the proposed technique in this section. The length of the GCMR is the most important factor to specify the additional notched frequencies.

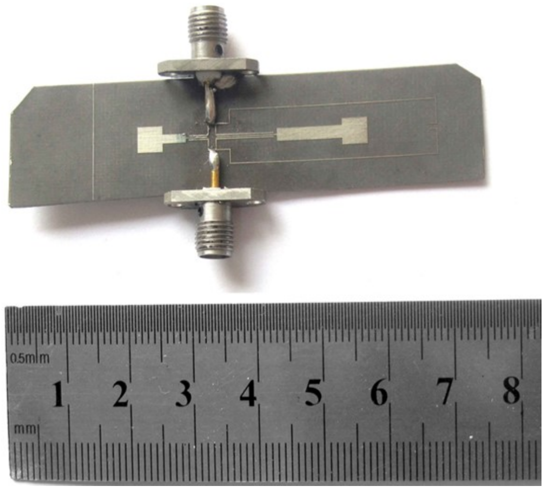

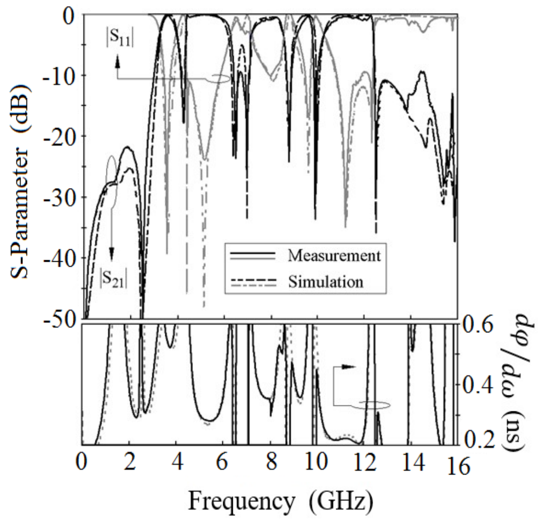

(a) (b)

Figure 4.10. (a) The digital photograph of the proposed QNB UWB BPF (b) the simulated and measured results of the filter including S-parameter and rate of the change in transmission phase with respect to frequency ($d\measuredangle S_{21}/d\omega = d\varphi/d\omega$).

4.5 Bandwidth reduction and improved pass-band behavior

For some applications, the parasitic interferences are focused on very narrow bandwidths, thus an alternative multi notch-band filter design would be desired to reduce the notch bandwidth. In this section modify the structure of the filter to reduce the bandwidth of the notches.

To further decrease the bandwidth of the notches, we observed that distributing the gaps (or capacitive coupling) along the GCMR realizes the notches with narrower bandwidth. Figure 4.11(a) shows the proposed configuration with G=0.2mm and S_1=0.15mm. Figure 4.11(b) provides the simulated insertion loss of the GCMR for the distributed layout with two additional gaps in the line. The proposed resonator is integrated with the double notch-band platform and a new triple notch-band filter is designed with the simulated results in Figure 4.12(a). In this case, one of the additional gaps is located at point A with L=18mm where the design is somehow modified to demonstrate four notch-bands by moving the gap to location B with L_1=14mm, as presented in Figure 4.12(b). This new design demonstrates multi notches with narrower bandwidth compared to the previous design.

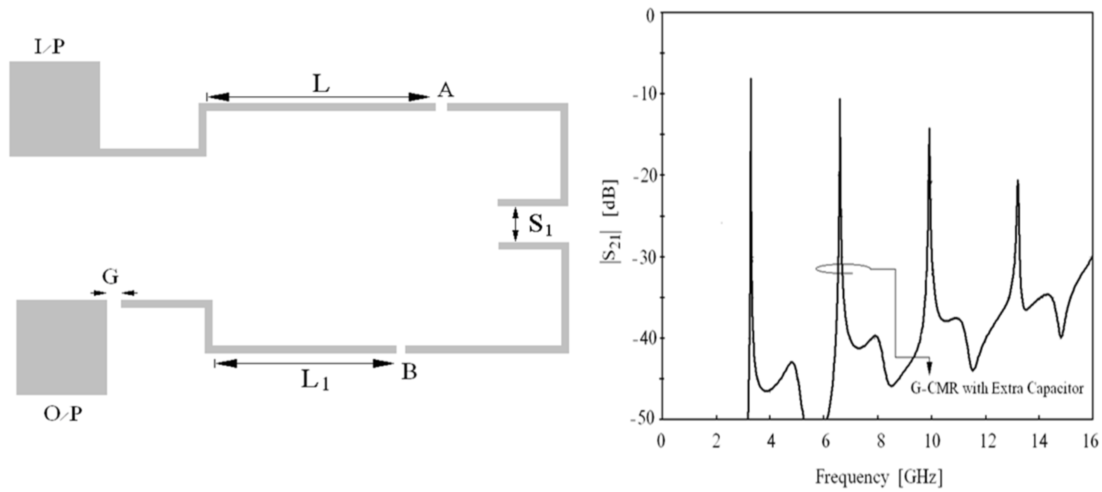

(a) (b)

Figure 4.11. (a) The layout (b) the simulated performance of the modified GCMR with extra gaps.

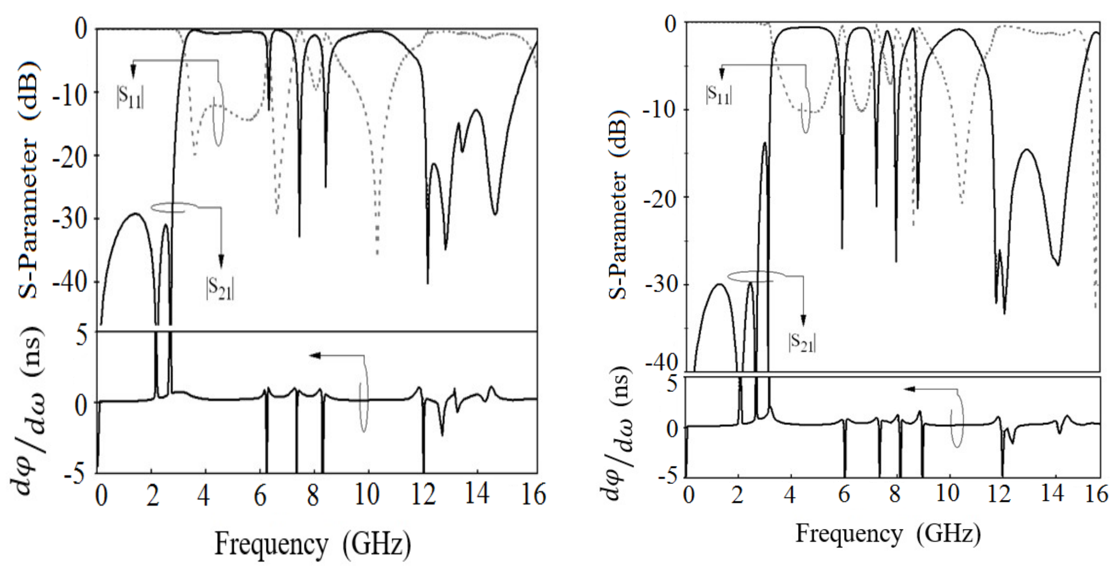

(a) (b)

Figure 4.12. The simulated performances of the proposed filter with the modified GCMR (a) TNB (b) QNB UWB BPFs.

Note that there is an insertion loss difference between the simulated and measured results for the prototypes in Figure 4.10 (0.5 dB to 1dB). The same loss difference is expected for the simulated and measured results of the new designs in Figure 4.12.

4.6 Conclusion

A new technique has been introduced to design multi notch-band ultra-wideband band-pass filter. The proposed technique is used to develop new triple and quadruple notch-band UWB filters. The proposed technique has been developed by the parallel integration of three resonators including two multiple-mode resonators (MMRs) and a gap-coupled μ-strip resonator (GCMR). Adopting the double notch-band (DNB) BPF, the two multiple (three and four) notch-band UWB BPFs have been designed and simulated by appropriately choosing the length of the third path to establish the desired transmission zeros in the pass-band of the filter. The triple and the quadruple notch-band UWB BPFs have been fabricated and measured. In comparison to the conventional triple notch-band UWB filters with multilayer structure, the fabricated prototype is low cost, compatible with MMIC technology, easy to fabricate with no via holes.

4.7 References

[1] C.-P. Chen et al., “Design of compact notched UWB filter using coupled external stepped-impedance resonator,” *Asia-Pacific Microw. Conf*, pp.945-948, Dec. 2009.

[2] M. Mokhtaari and J. Bornemann, “Ultra-wideband and notched wideband filters with grounded vias in microstrip technology,” *Asia-Pacific Microw. Conf.*, pp.1-4, Dec. 2008.

[3] M. Meeloon, S. Chaimool, and P. Akkaraekthalin, “A broadband bandpass filter with a notch-band using step-impedance resonator and embedded slots,” *Asia-Pacific Microw. Conf*, pp.1446-1449, Dec. 2009.

[4] G-M. Yang, et al., “Small ultra-wideband (UWB) bandpass filter with notched band,” *IEEE Microw. Wireless Compon. Lett*, vol.18, no.3, pp.176-178, Mar. 2008.

[5] P. Mondal and Y. L. Guan, “A coplanar stripline ultra-wideband bandpass filter with notch band,” *IEEE Microw. Wireless Compon. Lett.*, vol.20, no.1, pp.22-24, Jan. 2010.

[6] C.H. Lee, C.I.G. Hsu, and L.Y. Chen, “Notch-bands ultra-wideband bandpass filter design using combined modified quarter-wavelength tri-section stepped-impedance resonators,” *IET Microw. Antennas. Propag.*, vol.3, no.8, pp.1232-1236, Nov. 2009.

[7] Q.-X. Chu and X.-K. Tian, “Design of a compact UWB bandpass filter with notched band,” *Asia-Pac. Microw. Conf.,* pp.37-40, Dec. 2010.

[8] S. W. Wong and L. Zhu, “Implementation of compact UWB bandpass filter with a notch-band,” *IEEE Microw. Wireless Compon. Lett.*, vol.18, no.1, pp.10-12, Jan.2008.

[9] S. Ueno, K. - M. Hitke, and Y. Horii, “Ultra-wideband band pass filter with built-in notch filter configured by multi-layered CRLH unit cells,” *Asia-Pac. Microw. Conf.*, pp.1138-1141, Dec. 2010.

[10] S. Jung and S.-I. Yang, “Ultra-wideband band-pass filter with controllable arbitrary notched bands using CRLH-TL,” *Asia-Pac. Microw. Conf.*, pp.1059-1062, Dec.2010.

[11] S. Pirani, J. Nournia, and C. Ghobadi, “Band-notched UWB BPF design using parasitic coupled line,” *IEEE Microw. Wireless Compon. Lett.*, vol.20, no.8, pp.444-446, Aug. 2010.

[12] X. Luo, J-G. Ma, K. Ma, and K. S. Yeo, “Compact UWB bandpass filter with ultra-narrow notched band,” *IEEE Microw. Wireless Compon. Lett*, vol.20, no.3, pp.145-147, Mar. 2010.

[13] L. Chen, Y. Shang, and Y.L. Zhang, "Design of a UWB bandpass filter with a notched band and wide stopband," *Microw. J*, vol.52, no.11, pp.96-102, Nov. 2009.

[14] V. Sakar and K. Entesari, "Miniaturized UWB bandpass filters with notch using slow-wave CPW multiple-mode resonators," *IEEE Microw. Wireless Compon. Lett*, vol.21, no.2, pp.80-82, Feb. 2011.

[15] H.-W. Wu, M.-H. Weng, and C.-Y. Hung, "Ultra wideband bandpass filter with dual notch bands," *Asia-Pac. Microw. Conf.*, pp.33-36, Dec. 2010.

[16] K. Song and Q. Xue, "Asymmetric dual-line coupling structure for multiple-notch implementation in UWB bandpass filters," *Elec. Lett.*, vol.46, no.20, pp.1388-1390, Sept. 2010.

[17] K. Song and Q. Xue, "Ultra-wideband (UWB) bandpass filters with multiple notched bands using asymmetric dual-line coupling structure," *Asia-Pac. Microw. Conf.*, pp.1055-1058, Dec. 2010.

[18] F. Wei, Q. Y. Wu, X. W. Shi, and L. Chen, "Compact UWB bandpass filter with dual notched bands based on SCRLH resonator," *IEEE Microw. Wireless Compon. Lett.*, vol.21, no.1, pp.28-30, Jan. 2011.

[19] P.-Y. Hsiao and R.-M. Weng, "Compact tri-layer ultra-wideband band-pass filter with dual notch bands," *Prog. Electromag. Res.*, vol.106, pp.49-60, 2010.

[20] S.G. Mao, et al., "Compact ultra-wideband conductor–backed coplanar waveguide bandpass filter with a dual band-notched response," *IEEE Microw. Wireless Compon. Lett.*, vol.19, no.3, pp.149-151, Mar. 2009.

[21] J. Wang, et al., "Ultra-wide band bandpass filter with multiple frequency notched bands based on SIW and SIR technology," *Proc. of the 39th Europ. Microw. Conf.*, pp. 268-271, Oct. 2009.

[22] Z.C. Hao and J-S. Hong, "Compact UWB filter with double notch bands using multilayer LCP technology," *IEEE Microw. Wireless Compon. Lett.*, vol.19, no.8, pp. 149-151, Aug. 2009.

[23] Z.-C. Hao, et al, "Ultra-wideband bandpass filter with multiple notch-bands on multilayer liquid crystal polymer substrate," *IET Microw. Antennas Propag.*, vol.3, no.5, pp.749-756, Aug. 2009.

[24] Z-C. Hao, et al., "Ultra-wideband bandpass filter with multiple notch bands using nonuniform periodical slotted ground structure," *IEEE Trans. Microw. Theory and Tech*., vol.57, no.12, pp.3080-3088, Dec.2009.

[25] X. Luo, J.-G. Ma, K. S. Yeo, and E-P. Li, "Compact ultra-wideband (UWB) bandpass filter with ultra-narrow dual- and quad-notched bands," *IEEE Trans. Microw. Theory and Tech*., vol.59, no.6, pp.1509-1519, Jun. 2011.

[26] C.-Y. Chen, C.-Y. Hsu, and H.-R. Chuang, "Design of miniature planar dual-band filter using dual-feeding structures and embedded resonators," *IEEE Microw. Wireless Compon. Lett*., vol.16, no.12, pp.669-671, Dec. 2006.

[27] L.-H. Hsieh, G. L. Stolarczyk, and K. Chang, "Microstrip dual-band bandpass filters using parallel-connected open-loop ring resonators," *Int. J. of RF and Microw. Com.-Aided Eng*., vol.18, no.3, pp.219-224, May 2008.

[28] C.-M. Rao, T.-J. Wong, and M.-H. Ho, "A Parallel doubly coupled dual-band bandpass filter," *IEEE/MTT-S, Int. Microw. Symp*., pp.511-514, Jun. 2006.

[29] J.-E. Lim, et al., "Two-port balanced dual-band bandpass filter based on stepped impedance resonators," *Asia-Pac. Microw. Conf*., pp.1114-1117, Dec.2010.

[30] M. Nosrati and M. Daneshmand, "A novel compact dual-wideband band-pass filter using spiral-shaped multi-mode and complementary split ring resonators," *Microw. J*, vol.54, no.11, pp.100-108, Nov. 2011.

[31] C.-P. Chen, Z. Ma, and T. Anada, "Synthesis of ultra-wideband bandpass filter employing parallel-coupled stepped-impedance resonators," *IET Microw. Antennas Propag*., vol.2, no.8, pp.766-772, Dec. 2008.

[32] C.-K. Lung, K.-S. Chin, and J. S. Fu, "Tri-section stepped-impedance resonators for design of dual-band band stop filter," *Proc. of the 39th Europ. Microw. Conf*., pp.771-774, Oct. 2009.

[33] M. Nosrati and M. Daneshmand, "Compact microstrip UWB double/single notch-band BPF based on wave's cancellation theory," *IET Microw. Antennas Propag*., vol.6, no.8, pp.862-868, Jun.2012.

[34] D. M. Pozar, *Microwave Engineering*, 2nd Ed. New York: Wiley, 1998.

[35] J. Wang, et al., “UWB bandpass filter with multiple frequency notched bands,” *IEEE MTT-S Int. Microw. Workshop Series on Art of Miniaturizing RF and Microw. Passive Compon*, pp.106-109, Dec. 2008.

[36] S. Amari, U. Rosenberg, and J. Bornemann, “Adaptive synthesis and design of resonator filters with source/load-multiresonator coupling,” *IEEE Trans. Microw. Theory and Tech*., vol.50, no.8, pp.1969-1978, Aug. 2002.

Chapter 5 Compact MEMS-based ultra wide-band CPW band-pass filters with single/double tunable notch-bands

5.1 Introduction

The unlicensed use of ultra-wide-band (UWB) for commercial purposes, approved by FCC in 2002, has raised interest in academic and industrial research on various UWB devices [1]. Since the existing radio signals such as wireless local-area network (WLAN) or WiMax may interfere with the UWB radio system within the range defined by the FCC, the design of ultra-wide band-pass filters (UWB BPF) is required with single/multiple notch-bands to reject these interfering signals.

So far, several studies have focused on single and multiple notch-bands filters realization [2]-[16], however, they are limited to fixed notches. It is well known that the existing parasitic signals change from place to place and from time to time. Therefore, the recent investigations have attempted to design UWB filters with tunable notch-bands [17]-[21].

A single tunable notch-band UWB BPF has been reported in [17] based on harmonic characteristics of a half wavelength transmission line integrated with varactor diodes. Another tunable notch-band filter has been investigated using an open-stub microstrip structure in combination of varactor diodes [18]. An electronically reconfigurable notch-band UWB BPF on liquid crystal polymer (LCP) substrate has also been reported in the literature [19]. The same technology has been employed to develop a tunable single notch-band UWB BPF in [20].

However, these filters have been designed by incorporating varactor diodes and via holes which require hybrid integration with associated complexity. Besides, they consume power and show poor RF performance [21]. Active filters have also been employed in several studies to meet these requirements but at the expense of increased CMOS chip area, cost and power consumption [22]-[23].

The MEMS filter technology has been widely studied during the last decade due to the superior characteristics including low DC power consumption and low RF loss [24]. To capture such benefits, a miniaturized tunable notch-band UWB BPF has recently been investigated using the integration of transmission lines and MEMS capacitors [25]. This filter provides a tunable notch-band on a silicon-based substrate; however, it is limited to a single tunable notch-band.

In this Chapter, we propose a novel compact UWB filter with single/double tunable notch-bands. The proposed filter is based on a compact UWB filter with two incorporated MEMS capacitors. The integrated filter is designed in such a way that one of the notched frequencies can be independently tuned by actuating the corresponding MEMS capacitor. The basic idea behind the double-notch UWB BPF is previously shown in [26], here, the design procedure and the fabrication process of the filter integrated with the MEMS components are presented.

In the next section, the proposed tunable double-notch UWB BPF is initially introduced where the main components of the filter including UWB BPF and the RF MEMS capacitors are characterized. The UWB BPF will be initially explained with design, simulation and fabrication details on a 635-µm-thick alumina substrate with the dielectric constant of ε_r=9.8. Afterwards, a new concept of coupled transmission lines integrated with RF MEMS capacitors is proposed and mathematically analyzed to introduce a notch-band in the pass-band of the filter. Then, the transmission zero realized by the integration of MEMS capacitors with coupled TLs is employed to tune the notch-band. Finally, two UWB BPFs with the single/double tunable notch-band are experimentally demonstrated.

5.2 Principle operation of the proposed tunable UWB BPF

Figure 5.1(a) and (b) schematically show the proposed tunable double notch-band UWB band-pass filter and the expected behavior, respectively. Here, a half-wavelength resonator integrated with two quarter-wavelength lines is employed to demonstrate UWB filters [26]-[29]. As schematically shown in Figure **5.1**(a), the two MEMS capacitors with different plate areas are integrated with the coupling parts of the CPW UWB BPF at I/O ports. The capacitors are anchored to the one of the two coupled lines and extended over the resonator and the other coupling line. These RF MEMS capacitors are then integrated with the structure to design tunable notch-band UWB BPFs, as shown in Figure 5.1(b).

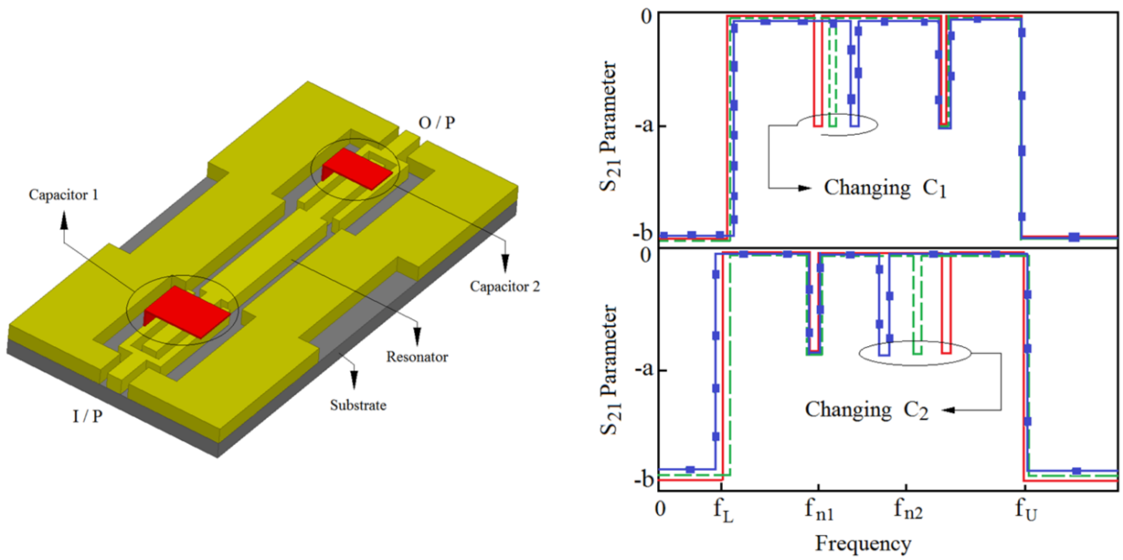

(a) (b)

Figure 5.1. (a) The proposed tunable DNB UWB BPF (b) the expected performance.

As will be explained in the next section, the integration of the MEMS capacitors and the half-wavelength resonator adds an extra transmission zero which can be independently tuned. The notched frequencies realized by these TZs can be continuously tuned by changing the capacitor of the MEMS actuator.

The detailed analysis and design procedure of such structures are explained in this Chapter. The UWB filter design without any notch-band will be explained in the next section. Then, the theory and the proposed concept of adding transmission zero will be elaborated to develop tunable single/double notch-bands.

5.3 Ultra-wide-band band-pass filter

The UWB BPFs have previously been designed by integration of half-wavelength resonators and two quarter-wavelength lines [27]-[29]; however, the entire structure is reported to be relatively large due to the λ/2 resonator.

Here, we apply this technique to design the filter shown in Figure **5.1**(a). In this filter, we use distinctive characteristic impedances (the lower ones at the I/O ports and the higher ones at the resonator) which results in the electrical length reduction of the main $\lambda/2$ length resonator (L_1). A size reduction of around 44% is reported in comparison to the conventional filters [27].

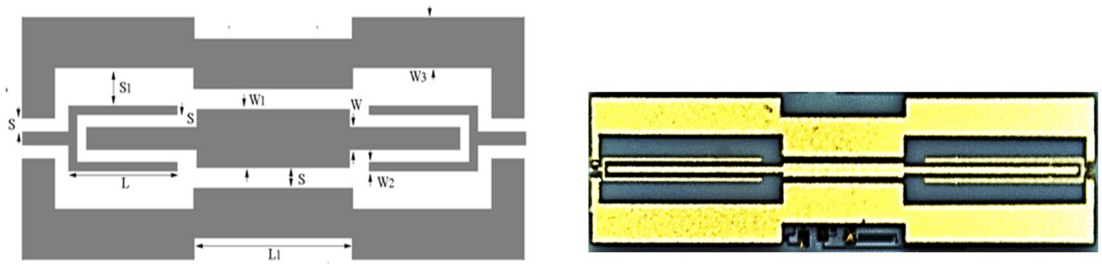

(a) (b)

Figure 5.2. (a) UWB BPF with: L=3.2mm, L_1=2.4mm, S= 0.05mm, S_1=0.275mm, W=0.1 mm, W_1=0.2mm, W_2=0.05mm and W_3=0.65mm (b) the fabricated UWB BPF on an alumina substrate with the thickness of 635μm and the dielectric constant of 9.8.

According to the given specifications, an UWB BPF is designed with the optimized parameters given in Figure 5.2. The UWB BPF is fabricated on an alumina 0.635-mm-thick substrate with the dielectric constant of ε_r= 9.8. The size of the entire layout is reported to be around 2.5×10 mm^2 where Figure 5.2(b) shows the digital photograph of the filter.

To verify the simulated performance of the filter, the S-parameter measurements are performed using an Agilent network analyzer from DC to 24 GHz.

Figure 5.3 compares the simulated and measured performances of the UWB BPF. The maximum insertion loss in the pass-band is measured to be around 1.8 dB which mainly comes from dielectric and conductor losses. Moreover, the main discrepancy between the simulated and measured insertion losses is due to the low conductivity of the sputtered gold which is measured to be 1.8×10^7 S/m (as oppose to nominal 4×10^7 S/m). Besides, confirmed by simulation, the increase of the gold thickness from 1 μm to around 3 μm can significantly reduce the insertion loss of the filter.

In the next section, the notch-band realization in the UWB pass-band is discussed using lumped-element analysis. To present the proposed model, the theoretical analysis is initially explained including the transmission zero realization and then a novel tunable single notch-band UWB BPF is designed and fabricated.

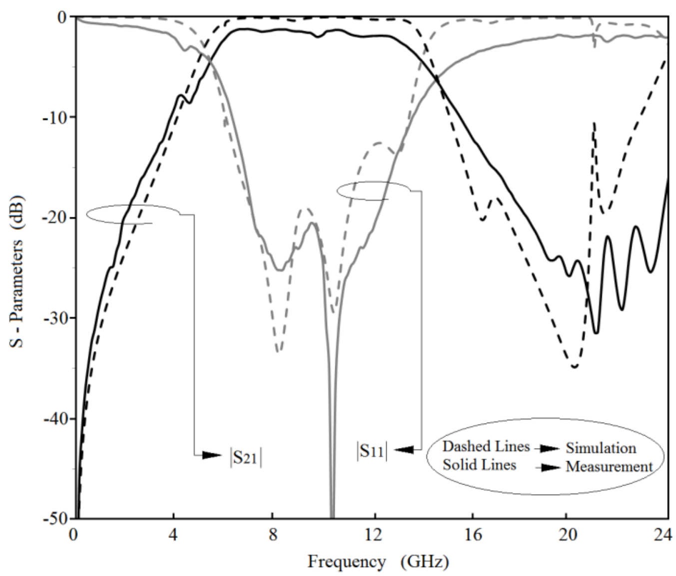

Figure 5.3. The simulated and measured performances of the UWB BPF in Figure **5.2** (b).

5.4 Tunable notch-band realization

5.4.1 Realization of transmission zeros (TZs)

As discussed in the previous section, an UWB BPF can be designed by the integration of a multiple mode resonator (MMR) and two coupled lines. In this section, the coupled lines are further developed to realize a transmission zero (TZ) resulting in a notch-band UWB BPF.

The Y_{21} parameter of the integrated structure is extracted to show that the extra TZ can be realized by integrating the coupled lines with an *L*-*C* circuit. The simplest way to derive the *Y* parameter and consequently the TZs of the proposed layout is using the ABCD matrix [31]. Figure 5.4 shows the proposed coupled transmission lines to realize three TZs. It should be noted that the coupled lines with three lines can be considered as two pairs of coupled lines where the middle line is divided into two lines using even/odd-mode analysis [29].

The developed structure consists of the two different paths from port 1 to port 2. Path1 includes a pair of coupled lines with electrical length θ and even/odd-mode characteristic impedances Z_e and Z_o while path2 consists of a pair of coupled lines integrated with a lumped element *L*-*C* circuit.

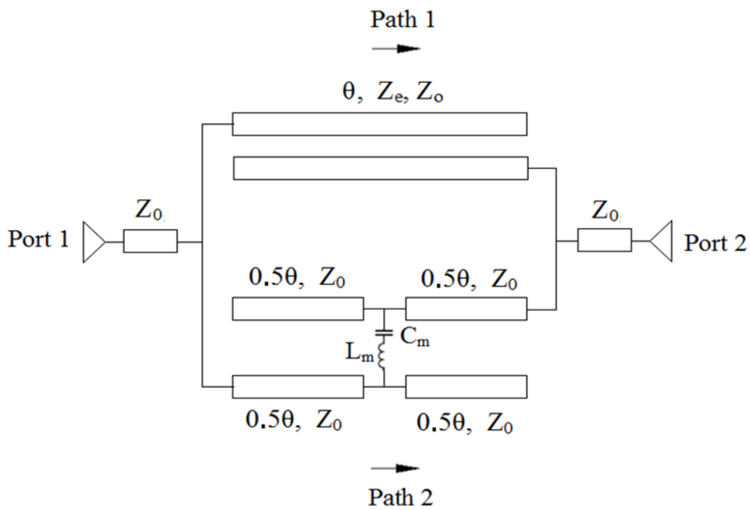

Figure 5.4. The proposed coupled lines integrated with *L*-*C* circuit.

The ABCD matrix for path1 can be determined as follows [31].

$$\begin{bmatrix} A_1 & B_1 \\ C_1 & D_1 \end{bmatrix}_{Path1} = \begin{bmatrix} \frac{Z_e+Z_o}{Z_e-Z_o}cos\theta & j(\frac{(Z_e-Z_o)^2-(Z_e+Z_o)^2cos^2\theta}{2(Z_e-Z_o)sin\theta}) \\ j\frac{2sin\theta}{Z_e-Z_o} & \frac{Z_e+Z_o}{Z_e-Z_o}cos\theta \end{bmatrix} \tag{5-1}$$

where its *Y* parameter can be calculated as (5-2):

$$(\boldsymbol{Y_{21}})_{\boldsymbol{Path1}} = \frac{\boldsymbol{-1}}{\boldsymbol{B_1}} \tag{5-2}$$

To make a simple analysis for path2, the coupling between the transmission lines is neglected; therefore, ABCD matrix is derived as given in (5-3).

Based on Richard’s Transformation [31], the *L*-*C* circuit is replaced by the two short- and open-circuited stubs with the electrical length of 0.5θ and the characteristic impedances calculated from L and $1/C$, respectively.

$$\begin{bmatrix} A_2 \\ B_2 \\ C_2 \\ D_2 \end{bmatrix}_{Path2} = \begin{bmatrix} \left(C_m \tan 0.5\theta - \frac{\cot 0.5\theta}{L_m}\right)[0.5\sin\theta(Y_0^2 tan^2 0.5\theta - 1) - Y_0 \tan 0.5\theta \cos\theta] + \cos\theta - Y_0 \tan 0.5\theta \sin\theta \\ j[\left(C_m \tan 0.5\theta - \frac{\cot 0.5\theta}{L_m}\right)(cos^2 0.5\theta + sin^2 0.5\theta tan^2 0.5\theta - Y_0 \tan 0.5\theta sin\theta) + sin\theta - 2Z_0 tan 0.5\theta sin^2 0.5\theta] \\ j[2Y_0 sin\theta - 4Y_0^2 sin^2 0.5\theta(C_m tan 0.5\theta - \frac{cot 0.5\theta}{L_m})] \\ \left(C_m tan 0.5\theta - \frac{cot 0.5\theta}{L_m}\right)[0.5 sin\theta(Y_0^2 tan^2 0.5\theta - 1) - Y_0 tan 0.5\theta cos\theta] + cos\theta - Y_0 tan 0.5\theta sin\theta \end{bmatrix} \quad \text{(5-3)}$$

The Y parameter for this path can be calculated as follows:

$$(\boldsymbol{Y_{21}})_{\boldsymbol{Path2}} = \frac{\boldsymbol{-1}}{\boldsymbol{B_2}} \quad \text{(5-4)}$$

Now, the Y_{21} admittance of the entire structure in Figure 5.4 can be derived as follows [31]:

$$(\boldsymbol{Y_{21}})_{\boldsymbol{Total}} = (\boldsymbol{Y_{21}})_{\boldsymbol{Path1}} + (\boldsymbol{Y_{21}})_{\boldsymbol{Path2}} \quad \text{(5-5)}$$

To solve (5-5), there are several degrees of freedom. The characteristic impedances are initially normalized to Z_0 = 50 **Ω** and then they are arbitrarily chosen. Figure 5.5 shows the solution of $(Y_{21})_{\text{Total}}$ where three TZs are realized.

To investigate the behavior of the structure in detail, the behavior of $(Y_{21})_{\text{path1}}$ and $(Y_{21})_{\text{path2}}$ parameters are discussed.

Figure 5.5 presents the graphical solution of Y_{21} parameter for the coupled lines integrated with the *L*-*C* circuit in path2 and the coupled lines in path1. Inspecting the given graphs, we observe that $(Y_{21})_{\text{Path1}}$ demonstrates two TZs as θ_{tz}= 0 and π corresponding to 0 and $2f_0$, respectively [29], [31] and [32]. It can be seen that $(Y_{21})_{\text{Path2}}$ follows the behavior of that of the conventional coupled lines except at the resonance of the *L*-*C* circuit.

The third notch is realized at $\theta=\theta_{tz3}$ by integrating the MEMS capacitor with the coupled lines. Inspecting the mathematical solution in Figure 5.5, we observe that the amplitudes of $Y_{21\ \text{path1}}$ and $Y_{21\ \text{path2}}$ parameters at $\theta=\theta_{tz3}$ are equal with inverse sign. This leads to the realization of an additional TZ where two signals with equal amplitudes and 180 phase shift add up to zero [7]. Similarly, it can be shown that the signals coupled through path1 and path2 could cancel out at a desired frequency by appropriately choosing the values for

L and *C* components as well as coupled-line parameters.

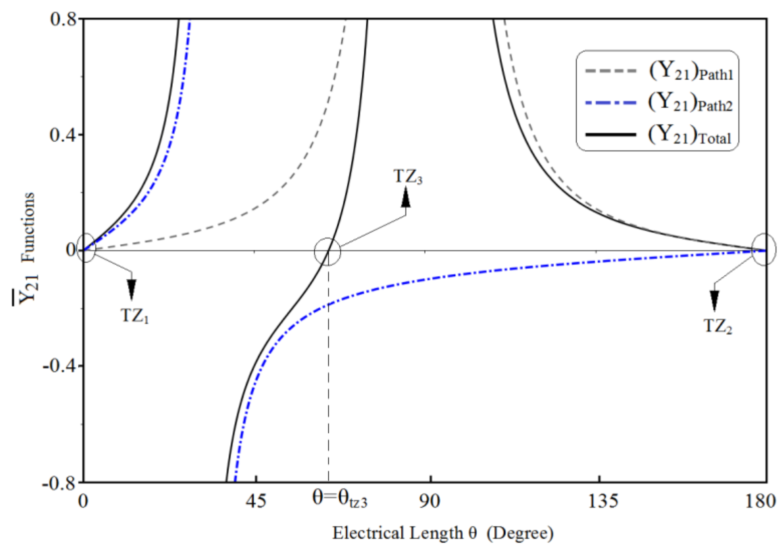

Figure 5.5. Solutions of $(Y_{21})_{\text{Path1}}$, $(Y_{21})_{\text{Path2}}$ and $(Y_{21})_{\text{Total}}$ with normalized $\bar{Z}_{\mathrm{e}} = 1.1, \bar{Z}_{\mathrm{o}} = 0.9, C_{\mathrm{m}} = 11, L_{\mathrm{m}} = 1$.

5.4.2 Transmission zero tuning

As discussed in the previous section, the coupled lines realize two TZs at two different frequencies while the *L*-*C* circuit in path2 demonstrates the third TZ. We use the third TZ for notch-band realization; therefore, its realization and tuning mechanism are explained in more detail.

Figure 5.6 shows that the frequency of this TZ can be tuned by changing C_m and L_m. As given in Table 5.1, C_m is normalized to L_m and the total admittance of the structure where $(Y_{21})_{\text{Total}}$ is calculated for the different values of these two components in Figure 5.5. We observe that the third TZ is shifted towards the lower frequencies by increasing $C_m L_m$.

Table 5.1 Different values of C_{m} capacitor.

	$(Y_{21})_{T1}$	$(Y_{21})_{T2}$	$(Y_{21})_{T3}$	$(Y_{21})_{T4}$	$(Y_{21})_{T5}$	$(Y_{21})_{T6}$
C_m	11	15	20	25	35	50
L_m	1	1	1	1	1	1

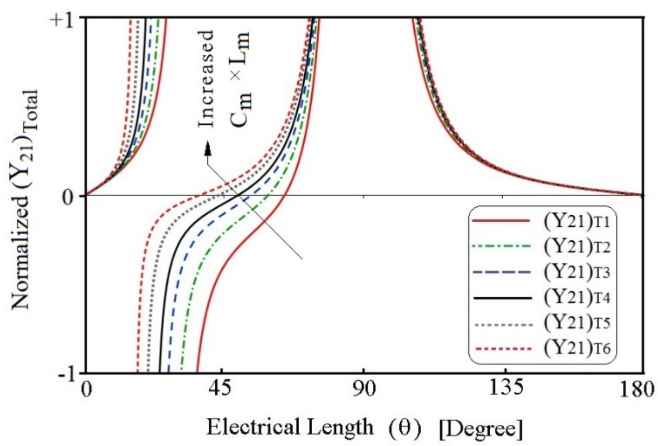

Figure 5.6. Solution of $(Y_{21})_{Total}$ for the different values of C_m capacitor in Table 5-1.

5.4.3 Confirmatory simulation

As theoretically demonstrated in the previous sections, the third TZ is realized by the integration of the *L*-*C* circuit and the coupled lines, therefore this technique is used to suppress an un-wanted frequency band. The proposed model in Figure 5.4 is designed and simulated to verify the theoretical results in Section 5.3. Figure 5.7(a) shows the simulated results for the proposed model in Figure 5.4, designed using CPW transmission lines on a substrate with the thickness of 635 µm and the dielectric constant of 9.8. It should be noted that the *L*-*C* circuit is replaced with a MEMS capacitor to realize a notch-band corresponding to the third TZ. Additionally, Figure 5.7(b) represents the simulated results for the circuit with the same parameters with variable C_m capacitor. In this simulation, the values of L_m and C_m are chosen based on the normalized values in Figure 5.6. Having one degree of freedom, L_m is chosen to be around 0.01 nH and C_m is calculated using the ratios in Table 5-1. It should be noted that the notch-band is tuned from 5.4 GHz to 4.7 GHz for the values of C_m in Figure 5.7(b).

Inspecting the theoretical and simulated results in Figure 5.6 and Figure 5.7, respectively, we observe that the realized notch-band corresponding to the third TZ is shifted towards the lower frequencies by increasing C_m.

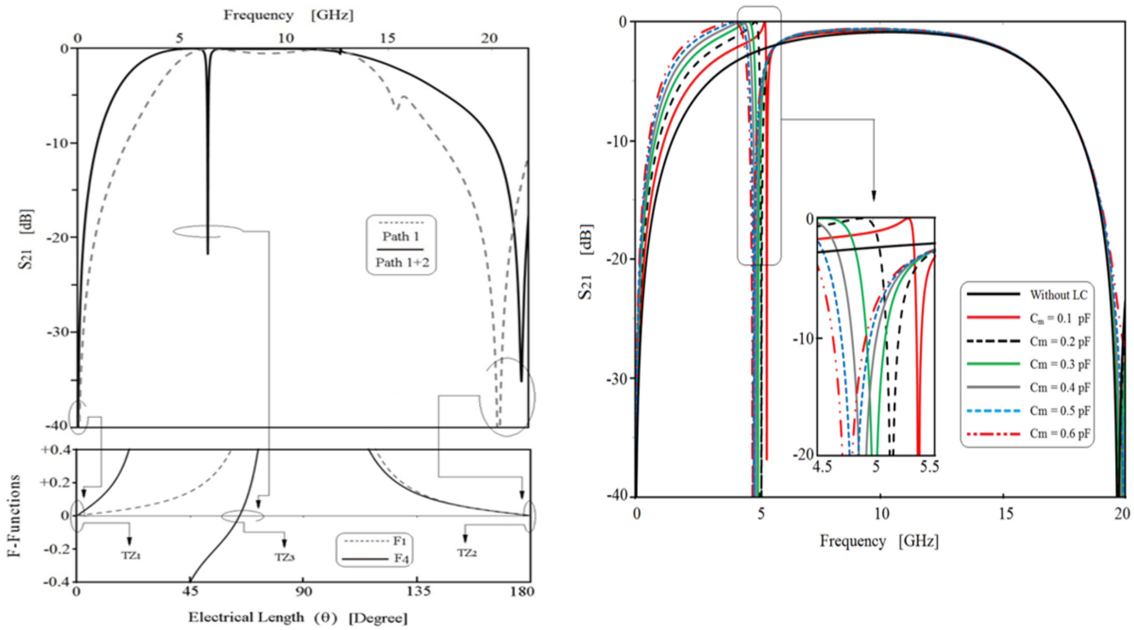

(a) (b)

Figure 5.7. EM simulated results of the proposed structure in Figure **5.4** with **(**a) MEMS capacitor (b) lumped element *L-C* circuit.

5.5 Tunable MEMS capacitor

The proposed UWB filter is fabricated through CMC Micro-system using the UWMEMS process; a 7-mask gold based multiuser fabrication process (Details provided in Appendix A). The summary of the process is as follows.

The process starts by sputtering 40 nm of Cr on a 25 mil thick Alumina wafer. The Cr layer is patterned by the 1st mask using the lift-off technique to define the bottom plate of the MEMS capacitors. A 0.3 µm PECVD silicon oxide layer is deposited and patterned by the 2nd mask which protects the Cr layer from oxidation and provides electrical isolation between the capacitor bottom plate and the top metallic layer. The process continues by evaporating a thin layer of Cr/Au (40 nm/100 nm) as the seed layer for the electroplating step. A photoresist mold is then formed using the 3rd mask to electroplate 1µm µm of gold. The main resonator part and the CPW ports are defined by this layer. The mold and the seed layer are removed at the end. A dielectric layer of 0.5µm PECVD silicon oxides is deposited to provide isolation between the main resonator and the top capacitor plate.

Polyimide is then spin coated as the sacrificial layer (2.5µm) for the MEMS capacitors and patterned to define the openings for the anchors. Finally, the top gold layer is sputtered and electroplated to achieve 1.25µm thicknesses and molded to define the main structural layer (top plate of MEMS capacitors). The MEMS capacitors are finally released using an oxygen plasma dry etching process.

Figure 5.8(b) shows a SEM picture of the released MEMS capacitor integrated with the proposed filter.

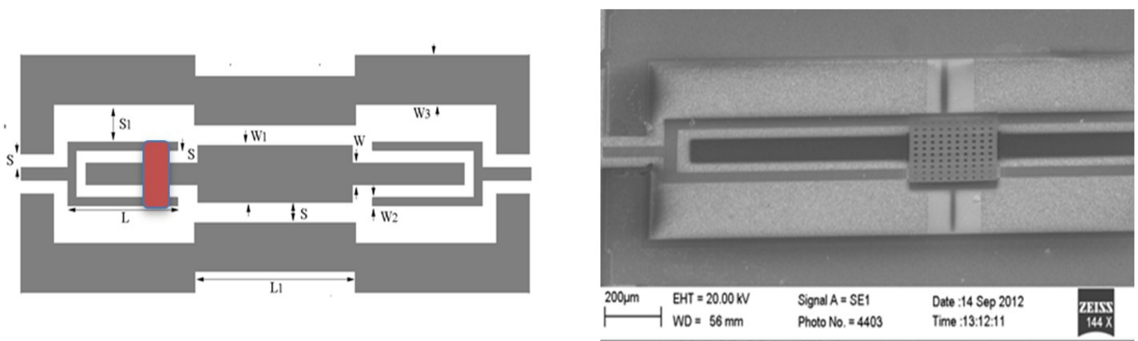

(a) (b)

Figure 5.8. (a) MEMS capacitor integrated with the UWB BPF (b) filter SEM picture.

As discussed in the previous sections, the third TZ is realized by integrating the *L-C* circuit with the UWB BPF where this TZ is tuned by changing the capacitor of the circuit. Note that the TZ tuning is performed by applying an electrostatic voltage to the MEMS capacitor.

Figure 5.9 shows the Zygo optical profile of the integrated MEMS capacitor in the UP state. By applying the voltage to the capacitor, the capacitor gap decreases resulting in the increase of capacitance in the circuit.

For this case, the voltage can be increased from 0 volt up to 60 volts where the snap down (pull-in) happens and the capacitor cannot be further tuned. Thus, the capacitance value is tuned between the Up and Down states of the MEMS capacitor. The capacitance value of a curled-up capacitor can be calculated using the following equations:

$$C = \frac{\varepsilon_0 A}{(d_2 - d_1)} Ln(\frac{d_2}{d_1}) \qquad (5\text{-}6)$$

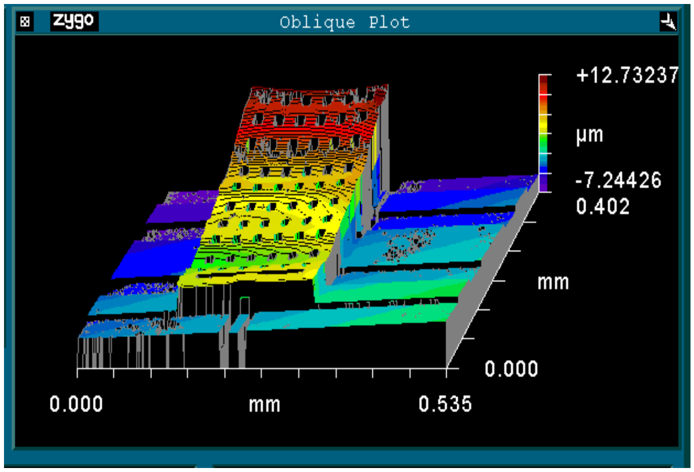

Figure 5.9. Zygo picture of the released MEMS capacitor.

Table 5.2 presents the calculated and simulated values of the capacitor for two UP and DOWN states based on the measured profile of the MEMS structure.

The small discrepancy between the calculated (based on the measured capacitor properties) and the simulated results is due to the curled-up plate of the fabricated capacitor which is not considered in the simulation.

Table 5.2 Calculated and simulated capacitance values.

	UP-state	Down-State
Calculated (Eq.(5-6))	0.09 pF	0.45 pF
Simulated	0.12 pF	0.54 pF

5.6 Ultra wide-band band-pass filter with tunable single notch-band

To verify the theory, a tunable notch-band UWB BPF is designed based on the integration of the MEMS capacitor and CPW-based filter.

According to the proposed structure in Figure 5.4, a notch-band is realized in the ultra-wide-band pass-band of the coupled lines. In this Section, a tunable single notch-band UWB BPF is designed and analyzed by replacing one of the coupled lines in the layout of the UWB BPF in Figure 5.2 with the proposed model in Figure 5.4.

An UWB BPF with tunable notch-band is realized by integrating the coupled lines and MEMS capacitor of C_m (420×350 µm^2) with 1.55 mm away from the input port.

The performance of the filter is simulated by an EM simulator tool (Agilent ADS Momentum) on the same substrate with the parameters in Figure 5.2. Figure 5.10 shows the performance of this filter considering PEC for the metals and ideal flat MEMS capacitor plate.

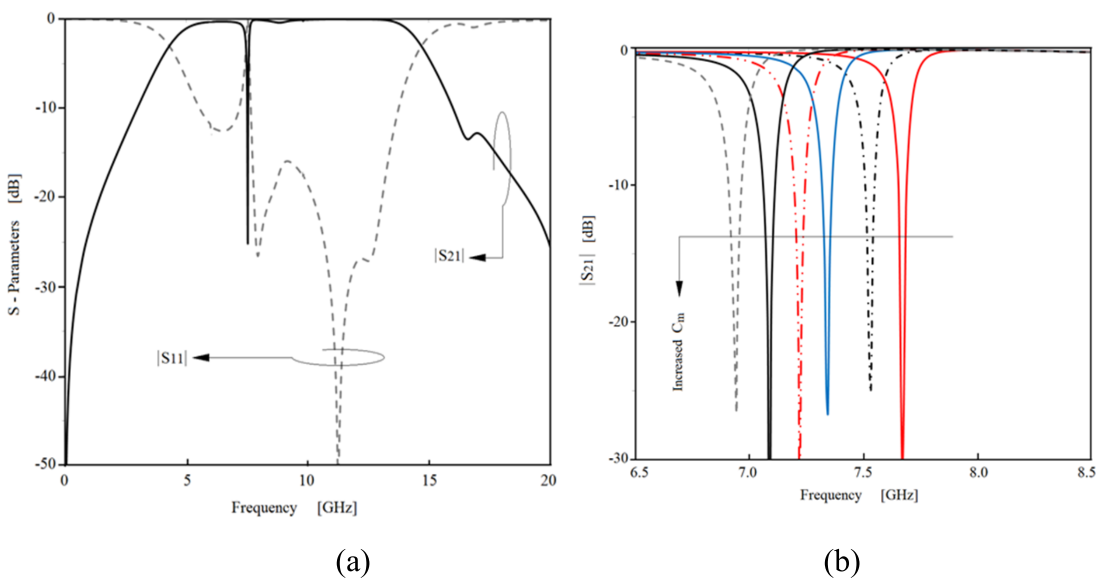

Figure 5.10. (a) Simulated results of the tunable single notch-band UWB BPF (b) the notch-band tuning.

Inspecting the simulated results of the tunable single notch-band UWB BPF in Figure 5.10, we observe that the simulated results confirm the theoretical ones in Figure 5.6 and Figure 5.7. As shown, the notch frequency is tuned and shifted towards the lower frequencies by increasing the tunable capacitor of C_m in the structure.

According to the proposed technique, a new compact UWB filter with single tunable notch-band is fabricated on a 0.635-mm-alumina substrate with the dielectric constant of 9.8. The size of the entire layout is reported to be an area of 2.5 × 10 mm^2. To experimentally verify the performance of the proposed filter, its S-parameter measurements are performed using an Agilent's network analyzer from DC to 25 GHz. Figure 5.11 provides the photo and the measured results of the filter. The maximum in-band insertion loss is measured to be around 3.4 dB where we observe a 1.6 dB loss difference in comparison to that of the UWB BPF in Figure 5.3. This extra loss can be attributed to the parasitic coupling of MEMS actuators with the CPW lines where its maximum loss occurs at their resonance or notch-bands. We have modeled the MEMS actuators only at their resonance using series L_m-C_m circuit in Figure 5.4. Based on the complete equivalent circuit of open-circuited stub in Figure 2.8, if we include the other capacitor of the MEMS actuator integrated with series L_m-C_m, this capacitor imposes extra loss by generating parasitic coupling between the CPW signal lines.

The measurement shows that the notch-band can be tuned from 7.7 GHz to 6.3 GHz with an actuation voltage of 0 to 60 volts. This notched frequency can be even further tuned to the lower frequencies. At the notch frequency, the insertion loss is measured to be around 10 dB where it slightly decreases by increasing the actuation voltage.

Moreover, the quality factor and the equivalent resistance of the MEMS capacitor are calculated to be 12.96 and 3.76 Ω, respectively using the measured 3-dB bandwidth of the notch-band, 6.23 GHz to 6.73 GHz and the resonance frequency of 6.48 GHz.

Inspecting the measured results, the suppression level or the notch depth becomes limited in practice, around 10 dB. To improve the performance of the filter in terms of suppression level in the notch-band, the performance of the filter is simulated again by considering the main sources of the loss including conductor and substrate losses. Moreover, the filter performance is improved by optimizing the MEMS capacitors where the capacitor is anchored on one of the lines and extended only over the resonator. Figure 5.12 compares the simulated and measured results of the primary filter to the simulated results of the modified filter.

In the modified filter, the physical dimensions of the two MEMS capacitors are somehow chosen to resonate at the same frequency. As the results of these modifications, a much deeper notch is demonstrated for the tunable single notch-band filter, as shown in Figure 5.12. Note that the capacitor plate size is increased to 620×420 μm^2 in the new design. This could also compensate the warpage of the MEMS beam shown in Figure 5.9. Note that there is a loss difference between the simulated and measured results of the filter in Figure 5.12 (0.5 dB to 1.5 dB). The same loss difference is expected for the simulated and measured results of the new design with improved notch suppression.

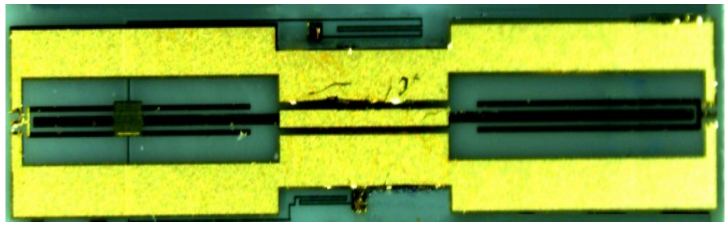

(a)

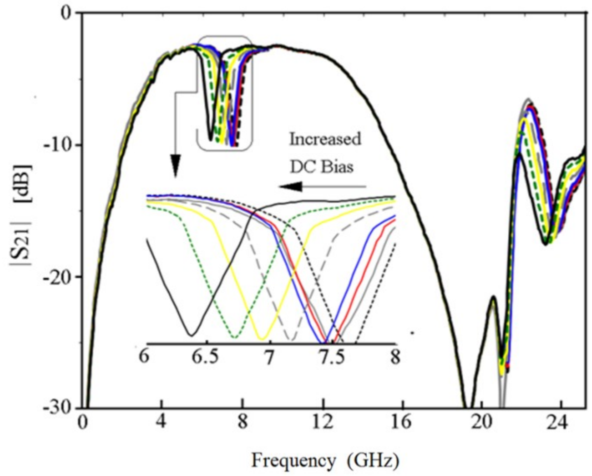

(b)

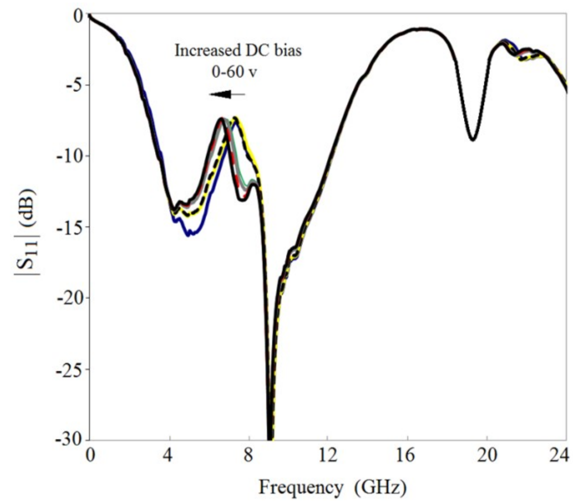

(c)

Figure 5.11. (a) Fabricated UWB BPF with tunable single notch-band and the measured performance of the filter (b) S_{21} (c) S_{11}.

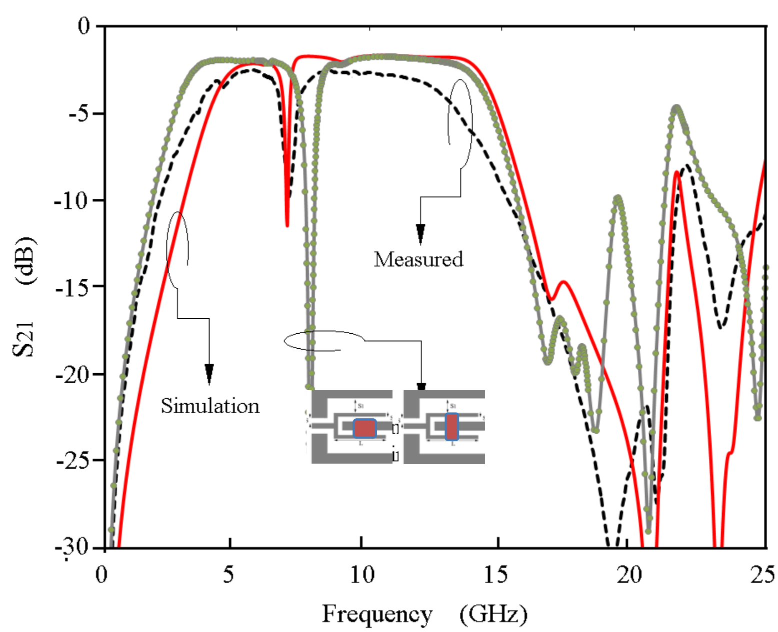

Figure 5.12. Simulated results of the modified filter (Agilent ADS Momentum).

5.7 Ultra wide-band band-pass filter with tunable double notch-bands

In this section, the structure of the filter is further developed to design an UWB BPF with tunable double notch-band where the structure is integrated with another MEMS capacitor. Similar to the theoretical results in Section 5.3, it can be shown that the location of the second notch can be arbitrarily tuned by changing the distance of the MEMS actuator from the output port (changing θ in equations (5-3)-(5-5)).

The first notch-band is established by integrating the MEMS capacitor of C_1 (420×350 μm^2) with the coupled lines of the structure, Figure 5.1(a), with 1.55 mm away from the input port. Similarly, the second tunable notch-band can also be realized by integrating another MEMS capacitor C_2 with the different capacitance value (350×320 μm^2), with 1.2mm away from the output port, to operate at a different frequency from the first notch-band.

Figure 5.13 shows the EM simulated results of the filter using ADS simulator where the first notch-band is independently tuned by changing the first MEMS capacitor of C_1,

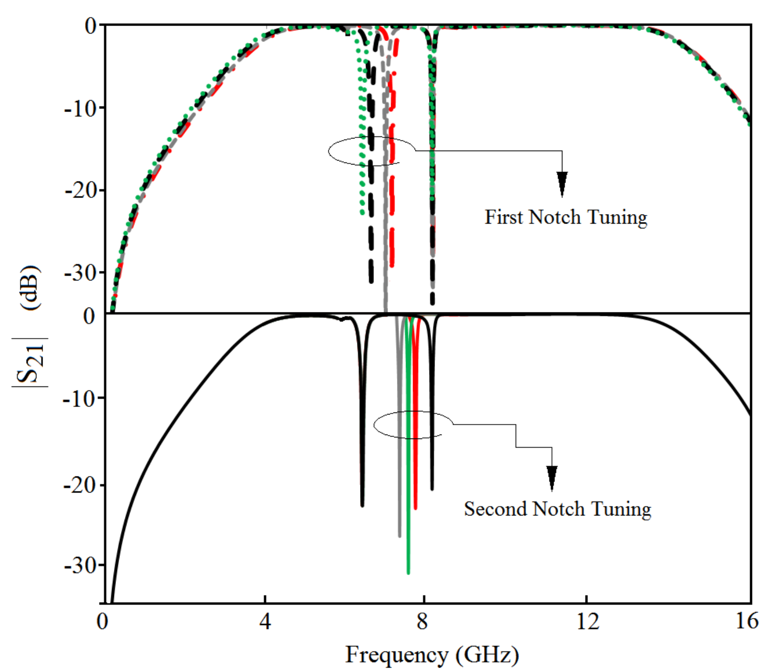

Figure 5.13. Simulated frequency responses of the proposed tunable double notch-band UWB BPF.

Similarly, the second notch is also tuned by actuating the second capacitor of C_2. It should be noted that the tuning range of the notched frequencies of the filter is limited to the MEMS capacitors tuning ratio which is equal to 1.5 for ideal standard parallel plate MEMS capacitors. Eliminating this constraint, the notch frequencies can be further tuned across a larger frequency band. The new compact UWB filter with dual tunable notch-bands is designed and fabricated. Figure 5.14 shows the fabricated filter integrated with the MEMS capacitors.

The size of the entire layout is reported to be an area of 2.5×10 mm^2. To experimentally verify the performance of the filter, its S-parameter measurements are performed using an Agilent's network analyzer from DC to 25 GHz.

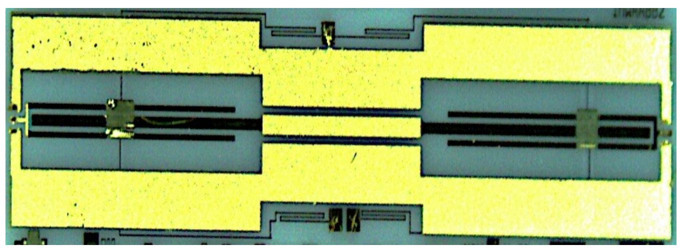

Figure 5.14. Digital photograph of the fabricated tunable double notch-band UWB BPF.

5.7.1 The first notch-band tuning

To tune the first notch-band, an actuation voltage of 0 to 60 volts is applied to the first capacitor (C_{m1}) where Figure 5.15 shows the measured results of the filter. The results show that the notch-band is continuously tuned as wide as 1 GHz from 7.5GHz to 6.5GHz.

The capacitor reaches to it pull-in state at 60 volts resulting in a sudden shift of the notch from 6.45 GHz to 5.5 GHz.

Fabrication process and thin gold loss excluded, the main source of simulated and measured insertion loss difference can be attributed to the parasitic coupling of MEMS actuator with CPW signal lines out of its resonance frequency. The measured results are performed on a gold layer of as thin as 1 μm whereas simulation is performed for PEC. The maximum in-band insertion loss is measured to be around 3.4 dB.

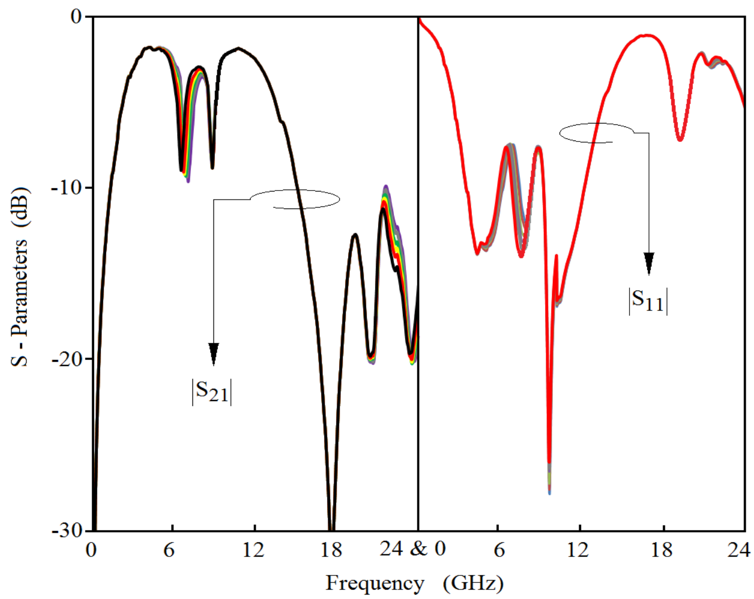

Figure 5.15. Measured frequency response of the proposed UWB BPF for the first notch tuning.

5.7.2 The second notch-band tuning

Figure 5.16 shows the measured performance of the filter when the second capacitor associated with the second notch-band (C_2) is tuned. The measurement shows a tuning range of 8.8GHz to 7.8GHz for the second notch-band while the first notch-band remains unchanged at 5.5 GHz. This notch frequency can be even further tuned to the lower frequencies; however, it overlaps with the first notch-band. The measured results indicate that while the notch-bands are tuned, the filter performance remains unchanged across the band. It is believed that the insertion loss can be considerably improved if thicker gold layers are used. It should also be noted that the same insertion loss is reported for the conventional tunable notch-band UWB filters [25].

Similarly, the depth of the notch-band can be further improved by considering all sources of loss in the structure. Figure 5.17 shows the performance of the improved filter in comparison to the previous design. In the new design, the capacitances' dimensions are increased to 720×200 µm^2 and 780×350 µm^2, anchored to one of the coupled lines and extended only over the central signal line.

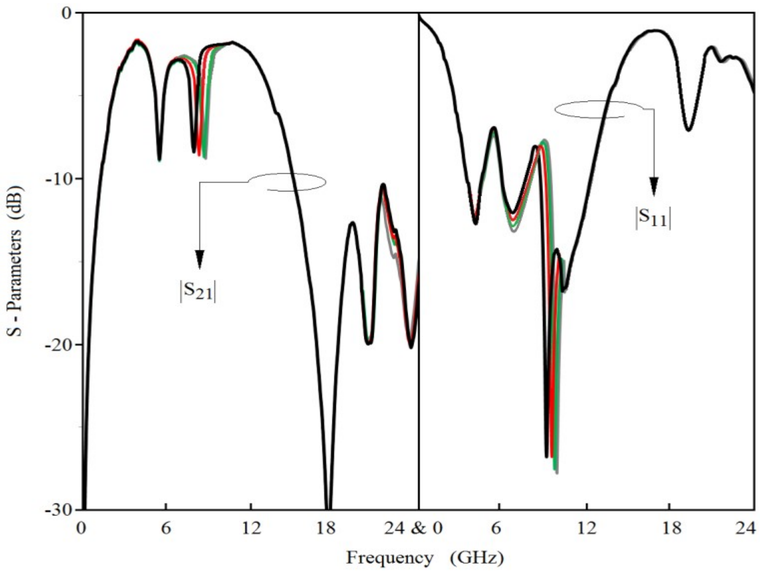

Figure 5.16. Measured frequency response of the UWB BPF for the second notch-band tuning.

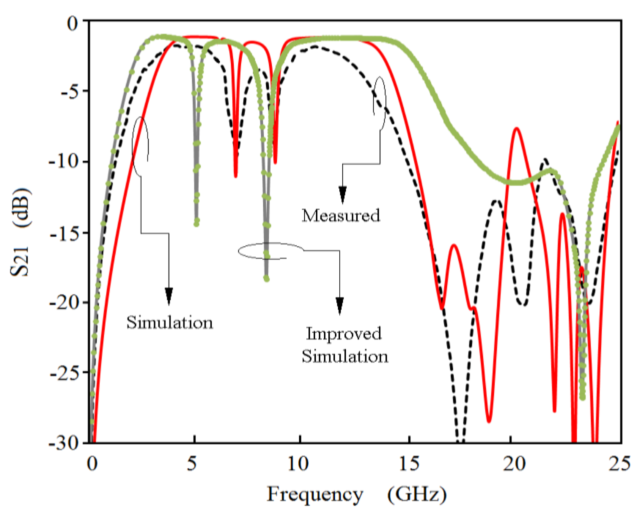

Figure 5.17. The performance of the modified double notch-band BPF.

Comparing the simulated and measured results of the filter included all losses; there is still a loss difference between them (0.7 dB to 1.5 dB). The same loss difference is expected between the simulated and measured results of the modified UWB BPF with tunable double notch-band.

Table 5.3 shows a summary of the existing UWB filters with tunable notch-bands in the literature. As it is clear, the proposed structure is the first MEMS-based UWB filter with the capability of demonstrating two tunable notch-bands.

Table 5.3 Summary of the existing UWB filters with tunable notch bands.

BPF	Size(mm^2)	IL(dB)	Technology	Notch_Band
[17]	Not Given	Not Given	Varactor Diode	One
[18]	20×40	Not Given	Varactor Diode	One
[20]	35×20	Not Given	Varactor Diode	One
[21]	35×17	~-5	Varactor Diode	One
[25]	4.8 ×2.9	2.6	MEMS	One
This Work	10×2.5	3.4	MEMS	One/Two

5.8 Conclusion

A novel model of micro-strip coupled lines integrated with MEMS capacitors has been developed and discussed to design UWB BPFs with tunable single and dual notch-bands. The behavior of this model has been mathematically analyzed by considering the *L*-*C* equivalent circuit of the MEMS capacitor to realize extra transmission zero (TZ). It has been shown that the *L*-*C* circuit resonance adds an extra TZ to the structure. An UWB BPF has been designed and fabricated using coplanar waveguide (CPW) integrated with MEMS capacitors to realize tunable single/double notch-bands.

It has also been shown that the notch-band frequencies can be independently tuned using MEMS capacitors while the filter performance across the ultra-wide pass-band remains unchanged. The measured results indicate up to 1GHz independent tuning range for each notched frequency. The proposed filter can be a good candidate for blocking interference in ultra-wide-band communication.

5.9 References

[1] FCC Code of Federal Register (CFR), Title 47, pt. 15, United States.

[2] M. Mokhtari and J. Bornemann, "Ultra-wide-band and notched wide-band filters with grounded vias in microstrip technology," *Asia-Pacific Microw. Conf.*, pp.1-4, Dec. 2008.

[3] G-M. Yang, et al., "Small ultra-wide-band (UWB) band-pass filter with notched band," *IEEE Microw. Wireless Compon. Lett.*, vol.18, no.3, pp.176-178, Mar. 2008.

[4] P. Mondal and Y. L. Guan, "A coplanar stripline ultra-wide-band band-pass filter with notch-band," *IEEE Microw. Wireless Compon. Lett.*, vol.20, no.1, pp. 2-24, Jan. 2010.

[5] C.H. Lee, C.I.G. Hsu, and L.Y. Chen, "Band-notched ultra-wide-band band-pass filter design using combined modified quarter-wavelength tri-section stepped-impedance resonators," *IET Microw. Antennas. Propag.*, vol.3, no.8, pp.1232-1236, Dec. 2009.

[6] S.G. Mao, et al., "Compact ultra-wide-band conductor–backed coplanar waveguide band-pass filter with a dual band-notched response," *IEEE Microw. Wireless Compon. Lett.*, vol.19, no.3, pp.149-151, Feb. 2009.

[7] M. Nosrati and M. Daneshmand, "Compact microstrip UWB double/single notch-band BPF based on wave's cancellation theory," *IET Microw. Antennas Propag.*, vol.6, no.8, pp.862-868, Jun. 2012.

[8] F. Wei, Q. Yi Wu, X. W. Shi, and L. Chen "Compact UWB band-pass filter with dual notched bands based on SCRLH resonator," *IEEE Microw. Wireless Compon. Lett.*, vol.21, no.1, pp.28-30, Jan. 2011.

[9] H-W. Wu, M. H. Weng, and C.Y. Hung, "Ultra wide-band band-pass filter with dual notch bands," *Asia-Pac. Microw. Conf.*, pp.33-36, Dec. 2010.

[10] K. Song and Q. Xue, "Asymmetric dual-line coupling structure for multiple-notch implementation in UWB band-pass filters," *Elec. Lett.*, vol.46, no.20, pp.1388-1390, Sept. 2010.

[11] F. Wei, Q. Y. Wu, X. W. Shi, and L. Chen, "Compact UWB band-pass filter with dual notched bands based on SCRLH resonator," *IEEE Microw. Wireless Compon. Lett.*, vol.21, no.1, pp.28-30, Jan. 2011.

[12] Z. C. Hao and J. S. Hong, "Compact UWB filter with double notch bands using multilayer LCP technology," *IEEE Microw. Wireless Compon. Lett*., vol.19, no.8, pp.149-151, Aug.2009.

[13] J. Wang, et al., "Ultra-wide band band-pass filter with multiple frequency notched bands based on SIW and SIR technology," *Proc. of the 39th Europ. Microw. Conf*., pp. 268-271, Oct. 2009.

[14] Z-C. Hao, J-S. Hong, J. P. Parry, and D. P. Hand, "Ultra-wide-band band-pass filter with multiple notch-bands using nonuniform periodical slotted ground structure," *IEEE Trans. Microw. Theory and Tech*, vol.57, no.12, pp.3080-3088, Dec. 2009.

[15] Z.-C. Hao, et al, "Ultra-wide-band band-pass filter with multiple notch-bands on multilayer liquid crystal polymer substrate," *IET Microw. Antennas Propag*., vol.3, no.5 pp.749-756, Aug. 2009.

[16] X. Luo, J.-G. Ma, K. S. Yeo, and E.P. Li, "Compact ultra-wide-band (UWB) band-pass filter with ultra-narrow dual- and quad-notched bands," *IEEE Trans. Microw. Theory and Tech*., vol.59, no.6, pp.1509-1519, Jun. 2011.

[17] M. Mokhtaari and J. Bornemann, "Tunable notch characteristics in microstrip ultra-wide-band filters," *Asia -Pacific Microw. Conf*., pp.937-940, Dec. 2009.

[18] Y. Yamamoto, K. Li, and O. Hashimoto, "Tunable sharp notch filter for UWB application," *Microw. Opt. Tech. Lett*., vol.50, no.10, pp.2712-2715, Oct. 2008.

[19] H. R. Arachchige, J. S. Hong, and Z. C. Hao, "UWB band-pass filter with tunable notch on liquid crystal polymer substrate," *Asia-Pacific Microw. Conf*., pp.1-4, Dec. 2008.

[20] F. Wei, L. Chen, X.-W. Shi, and B. Liu, "Compact UWB band-pass filter with tunable notch-band based on folded SIR," *Electronic Lett*., vol.47, no.22, pp.1229-1230, Oct. 2011.

[21] F. Wei, L. Chen, X.-W. Shi, and C.-J. Gao, "UWB band-pass filter with one tunable notch-band based on DGS," *J. of Electromagn. Waves and Appl*., vol.26, pp.673-680, Jul. 2012.

[22] G. Cusmai, M. Brandolini, P. Rossi, and F. Svelto, "A 0.18-μm CMOS selective receiver front-end for UWB applications," *IEEE J. Solid- State Circuits*, vol.41, no.8, pp.1764-1771, Aug. 2006.

[23] A. Vallese, A. Bevilacqua, C. Sandner, M. Tiebout, A. Gerosa, and A. Neviani, "Analysis and design of an integrated notch filter for the rejection of interference in UWB systems," *IEEE J. Solid-State Circuits*, vol.44, no.2, pp.331-343, Feb. 2009.

[24] G. M. Rebeiz, *RF MEMS: Theory, Design, and Technology*, Hoboken, NJ: Wiley, 2003.

[25] Z. Wu, Y. Shim, and M. Rais-Zadeh, "Miniaturized UWB filters integrated with tunable notch filters using a silicon-based integrated passive device technology," *IEEE Trans. Microw. Theory and Tech*., vol.60, no.3, pp.518-527, Mar. 2012.

[26] M. Nosrati, N. Vahabisani, and M. Daneshmand, "A novel tunable double notch-band UWB BPF using MEMS capacitors," *IEEE/MTT-S Int. Microw. Symp.,* pp.1-3, Jun. 2013.

[27] L. Zhu, S. Sun, and W. Menzel, "Ultra-wide-band (UWB) band-pass filters using multiple-mode resonator," *IEEE Microw. Wireless Compon Lett*., vol.15, no.11, pp.796-798, Nov. 2005.

[28] M. Nosrati and M. Mirzaee, "Compact wide-band microstrip band-pass filter using quasi-spiral loaded multiple-mode resonator," *IEEE Microw. Wireless Compon. Lett*., vol.20, no.11, pp.607-609, Nov. 2010.

[29] W. J. Feng, W. Q. Che, Y. M. Chang, S. Y. Shi, and Q. Xue, "High selectivity fifth-order wide-band band-pass filters with multiple transmission zeros based on transversal signal-interaction concepts," *IEEE Trans. Microw. Theory and Tech*., vol.61, no.1, pp.89-97, Jan. 2013.

[30] Y. P. Zhang and M. Sun, "Dual-band microstrip bandpass filter using stepped-impedance resonators with new coupling schemes," *IEEE Trans. Microw. Theory and Tech*, vol.54, no.10, pp.3779-3785, Oct. 2006.

[31] D. M. Pozar, *Microwave Engineering*, 2nd Ed. New York:Wiley, 1998.

[32] J.-S. Hong and M. J. Lancaster, *Microstrip Filters for RF/Microwave Applications*. New York: Wiley, 2001.

Chapter 6 Substrate integrated waveguide L-shaped iris for realization of transmission zero and evanescent-mode pole

6.1 Introduction

With the recent progress in wireless and satellite communication and the 5G requirements for increased multi band structures, integrated platforms with simple configurations are in need to offer flexibility in design, selective pass-band generation and/or unwanted frequencies suppression. Discontinuities including irises, coupling aperture, or gaps are very commonly used for this purpose [1]-[2].

In 3D waveguide structures, irises are specifically employed to realize either the transmission poles and zeros (TZ) above the cut-off frequency of waveguide or the transmission poles below this frequency, known as evanescent-mode pole. In both cases, many studies have been reported in the literature. In connection to TZs realization with irises in 3D structures [3]-[9], other techniques in the literature offer either cross coupling between nonadjacent cavities or higher order excitation resulting in controllable TZ realization at the expense of complicated and bulky 3D structures [10]-[19]. For example, the technique proposed in [10]-[11] makes the cross section of the filter non-uniform and increases the volume of the structure resulting in complexity in integration with other components. Other designs based on this approach usually employ extra cavities in line or in transverse direction to realize TZs [13], [15], [17] and [19].

On the other hand, evanescent-mode technique is an alternative for miniaturization, categorized into two different classes: non-touching irises integrated with capacitive plates [20]-[29] and composite right/left-handed transmission lines [30]-[34]. Although this technique is effective in single band evanescent-mode BPFs realization, further research is required to realize dual/multi-band evanescent-mode BPFs. Moreover, the upper stop-band of these evanescent-mode filters is restricted by the cut-off frequency of waveguide [20]-[34].

It has been shown that the location of an iris inside a waveguide significantly impacts the performance of the waveguide [6] and [9]. We will emphasize here that the shape of an iris also plays a very important role. This study is aimed at advocating the L-shaped iris integrated with 3D structures for filter realization. The application of similar iris has been briefly suggested in [35]-[37] to realize TZ in 3D structures as continuous ridge; however, this structure has not been previously detailed in filter design.

In this paper, the L-shaped iris is investigated in detail and characterized using lumped element equivalent circuit. The structure is further developed for TZ realization and evanescent-mode pole development. A lumped element-based prescribed filtering function is discussed in terms of evanescent-mode pole and close-in TZ. The proposed concept provides design flexibility and superior performance in a small footprint. It is also shown that TZs and evanescent-mode transmission poles can be realized at the same time in one structure. In addition, the upper stop band can be extended. As another indication of the design flexibility, it is illustrated that compact dual-band evanescent-mode BPFs can be designed with two independent bands.

6.2 Embedded L-shaped iris circuit model

Figure 6.1(a) shows the proposed embedded L-shaped iris (LSI) inside a slice of substrate integrated waveguide (SIW). Assuming the simple transverse model of the SIW as an inductor for the frequencies below its cut off frequency [1], the simple lumped element equivalent circuit of the integrated structure can be modeled as illustrated in Figure 6.1(b). C_c stands for the coupling between the top layer of the SIW and that of the LSI, and L_1 and L_2 represent the inductive behavior of the SIW and the LSI below their cut-off frequencies, respectively, seen from the reference plane T-T' at the center [1].

The input impedance of the lumped element equivalent circuit of the LSI integrated with the slice of SIW can be calculated as follows:

$$Z_{in} = Z_{in1} \parallel Z_{in2} = \frac{j\omega L_1 L_3 (1-\omega^2 L_2 C_c)}{(L_1+L_3)-\omega^2 C_c (L_1 L_2 + L_1 L_3 + L_2 L_3)} \quad (6\text{-}1)$$

Inspecting the input impedance of the integrated structure, we calculate a TZ and a transmission pole at $\omega_{TZ} = 1/\sqrt{C_c L_2}$ and $\omega_P = \sqrt{L_1 + L_3}/\sqrt{C_c(L_1L_2 + L_1L_3 + L_2L_3)}$ frequencies, respectively. These frequencies can be controlled and manipulated by the values of the lumped elements in the circuit. It is expected that the structure in Figure 6.1(c) will have the same circuit model where the *L-C* model (L_2 and C_c) of the LSI is generated by the wave propagation in the propagation direction.

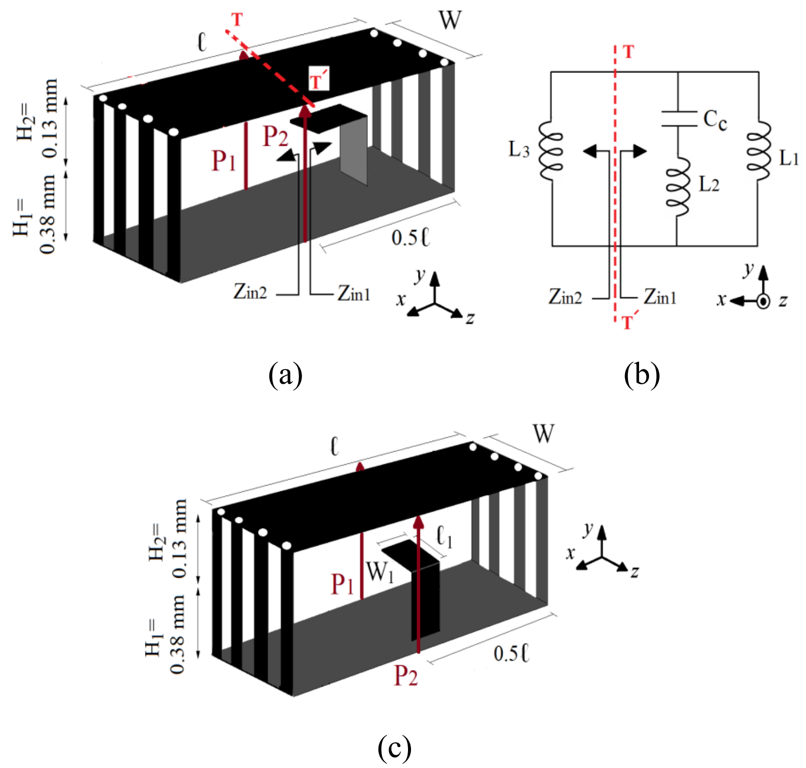

Figure 6.1 (a) Embedded L-shaped iris (LSI) inside a slice of SIW (b) the lumped element equivalent circuit of the structure below the cut-off frequency of the SIW in the transverse direction (c) the LSI oriented in the propagation direction.

To achieve a lumped element equivalent circuit that is able to accurately model the behavior of a distributed-element structure in a wider frequency band, we expand the conventional lumped element equivalent circuit for the integrated SIW and LSI in the transverse direction.

6.2.1 Waveguide transverse circuit model

In Chapter 2, Section 2.2, we illustrated how to model a short circuit for loaded TL. Now, we emphasize on the aspect that a waveguide can be a parallel integration of two short-circuited stubs in the transverse direction. This aspect is represented in Figure 6.2(a) around the reference plane of T-T'. Consequently, the equivalent *L*-*C* circuit of Figure 6.2 (a) can be represented by integrating the two *L*-*C* circuits (Figure 2.7(b), Chapter 2) to get the circuit in Figure 6.2(b). Since the general *L*-*C* circuit in Figure 2.7 (b) is reduced to that in Figure 2.8(a), the original π-network *L*-*C* circuit is reduced to a parallel *L*-*C* circuit. Thus, their *L*-*C* components can be directly calculated from (2-6)-(2-7):

$$\theta = \frac{\lambda}{4} at\ \omega_c, \rightarrow\ L = \frac{2Z_0}{\omega_c}, C = 1/2Z_0\omega_c \tag{6-2}$$

where ω_c and Z_0 are the cut-off frequency and the characteristic impedance of the structure, respectively. Moreover, Z_0 is calculated from the longitudinal length, the dielectric constant and the height of the structure.

To evaluate the analysis, Figure 6.2(d) compares the results of the *L*-*C* and EM simulations (©Agilent ADS) [38] accompanied by the measurement. SIW operating at TE_{10} mode, Figure 6.2(d) shows the results of the first two modes realized at around 3 GHz and 5.5 GHz, respectively. These results are compared for a slice of SIW with the longitudinal length of W=20 mm, the width of ℓ=40 mm on a 5880 substrate with the dielectric constant of 2.2 and the height of 0.51 mm. Assuming that f_c=*2.53 GHz*, we get L_1=0.755 nH and C_1= 5 pF for the *L* and *C* components, respectively. Inspecting the results, we observe that the *L*-*C* circuit simulation follows the measurement and EM simulation (Agilent ADS Software [38]) up to 3 GHz (up to the first mode of SIW; TE_{10}) where a discrepancy is observed for higher frequencies, since the equivalent *L*-*C* circuit of the structure has not been taken into account in the propagation direction for this modeling.

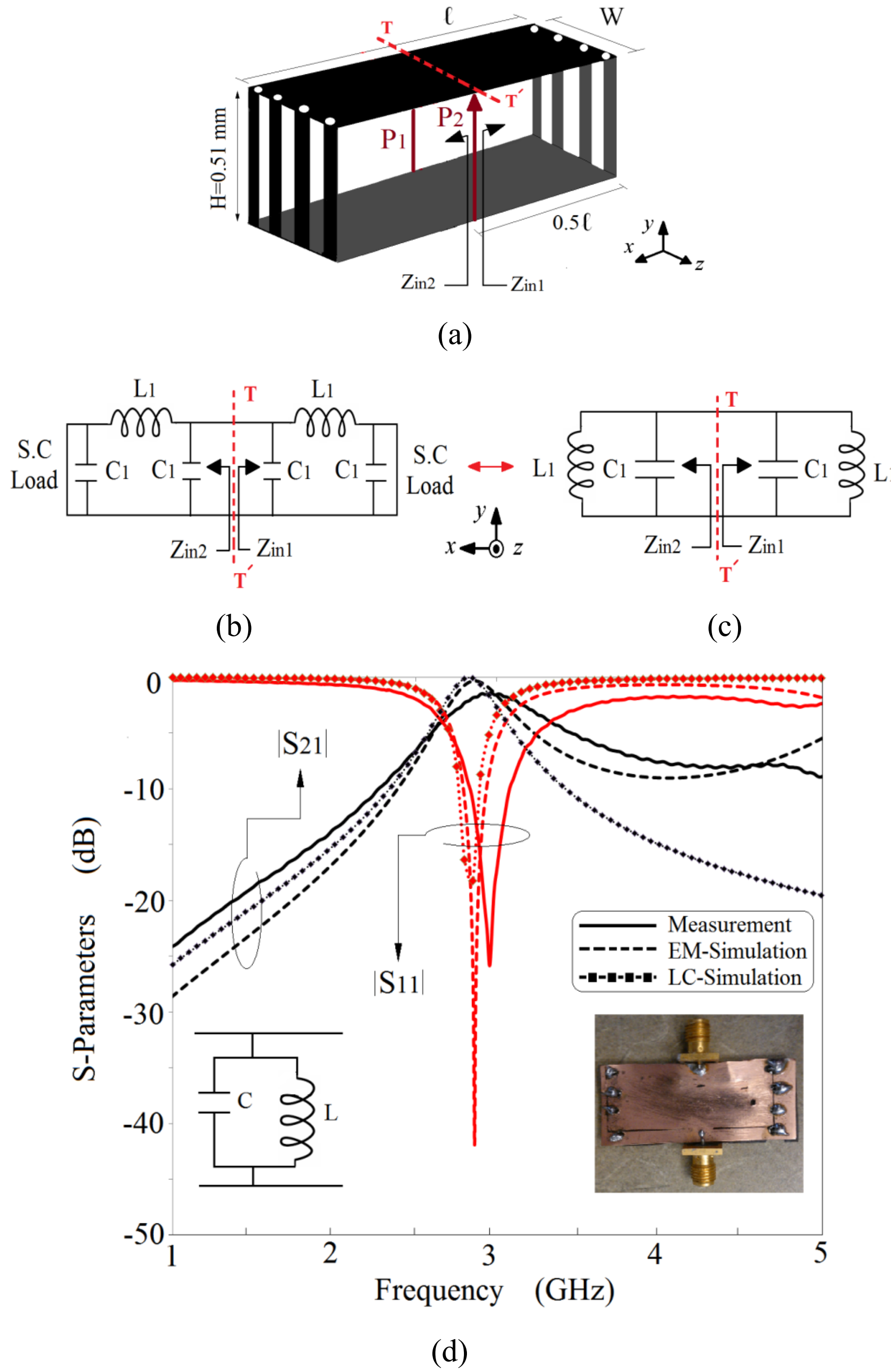

Figure 6.2. (a) Slice of SIW (b) and (c) equivalent π-network and parallel *L*-*C* circuit (d) comparison between *L*-*C*, EM simulation (©Agilent ADS [38]) and the measurement with L=0.37 nH and C=10 pF and W= 20 mm, ℓ=36 mm.

Inversely, the width and length of the SIW can be calculated given the bandwidth and the resonance frequency of the corresponding parallel *L*-*C* circuit (details presented in Section

6.2.2). Assuming a pass-band resonance at 3 GHz with the 3-dB bandwidth of 0.25 GHz, L and C components are calculated to be equal to 0.36 nH and 7.8 pF, respectively, using $L=2R\Delta\omega/(\omega_0)^2$ and the resonance frequency [3]. Substituting these values in (6.2) alongside the cut-off frequency of f_c=2.5 GHz and Z_0 = 5.65 Ω, we compute ℓ=40 mm and W=21.4 mm with the substrate characteristics of H=0.51mm and ε_r=2.2.

6.2.2 Embedded LSI waveguide transverse circuit model

Shown in Figure 6.3(a), the lumped element L-C circuits of the integrated SIW and LSI are derived by disassembling the entire structure into the four sub-sections around the symmetric plane of T-T'. Each sub-section of the SIW is equivalent to a parallel L-C circuit, while the embedded LSI is equivalent to a parallel L-C circuit series with the C_C capacitor which stands for the capacitive coupling between the LSI and SIW's top layers, as shown in Figure 6.3(b).

To conceptually inspect the performance of the integrated structure for TZ or evanescent-mode pole realization, the behavior of its corresponding equivalent L-C circuit is discussed versus frequency. The L-C circuit in Figure 6.3(b) is more simplified to that in Figure 6.3(c) where L_{eq} and C_{eq} components represent the total equivalent inductor (L, L_1 and L_2) and capacitor (C, C_1 and C_2) of the structure, respectively.

Taking the length of the LSI smaller than that of the SIW in the transverse direction, the cut-off frequency of the SIW is expected to be smaller than that of the LSI ($f_{c\text{-}SIW} < f_{c\text{-}LSI}$). Therefore, three distinguished states can be totally expected for the behavior of simplified L-C circuit versus frequency as shown in Figure 6.3(c). For the frequencies below the cut-off frequency of the SIW ($f < f_{c\text{-}SIW}$), state 1 gives the equivalent L-C circuit of the integrated structure representing the SIW and LSI with the two inductors of L_{eq} and L_3, respectively. In state 2, the equivalent L-C circuit of the SIW becomes a capacitor (C_{eq}) while that of the LSI remains as an inductor. In state 3, both structures operate above their cut-off frequencies, therefore, they both are modeled with capacitors up to the second higher order mode of the SIW.

In this section, the performance of this structure is evaluated in favor of TZ realization above the SIW cut-off frequency and later the concept is discussed for evanescent-mode pole realization.

To compare the performance of the equivalent L-C circuit with its corresponding distributed elements, the values of the L-C components, except C_C, are calculated using (2-6)-(2-7) in Chapter 2, given Z_0 and f_c. Taking the width and length of the SIW equal to W=20 mm and ℓ=36 mm on a 0.51-mm-substrate with the dielectric constant of 2.2, the characteristic impedance (Z_0) and the cut-off frequency (f_c) are calculated to be 6 Ω and 2.8 GHz, respectively. To compensate the error of the model and calculation, the values of the L-C components are slightly optimized to match the frequency responses of the lumped and the distributed elements. Table 6-1 gives the calculated and optimized values and Figure 6.3(d) compares the EM (distributed elements) and the L-C (lumped elements) simulated results.

Table 6.1 Calculated and optimized L-C values of the lumped element equivalent circuit of the proposed structure in Figure 6.1.

L-C	L (nH)	C (pF)	L_1(nH)	C_1(pF)
Calculated	0.682	4.735	1.38	2.33
Optimized	0.680	4.750	1.36	2.35
L-C	L_2 (nH)	C_2 (pF)	L_3 (nH)	C_3(pF)
Calculated	2.32	0.275	1.98	1.10
Optimized	3.20	0.200	1.64	1.25

It should be noted that as it was predicted using simplified model of the embedded LSI in Section 6.2 equation (6-1), the structure illustrates an evanescent-mode pole at 2.6 GHz below the cut off frequency of 2.8GHz where it can be further shifted toward lower frequencies (Figure 6.7). The next two sections will focus on utilizing such structure to create transmission zero (TZ) and evanescent-mode pole in filter design.

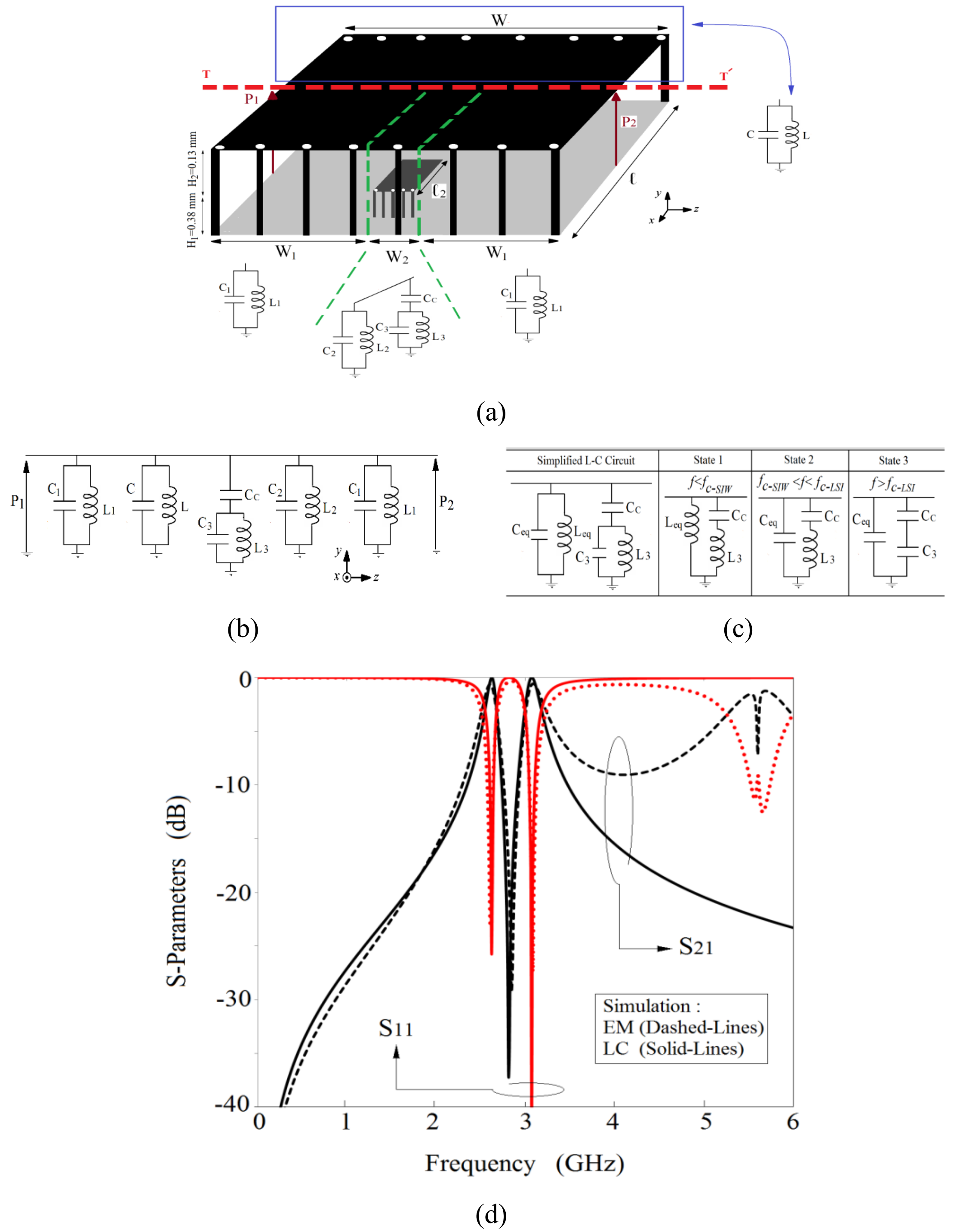

Figure 6.3. (a) Disassembled integration of a slice of SIW integrated with LSI (b) corresponding lumped element equivalent circuit (c) simplified *L-C* circuit and expected three states for its behavior in terms of frequency (d) comparison between EM and lumped element equivalent circuit simulations of the structure with ℓ=36 mm, ℓ_2=15.8 mm, W=20 mm, W_1=9.27 mm, W_2=3.6 mm, H_1=0.38 mm and H_2=0.13 mm.

We demonstrated how the rigorous equivalent *L*-*C* circuits of the integrated L-shaped iris with SIW can be derived. For evanescent-mode BPFs, the prescribed filtering function of the structure is used to calculate the *L* and *C* components in terms of given bandwidth, transmission pole and zero. Since the operation frequency of interest is below the cut-off frequency of the SIW ($f < f_{c\text{-}SIW}$), the equivalent *L*-*C* circuit of state 1 in Figure 6.3(c) is used to realize evanescent-mode BPF delivering power to a standard 50 ohm load as shown in Figure 6.4(a).

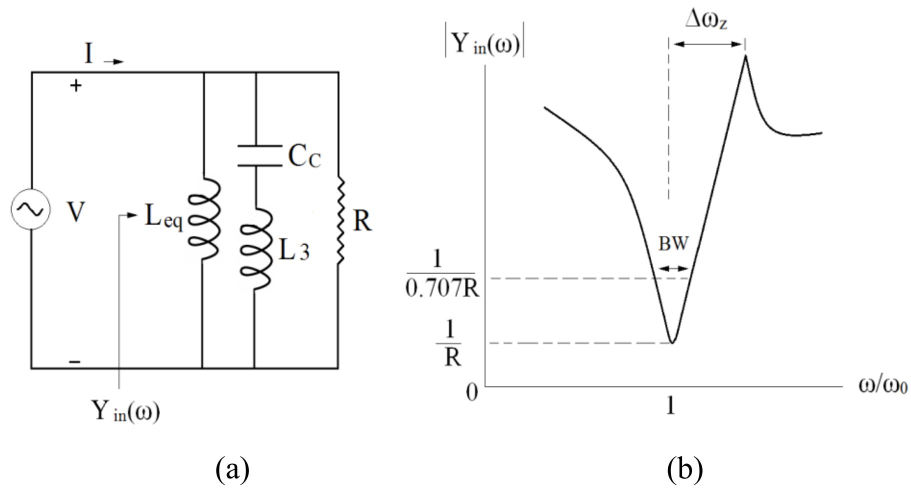

Figure 6.4. (a) Lumped element equivalent circuit of evanescent-mode BPF (b) input admittance magnitude versus normalized frequency.

The prescribed filtering function of a simple parallel *L*-*C* circuit has been studied in [3]; however, it merely discusses the filter frequency response in terms of its pole or pass-band. The candidate *L*-*C* circuit for the evanescent-mode BPF illustrated in Figure 6.4(a) includes both the evanescent-mode pole and transmission zero. Similar to the procedure presented in [3], the input admittance magnitude of the circuit is calculated and equated to the corresponding admittance at 3-dB bandwidth frequency for half-power fractional bandwidth, Figure 6.4(b), as follows:

$$|Y_{in}|_{3-dB} = \sqrt{\left[\frac{1-\omega^2 C_C(L_{eq}+L_3)}{\omega L_{eq}(1-\omega^2 L_3 C_C)}\right]^2 + \frac{1}{R^2}} = \frac{1}{0.707R} \tag{6-3}$$

The given equation can be simplified as follows:

$$\frac{1-\omega^2 C_C(L_{eq}+L_3)}{\omega L_{eq}(1-\omega^2 L_3 C_C)} = \frac{1}{R} \quad \leftrightarrow \quad \frac{1-(\omega/\omega_0)^2}{\omega L_{eq}(1-(\omega/\omega_z)^2)} = \frac{1}{R} \tag{6-4}$$

where ω_0 and ω_z are the frequencies of the evanescent-mode pole and TZ, respectively.

$$\omega_0 = \frac{1}{\sqrt{C_C(L_{eq}+L_3)}} \quad , \qquad \omega_z = \frac{1}{\sqrt{L_3 C_C}} \tag{6-5}$$

Equation (6-4) can be further simplified using the same approximation made in [3] to:

$$\omega^2 - \omega_0^2 = (\omega - \omega_0)(\omega + \omega_0) = \Delta\omega(2\omega - \Delta\omega) \approx 2\omega\Delta\omega \tag{6-6}$$

Similarly, by defining the difference of the evanescent-mode pole and TZ's frequencies as $\Delta\omega_z$, the prescribed filtering function in (6-4) is simplified as follows:

$$L_{eq} = \frac{R f_z \Delta f}{2\pi f_0^2 \Delta f_z} \tag{6-7}$$

Finally, the values of the other two unknown components of the circuit are calculated using (6-5) as follows:

$$C_C = \frac{1-(\frac{\omega_0}{\omega_z})^2}{L_{eq}\omega_0^2} \quad , \ L_3 = \frac{1}{C_C \omega_z^2} \tag{6-8}$$

Later in Section 6.5, it will be explained how to utilize these L and C components to find the geometrical dimensions of the SIW and L-shaped Iris in the filter structure.

6.3 EM analysis of TZ realization using L-shaped iris (LSI) inside a SIW

Previously, lumped-element *L*-*C*-based analysis was performed for the embedded LSI inside the SIW to realize TZ. Here, we will provide mathematical evaluation for EM simulated performance of the structure as a double-layer transmission line, Figure 6.5(a). To evaluate the imapct of the LSI on the SIW's performance, the input impedance of Z_{in1}, seen from |A-B| points, is calculated and compared to that of a slice of the conventional SIW without LSI.

Assuming the charactristic impedances of Z_3 for the waveguide part, ℓ_1-ℓ_2 and Z_2 and Z_1 for the internal and the top parts, between the top layer of the structure and the top layer of the internal stub, respectively, the input impedance of Z_{in1} is calculated as follows:

$$Z_{in1} = j[Z_1 \frac{Ktan(k_x(\ell_1-\ell_2))+\tan(k_x\ell_2)}{1-Ktan(k_x(\ell_1-\ell_2))\tan(k_x\ell_2)} + Z_2\tan(k_x\ell_2)] \quad (6\text{-}9)$$

where K is the ratio of Z_3/Z_1 and k_x is the propagation constant in the transverse direction. To evaluate the accuracy of this estimation, the calculated input impedance in (6-9) is mathematically drawn in Figure 6.5(b) and compared to that of the conventional one without the embedded LSI. As illustrated, the proposed structure realizes an additional TZ. The realized TZ can be also tuned for a large frequency range by changing the length of the L-shaped iris. Additionally, Figure 6.5(b) graphically shows that the different lengths of the internal short-circuited stub, ℓ_2, or θ_2 for different values of $\pi/15$, $\pi/8$ and $\pi/5$, realizes the transmission zero at different frequencies.

To experimentally verify the theoretical results of the L-C and EM simulations, the developed structure in Figure 6.1(a) is fabricated to realize two TZs at different frequencies. The structure is examined for the two cases where the realized TZ is put at the lower and upper sides of the pass-band of the structure. Figure 6.6 shows the simulated and measured results of the two cases where the TZ is realized at the two different frequencies of 2.5 GHz and 3.1 GHz.

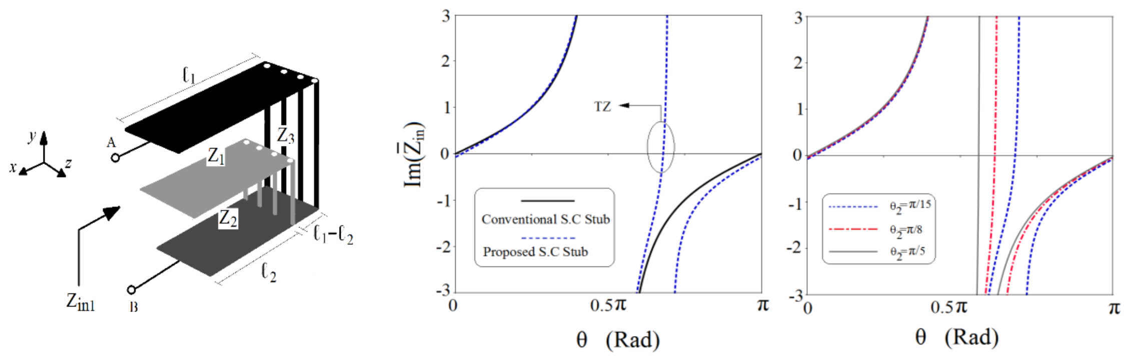

(a) (b)

Figure 6.5. (a) Embedded LSI inside a short-circuited stub (b) comparison between the conventional and the developed structure as well as TZ tuning for the different values of ℓ_2.

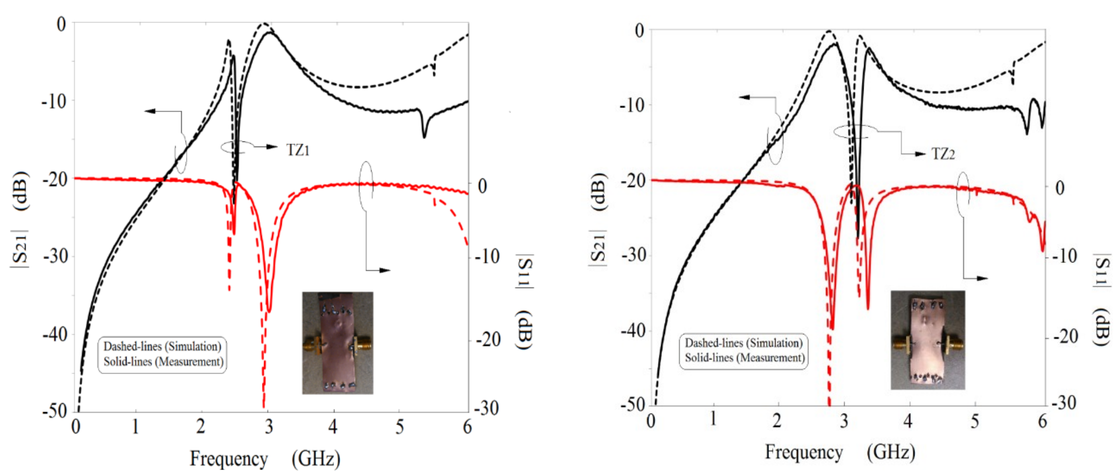

(a) (b)

Figure 6.6. Measured and simulated results of the two TZs realized at two different frequencies.

Inspecting the EM simulated and measured results in Figure 6.6, we observe a discrepancy between the simulation and the measurement. In this structure, a slice of waveguide is simulated using ADS. In this software, when assigning a port, coax structures are not considered and a planar 50 ohm port is assigned. This port is optimized for the frequency band of interest and therefore, larger error is observed out of band. Note that this discrepancy can be obviated by using matching tapered lines at I/O ports (Figure 6.9).

6.4 Evanescent-mode pole realization using LSI

Reviewing the recent studies reveals that metallic posts or irises can be employed to realize either transmission zeros [3]-[9] or evanescent-mode pass-bands [20]-[29] in 3D structures. In the previous section, it has been shown how a TZ can be realized by integrating an LSI with a slice of SIW. Here, the proposed integration of the SIW and LSI is more conceptually studied to employ this structure in favor of an evanescent-mode pole below the cut-off frequency of the SIW accompanied by a TZ above the evanescent-mode pole for stop-band extension.

Considering the fact that the operation frequency of interest is below the SIW cut-off frequency ($f < f_{c\text{-SIW}}$), we calculate the Z_{21} impedance parameter of the circuit in Figure 6.5(c), state 1, as follows:

$$\boldsymbol{Z_{21}} = \frac{j\omega L_{eq}(1-\omega^2 L_3 C_c)}{1-\omega^2 C_c(L_3+L_{eq})} \tag{6-10}$$

Equating the numerator and the denominator of the Z_{21} impedance to zero, we observe that the proposed integration of the SIW and the LSI realizes a TZ and an evanescent-mode pole below the cut-off frequency of the SIW as $\omega_{TZ} = 1/\sqrt{L_3 C_c}$ and $\omega_P = 1/\sqrt{C_c(L_3+L_{eq})}$, respectively. The frequencies of the TZ and evanescent-mode pole can be controlled by tuning L_3 or C_c components. To examine this concept, an integration of a SIW and two LSIs is designed, simulated and fabricated.

Figure 6.7 compares the simulated and measured results of the developed structure. The results show that the integrated structure realizes an evanescent-mode pole at 2.4 GHz as well as a TZ at 2.7 GHz. Note that these evanescent-mode pole and TZ are located below the SIW cut-off frequency with the transverse length of ℓ=33 mm where the cut-off occurs at 3 GHz. The insertion loss is measured to be 1 dB with the fractional BW of 4.5%.

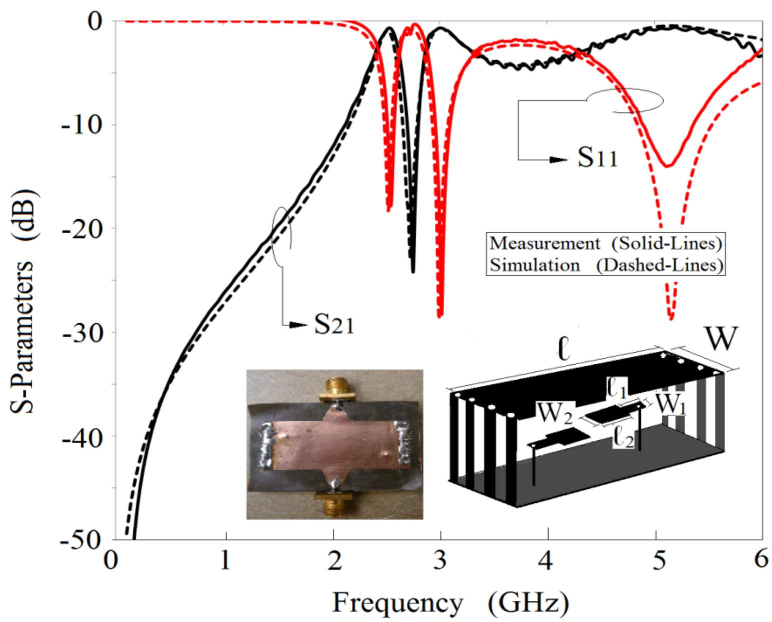

Figure 6.7. Comparison between simulated (dashed-lines) and measured results (solid-lines) with the optimized parameters for the two resonators as follows: ℓ=33 mm and W=20 mm for the SIW structure, the first LSI: ℓ_1=9 mm, ℓ_2=5.3 mm, W_1=1.4 mm and W_2=3.8 mm, the second L-shaped iris: ℓ_1=7 mm, ℓ_2=4.8 mm, W_1=1.4 mm and W_2=3.8 mm.

6.5 Higher-order filter design using multiple embedded L-shaped iris

6.5.1 Lumped element-based analysis of higher-order evanescent-mode BPFs including TZ

Higher-order filters are designed by cascading the same resonators in series to improve the performance of filters. Here, a higher-order evanescent-mode BPF can be designed by cascading the two integrated structures (shown in Figure 6.3(a)) that are coupled by means of a μ-strip transmission line. As shown in Figure 6.8, we develop the lumped element equivalent circuit of the entire structure by integrating those of the evanescent-mode resonators and the μ-strip TL (Figure 6.3(c), state 1, and Figure 2.7(b), respectively).

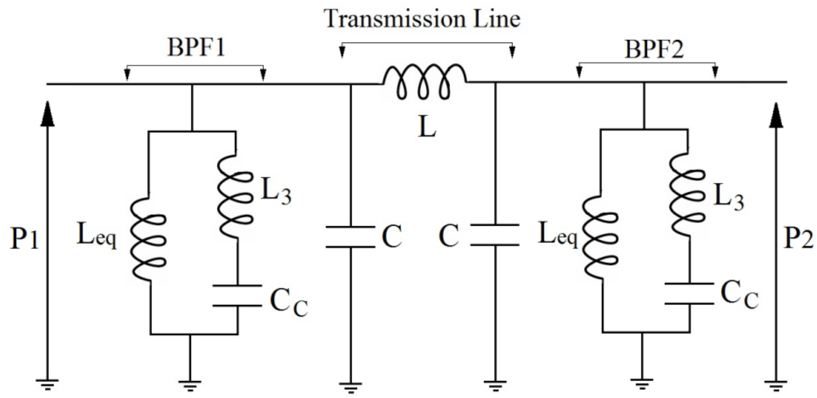

Figure 6.8. Lumped element equivalent circuit of a two-pole evanescent-mode BPF.

It should be noted that the lumped element equivalent circuit of the structure in Figure 6.8 is composed of the two circuits presented in the image parameter and insertion loss methods in higher-order filters design [3]. The series L_3-C_C and the parallel C-L_{eq} components of the circuit in Figure 6.8 represent these two methods that are focused on higher-order transmission zero and transmission pole, respectively [3].

Not only can the order of the filter be increased, but the order of the TZs can also be increased using the configuration of the L-shaped iris. As shown in Figure 6.9(a), the L-shaped iris is further developed integrating two short- and open-circuited stubs in parallel. Figure 6.9(b) shows the lumped element equivalent circuit of this developed LSI extracted from the structures in Figure 2.8. Note that the $L_{O.C}$ and $C_{O.C}$ components stand for the inductor and the capacitor of the open-circuited stub and the $L_{S.C}$ and $C_{S.C}$ components for those of the short-circuited stub in the developed LSI. Figure 6.9(c) shows the simplified lumped element equivalent circuit of the developed L-shaped iris.

As previously discussed in the previous section, the short-circuited LSI is able to realize TZ. Here, the lumped element equivalent circuit of the developed LSI, composed of the open- and short-circuited stubs, integrated with a 3D structure (e.g., Figure 6.11(c), the LSI4 in the propagation direction) is mathematically discussed to explain the higher-order transmission zero.

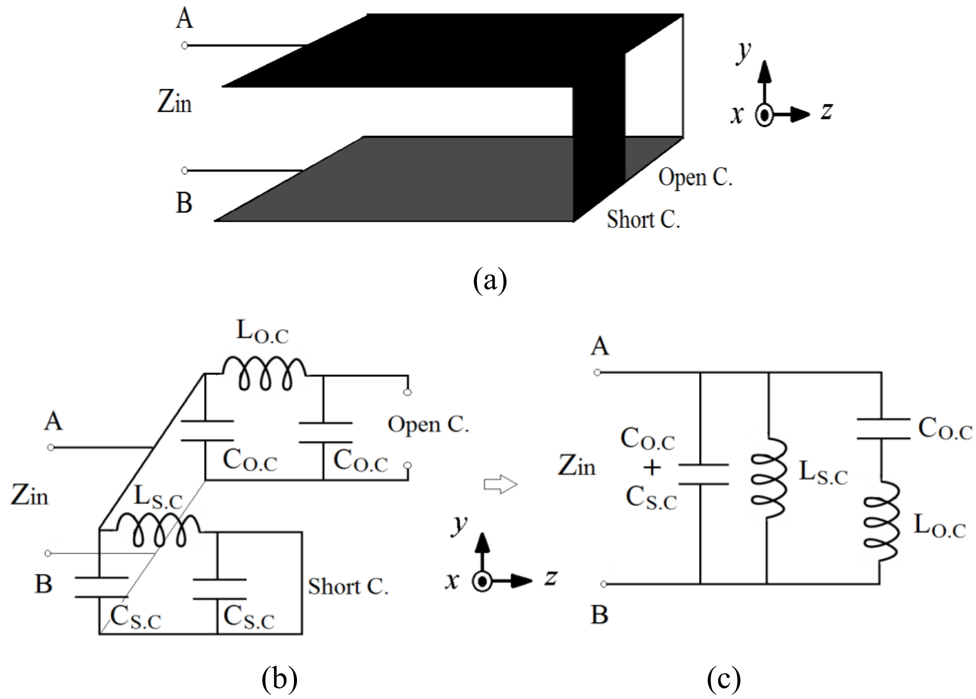

Figure 6.9. (a) Developed LSI (b) its corresponding lumped element equivalent circuits of open-circuited (O.C) and short-circuited (S.C) stubs (c) simplified circuit.

Since the frequency of interest for TZ's realization is above the cut-off frequency of the SIW ($f > f_{c\text{-SIW}}$), the SIW is modeled with its corresponding lumped element equivalent circuit (capacitor C_{eq}, Figure 6.3(c), state 2). Figure 6.10 shows the integration of the C_{eq} capacitor and the lumped element equivalent circuit of the developed LSI accompanied with the coupling capacitor of C_C.

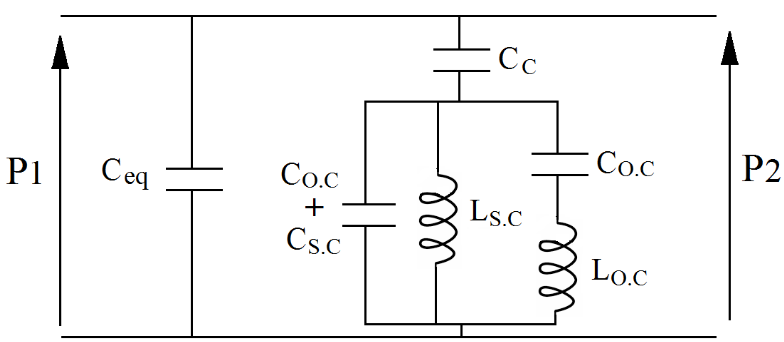

Figure 6.10. Lumped element equivalent circuit of 3D SIW integrated with the developed LSI in Figure 6.9 to design BPFs with higher-order TZs.

The total shunt admittance of the circuit is calculated to extract the higher-order TZs of the circuit. Equating the denominator of the shunt admittance of the circuit to zero gives the following fourth-order polynomial to calculate the TZs of the structure.

$$A_{TZ}\omega^4 - B_{TZ}\omega^2 + 1 = 0 \tag{18}$$

where the two coefficients of A_{TZ} and B_{TZ} are calculated as follows:

$$A_{TZ} = L_{S.C}L_{O.C}C_{O.C}(C_C + C_{S.C} + C_{O.C}) \tag{19}$$

$$B_{TZ} = L_{S.C}(C_C + C_{S.C} + C_{O.C}) + C_{O.C}(L_{S.C} + L_{O.C}) \tag{20}$$

To evaluate the analysis of the higher-order TZ, the structure in Figure 6.11(c) is simulated twice with the short-circuited and the developed LSIs (LSI1 to LSI4). Figure 6.11(e) shows the EM simulated results (Agilent ADS Momentum) where the structure with the developed LSIs demonstrates the higher-order TZs. Intuitively, these TZs are realized by the two series *L*-*C* paths between the top and the bottom layers of the structure (the series C_{C}-$L_{\mathrm{S.C}}$ and C_{C}-$C_{\mathrm{O.C}}$-$L_{\mathrm{O.C}}$ circuits).

6.5.2 Evanescent-mode filter with enhanced stop-band

According to the aforementioned analysis, two different types of filters are designed and explained as follows: 1-An evanescent-mode filter with enhanced stop-band 2- A dual-band filter.

Inspecting the results in Figure 6.7, we can realize an evanescent-mode filter by integrating a slice of SIW with two LSIs; however, the upper stop-band of the filter is restricted by the cut-off frequency of the SIW. Note that this problem has been addressed in some research studies on evanescent-mode filters [20]-[34].

As shown conceptually in Figure 6.11(a) and (b), we can attenuate the signal propagated above the cut-off frequency of the SIW using some TZs. As shown schematically in Figure 6.11(c), we develop the integration of the LSIs and the SIW in Figure 6.7 to realize some extra TZs at the upper stop-band of the filter. These extra TZs are realized by embedding some additional LSIs with different resonance frequencies, oriented in the propagation direction. As shown in Figure 6.11(d), the entire structure is modeled using the lumped element equivalent circuit in the transverse direction. The slice of SIW is modeled with the two parallel *L*-*C* circuits standing for its cut-off frequency (f_c), and each LSI is modeled with the parallel *L*-*C* circuit capacitively-coupled to the top layer of the SIW. While these L-shaped irises all are the same in shape and configuration; however, their different electrical lengths and widths (characteristic impedance) result in the corresponding *L*-*C* components with different values and subsequently different resonance frequencies.

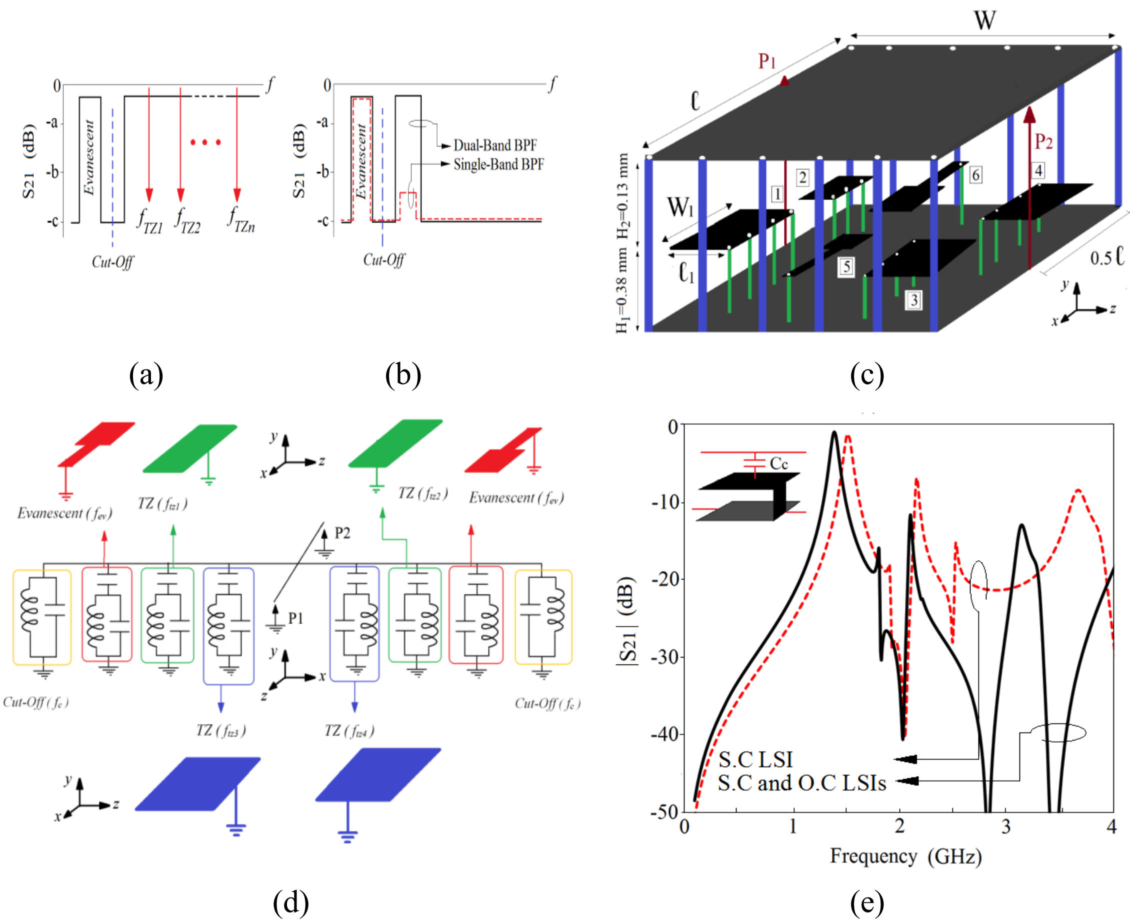

Figure 6.11. (a) and (b) conceptually development of the proposed single/dual-band evanescent-mode BPFs (c) the proposed slice of SIW integrated with some LSIs to realize attenuation poles in the upper stop-band of the filter (d) the lumped element equivalent circuit of the developed structure (e) EM simulated results (Agilent ADS Momentum) for the structure in Figure 6.11 (c) with the short-circuited and developed LSIs in Figure 6.9.

Given f_0, f_z and FBW for evanescent-mode BPF, *L*-*C* initial values of corresponding circuit are calculated using (6-7) and (6-8). The transverse and longitudinal lengths of the SIW are then computed using (6-2) and calculated *L*-*C* values.

Here in the following example with given f_0=1.5 GHz, f_z= 2 GHz *and* FBW=3%, respectively, the design procedure can be summarized as follows:

- Taking *L*-*C* circuit illustrated in Figure 6.4(a), L_{eq} is initially calculated to be 0.64 nH ((6-7)).
- Since, the evanescent-mode pole and TZ are supposed to be located below the cut-off frequency of the SIW, f_c is chosen to be 2.5 GHz. Therefore, the required Z_0 of the SIW is computed to be 5 Ω given L_{eq}, ω_c and $\theta=\lambda/4$ at the cut-off frequency ((6-2)).
- Next, the initial value of the transverse length of the SIW is calculated to be $\ell = \frac{c}{2\sqrt{\varepsilon_r} f_c} = 40\ mm$ on a substrate with ε_r= 2.2.
- Next, the value of the longitudinal length of the SIW is computed to be *W*=24 mm using THE calculated Z_0 on a 0.51-mm-substrate with ε_r=2.2 [38].
- Next, THE other two unknown C_C and L_3 components of *L*-*C* circuit in Figure 6.4 (a) are computed to be 7.7 pF and 0.82 nH, respectively ((6-8)).
- Illustrated in state 2, Figure 6.3(c), the cut-off frequency of LSI is chosen to be greater than that of THE SIW. Given $f_{c\text{-}LSI}$= 3.5 GHz, THE transverse length of LSI (LSI5 or 6 in Figure 6.8(c)) is computed to be 14.4 mm using the condition of $\beta\ell=\pi/2$ at the cut-off frequency of $f_{c\text{-}LSI}$.
- Next, the longitudinal length of LSI (*W*) is computed having L_3=0.82 nH and $f_{c\text{-}LSI}$=3.5 GHz to be 9.6 mm on a 0.38-mm-substrate with ε_r= 2.2 ((6-2)).
- Next step is to calculate the values of *L*-*C* components of the other LSIs in the structure to realize TZs at the higher spurious resonance frequencies of the filter. Similarly, *L*-*C* initial values of each LSI can be calculated by equating the resonance frequency to that of the higher spurious resonance frequency.

To experimentally evaluate the theoretical results, a two-pole evanescent-mode BPF with the developed LSIs is designed and fabricated on a two-layer RT/Doroid 5880 substrate with the dielectric constant of 2.2 and the different heights of 0.38 mm and 0.13 mm. Figure 6.12(a) compares the measured and simulated results as well as the digital photographs of the two top and middle layers of the structure. An evanescent-mode BPF is realized with the measured insertion loss of around 3.4 dB, the fractional BW of 2.5%, the quality factor of 123 at 1.42 GHz and the suppression level of 30 dB at the frequencies up to 4 GHz. Note that the discrepancy between the simulated and measured insertion losses can be attributed to the misalignment between the two layers of the structure. Figure 6.12(b) shows the measured and simulated group delays of the filter.

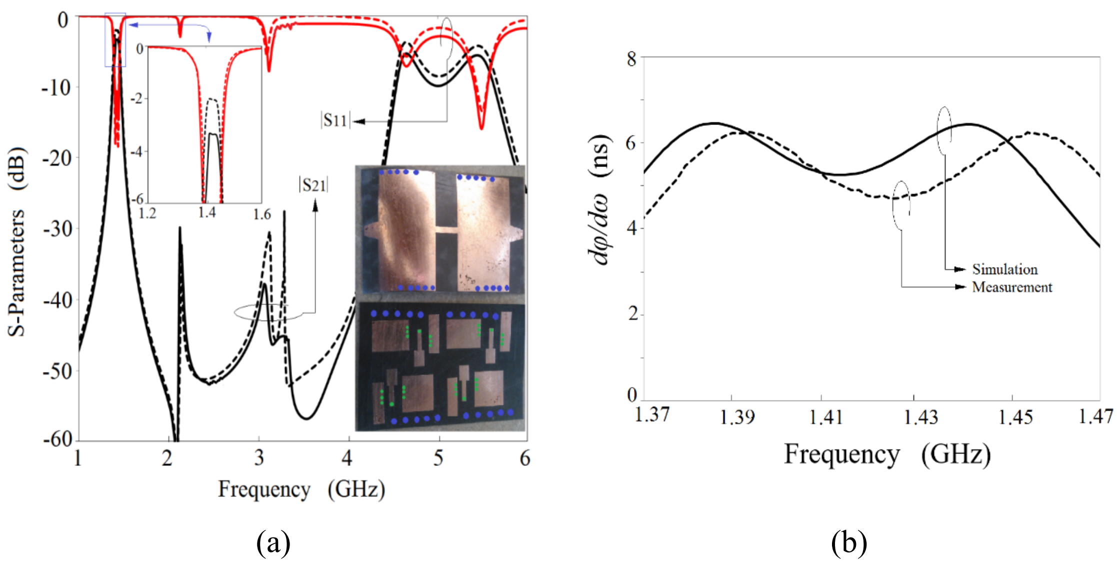

Figure 6.12. (a) Comparison between simulated and measured results for the proposed 2-pole evanescent-mode BPF with optimized W=20 mm, ℓ=37.5 mm, L-shaped iris (LSI) 1: W_1=17.5 mm, ℓ_1=3.4 mm, LSI2: W_2=14.2 mm, ℓ_2=9.6 mm, LSI3: W_3=12.5 mm, ℓ_3=12 mm, LSI4: W_4=16.9 mm, ℓ_4=4 mm, LSI5: ℓ_{15}=8.4 mm, ℓ_{25}=6.2 mm, W_{15}=1.5 mm, W_{25}=3.9, LSI6:ℓ_{16}=8.2, ℓ_{26}=6.2, W_{16}=1.5 mm, W_{26}=3.9 mm, the line between two resonators with length of 9 mm and width of 1.2 mm (b) measured and simulated group delays.

Table 6-2 compares the developed two-pole evanescent-mode BPF to the conventional counterparts in terms of size, insertion loss, FBW and the ratio of spurious and main resonance frequencies. This clearly indicates that the L-shaped iris can be used to enhance the performance of SIW filters. This technique offers a wider stop-band for evanescent-mode filters. In comparison to the evanescent-mode BPF developed by semi-lumped technology in [39], it provides a higher upper stop-band but at the expense of a higher FBW and a 6-order complicated waveguide structure.

Table 6.2 Comparison between the proposed evanescent BPF and the conventional ones.

BPF	Technology	Size (λ^2)	IL (dB)	FBW%	f_s/f_0
[26]	3D waveguide	0.12×0.06	5.36	0.94	1.60
[28]	Multi-Layer LTCC	0.5×0.40	1.23	8.72	1.70
[30]	5-stage CSRR	1.6×0.30	5.45	3.42	1.64
[31]	3D waveguide	2.8×0.38	0.91	0.91	2.50
[39]	Semi-lumped	N-Given	1.67	11.0	9.00
New	3D SIW	0.42×0.30	3.42	2.51	3.50

6.5.3 Dual-band filter design

As illustrated in Figure 6.11(b), another option is to partially suppress the signal above the cut-off frequency of the SIW. Allowing the signal to be partially transmitted above the cut-off frequency, we can design a dual-band evanescent-mode BPF by appropriately choosing the TZ's frequencies of the LSI1-LSI4. Figure 6.13 compares the EM simulated and measured results of the dual-band BPF as well as the fabricated filter under the experimental setup. A good agreement is observed between the simulated and measured results except at the frequency region of 3 GHz to 4 GHz (between the first two modes of the SIW). The dual-band BPF is realized with the measured insertion losses of around 1 dB and 4.6 dB and the fraction BWs of 6.6% and 3.3% at 1.55 GHz and 3.05 GHz, respectively. Figure 6.13(c) and (d) show the filter measured and simulated group delays of the first and second pass-bands, respectively.

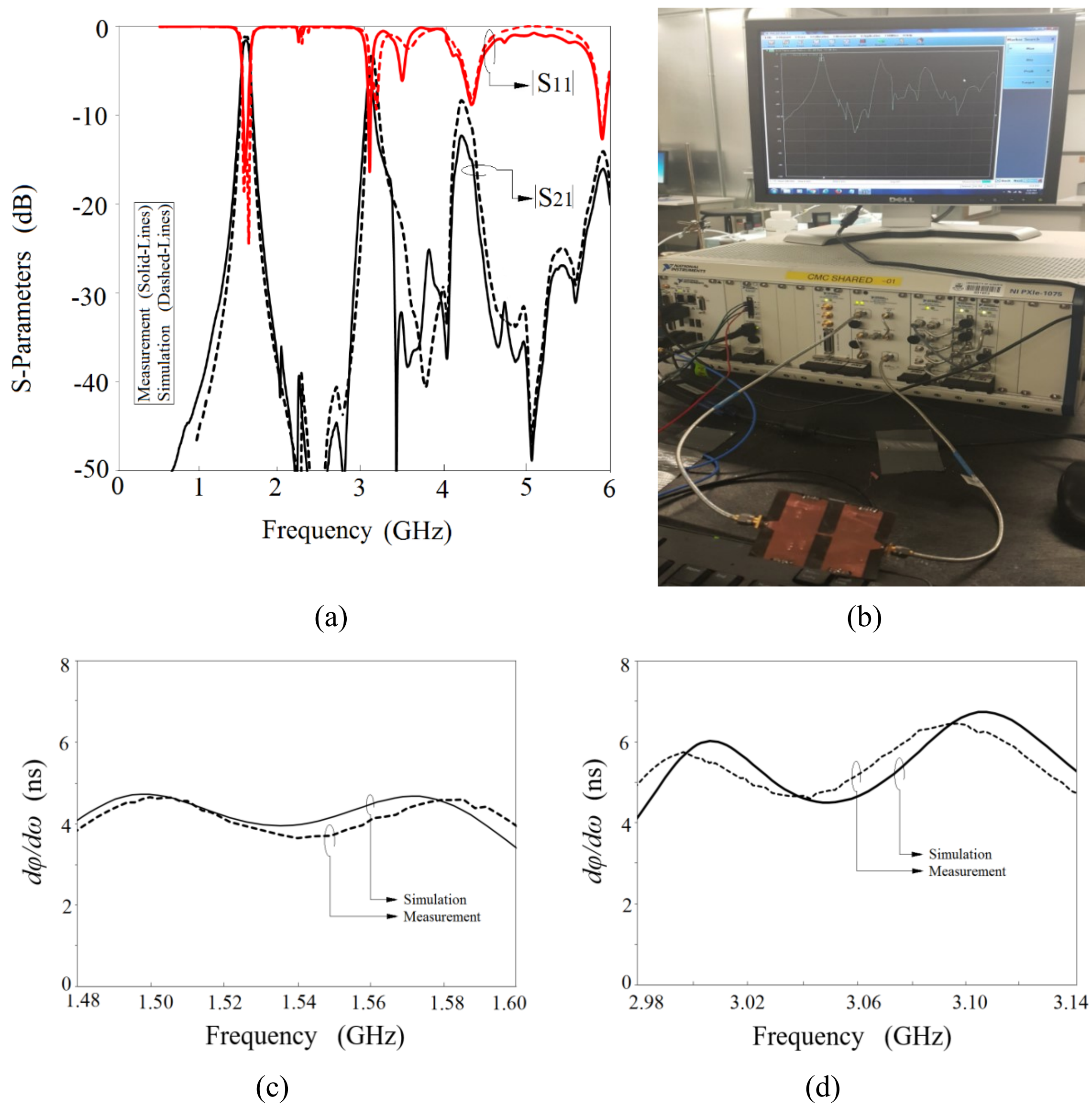

Figure 6.13. (a) Comparison between simulated and measured results of the dual-band evanescent-mode BPF with optimized W=22 mm, ℓ=50 mm, L-shaped iris (LSI) 1: W_1=18 mm, ℓ_1=13.5 mm, LSI2: W_2=17.6 mm, ℓ_2=5.2 mm, LSI3: W_3=16.8 mm, ℓ_3=6.7 mm, LSI4: W_4=18.4 mm, ℓ_4=14.3 mm, LSI5: ℓ_{15}=9.8 mm, ℓ_{25}=7.5 mm, W_{15}=1.5 mm, W_{25}=3.8, LSI6:ℓ_{16}=9.8, ℓ_{26}=7.5, W_{16}=1.5 mm, W_{26}=3.8 mm with 0.05 mm air between the two layers (b) two-pole filter under the experimental setup and measured and simulated group delays (c) first pass-band (d) second pass-band.

Table 6-3 compares the proposed dual-band evanescent-mode BPF with the conventional ones in terms of size, FBW, insertion loss and the ratio of the spurious and main resonance frequencies.

Table 6.3 Comparison between the proposed dual-band BPF and the conventional counterparts.

BPF	Size ($\lambda_g \times \lambda_g$)	FBW (%)1st,2nd Bands	IL (dB) 1st,2nd Bands	f_s/f_{02}	Tech.	Type of Operation	Independency of two bands
[40]	0.67×0.3	8.6, 6.1	0.81, 1.12	1.44	SIW	TE_{10}	N-Given
[41]	0.70×0.3	16,8.6	1.78, 2.53	1.43	Planar	TEM	N-Given
[42]	0.17×0.07	6.2,5.2	1.40, 1.61	1.39	4-layer SIW	TE_{10}-TE_{30}	No
[43]	0.93×0.88	4.5,4.1	4.81, 4.81	1.53	10-layer LTCC	TE_{10}-TE_{20}	No
[44]	2.10×1.30	3.0,2.9	1.37, 1.11	1.21	SIW	TE_{10}	No
[45]	0.15×0.16	5.8,6.45	3.60, 3.12	2.03	SIW	Evanescent	No
[46]	2.70×1.27	2.8,5.57	2.92, 2.71	1.14	SIW	TE_{10}-TE_{20}	Yes
[47]	0.64×0.18	8.0,5.0	2.82, 4.51	1.35	Planar	TEM	Yes
[48]	0.20×0.19	4.6,3.58	2.25,2.25	1.37	CSRR	Evanescent	Yes
[49]	0.42×0.12	19.3,13	1.12,1.32	1.41	CSRR	Evanescent	Yes
New	0.36×0.33	6.6,3.3	1.12,4.61	1.42	SIW	Evanescent	Yes

Comparing the proposed filter to those reported in the literature in Table 6-3, we observe that the size of the proposed structure is very small and comparable to [44] and [47] while it offers the smallest fractional bandwidth and low insertion loss.

6.6 Conclusion

In this Chapter, an L-shaped iris embedded in substrate integrated waveguide has been proposed and a complete lumped element equivalent circuit analysis for wide frequency band has been developed. It has been illustrated that the proposed iris demonstrates an extra degree of freedom; therefore, it offers design flexibility to realize transmission zeros and evanescent-mode poles. Based on the developed lumped element equivalent circuit, a prescribed filtering function has been demonstrated to realize evanescent-mode PBFs with adjacent transmission zero. The concept has been also employed to realize evanescent-mode filter with extended stop-band and dual-band filter utilizing evanescent and ordinary modes excitation. It has been shown that the L-shaped iris integrated with SIW structures provides flexibility of design, size reduction and performance enhancement. This structure promises to substitute the conventional irises in substrate integrated waveguide structures.

6.7 References

[1] N. Marcuvitz, *Waveguide Handbook*, New York, NY, USA: McGraw-Hill, 1951.

[2] G.L. Matthaei, L. Young, E.M.T. Jones, *Microwave Filters, Impedance-Matching Networks, and Coupling Structures*, Artech House, McGraw-Hill, 1964.

[3] D.M. Pozar, *Microwave Engineering*, 3rd ed. New York: Wiley, 2005.

[4] S. Bastioli and R. Snyder, "Inline pseudoelliptic TE_{01}-mode dielectric resonator filters using multiple evanescent modes to selectively bypass orthogonal resonators," *IEEE Trans. Microw. Theory and Tech*., vol.60, no.12, pp.3988-4001, Dec. 2012.

[5] O. Glubokov and D. Budimir, "Extraction of generalized coupling coefficients for inline extracted pole filters with nonresonating nodes," *IEEE Trans. Microw. Theory and Tech*., vol.59, no.12, pp.3023-3029, Dec. 2011.

[6] R. Tomassoni and R. Sorrentino, "A new class of pseudoelliptic waveguide filters using dual-post resonators," *IEEE Trans. Microw. Theory and Tech*., vol.61, no.6, pp.2332-2339, Jun. 2013.

[7] Y. Wang and M. Yu, "True inline cross-coupled coaxial cavity filters," *IEEE Trans. Microw. Theory and Tech*., vol.57, no.12, pp.2958-2965, Dec. 2009.

[8] C. Tomassoni, S. Bastioli, and R. V. Snyder, "Pseudo-elliptic in-line filters with dielectric resonators in propagating waveguide*," IEEE-MTT-S, Int. Microw., Symp*.pp.1-4, May 2015.

[9] L. P. Mospan, S. A. Prikolotin, and A. A. Kirilenko, "Rectangular waveguide section with a pair of antipodal posts; spectral characteristics*,*" *Int. Conf., Antenna Theory and Tech.*, pp.1-3, Apr.2015.

[10] U. Rosenberg, S. Amari, and J. Bornemann, "Inline TM_{110}-mode filters with high-design flexibility by utilizing bypass coupling of nonresonating $TE_{10/01}$ modes," *IEEE Trans. Microw. Theory and Tech*., vol.51, no.6, pp.1735-1742, Jun. 2003.

[11] S. Amari and U. Rosenberg, "Synthesis and design of novel in-line filters with one or two real transmission zeros," *IEEE Trans. Microw. Theory and Tech*., vol.52, no.5, pp.1464-1478, May 2004.

[12] I. Ohira, H. Deguchi, M. Tsuji, and H. Shigesawa, "Novel waveguide filters with multiple attenuation poles using dual-behavior resonance of frequency-selective

surfaces," *IEEE Trans. Microw. Theory and Tech*., vol.53, no.11, pp.3320-3326, Nov. 2005.

[13] Amari and U. Rosenberg, "Charactristics of cross (bypass) coupling through higher/lower order modes and their applications in elliptic filter design," *IEEE Trans. Microw. Theory and Tech*., vol.53, no.10, pp.3135-3141, Oct. 2005.

[14] M. Guglielmi, P. Jarry, E. Kerherve, O. Requebrm, and D. Schmitt, "A new family of all-inductive dual-mode filters," *IEEE Trans. Microw. Theory and Tech.*, vol.49, no.10, pp.1764-1769, Oct. 2001.

[15] S. Bastioli, C. Tomassoni, and. R. Sorrentino, "A new class of waveguide dual-mode filters using TM and nonresonating modes," *IEEE Trans. Microw. Theory and Tech*., vol.58, no.12, pp.3909-3917, Dec. 2010.

[16] K. Gong, W. Hong, Y. Zhang, P. Chen, and C.J. You, "Substrate integrated waveguide quasi-elliptic filters with controllable electric and magnetic mixed coupling," *IEEE Trans. Microw. Theory and Tech*., vol.60, no.10, pp.3071-3077, Oct. 2012.

[17] M. Garai, J. A. R. Cruz, J. M. Rebollar, M. J. P. Cruz, A.O. Navarro, and I. H. Carpintero, "Synthesis and design of in-line N-order filters with N real transmission zeros by means of extracted poles implemented in low-cost rectangular H-plane waveguide," *IEEE Trans. Microw. Theory and Tech*., vol.53, no.5, pp.1636-1642, May 2005.

[18] D. J. Kim and J.-H. Lee, "Partial H-plane filters with multiple transmission zeros," *IEEE Trans. Microw. Theory and Tech*., vol.56, no.7, pp.1693-1698, Jul. 2008.

[19] X. P. Chen, K. Wu, and D. Drolet, "Substrate integrated waveguide filter with improved stopband performance for satellite ground terminal," *IEEE Trans. Microw. Theory and Tech*., vol.57, no.3, pp.674-683, Mar. 2009.

[20] G. F. Craven and C. K. Mok, "The design of evanescent-mode waveguide bandpass filters for a prescribed insertion loss characteristic," *IEEE Trans. Microw. Theory and Tech*, vol.19, no.3, pp.295-308, Mar. 1971.

[21] L. Harle and L. P. B. Katehi, "A silicon micromachined four-pole linear phase filter," *IEEE Trans. Microw. Theory and Tech*., vol.52, no.6, pp.1598-1607, Jun. 2004.

[22] H. Joshi, H. H. Sigmarsson S. Moon, D. Peroulis, and W. J. Chappell, "High-Q fully reconfigurable tunable bandpass filters," *IEEE Trans. Microw. Theory and Tech*., vol.57, no.12, pp.3525-3533, Dec. 2009

[23] S. Bastioli and R. V. Snyder, "Broad passband, wide stopband, high power evanescent mode filters using capacitively-loaded ridges," *Europ. Microw. Conf., (EuMC)*, pp.176-179, Nov. 2012.

[24] S. Bastioli and R. V. Snyder, "Waveguide evanescent mode filters using high-Q bypassed cavities for extreme close-in rejection," *Europ. Microw. Conf., (EuMC)*, pp.175-178, Oct. 2014.

[25] R. V. Snyder and S. Bastioli, "Transmission zero generation for wideband high frequency evanescent mode filters," *IEEE/MTT-S, Int. Microw. Symp*., pp.1-4, Jun. 2014.

[26] S. J. Park, I. Reines, C. Patel, and G.M. Rebeiz, "High-Q RF-MEMS 4-6 GHz tunable evanescent-mode cavity filter," *IEEE Trans. Microw. Theory and Tech*., vol.58, no. 2, pp. 381-389, Feb. 2010.

[27] M. S. Arif and D. Peroulis, "All-silicon technology for high-Q evanescent mode cavity tunable resonators and filters," *Journal of Microelectromechanical Systems*, vol.23, no.3, pp.727-739, Jun. 2014.

[28] L. S. Wu, X. L. Zhou, W.Y. Yin, L. Zhou, and J. F. Mao, "A substrate-integrated evanescent-mode waveguide filter with nonresonating node in low-temperature co-fired ceramic," *IEEE Trans. Microw. Theory and Tech*., vol.58, no.10, pp.2654-2662, Oct. 2010.

[29] E. J. Naglich, J. Lee, H. H. Sigmarsson, D. Petroulis, and W. J. Chappell, "Intersecting parallel-plate waveguide loaded cavities for dual-mode and dual-band filters," *IEEE Trans. Microw. Theory and Tech*., vol.61, no.5, pp.1829-1838, May 2013.

[30] Y. D. Dong, T. Yang, and T. Itoh, "Substrate integrated waveguide loaded by complementary split-ring resonators and its application to miniaturized waveguide filters," *IEEE Trans. Microw. Theory and Tech*., vol.57, no.9, pp.2211-2223, Sep. 2009.

[31] Q. L. Zhang, W. Y. Yin, and S. He, “Evanescent-mode substrate integrated waveguide (SIW) filters implemented with complementary split ring resonators,” *Prog. Electromag. Res*., vol.111, pp.419-432, 2011.

[32] X. P. Cheng and K. Wu, “Substrate integrated waveguide cross-coupled filter with negative coupling structure,” *IEEE Trans. Microw. Theory and Tech*., vol.56, no.1, pp.142-149, Jan. 2008.

[33] T. Yang, P. L. Chi, R. Xu, and W. Lin, “Folded substrate integrated waveguide based composite right/left-handed transmission line and its application to partial H-plane filters,” *IEEE Trans. Microw. Theory and Tech*., vol.61, no.2, pp.789-799, Feb. 2013.

[34] F. Farzami and M. Norooziarab, “Experimental realization of tunable transmission lines based on single-layer SIWs loaded by embedded SRRs,” *IEEE Trans. Microw. Theory and Tech*., vol.61, no.8, pp.2848-2857, Aug. 2013.

[35] A. V. G. Subramanyam, D. Sivareddy, V. V. Krishna, V. V. Srinivasan, and Y. Mehta, “Compact iris-coupled evanescent-mode filter for spacecraft S-band data transmitters,” *IEEE/ MTT, Microw. RF Conf*., *(IMaRC)*, pp.125-127, Dec. 2015.

[36] G. F. Zargano, V. V. Zemlyakov, and V. V. Krivopustenko, “Electrodynamic analysis of eigenmodes in a rectangular waveguide with Two L-shaped septa,” *Journal of Communications Tech. and Electronics*, vol.56, no.3, pp.259-268, 2011.

[37] V. V. Zemlyakov, “The band-pass SIW-filter based on L-ridged rectangular waveguide,” *Prog., Electromag., Res., Symp*., pp.605-609, Aug. 2013.

[38] Advanced Design System, ADS 2015.

[39] S. Bastioli and R. V. Snyder, “Ultra-compact evanescent mode filter using inhomogeneous semi-lumped capacitive elements,” *Int. Microw Conf., Radar and Wireless Communication*., pp.1-4, Jun. 2014.

[40] L.- S. Wu, J.- F. Mao, W.- Y. Yin, and Y.- X. Guo, “A dual-band filter using stepped-impedance resonator (SIR) embedded into substrate integrated waveguide (SIW),” *IEEE Elect. Design of Advanced Package & Systems Symposium*, pp.1-4, Dec. 2010.

[41] J. Shi and Q. Xue, “Novel balanced dual-band bandpass filter using coupled stepped-impedance resonators,” *IEEE Microw. Wireless Compon. Lett*, vol.20, no.1, pp.19-21, Mar. 2010.

[42] W. Shen, W.-Y. Yin, and X.-W. Sun, “Miniaturized dual-band substrate integrated waveguide filter with controllable bandwidths,” *IEEE Microw. Wireless Compon. Lett*, vol.21, no.8, pp.418-420, Aug. 2011.

[43] B. J. Chen, T. M. Shen, and R. B. Wu, “Dual-band vertically stacked laminated waveguide filter design in LTCC technology,” *IEEE Trans. Microw. Theory and Tech*., vol.57, no.6, pp.1554-1562, Jun. 2009.

[44] X.-P. Chen, K. Wu, and Z.-L. Li, “Dual-band and triple-band substrate integrated waveguide filters with Chebyshev and quasi-elliptic responses,” *IEEE Trans. Microw. Theory and Tech*., vol.55, no.12, pp.2569-2578, Dec. 2007.

[45] S. Xu, K. Ma, F. Meng, and K. S. Yeo, “Novel defected ground structure and two-side loading scheme for miniaturized dual-band SIW bandpass filter designs,” *IEEE Microw. Wireless Compon. Lett*, vol.25, no.4, pp.217-219, Apr. 2015.

[46] Y. Shen, H. Wang, W. Kang, and W. Wu, “Dual-band SIW differential bandpass filter with improved common-mode suppression,” *IEEE Microw. Wireless Compon. Lett*, vol.25, no.2, pp.100-102, Feb. 2015.

[47] L. Gao, X. Y. Zhang, B.-J. Hu, and Q. Xue, “Novel multi-stub loaded resonators and their applications to various bandpass filters,” *IEEE Trans. Microw. Theory and Tech.*, vol.62, no.5, pp.1162-1172, May 2014.

[48] Y. Dong and T. Itoh, “Miniaturized dual-band substrate integrated waveguide filters using complementary split-ring resonators,” *IEEE/MTT-S, Int. Microw. Symp*., pp.1-4, Jun. 2011.

[49] T. Yan and X.-H. Tang, “Substrate integrated waveguide dual-band bandpass filter with complementary modified split-ring resonators,” *IEEE Wireless Symp., (IWS)*, pp.1-4, Apr. 2015.

Chapter 7 Single/dual-band BPFs using inductively coupled SIW stepped impedance resonator

7.1 Introduction

Stepped impedance resonators (SIRs) have been substantially studied for the design of single and dual-band band-pass filters (BPFs). SIR-based filters offer compact sizes and the ability to independently control and tune the resonance frequencies of the structure by changing the length and characteristic impedance of the resonator [1]-[8]. A variety of SIR designs including stub-loaded [1]-[2] and tri-section geometries [3] have also been proposed to improve the filter's stop-band. On the other hand, SIW filters are dominantly considered for low loss and high power applications. In this line of research, evanescent SIW filters have been studied to introduce significant size reduction and higher quality factor in comparison to the conventional bulky SIW filters operating in the ordinary modes [9]-[11]. However, the upper stop-band of the evanescent SIW filters are limited to the first spurious resonance frequency of the filter which is reported to be a ratio of around two [9]-[10] .

In this Chapter, a new integration of SIW structures and planar SIRs is developed to design full/half-mode BPFs. In the proposed technique, the main filtering response is achieved through the SIR while the SIW sections, operating in evanescent-mode, are incorporated to provide inductive evanescent-mode coupling.

The integration results in a significant size reduction, a wide spurious-free stop-band, and a low loss operation especially for the case of dual-band filters. The wide stop-band is achieved by means of transmission zeros (TZs) that are realized through stepped open side-walls in the SIW coupling sections. It will be demonstrated that additional TZ realization is also possible by embedding open- and short-circuited stubs in the SIR structure.

In Section 7.2, the operation principal of the proposed SIW-based SIR filter is initially presented. It is shown that the developed structure provides a low-loss single-band BPF; however, it suffers from the limited upper stop-band due to the cut-off frequency of input/output SIW sections. Moreover, some additional TZs are realized to suppress the first spurious resonance frequency and increase the upper stop-band of the filter using stepped open side-walls in the SIW coupling sections. It is also shown that the developed structure provides a BPF with an ultra-wide upper stop-band in both half-mode and full-mode configurations.

In Section 7.3, the proposed technique is further investigated to realize dual-band BPFs by cascading another SIR to the structure. Here, the isolation between two bands is further improved by adding additional TZs which are accommodated in the SIR structure. The performances of all the filters are verified by measurements.

The proposed design technique offers flexibility in terms of the number of pass-bands and transmission zeros and provides a trade-off between the evanescent-mode SIW and SIR structures to achieve required design criteria such as the size, the quality factor, and the upper stop-band of the integrated structure.

7.2 3D structure integrated with planar resonator

As shown schematically in Figure 7.1, the integration of 3D coupling structures with a planar µ-strip stepped-impedance resonator is studied.

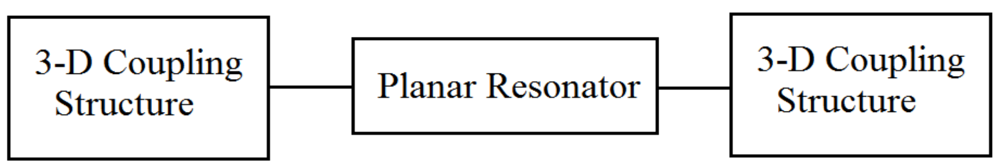

Figure 7.1. The integration of 3D coupling structures and a planar resonator.

The EM behavior of the integrated distributed-element structure is analyzed using the lumped element equivalent circuit presented in Chapter 2.

As provided in Chapter 2, Figure 2.8, each 3-D coupling structure, as a slice of 3D SIW, can be modeled by a parallel *L*-*C* circuit with a cut-off frequency corresponding to the resonance frequency of the circuit.

To realize inductive coupling in the proposed integration, the resonance frequency of the planar resonator is chosen to be below the cut-off frequency of 3D structure (or below the resonance of corresponding parallel *L*-*C* circuit).

As shown in Figure 7.2(a), a slice of 3D structure is modeled by a parallel *L*-*C* circuit with a resonance frequency of around 5.6 GHz.

Similarly, the μ-strip planar resonator with electrical length of π ($\lambda/2$) corresponding to its resonance frequency is modeled by two cascaded π-network C_2-L_2-C_2 circuits where each π-network represents the half length of the resonator corresponding to the electrical length of $\pi/2$ ($\lambda/4$).

Figure 7.2(b) shows the EM and *L*-C simulations of the integrated structure. Note that the values of the capacitors and the inductors are calculated using (2-6)-(2-7) and (2-11)-(2-12) for the 3D and planar structures, respectively.

The discrepancy between the EM and *L-C* simulated results comes from the fact that the calculated lumped element values are simulated without optimization.

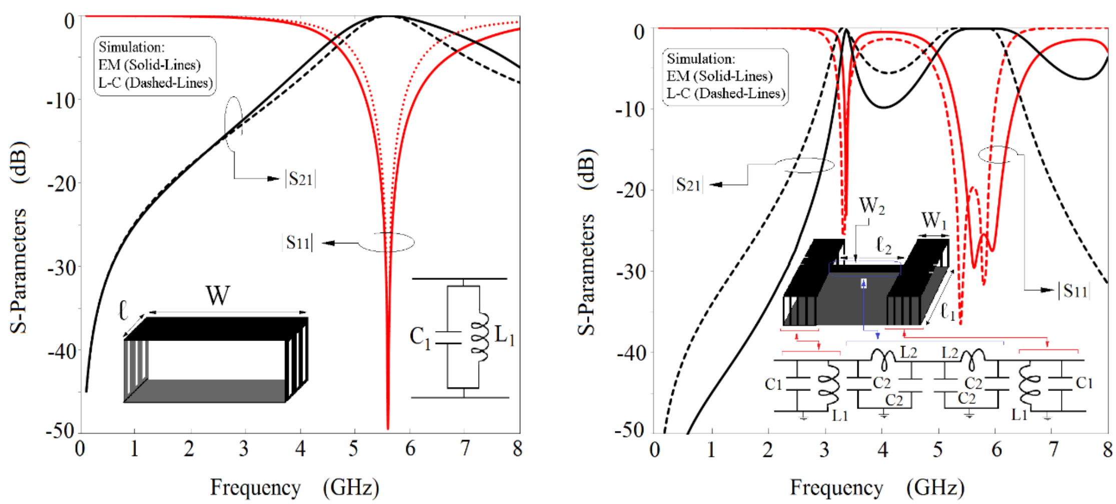

(a) (b)

Figure 7.2. EM and L-C simulations: (a) a slice of 3D structure (b) integrated structure with C_1=1.8 pF, C_2=1.1 pF, L_1=0.45 nH and L_2=1.1 nH for the lumped-element circuit and ℓ_1=10 mm, ℓ_2=10.1 mm, W_1=4.4 mm and W_2=1.6 mm for the distributed-element structure.

Inspecting the results in Figure 7.2, we observe that the planar μ-strip resonator realizes a transmission pole at around 3.1 GHz which is located below the cut-off frequency of the 3D structure.

Moreover, the performance of the lumped-element circuit models that of the distributed-element structure which can be effective for understanding the EM behavior of the structure. The integrated structure is further developed to enhance the performance in the next sections.

7.3 Single-band SIW-coupled SIR filter

In Section 7.2, we discussed the integration of the 3D-structure coupling and planar resonator based on the corresponding lumped element equivalent circuit. Here, we further develop the resonator integrated with some open-circuited stubs to enhance its performance. We also mathematically discuss the realization of transmission pole and transmission zero using this integration. Moreover, we further study the proposed structure to design half-mode BPFs with extra transmission zero in its stop-band.

7.3.1The primary structure of the proposed BPF

Figure 7.3(a) shows the structure of the developed filter where the preliminary structure in Figure 7.2 is loaded with two open-circuited stubs in the transverse direction. Note that the entire planar resonator can be considered as a stepped-impedance resonator.

The lumped element equivalent circuit of the structure provides a clear insight on how to manipulate and control the behavior of the filter in suppressing unwanted harmonics, realizing another band and/or adding a transmission zero.

Disassembling the planar resonator and 3D structures for simplicity, we analyze the EM behavior of the integrated structure using the lumped element equivalent circuits. As shown in Figure 7.3(b) and (c), the lumped element equivalent circuit of the SIR is extracted using the discussion in Chapter 2, Section 2.2.1.

Note that we use an approximation for simplicity where the effect of the C_3 capacitors is evenly added to the four C capacitors ($\overline{C_2}$). To calculate the resonance frequencies of the resonator, ABCD matrix analysis is employed [23].

$$\begin{bmatrix} A & B \\ C & D \end{bmatrix}_T = \begin{bmatrix} A_1 & B_1 \\ C_1 & D_1 \end{bmatrix} \begin{bmatrix} 1 & 0 \\ Y & 1 \end{bmatrix} \begin{bmatrix} A_1 & B_1 \\ C_1 & D_1 \end{bmatrix} \tag{7-1}$$

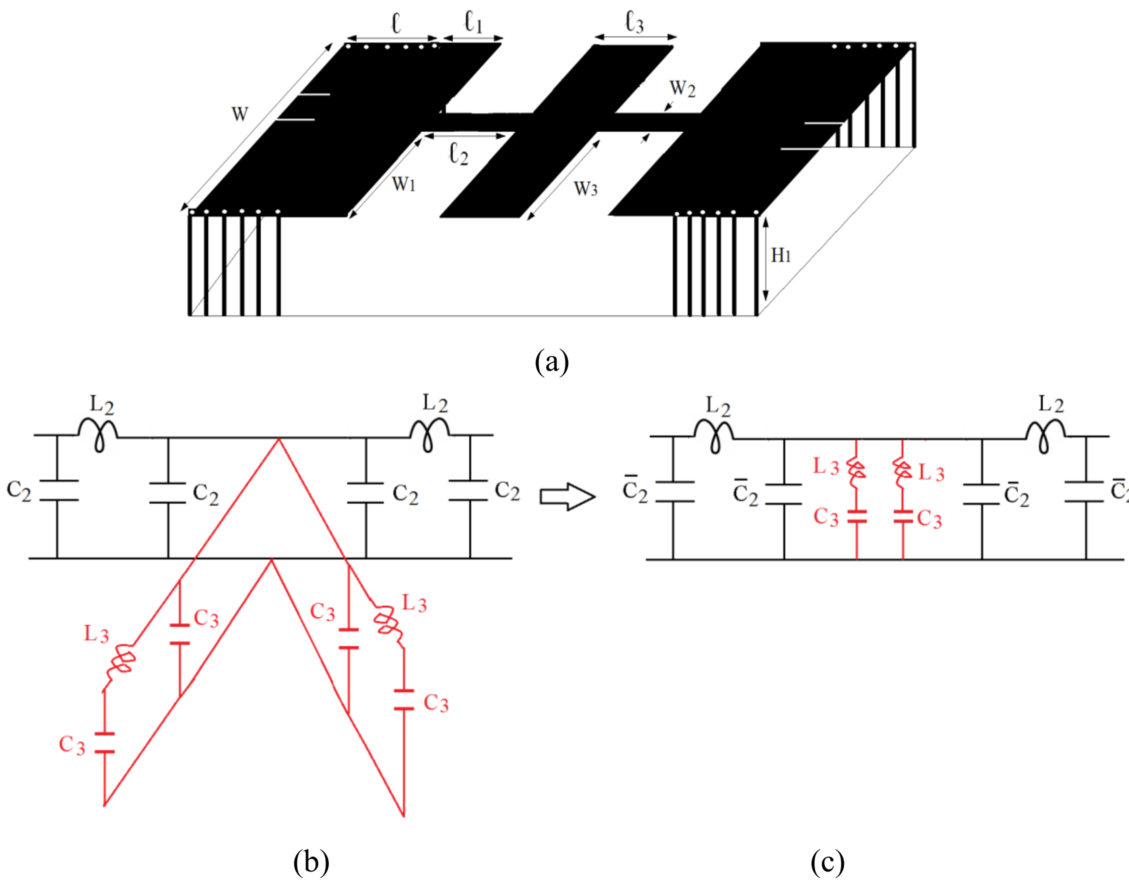

Figure 7.3. (a) The proposed structure to realize evanescent-mode filters (W= 10.1 mm, W_1=4.3 mm, W_2=1.6 mm, W_3=5.4 mm, ℓ=2.1 mm, ℓ_1=1.8 mm, ℓ_2= 1.75 mm, ℓ_3= 1.84 mm, H_1 =50 mil), and (b) and (c) the lumped element equivalent circuit of the SIR.

Next, the impedance of Z_{21} is calculated from the C parameter of the ABCD matrix as (7-2):

$$Z_{21} = \frac{1}{C_T} = \frac{(1-\omega^2 L_3 C_3)}{j2\omega(1-\omega^2 L_2 \overline{C}_2)[\overline{C}_2(2-\omega^2 L_2 \overline{C}_2)(1-\omega^2 L_3 C_3)+C_3(1-\omega^2 L_2 \overline{C}_2)]} \tag{7-2}$$

As observed from the impedance of Z_{21}, the series combination of L_3-C_3 circuit realizes a transmission zero at the following frequency:

$$\omega_{TZ} = \frac{1}{\sqrt{L_3 C_3}} \tag{7-3}$$

Similarly, the transmission poles of the resonator can be calculated by equating the denominator of Z_{21} to zero:

$$\omega_{01} = \frac{1}{\sqrt{L_2\overline{C}_2}}, \ \ \overline{C}_2\left(2-\omega^2 L_2\overline{C}_2\right)\left(1-\omega^2 L_3 C_3\right) + C_3\left(1-\omega^2 L_2\overline{C}_2\right) = 0 \qquad (7\text{-}4)$$

In the same way, the EM behavior of 3D-structure sections can be analyzed using lumped element equivalent circuit. Since these I/O transitions are realized based on 3D SIW structures, they are modeled with two parallel *L*-*C* circuits in the transverse direction (Chapter 2, Section 2.2.1)

Designating two parallel L_1-C_1 circuits for I/O sections (Figure 7.2(a)), the impedance of each section is calculated in the transverse direction as follows:

$$Z = \frac{j\omega L_1}{1-\omega^2 L_1 C_1} \qquad (7\text{-}5)$$

For the frequencies below the 3D structure cut-off frequency or $\omega \le \frac{1}{\sqrt{\mathrm{L_1 C_1}}}$, the two I/O transition sections provide inductive coupling [12] for the SIR as the resonator of the integrated structure.

The primary structure of the filter is simulated using Advanced Design Software (Agilent ADS Momentum) and fabricated on a 50 mil substrate with the dielectric constant of $\varepsilon_r = 10.2$. Figure 7.4 shows the digital photograph and the performance of the filter.

As shown in Figure 7.4, the proposed structure realizes a transmission pole at 2 GHz where the cut-off frequency of the SIW is calculated to be 4.57 GHz with the width of a_{SIW} = 10.1 mm, via holes diameter d=0.2 mm and via pitch p=0.3 mm [24]. Note that the upper stop-band of the filter is limited by the first spurious resonance frequency of the inductors ($\frac{f_s}{f_r}$~2); a common problem in the design of evanescent-mode waveguide filters in the literature [9]-[11]. In the next part, the proposed structure is further developed using the lumped element equivalent circuit of the filter to suppress the first spurious resonance frequency of the structure.

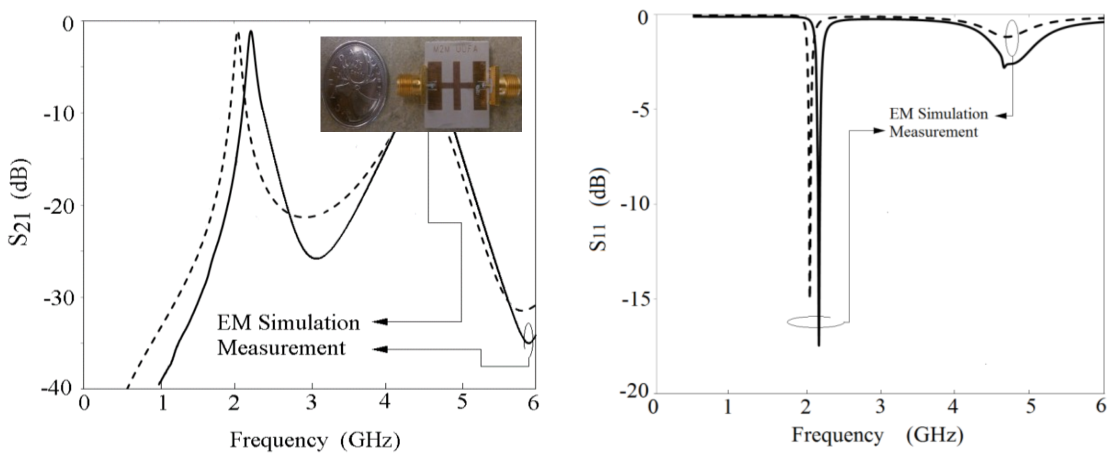

(a) (b)

Figure 7.4. EM simulated and measured results of the proposed filter in Figure 7.3 (a) S_{21} (b) S_{11}.

7.3.2 Full-mode BPF with ultra-wide stop-band

Inspecting the simulated and measured results shown in Figure 7.4, we observe that the upper stop-band of the filter is limited by the first spurious resonance frequency of the structure. Here, to increase the upper stop-band, the primary structure is further developed where a transmission zero is added to suppress the spurious resonance frequency. To show how the spurious resonance frequency is suppressed, the integration of the SIW with a vertically stepped-impedance open-circuited stub is analyzed using the input impedance. Figure 7.5 shows the integration where K and α are the impedance and length ratios of the vertically stepped-impedance and normal-height open-circuited stubs, respectively.

The total impedance relative to the ground can be found using the two parallel Z_A (SIW) and Z_B (open-circuited stub) impedances as shown in Figure 7.5, calculated by (7-6).

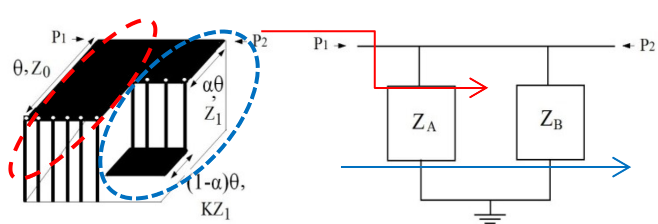

Figure 7.5. Integration of the short- and reduced-height open-circuited stubs with the corresponding impedance circuit.

$$Z_{in} = \frac{Z_0 \tan\theta[\tan(\alpha\theta)\tan((1-\alpha)\theta)-K]}{Z_0 \tan\theta[\tan((1-\alpha)\theta)+K\tan(\alpha\theta)]+[\tan(\alpha\theta)\tan((1-\alpha)\theta)-K]} \tag{7-6}$$

Inspecting the impedance presented in (7-6), there are two primary parameters to manipulate the TZ including K and α. Figure 7.6 shows the results of changing the impedance ratio from K_1=1 (the conventional case) to K_3=0.1 resulting in the TZ tuning to suppress the first spurious resonance frequency of the structure.

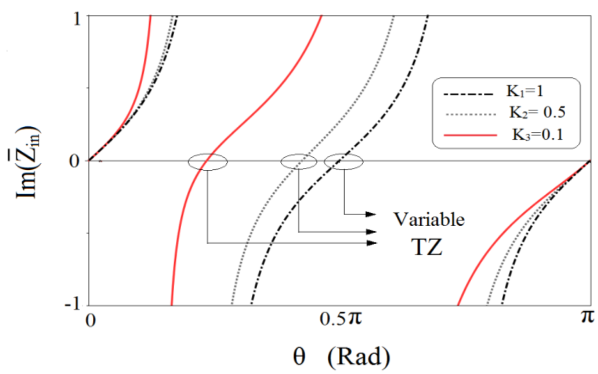

Figure 7.6. Plotted imaginary part of the input impedance of the structure in Figure 7.5.

Moreover, these results can be explained based on the lumped element equivalent circuit. As given in Figure 7.4, the structure demonstrates a TZ at the frequency of 6 GHz. To bring this TZ to the frequency of the first spurious resonance frequency located at around 4.5 GHz, the C_3 capacitance in the *L-C* circuit is increased ((7-3)). To do this, the capacitance is increased by decreasing the gap between the top and bottom layers of the structure as shown in Figure 7.5. This is achieved by adding an extra connected metal layer using via holes to the top layer as indicated in the structure in Figure 7.7(a). Moreover, Figure 7.7(b) provides the current distribution at the resonance frequency showing the resonance of the SIR at this frequency.

To experimentally evaluate the performance of the modified BPF with wider stop-band, the filter is fabricated on a 50 mil substrate with the dielectric constant of $\varepsilon_r = 10.2$. Figure 7.8 shows the simulated and measured results accompanied by the digital photograph of the filter.

Inspecting the measured performance of the filter, the structure provides an evanescent-mode BPF with the 25 dB rejection level at a wider stop-band ($\frac{f_s}{f_r}$=4.8).

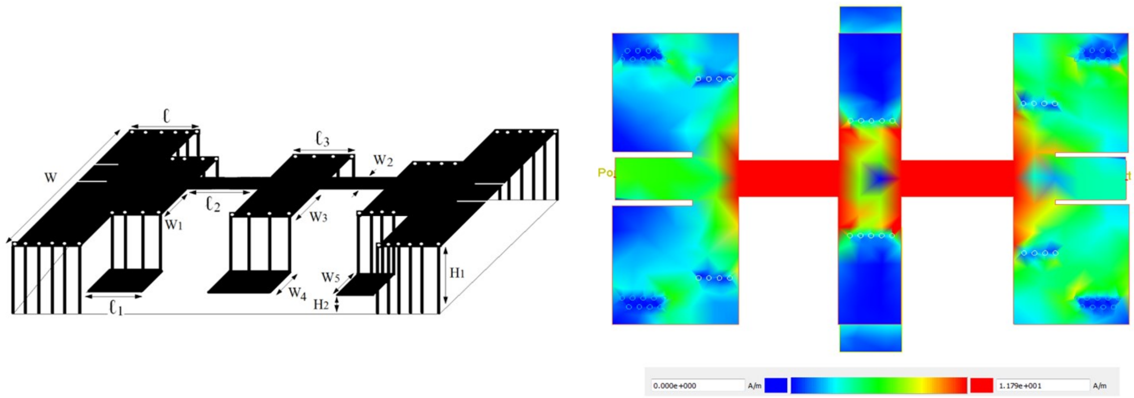

(a) (b)

Figure 7.7. (a) Proposed single-band BPF to suppress the higher spurious resonance frequency with W= 10.1 mm, W_1=3.5 mm, W_2=1.6 mm, W_3=3.5 mm, W_4=2.43 mm, W_5=2.8 mm, ℓ=2.1 mm, ℓ_1=1.8 mm, ℓ_2= 1.75 mm, ℓ_3= 1.84 mm, and H_1=H_2= 25 mil (b) current distribution at the resonance frequency.

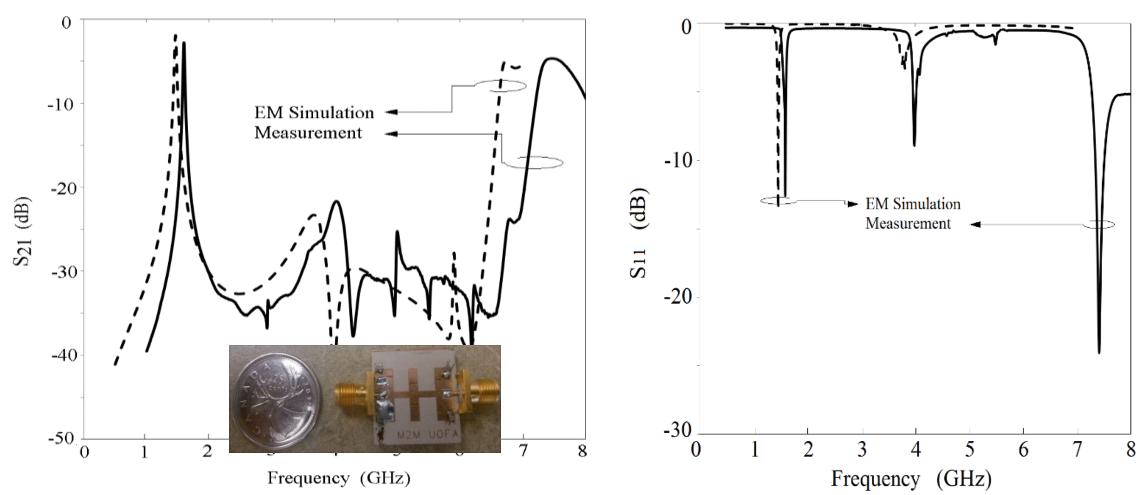

(a) (b)

Figure 7.8. Simulated and measured performances of the single-band full-mode evanescent-mode BPF with improved stop-band rejection (a) S_{21} (b) S_{11}.

To analyze the EM behavior of the integrated structure in Figure 7.7(a), its performance is discussed using lumped element equivalent circuit.

As discussed in Chapter 2, Section 2.2, an open-circuited stub is capable of TZ realization due to the series *L*-*C* circuit in its corresponding lumped element equivalent circuit.

Therefore, to improve the performance of the structure in Figure 7.2, it is loaded with some reduced-height open-circuited stubs in the transverse direction.

Given in Figure 7.7(a), the entire planar resonator can be considered as a stepped-impedance resonator. Similarly, the short- and open-circuited stubs in the structure are replaced with their corresponding lumped element equivalent circuits in Figure 2.8.

Figure 7.9(a) provides the lumped element equivalent circuit of the integrated structure where the parallel L_1-C_1 and the π-network C_2-L_2-C_2 circuits stand for the 3D and the planar SIR structures, respectively. Moreover, the C_{44}/L_4-C_4 and C_{33}/L_3-C_3 circuits model the open-circuited stubs in the structure. The capacitors and inductors values of the short- and open-circuited stubs are calculated using (2-6)-(2-7) and (2-11)-(2-12), respectively.

Note that each open-circuited stub consists of two sections one with normal height and the other with reduced height. We have approximately merged their lumped element equivalent circuits with distinguished capacitors (C_3/C_{33} or C_4/C_{44}, C_3 and C_{33} represent the capacitors of the normal and the reduced-height sections, respectively).

Figure 7.9(b) shows the L-C performance of the structure in Figure 7.7(a) with the EM simulated and measured performances in Figure 7.8. Note that the L-C circuit models the behavior of the distributed-element structure both in the pass-band and the stop-band including the transmission zero at 4.15 GHz.

Table 7.1 compares the performance of the developed single-pole evanescent-mode BPF with the conventional counterparts in terms of the size, insertion loss, FBW and the ratio of spurious resonance frequency.

Based on the results in Table 7.1, the highlights of the proposed single-pole filter in comparison to the previous works can be listed as follows:

- We are flexible in the design and targeting different parameter improvements.
- The upper stop-band ($\frac{f_s}{f_r}$) is wider compared to all the conventional evanescent-mode BPFs.
- The insertion loss is the same as the conventional SIW presented in [11], but the stop-band is highly improved.

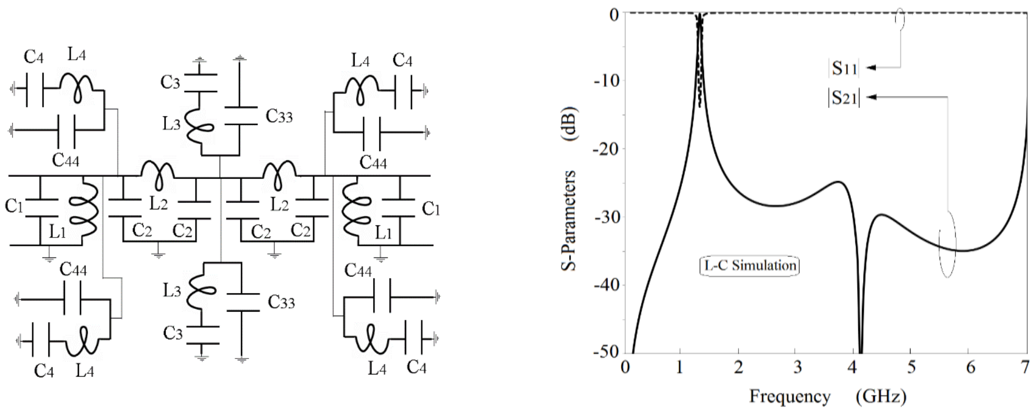

(a) (b)

Figure 7.9. *L-C* simulation of the proposed single-band BPF in Figure 7.7(a) with L_1=0.55 nH, C_1=1.1 pF, L_2=1.1 nH, C_2=1.1 pF, L_3=0.3 nH, C_3=5 pF, C_{33}=2 pF, L_4=0.05 nH, C_4=0.5 pF and C_{44}=0.5 pF.

Table 7.1 Comparison between the proposed BPF and the conventional counterparts.

	Technology	f_0 (GHz)	IL(dB)	f_s/f_0	BW%	Size ($\lambda_g \times \lambda_g$)
[1]	SIR	2.40	2.1	3.3	5.0	2.20 ×1.81
[3]	SIR	2.10	1.3	3.8	2.4	0.17× 0.17
[4]	SIR	1.08	3.5	5.5	12	0.21× 0.22
[6]	SIW-SIR	2.40	2.4	8.8	Not given	0.13×0.08
[7]	SIR	12.0	0.8	Not given	28	0.10× 0.09
[8]	SIW-SIR	1.50	2.0	6.5	10	0.80 ×0.70
[9]	3D waveguide evanescent	4.0-6.0 tunable	5.4	1.6	0.94	0.12× 0.06
[10]	Multi-layer LTCC evanescent	3.50	1.2	2.4	8.7	0.52× 0.41
[11]	SIW evanescent	3.78	3.1	2.5	3.0	0.23× 0.14
This work, full-mode	SIW-SIR	1.50	3.5	4.8	2.5	0.32× 0.20
This work, half-mode	SIW-SIR	2.00	2.8	4.6	3.6	0.31× 0.12

7.3.3 Half-mode BPF with ultra-wide stop-band

For some applications, the bandwidth is sacrificed in favor of more size reduction. Therefore, to further reduce the size, the half-mode evanescent BPF is designed and developed using the structure in Figure 7.7(a). Considering the lumped element equivalent circuit of this structure, the inductor and capacitor values are twice and half of those of the full-mode filters, respectively. Therefore, the resonance frequency is expected to be the same but the bandwidth will be increased. Figure 7.10 compares the simulated and the measured results as well as the digital photograph of the half-mode evanescent BPF. The half-mode BPF demonstrates a fractional bandwidth of FBW=3.6 with an insertion loss of 2.8 dB while the upper stop-band ratio of 4.8 is maintained ($\frac{f_s}{f_r}$ = 4.8).

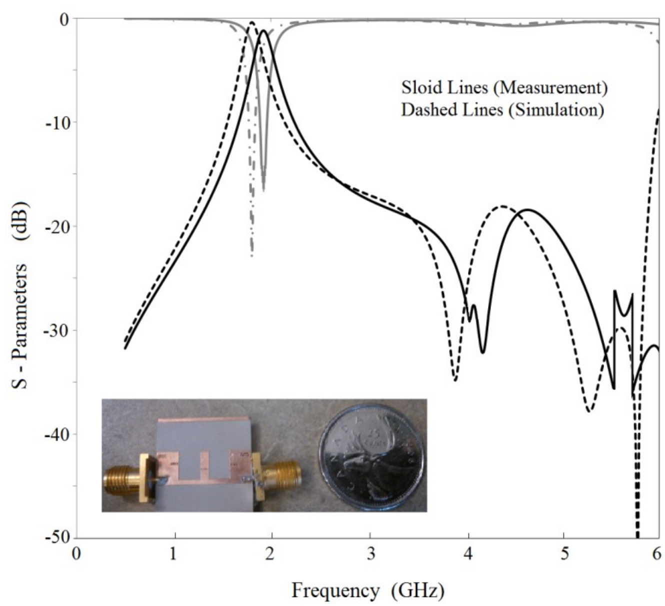

Figure 7.10. Single-band half-mode evanescent-mode BPF with improved stop-band and the digital photograph of the filter.

7.4 Dual-band SIW-coupled SIR filter

7.4.1 Full-mode dual-band filters

So far, a variety of dual-band filters have been developed using either planar or 3D structures operating in TEM or ordinary TE_{10} modes. In the first case, the resonance frequencies can be arbitrarily controlled and tuned; however, loss and quality factor are mainly sacrificed. On the other hand, the developed dual-band 3D structure BPFs are reported to provide a higher quality factor but at the expense of large size and lack of any possibility to arbitrarily tune and control the two bands. Here, the proposed structure in the previous section is further developed to design a dual-band evanescent-mode BPF. Figure 7.11(a) shows the developed structure to realize another resonance frequency where two parallel open-circuited stubs are added to the structure.

In reference to the structures given in Figure 7.7(a), two additional vertically stepped-impedance open-circuited stubs (shown by gray color) are added to realize the second band in Figure 7.11(a). These two open-circuited stubs add an extra *L*-*C* circuit to the initial lumped element equivalent circuit of the primary filter (Figure 7.5(b)) resulting in another resonance. Figure 7.11(a) shows the EM simulated performance of the dual-band filter where the second band can be tuned by changing the width of the lower open-circuited stub in the structure, ℓ_6, from 1.7 mm to 0.9 mm. Tuning this parameter changes the inductor and capacitor values of the open-circuited stub. As shown in Figure 7.11(a), the second pass-band can be arbitrarily tuned by changing the parameter ℓ_6 in the structure. Moreover, the proposed structure is further developed to design a two-pole dual-band evanescent-mode BPF (both resonance frequencies below the cut-off frequency of 3D-structure). A two-pole dual-band evanescent-mode BPF is designed by cascading the two resonators in Figure 7.11(a) where Figure 7.11(b) and (c) show the EM simulated performance and the layout of the filter, respectively.

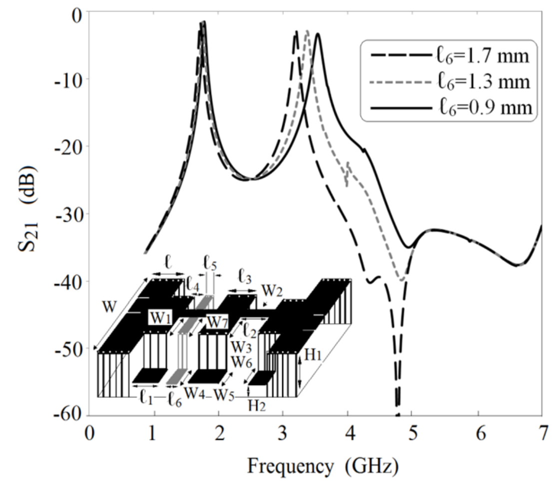

(a)

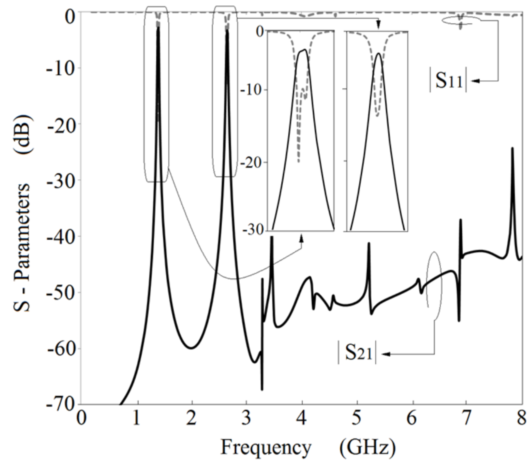

(b)

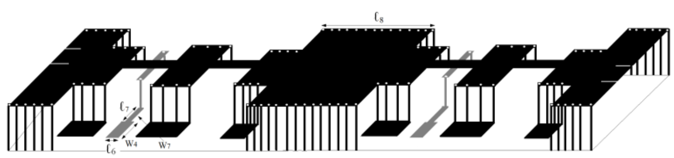

(c)

Figure 7.11. (a) The dual-band full-mode evanescent-mode BPF and the simulated results with W= 10.1 mm, W_1=3.5 mm, W_2=1.6 mm, W_3=3.5 mm, W_4=2.43 mm, W_5=2.8 mm, W_6=2.9 mm, W_7=2.5 mm, ℓ=2.1 mm, ℓ_1=1.8 mm, ℓ_2= 1.75 mm, ℓ_3= 1.84 mm, ℓ_4=0.6 mm, ℓ_5= 4.4 mm, ℓ_6 changing from 1.7 mm to 0.9 mm and H_1=H_2= 25 mil (b) the EM simulated performance of the two-pole dual-band evanescent-mode BPF (c) the layout of the filter with the same dimensions except: ℓ_6=1.64 mm, ℓ_7=1.57 mm, ℓ_8=8.2 mm, W_4=2 mm and W_7=0.25 mm.

To experimentally verify the EM simulated results, the single-pole full-mode evanescent-mode filter in Figure 7.11(a) is designed and fabricated on a double-layer (25-mil-thickness for each layer) RT/Duriod 6010 with dielectric constant of ε_r =10.2. Figure 7.12 compares the simulated and measured results as well as the digital photograph of the filter.

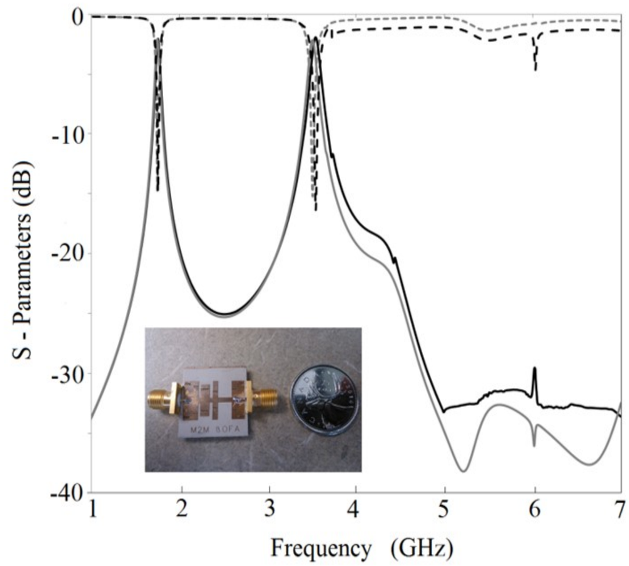

Figure 7.12. Measured (black color lines) and simulated (grey color lines) performances of the dual-band full-mode evanescent-mode BPF.

7.4.2 Half-mode dual-band filters

Similar to the previous case, for the purpose of size reduction, the half-mode counterpart of the dual-band BPF is designed and fabricated with the same parameters. Figure 7.13 compares the simulated and measured results as well as the digital photograph of the filter.

Table 7-2 summarizes the performances of the two fabricated full- and half-mode BPFs in terms of the center frequencies, insertion loss and BW.

Table 7.2 Comparison between the measured results of the half- and full-mode evanescent-mode BPFs.

First band, Second band	Full-mode	Half-mode
f_{01}, f_{02} (GHz)	1.76, 3.54	1.72, 3.32
IL (dB)	2.09, 1.93	1.81, 2.10
BW(GHz)	0.06, 0.12	0.25, 0.18

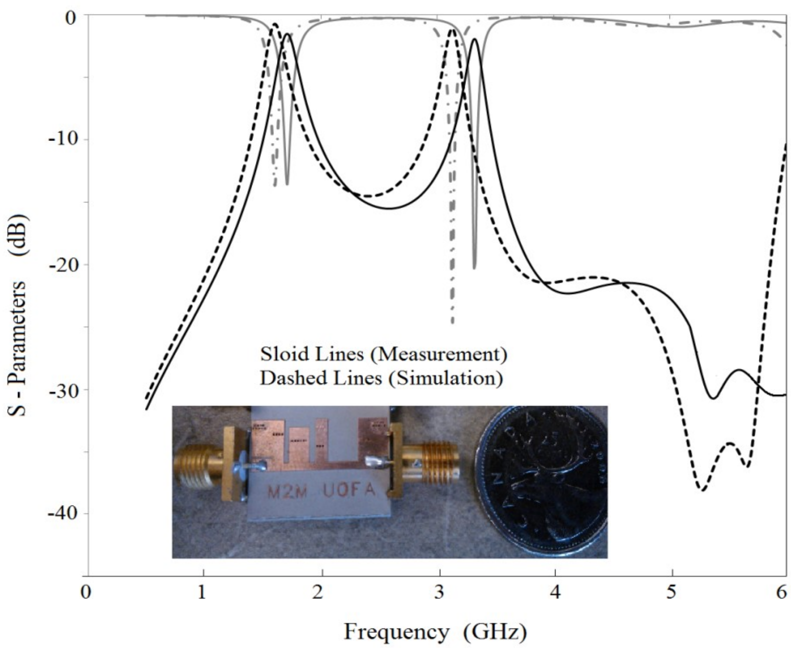

Figure 7.13. Measured (solid lines) and simulated (dashed lines) performances of the dual-band half-mode evanescent-mode BPF.

7.5 Additional transmission zero

Inspecting the performance of the half-mode dual-band filters in Figure 7.13, we are aimed to increase the attenuation level between the two bands by adding an extra TZ to the filter. To realize the TZ, a series *L*-*C* circuit is required to connect the top and bottom layers of the structure. This is shown in Figure 7.14 where the integration of the two vertically stacked open- and short-circuited stubs is embedded in the structure. Here, the open-circuited stub is vertically placed on the top of the short-circuited stub in the middle layer of the structure corresponding to the capacitor and inductor *C* and *L* in Figure 7.14, respectively.

Up to the frequency corresponding to $\lambda/4$, the short-circuited stub acts as an inductor where it realizes the series L-C_c circuit in integration with the open-circuited stub.

Figure 7.14 shows the EM simulated results for this integration where a TZ is realized at the frequency of 2.68 GHz due to the resonance of the series L-C_c circuit. As demonstrated in Figure 7.15, the proposed dual-band half-mode evanescent-mode filter in Figure 7.13 is further developed by adding the extra TZ to the structure. The length of the open- (ℓ_8) and short-circuited (ℓ_9) stubs are equal to 7 mm with the widths of W_8=3 mm and W_9 =2.3 mm, respectively.

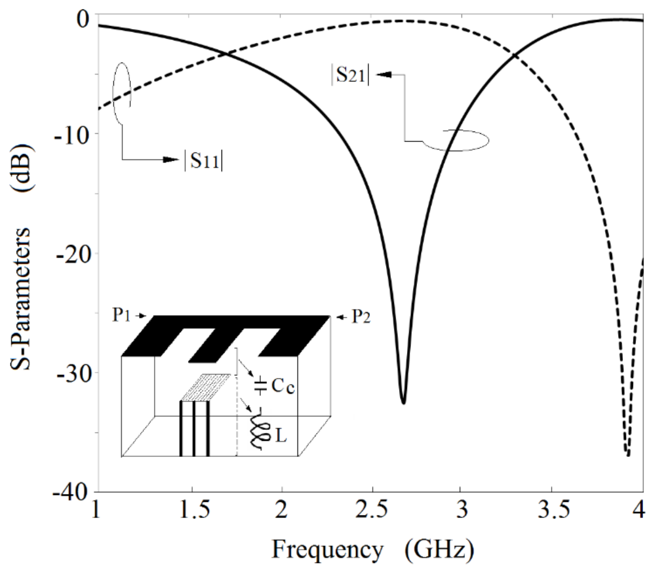

Figure 7.14. The proposed vertically integration of open- and short-circuited stubs for TZ realization and its EM simulated results.

To experimentally verify the structure, a half-mode filter with extra TZ is designed and fabricated on a double-layer 25-mil-thick substrate with the same properties as the filter without the TZ. Figure 7.15 compares the EM simulated and measured results of the filter.

Table 7-3 compares the performance of the developed single-pole dual-band full-mode evanescent BPF in Figure 7.12 with the conventional counterparts in terms of size, insertion loss, FBW and the ratio of the main and spurious resonance frequencies.

Based on the results in Table 7.3, the highlights of the proposed dual-band filter in comparison to the previous works can be listed as follows:

- The upper stop-band (f_s/f_r) is wider compared to all the conventional BPFs except those in [21] and [19] where the proposed structure shows better performance (IL and stop-band rejection).
- In comparison to the planar ones, the size has been reduced with similar IL and less FBW.

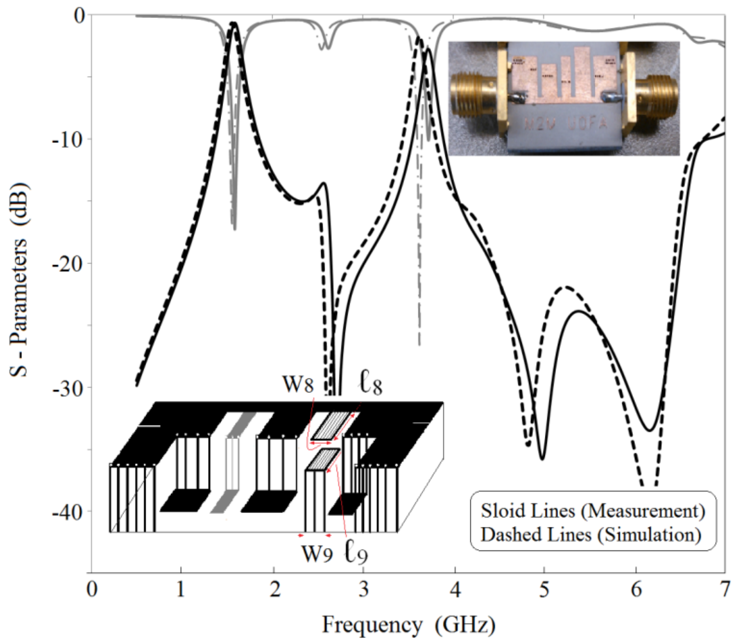

Figure 7.15. The simulated and measured results of the dual-band half-mode evanescent-mode BPF with ℓ_8=ℓ_9= 7 mm, W_8= 3 mm and W_9= 2.3 mm.

It should be noted that the complete lumped element equivalent circuit of the short-circuited stub in the proposed vertically stacked open- and short-circuited stubs is a parallel *L*-*C* circuit (Figure 2.8, Chapter 2); therefore, this integration realizes a transmission zero accompanied by a transmission pole. Inspecting the performance of the filter in Figure 7.15, we observe that the structure realizes a TZ and a transmission pole at around 2.9 GHz and 2.5 GHz, respectively. To improve the performance of the filter, we attenuate the transmission pole.

7.6 Two-pole single/dual band SIW inductively coupled SIR filters

The performance of the proposed SIW-SIR BPF can be further improved in terms of sharper skirts of the band-pass and the harmonic suppression in the upper stop-band by increasing the number of the transmission poles of the structure. A two-pole BPF is designed and simulated by cascading the structure and small optimization. Figure 7.16 shows the cascaded two resonators and their EM simulated performance. The BPF theoretically demonstrates a pass-band with the fractional bandwidth of FBW=1.7% at 1.18

GHz and the insertion loss of 3.8 dB as well as the upper stop-band ratio of 6.5 (Suppression level of 30 dB).

Table 7.3 Comparison between the proposed single-pole full-mode dual-band evanescent-mode BPF and the conventional counterparts.

	Technology	f_{01}, f_{02} (GHz)	IL1, IL2 (dB)	$f_s, /f_{02},$	FBW1, FBW2%	Size ($\lambda_g \times \lambda_g$)
[13] 2 BPFs	SIR	2.4, 5.7	1.63,2.91 2.15,2.91	1.6	8.9, 3.1 5.8, 3.8	28 × 20.4 (mm^2)
[14]	SIR	2.5,4.1	1.62,1.31	1.8	3.9, 4.4	0.18×0.18
[15]	SIR	2.4,4.2	2.90,3.07	1.3	6.0, 6.0	0.5×0.27
[16]	SIR	1.5, 3.4	1.30, 1.50	1.3	9.5, 8.2	0.28× 0.22
[17]	SIR	2.4, 3.6	1.10, 3.16	1.5	5.8, 3.6,	Not given
[18]	SIR	2.4,5.6	1.16, 2.00	1.2	8.1, 5.8	19.0 × 9.2 (mm^2)
[19]	SIR	2.4,5.2	1.30, 2.40	2.7	6.0, 4.0	22.0× 12.8 (mm^2)
[20]	SIW evanescent	4.1, 5.8	2.72,1.98	1.4	3.8, 3.4	0.21×0.19
[21]	SIW evanescent	2.4,5.2	3.60, 3.10	2.0	5.8,6.5	0.15×0.16
[22]	SIW evanescent	6.2,10	1.00,1.00	1.4	19.3,13	0.42×0.12
This work	SIW evan.-SIR	1.7, 3.5	2.09,1.93	2.0	3.4,3.3	0.30×0.20

Moreover, the proposed structure can be further developed to design dual-pole dual-band BPFs. A two-pole dual-band evanescent-mode BPF is designed and simulated by cascading two resonators given in Figure 7.11(a) where Figure 7.17 shows the layout and EM simulated performance of this filter. The dual-band BPF theoretically demonstrates two pass-bands with the fractional bandwidths of FBW=2.1% and 0.75% at 1.41 GHz and 2.65 GHz with the insertion losses of 2.8 dB and 3.3 dB, respectively.

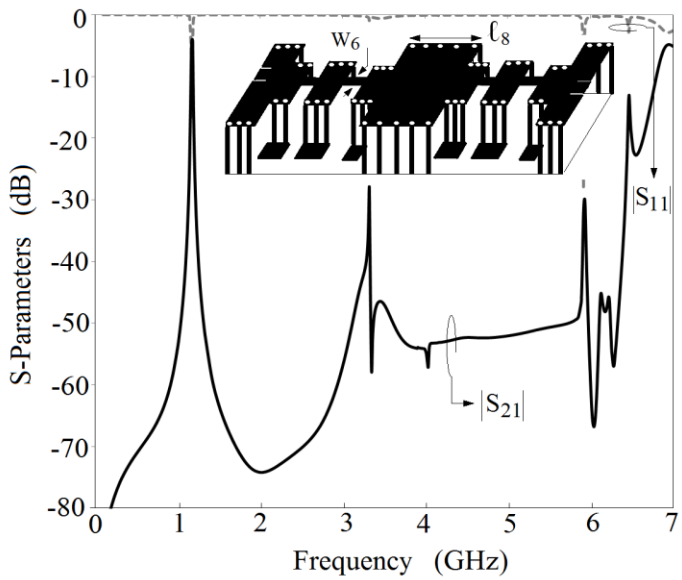

Figure 7.16. The EM simulated performance of the two-pole single-band BPF with the same dimensions as before except ℓ_8=6 mm and W_6=0.63 mm.

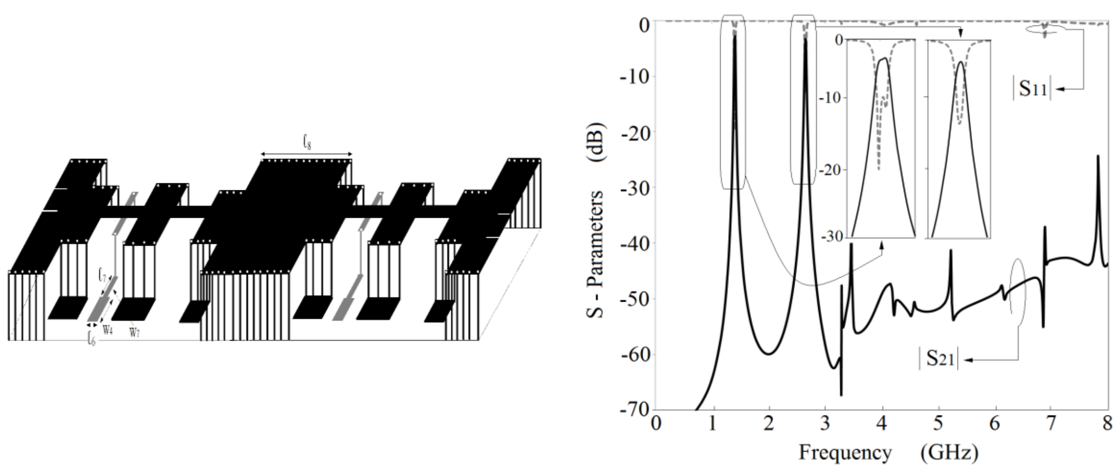

(a) (b)

Figure 7.17. (a) the layout and (b) the EM simulated performance of the two-pole dual-band BPF with the same dimensions as before except: ℓ_6=1.64 mm, ℓ_7=1.57 mm, ℓ_8=8.2 mm, W_4=2 mm and W_7=0.25 mm.

7.7 Conclusion

A new design technique based on the integration of evanescent-mode coupling and SIR resonators has been introduced. It has been shown that evanescent-mode coupling can be used to create inductively coupled single/dual-band BPFs with ultra-wide upper stop-band. It has also been shown that the proposed configuration provides the design flexibility in performance enhancement and size reduction. Moreover, the vertical integration of the short- and open-circuited stubs has been incorporated into the structure to realize a TZ between the bands resulting in further attenuation. The simulated performances of the filters have been verified by measurements for both half-mode and full-mode structures. The proposed technique offers a trade-off between the evanescent-mode SIW BPF and SIR filters to achieve required design criteria such as size, quality factor, and upper stop-band.

7.8 References

[1] M. Chongcheawchamnan, R. Phromloungsri, M. Krairiksh, and I. D. Robertson, "Microstrip ring resonator filter with inductively-compensated parallel-coupled feed and stepped-impedance design," *Elect. Lett.*, vol.43, no.23, Nov. 2007.

[2] L. Zhu and K. Wu, "Accurate circuit model of interdigital capacitor and its application to design of new quasi-lumped miniaturized filters with suppression of harmonic resonance," *IEEE Trans. Microwave Theory Tech.*, vol.48, no.3, pp.347-356, Mar. 2000.

[3] Y. Wang, B-Z Wang, and J. Wang, "A tri-section stepped impedance bandpass filter with harmonic suppression," *7th Int. Conf. on ASIC*, pp.592-595, Oct. 2007.

[4] S. Yang, L. Lin, J. Chen, K. Deng, and C. H. Liang, "Design of compact dual-band bandpass filter using dual-mode stepped-impedance stub resonators," *Elect. Lett.*, vol.50, no.8, pp.611-613, Apr. 2014.

[5] C. H. Wu, C. H. Wang, and C. H. Chen, "Stopband-extended balanced bandpass filter using coupled stepped-impedance resonators," *IEEE Microw. Wireless Compon. Lett.*, vol.17, no.7, pp.507-509, Jul. 2007.

[6] P. Chu *et al.*, "Wide stopband bandpass filter implemented with spur stepped impedance resonator and substrate integrated coaxial line technology," *IEEE Microw. Wireless Compon. Lett.*, vol.24, no.4, pp.218-220, Apr. 2014.

[7] X. Li, C. J. You, Z. Shao, and Z. He, "A wideband bandpass filter based on stepped impedance stubs and substrate integrated coaxial line," *Asia-Pacific Microw. Conf.*, pp.1-3, Dec. 2015.

[8] J. T. Kuo and E. Shih, "Microstrip stepped impedance resonator bandpass filter with an extended optimal rejection bandwidth," *IEEE Trans. Microw. Theory and Tech.*, vol.51, no.5, pp.1554-1559, May 2003.

[9] S.J. Park, I. Reines, C. Patel, and G.M. Rebeiz, "High-Q RF-MEMS 4-6 GHz tunable evanescent-mode cavity filter," *IEEE Trans. Microw. Theory and Tech.*, vol.58, no.2, pp.381-389, Feb. 2010.

[10] L.S. Wu, X.L. Zhou, W.Y. Yin, L. Zhou, and J.F. Mao, "A substrate-integrated evanescent-mode waveguide filter with nonresonating node in low-temperature co-

fired ceramic," *IEEE Trans. Microw. Theory and Tech*., vol.58, no.10, pp.2654-2662, Oct. 2010.

[11] Q. L. Zhang, W.Y. Yin, and S. He, "Evanescent-mode substrate integrated waveguide (SIW) filters implemented with complementary split ring resonators," *Prog. Electromag. Res*., vol.111, pp.419-432, 2011.

[12] A. Garcia-Lamperez and M. Salazar-Palma, "Single-band to multiband frequency transformation for multiband filters," *IEEE Trans. Microw. Theory and Tech*., vol.59, no.12, pp.3048-3058, Dec. 2011.

[13] J. T. Kuo and T. W. Lin, "Dual-mode dual-band ring resonator bandpass filter with transmission zeros," *Asia-Pacific Microw. Conf.,* pp.1865-1870, Dec. 2010.

[14] G. Wu, L. Yang, and Q. Xu, "Miniaturised dual-band filter with high selectivity using split ring scheme," *Electronics Lett.*, vol.51, no.7, pp.570-572, Apr. 2015.

[15] W. S. Chang and C. Y. Chang, "Analytical Design of Microstrip Short-Circuit Terminated Stepped-Impedance Resonator Dual-Band Filters," *IEEE Trans. Microw. Theory and Tech*., vol.59, no.7, pp.1730-1739, Jul. 2011.

[16] F. Qiu, L. Z. Zhang, and B. Wu, "High selective dual-band microstrip filter using zero-degree coupled SIR feed lines," *Antennas and Propagation (APCAP), Asia-Pacific Conf.,* pp.731-733, Dec. 2014.

[17] Z. Xia and F. Liu, "Dual-band bandpass filters using SIRs with open-stub line and zero-degree feed structure," *IEEE Int. Wireless Symp. (IWS),* pp.1-4, Apr. 2013.

[18] J. E. Lim and J. H. Lee, "A novel design method of microstrip dual-band filter using feed line with SIR," *Asia-Pacific Microw. Conf.,* pp.1274-1277, Dec. 2011.

[19] Y. C. Chang, C. H. Kao, M. H. Weng, and R. Y. Yang, "A novel compact dual-band bandpass filter with a wide stopband using asymmetric SIRs for WLANs," *Asia-Pacific Microw. Conf.,* pp.1-4, Dec. 2008.

[20] Y. Dong and T. Itoh, "Miniaturized dual-band substrate integrated waveguide filters using complementary split-ring resonators," *IEEE/ MTT-S, Int. Microw. Symp*., pp.1-4, Jun. 2011.

[21] S. Xu, K. Ma, F. Meng, and K. S. Yeo, "Novel defected ground structure and two-side loading scheme for miniaturized dual-band SIW bandpass filter designs," *IEEE Microw. Wireless Compon. Lett*, vol.25, no.4, pp.217-219, Apr. 2015.

[22] T. Yan and X.-H. Tang, “Substrate integrated waveguide dual-band bandpass filter with complementary modified split-ring resonators,” *IEEE Wireless Symp*., (IWS), pp.1-4, Apr. 2015.

[23] D.M. Pozar, *Microwave Engineering*, 3rd ed. New York:Wiley, 2005.

[24] Z. Kordiboroujeni and J. Bornemann, “Designing the width of substrate integrated waveguide structures,” *IEEE Microw. Wireless Compon. Lett*, vol.23, no.10, pp.518-520, Oct. 2013.

Chapter 8 Conclusions

8.1 Contributions

The main objective of this thesis was to develop and propose new techniques for transmission zeros and poles' realization in both planar and 3D structures. The main contributions of this study can be summarized as follows:

8.1.1. TZs realization in planar structures

In the first part of this study, two different configurations have been developed to demonstrate transmission zeros (TZs) in the pass-band of UWB BPFs known as notch-band frequencies. The first proposed technique has been reported to be based on the cross coupling between higher spurious harmonics to cancel out the signal at specific frequencies. Based on this technique, a new configuration has been proposed to design an ultra-wideband band-pass filter that demonstrates double/single notch-bands using micro-strip transmission lines without via-holes. The proposed approach has been developed using two parallel stepped-impedance resonators (SIR) providing two paths with different electrical lengths between I/O ports. In this approach, the mechanism notch-band realization has been developed based on the waves' cancellation theory.

To realize single and/or double notch-bands within the pass-band of an UWB BPF, the conventional tri-section SIR has been used where its fundamental and first spurious resonance frequencies have been determined to be either suppressed or supported. New parallel dual-section T-shaped and tri-section SIRs have been proposed, optimized and fabricated to provide single and double notch-bands, respectively. A size reduction of around 75% has been reported in comparison to the conventional BPFs with a single notch-band accompanied by two TZs at the lower and upper pass-band of the filter. Moreover, the proposed double notch-band UWB BPF has been reported to demonstrate a comparable performance to that of the latest UWB BPF designed using complicated and multilayer LCP technology with a size reduction of 12.6%.

Moreover, a systematic approach has been developed to realize UWB BPFs with one to four notch-bands on a single-layer substrate using μ-strip technology with no via-holes.

8.1.2. Tunable TZs in planar structures

Novel ultra-wide-band band-pass filters (UWB BPF) with tunable single/double notch-bands have been developed based on the integration of MEMS actuators with CPW structures. To our knowledge, this is the first MEMS based UWB filter reported with double tunable notch-bands. Each notched frequency has been shown to be independently tuned up to 1 GHz using the MEMS actuators.

8.1.3. TZs and evanescent-mode poles realization in substrate integrated waveguide structures

An L-shaped iris embedded in substrate integrated waveguide has been proposed and a complete lumped element equivalent circuit analysis has been developed for wide frequency band. It has been illustrated that the proposed iris demonstrates an extra degree of freedom; therefore, it offers design flexibility to realize transmission zeros and evanescent-mode poles. Based on the developed lumped element equivalent circuit, a prescribed filtering function has been demonstrated to realize evanescent-mode PBFs with adjacent transmission zero. The concept has been also employed to realize evanescent-mode filter with extended stop-band and dual-band filter utilizing evanescent and ordinary modes excitation. It has been shown that the L-shaped iris integrated with SIW structures provides flexibility of design, size reduction and performance enhancement. This structure promises to substitute the conventional irises in substrate integrated waveguide structures.

8.2 Future work

In this study, some new techniques have been investigated to realize TZs in both planar and 3D structures. The applications of these techniques have been studied on different structures presented in Chapters 3 to 7; however, these techniques can be further studied to enhance the performance of the structures. Following some extra works are recommended.

- In connection with the developed single/dual notch-band UWB BPFs in Chapter 3, the main resonators in the integrated structure have been designed based on SIRs where the second notch-band has been realized using the first spurious resonance of the first SIR. This idea can be more developed by using the second spurious resonance frequency of the first SIR in such a way that it will be located within the pass-band of the second wide-band BPF. Therefore, an UWB BPF can be designed with triple notch-bands utilizing the first and the second spurious resonance frequencies of the first SIR.

- In connection with the proposed triple and quadruple notch-band UWB BPFs in Chapter 4, the gap coupled μ-strip lines contribute to notch-bands; however, they dramatically impact the insertion loss of the filter. Further studies are necessary to improve the performance of the filter integrated with gap coupled TLs. The gap coupled lines are high impedance lines with the same impedance; the use of stepped impedance transmission lines integrated with double notch-band filters can be studied to enhance the performance and also reduce the size of the structure.
- In connection with the proposed filter with tunable single/double notch-band in Chapter 5, the bandwidth of two notches is reported to be wide. Inspecting the stepped-impedance L-shaped irises in Chapter 6 with different widths for their horizontal arms, the bandwidth and quality factor can be controlled by changing the widths of these arms. This technique can be applied to the capacitors of the structure in Chapter 5 for notch-bands realization. Based on this technique the bandwidth of the notch-bands can be further controlled.
- In connection with the developed structure in Chapter 7, the vertical reduced-height open-circuited stubs act as stepped-impedance resonators in the transverse direction, the performance of these stubs can be further improved by changing their widths and manipulating their inductors and capacitors. Additionally, the arbitrary tuning range of the two bands can be studied. Moreover, the number of bands can be increased by adding more stubs in transverse direction.
- Another main future work can be the development of the proposed integration of L-shaped iris and 3D waveguide to design band-pass filters with arbitrary multi evanescent-mode poles under the SIW cut-off frequency.
- In connection to the developed structure for evanescent-mode pole realization in Chapter 7, transmission pole realization in 3D structures has been analytically studied based on lumped element equivalent circuit. It has been shown that this transmission pole can be realized at any frequency either above or below the cut-

off frequency of waveguide known as evanescent-mode in the literature. Inspecting the proposed technique in the study, evanescent-mode resonance frequency has been realized using a structure oriented in the transverse direction. The question arises here is whether this type of resonance frequency, known as evanescent-mode pole, can be realized using an embedded structure in a 3D waveguide oriented in the propagation direction or not?

In connection to this question, one of the main topics for the future work can be the development of the lumped element equivalent circuit of the 3D structure in Chapter 6 to enhance the performance of 3D waveguides using the new techniques of transmission zero and evanescent-mode pole realization in the propagation direction.

Due to the importance of the subject, a novel integration of gap-coupled discontinuity and 3D waveguide cavity is proposed in which the coupling is realized by means of gap-coupled discontinuity instead of aperture coupling. The proposed structure is left for the future work with the following questions:

- What type of operation might this integration have? Operating below or above the cut-off frequency of 3D structure or capable of operating in both below and above cut-off frequency.
- Suffering from high attenuation is one of the problems in the reduced-height 3D structures with aperture coupling [1] with sacrificing quality factor in favor of insertion loss [2]-[4], the question arises here is whether this integration can obviate this problem to some extent or not?
- Signal distortion is still one of the challenging problems in the literature, especially in 3D structures due to waveguide modes [5], the question arises here is that this integration with new coupling structure can be effective to reduce signal distortion or not?

8.3 References

[1] M. Vahidpour and K. Sarabandi, “Micromachined J-band rectangular waveguide filter,” *General Assembly and Sci. Symp*., pp.1-4, Aug. 2011.

[2] X. Shang, M. Ke, Y. Wang, and M. Lancaster, “WR-3 band waveguides and filters fabricated using SU8 photoresist micromachining technology,” *IEEE Tran. THz. Sci. Tech*., vol.2, no.6, pp.629-637, Nov. 2012.

[3] J.-X. Zhuang, Z.-C. Hao, and W. Hong, “Silicon micromachined terahertz bandpass filter with elliptic cavities,” *IEEE Tran. THz. Sci. Tech*., vol.5, no.6, pp.1040-1047, Nov. 2015.

[4] J. Hu, S. Xie and Y. Zhang, “Micromachined terahertz rectangular waveguide bandpass filter on silicon-substrate,” *IEEE Microw. Wireless Compon. Lett*., vol.22, no.12, pp.636-638, Dec. 2012.

[5] K. Meykens, B.V. Rompaey, and H. Janseen, “Dispersion in acoustic waveguides-a teaching laboratory experiment,” *Am. J. phys*., vol.67, no.5, pp.400-406, May 1999.

Bibliography

P. I. Richard, "Resistor-transmission line circuits," *Proceedings of the IRE*, vol.36, no.2, pp.217-220, Feb. 1948.

N. Marcuvitz, *Waveguide Handbook*, New York, NY, USA: McGraw-Hill, 1951.

I. V. Lebedev and E. M. Guttsait, "Resonator of the subcritical waveguide type," *Radiotekh Electron*, Oct.1956.

S.B. Cohn, "Direct-coupled-resonator filters," *Proc. IRE*, vol. 45, no.2, pp.187-196, Feb. 1957.

E. T. Jaynes, "Ghost modes in imperfect waveguides," *Proceedings of the IRE*, pp.416-418, Feb. 1958.

L. Young, "Table for cascaded homogeneous quarter-wave transformers," *IRE Trans. Microw. Theory and Tech*., vol.7, no.2, pp.233-237, Apr. 1959.

W.A. Edson, "Microwave filters using ghost-mode resonance," *IRE Electron Components Conf*., vol.19, p.2, 1961.

L. Young, "Direct-coupled cavity filters for wide and narrow band-widths," *IEEE Trans. Microw. Theory and Tech*., vol.11, no.3, pp.162-178, May 1963.

G.L. Matthaei, L. Young, E.M.T. Jones, *Microwave Filters, Impedance-Matching Networks, and Coupling Structures*, McGraw-Hill, 1964.

G. Craven, "Waveguide bandpass filters using evanescent modes," *Electron Lett*., vol.2. no.7, pp.251-252, Jul. 1966.

R. Levy, "Theory of direct-coupled-cavity filters," *IEEE Trans. Microw. Theory and Tech*., vol.15, no.6, pp.340-348, Jun. 1967.

J. D. Rhodes, "The generalized direct-coupled cavity linear phase filter," *IEEE Trans. Microw. Theory and Tech*., vol.18, no.6, pp.308-313, Jun. 1970.

G. Craven, "Waveguide below cutoff: a new type of microwave integrated circuit," *Microwave J*., vol.13, pp.51, Aug.1970.

G. F. Craven and C. K. Mok, "The design of evanescent-mode waveguide bandpass filters for a prescribed insertion loss characteristic," *IEEE Trans. Microw. Theory and Tech*, vol.19, no.3, pp.295-308, Mar. 1971.

R.V. Snyder, “New application of evanescent mode waveguide to filter design,” *IEEE Trans. Microw. Theory and Tech*, vol.25, no.12, pp.1013-1021, Dec. 1977.

J. A. G. Malherbe, *Microwave Transmission Line Filters*, Artech House, Dedham, Mass., 1979.

M. Makimoto and S. Yamashita, “Bandpass filters using parallel coupled stripline stepped impedance resonators,” *IEEE Trans. Microw. Theory and Tech*, vol.28, no.12, pp.1413-1417, Dec. 1980.

R.V. Snyder, “Broadband waveguide or coaxial filters with wide stopbands, using a stepped-wall evanescent mode approach,” *Microwave J.*, vol.26, pp.53-58, Dec. 1983.

Q. Zhang and T. Itoh, “Computer-aided design of evanescent-mode waveguide filter with nontouching E-plane fins,” *IEEE Trans. Microw. Theory and Tech.*, vol.36, no.2, pp.404-412, Feb. 1988.

H. Shigesawa, M. Tsuji, T. Nakao, and K. Takiayama, “Two-path cutoff waveguide dielectric resonator filters,” *IEEE Trans. Microw. Theory and Tech.*, vol.37, no.7, pp. 1105-1112, Jul. 1989.

H.C. Chang and K.A. Zaki, “Evanescent-mode coupling of dual-mode rectangular waveguide filters,” *IEEE Trans. Microw. Theory and Tech.*, vol.39, no.8, pp.1307-1312, Aug. 1991.

M. Guglielmi, F. Montuati, L. Pellegrini, and P. Arcioni, “Implementing transmission zeroes in inductive-window bandpass filters,” *IEEE Trans. Microw. Theory and Tech.*, vol.43, no.8, pp.1911-1915, Aug. 1995.

K. Meykens, B. V. Rompaey, and H. Janseen, “Dispersion in acoustic waveguides-a teaching laboratory experiment,” *Am. J. phys.*, vol.67, no.5, pp.400-406, May 1999.

L. Zhu and K. Wu, “Accurate circuit model of interdigital capacitor and its application to design of new quasi-lumped miniaturized filters with suppression of harmonic resonance,” *IEEE Trans. Microwave Theory Tech.*, vol.48, no.3, pp.347-356, Mar. 2000.

J.-S. Hong and M. J. Lancaster, *Microstrip Filters for RF/Microwave Applications*, John Wiley & Sons, 2001.

M. Guglielmi, P. Jarry, E. Kerherve, O. Requebrm, and D. Schmitt, “A new family of all-inductive dual-mode filters,” *IEEE Trans. Microw. Theory*, vol.49, no.10, pp. 1764-1769, Oct. 2001.

S. Bastioli, L. Marcaccioli, and R. Sorrentino, “Waveguide psedoelliptic filters using slant and transverse rectangular ridge resonators,” *IEEE Trans. Microw. Theory*, vol.49, no.10, pp.1764-1769, Oct. 2001.

S. Amari, U. Rosenberg, and J. Bornemann, “Adaptive synthesis and design of resonator filters with source/load-multiresonator coupling,” *IEEE Trans. Microw. Theory and Tech*., vol.50, no.8, pp.1969-1978, Aug. 2002.

G. M. Rebeiz, *RF MEMS: Theory, Design, and Technology*, Hoboken, NJ: Wiley, 2003.

J. T. Kuo and E. Shih, “Microstrip stepped impedance resonator bandpass filter with an extended optimal rejection bandwidth,” *IEEE Trans. Microw. Theory and Tech.*, vol.51, no.5, pp.1554-1559, May 2003.

U. Rosenberg, S. Amari, and J. Bornemann, “Inline TM_{110}-mode filters with high-design flexibility by utilizing bypass coupling of nonresonating $TE_{10/01}$ modes,” *IEEE Trans. Microw. Theory and Tech*., vol.51, no.6, pp.1735-1742, Jun. 2003.

T. Shen and K.A. Zaki, “Length reduction of evanescent-mode ridge waveguide bandpass filters,” *Prog. In Electromag. Res.,* PIER 40, pp.71-90, 2003.

S. Amari and U. Rosenberg, “Synthesis and design of novel in-line filters with one or two real transmission zeros,” *IEEE Trans. Microw. Theory and Tech*., vol.52, no.5, pp.1464-1478, May 2004.

L. Harle and L. P. B. Katehi, “A silicon micromachined four-pole linear phase filter,” *IEEE Trans. Microw. Theory and Tech*, vol.52, no.6, pp.1598-1607, Jun. 2004.

X. Gong, A. Margomenos, B. Liu, S. Hajela, L. P.B. Katehi, and W. J. Chappell, “Precision fabrication techniques and analysis on high-Q evanescent-mode resonators and filters of different geometries,” *IEEE Trans. Microw. Theory and Tech*, vol.52, no.11, pp.2557-2566, Nov. 2004.

D. M. Pozar, Microwave Engineering, 3rd Ed. New York: Wiley, 2005.

D. Kajfez, *Q-Factor-Encyclopedia of RF and Microwave Engineering,* John Wiley & Sons, Inc, 2005.

S. Hrabar, J. Bartolic and Z. Sipus, “Waveguide miniaturization using uniaxial negative permeability metamaterial," *IEEE Trans. Antenn*as *Propag*., vol.53, no.1, pp.110-119, Jan. 2005.

M. Garai, J. A. R. Cruz, J. M. Rebollar, M. J. P. Cruz, A. O. Navarro, and I. H. Carpintero, "Synthesis and design of in-line N-order filters with N real transmission zeros by means of extracted poles implemented in low-cost rectangular H-plane waveguide," *IEEE Trans. Microw. Theory and Tech*., vol.53, no.5, pp.1636-1642, May 2005.

H. Zhang and K. J. Chen, "A tri-section stepped-impedance resonator for cross-coupled bandpass filters," *IEEE Microw. Wireless Compon. Lett*., vol.15, no.6, pp.401-403, Jun. 2005.

S. Amari and U. Rosenberg, "Characteristics of cross (bypass) coupling through higher/lower order modes and their applications in elliptic filter design," *IEEE Trans. Microw. Theory and Tech*., vol.53, no.10, pp.3135-3141, Oct. 2005.

L. Zhu, S. Sun, and W. Menzel, "Ultra-wide-band (UWB) band-pass filters using multiple-mode resonator," *IEEE Microw. Wireless Compon Lett*., vol.15, no.11, pp.796-798, Nov. 2005.

I. Ohira, H. Deguchi, M. Tsuji, and H. Shigesawa, "Novel waveguide filters with multiple attenuation poles using dual-behavior resonance of frequency-selective surfaces," *IEEE Trans. Microw. Theory and Tech*., vol.53, no.11, pp.3320-3326, Nov. 2005.

D. Packiaraj, M. Ramesh, and A. T. Kalghatgi, "Design of a tri-section folded SIR filter," *IEEE Microw. Wireless Compon. Lett.*, vol.16, no.5, pp.317-319, May 2006.

C.-M. Rao, T.-J. Wong, and M.-H. Ho, "A Parallel doubly coupled dual-band bandpass filter," *IEEE/MTT-S, Int. Microw. Symp*., pp.511-514, Jun. 2006.

Y-C. Chiou, J-T. Kuo, and E. Cheng, "Broadband quasi-chebyshev bandpass filters with multimode stepped-impedance resonators (SIRs)," *IEEE Trans. Microw. Theory and Tech*, vol.54, no.8, pp.3352-3358, Aug. 2006.

G. Cusmai, M. Brandolini, P. Rossi, and F. Svelto, "A 0.18-μm CMOS selective receiver front-end for UWB applications," *IEEE J. Solid- State Circuits*, vol.41, no.8, pp.1764-1771, Aug. 2006.

I. Shapir, "Suggestion for a new formula to calculate group delay from frequency domain measurements," *Proceedings of the 36th European Microw. Conf.*, pp.1233-1236, Sept. 2006.

Y. P. Zhang and M. Sun, "Dual-band microstrip bandpass filter using stepped-impedance resonators with new coupling schemes," *IEEE Trans. Microw. Theory and Tech*, vol.54, no.10, pp.3779-3785, Oct. 2006.

C.-Y. Chen, C.-Y. Hsu, and H.-R. Chuang, "Design of miniature planar dual-band filter using dual-feeding structures and embedded resonators," *IEEE Microw. Wireless Compon. Lett*., vol.16, no.12, pp.669-671, Dec. 2006.

H. Joshi, H. H. Sigmarsson, D. Peroulis, and W. Chappell, "Highly loaded evanescent cavities for widely tunable high-Q filters," *IEEE/MTT-S Int. Microw. Symp*., pp.2133-2136, Jun. 2007.

C. H. Wu, C. H. Wang, and C. H. Chen, "Stopband-extended balanced bandpass filter using coupled stepped-impedance resonators," *IEEE Microw. Wireless Compon. Lett.*, vol.17, no.7, pp.507-509, Jul. 2007.

Y. Wang, B-Z Wang, and J. Wang, "A tri-section stepped impedance bandpass filter with harmonic suppression," *7th Int. Conf. on ASIC*, pp.592-595, Oct. 2007.

M. Chongcheawchamnan, R. Phromloungsri, M. Krairiksh, and I. D. Robertson, "Microstrip ring resonator filter with inductively-compensated parallel-coupled feed and stepped-impedance design," *Elect. Lett.*, vol.43, no.23, Nov. 2007.

X.-P. Chen, K. Wu, and Z.-L. Li, "Dual-band and triple-band substrate integrated waveguide filters with Chebyshev and quasi-elliptic responses," *IEEE Trans. Microw. Theory and Tech*., vol.55, no.12, pp.2569-2578, Dec. 2007.

A. Velez, J. Bonache, and F. Martin, "Varactor-loaded complementary split ring resonators (VLCSRR) and their application to tunable metamaterial transmission lines," *IEEE Microw. Wireless Compon. Lett*., vol.18, no.1, pp.28-30, Jan. 2008.

S. W. Wong and L. Zhu, "Implementation of compact UWB bandpass filter with a notch-band," *IEEE Microw. Wireless Compon. Lett.,* vol.18, no.1 pp.10-12, Jan. 2008.

C.-I G. Hsu, C-H. Lee, and Y.-H. Hsieh, "Tri-band bandpass filter with sharp passband skirts designed using tri-section SIRs," *IEEE Microw. Wireless Compon. Lett.*, vol.18, no.1, pp.19-21, Jan. 2008.

X. P. Cheng and K. Wu, "Substrate integrated waveguide cross-coupled filter with negative coupling structure," *IEEE Trans. Microw. Theory and Tech*., vol.56, no.1, pp.142-149, Jan. 2008.

G-M. Yang, R. Jin, C. Vittoria, V. G. Harris, and X. Sun, “Small ultra-wideband (UWB) bandpass filter with notched band,” *IEEE Microw. Wireless Compon. Lett.,* vol.18, no.3, pp.176-178, Mar. 2008.

L.-H. Hsieh, G. L. Stolarczyk, and K. Chang, “Microstrip dual-band bandpass filters using parallel-connected open-loop ring resonators,” *Int. J. of RF and Microw. Com.-Aided Eng*., vol.18, no.3, pp.219-224, May 2008.

W.H. Tu, “Compact double-mode cross-coupled microstrip bandpass filter with tunable transmission zeros,” *IET Microw Antennas Propag*., vol.2, no.4, pp.373-377, Jun. 2008.

D.J. Kim and J.-H. Lee, “Partial H-plane filters with multiple transmission zeros,” *IEEE Trans. Microw. Theory and Tech*., vol.56, no.7, pp.1693-1698, Jul. 2008.

Y. Yamamoto, K. Li, and O. Hashimoto, “Tunable sharp notch filter for UWB application,” *Microw. Opt. Tech. Lett*., vol.50, no.10, pp.2712-2715, Oct. 2008.

H. R. Arachchige, J. S. Hong, and Z. C. Hao, “UWB bandpass filter with tunable notch on liquid crystal polymer substrate,” *Asia-Pacific Microw. Conf*., pp.1-4, Dec. 2008.

C.-P. Chen, Z. Ma, and T. Anada, “Synthesis of ultra-wideband bandpass filter employing parallel-coupled stepped-impedance resonators,” *IET Microw. Antennas Propag*., vol.2, no.8, pp.766-772, Dec. 2008.

Y. C. Chang, C. H. Kao, M. H. Weng, and R. Y. Yang, “A novel compact dual-band bandpass filter with a wide stopband using asymmetric SIRs for WLANs,” *Asia-Pacific Microw. Conf.,* pp.1-4, Dec. 2008.

J. Wang, et al., “UWB bandpass filter with multiple frequency notched bands,” *IEEE MTT-S Int. Microw. Workshop Series on Art of Miniaturizing RF and Microw. Passive Compon*, pp.106-109, Dec. 2008.

M. Mokhtari and J. Bornemann, “Ultra-wideband and notched wideband filters with grounded vias in microstrip technology,” *Asia Pacific Microw., Conf.*, pp.1-4, Dec. 2008.

Y.-C. Chang, C.-H. Kao, and M.-H. Weng, “A compact wideband bandpass filter using asymmetric SIR with low loss and high selectivity,” *Microw. Opt. Tech. Lett*., vol.51, no.1, pp.242-244, Jan. 2009.

A. Vallese, A. Bevilacqua, C. Sandner, M. Tiebout, A. Gerosa, and A. Neviani, “Analysis and design of an integrated notch filter for the rejection of interference in UWB systems,” *IEEE J. Solid-State Circuits*, vol.44, no.2, pp.331-343, Feb. 2009.

S. G. Mao, Y.Z. Chueh, C.H. Chen, and M. C. Hsieh, “Compact ultra-wideband conductor–backed coplanar waveguide bandpass filter with a dual band-notched response,” *IEEE Microw. Wireless Compon. Lett.*, vol.19, no.3, pp.149-151, Mar. 2009.

X.P. Chen, K. Wu, and D. Drolet, “Substrate integrated waveguide filter with improved stopband performance for satellite ground terminal,” *IEEE Trans. Microw. Theory and Tech*., vol.57, no.3, pp.674-683, Mar. 2009.

F. Mira, J. Mateu, S. Cogollos, and V. E. Boria, “Design of ultra-wideband substrate integrated waveguide (SIW) filters in zigzag topology,” *IEEE Microw. Wireless Compon. Lett*., vol.19, no.5, pp.281-283, May 2009.

S. J. Park, I. Reines, and G. Rebeiz, “High-Q RF-MEMS tunable evanescent-mode cavity filter,” *IEEE/MTT-S Int. Microw. Symp.,* pp.1145-1148, Jun. 2009.

B. J. Chen, T. M. Shen, and R. B. Wu, “Dual-band vertically stacked laminated waveguide filter design in LTCC technology,” *IEEE Trans. Microw. Theory and Tech*., vol.57, no.6, pp.1554-1562, Jun. 2009.

X. Liu, L.P.B. Katehi, W.J. Chappell, and D. Peroulis, “A 3.4-6.2GHz continuously tunable electrostatic MEMS resonator with quality factor of 460-530,” *IEEE/MTT-S Int. Microw. Symp*., Jun. 2009.

Z.-C. Hao, J.-S. Hong, S. K. Alotabi, J.P. Parry, and D.P. Hand, “Ultra-wideband bandpass filter with multiple notch-bands on multilayer liquid crystal polymer substrate,” *IET Microw. Antennas Propag*., vol.3, no.5, pp.749-756, Aug. 2009.

Z. C. Hao and J-S. Hong, “Compact UWB filter with double notch bands using multilayer LCP technology,” *IEEE Microw. Wireless Compon. Lett.*, vol.19, no.8 pp.149-151, Aug. 2009.

Y.D. Dong, T. Yang, and T. Itoh, “Substrate integrated waveguide loaded by complementary split-ring resonators and its application to miniaturized waveguide filters,” *IEEE Trans. Microw. Theory and Tech*., vol.57, no.9, pp.2211-2223, Sep. 2009.

J. Wang, W. Hong, H. Tang, C. Y. J. Zhang, and J. Zhou, “Ultra-wide band bandpass filter with multiple frequency notched bands based on SIW and SIR technology,” *Proc. of the 39th Europ. Microw. Conf*., pp.268-271, Oct. 2009.

C.-K. Lung, K.-S. Chin, and J. S. Fu, “Tri-section stepped-impedance resonators for design of dual-band band stop filter,” *Proc. of the 39th Europ. Microw. Conf.*, pp.771-774, Oct. 2009.

J. Wang, et al., “Ultra-wide band band-pass filter with multiple frequency notched bands based on SIW and SIR technology,” *Proc. of the 39th Europ. Microw. Conf.*, pp. 268-271, Oct. 2009.

L. Chen, Y. Shang, and Y.L. Zhang, “Design of a UWB bandpass filter with a notched band and wide stopband,” *Microw. J,* vol.52, no.11, pp.96-105, Nov. 2009.

C.H. Lee, C.I.G. Hsu, and L.Y. Chen, “Band-notched ultra-wide-band band-pass filter design using combined modified quarter-wavelength tri-section stepped-impedance resonators,” *IET Microw. Antennas. Propag*., vol.3, no.8, pp.1232-1236, Dec. 2009.

M. Mokhtaari and J. Bornemann, “Tunable notch characteristics in microstrip ultra-wideband filters,” *Asia Pacific Microw., Conf.*, pp. 937-940, Dec. 2009.

Z-C. Hao*,* J-S. Hong, J. P. Parry, and D. P. Hand, “Ultra-wideband bandpass filter with multiple notch bands using nonuniform periodical slotted ground structure,” *IEEE Trans. Microw. Theory and Tech*., vol.57, no.12, pp.3080-3088, Dec. 2009.

C.-H. Lee, C.-I.G. Hsu, and L.-Y. Chen, “Band-notched ultra-wideband bandpass filter design using combined modified quarter-wavelength tri-section stepped-impedance resonator,” *IET Microw. Antennas Propag*., vol.3, no.8, pp.1232-1236, Dec. 2009.

C.-P. Chen et al., “Design of compact notched UWB filter using coupled external stepped-impedance resonator,” *Asia-Pacific Microw. Conf*, pp.945-948, Dec. 2009.

M. Meeloon, S. Chaimool, and P. Akkaraekthalin, “A broadband bandpass filter with a notch-band using step-impedance resonator and embedded slots,” *Asia-Pacific Microw. Conf*, pp.1446-1449, Dec. 2009.

Y. Wang and M. Yu, “True inline cross-coupled coaxial cavity filters,” *IEEE Trans. Microw. Theory and Tech*., vol.57, no.12, pp.2958-2965, Dec. 2009.

H. Joshi, H.H. Sigmarsson S. Moon, D. Peroulis, and W. J. Chappell, “High –Q fully reconfigurable tunable bandpass filters,” *IEEE Trans. Microw. Theory and Tech*., vol.57, no.12, pp.3525-3533, Dec. 2009.

P. Mondal and Y. L. Guan, “A coplanar stripline ultra-wideband bandpass filter with notch-band*,” IEEE Microw. Wireless Compon Lett*., vol.20, no.1, pp.22-24, Jan. 2010.

S. J. Park, I. Reines, C. Patel and G. Rebeiz, “High-Q RF-MEMS 4-6 GHz tunable evanescent-mode cavity filter,” *IEEE Trans. Microw. Theory and Tech.*, vol.58, no.2, pp.381-389, Feb. 2010.

X. Luo, J-G. Ma, K. Ma, and K. S. Yeo, “Compact UWB bandpass filter with ultra-narrow notched band,” *IEEE Microw. Wireless Compon. Lett.,* vol.20, no.3, pp.145-147, Mar. 2010.

J. Shi and Q. Xue*,* “Novel balanced dual-band bandpass filter using coupled stepped-impedance resonators,” *IEEE Microw. Wireless Compon. Lett*, vol.20, no.1, pp.19-21, Mar. 2010.

K-S. Chin, K-M. Lin, Y-H. Wei, T-H. Tseng, and Y-J. Yang, “Compact dual-band branch-line and rat race couplers with stepped-impedance stub lines,” *IEEE Trans. Microw. Theory and Tech*, vol.58, no.5, pp.1213-1221, May 2010.

S. Moon, H. H. Sigmarsson, H. Joshi, and W.J. Chappell, “Substrate integrated evanescent-mode cavity filter with a 3.5 to 1 tuning ration,” *IEEE Microw. Wireless Compon. Lett*. vol.20, no.8, pp.450-452, Aug. 2010.

S. Pirani, J. Nournia, and C. Ghobadi, “Band-notched UWB BPF design using parasitic coupled line,” *IEEE Microw. Wireless Compon. Lett.,* vol.20, no.8, pp.444-446, Aug. 2010.

K. Song and Q. Xue, “Asymmetric dual-line coupling structure for multiple-notch implementation in UWB bandpass filters,” *Electron. Lett*., vol.46, no.20, pp.1388-1390, Sept. 2010.

L. S. Wu, X.L. Zhou, W.Y. Yin, L. Zhou, and J.F. Mao, “A substrate-integrated evanescent-mode waveguide filter with nonresonating node in low-temperature co-fired ceramic,” *IEEE Trans. Microw. Theory and Tech*., vol.58, no.10, pp.2654-2662, Oct. 2010.

M. Nosrati and M. Mirzaee, “Compact wideband microstrip bandpass filter using quasi-spiral loaded multi-mode resonator,” *IEEE Microw. Wireless Compon. Lett*., vol.20, no.11, pp.607-609, Nov. 2010.

L.-S. Wu, J.- F. Mao, W.- Y. Yin, and Y.- X. Guo, “A dual-band filter using stepped-impedance resonator (SIR) embedded into substrate integrated waveguide (SIW),” *IEEE Elect. Design of Advanced Package & Systems Symposium*, pp.1-4, Dec. 2010.

J. T. Kuo and T. W. Lin, “Dual-mode dual-band ring resonator bandpass filter with transmission zeros,” *Asia-Pacific Microw. Conf.,* pp.1865-1870, Dec. 2010.

S. Bastioli, C. Tomassoni, and R. Sorrentino, "A new class of waveguide dual-mode filters using TM and nonresonating modes," *IEEE Trans. Microw. Theory and Tech*., vol.58, no.12, pp.3909-3917, Dec. 2010.

Q.-X. Chu and X.-K. Tian, "Design of a compact UWB bandpass filter with notched band," *Asia-Pac. Microw. Conf.,* pp.37-40, Dec. 2010.

S. Ueno, K. - M. Hitke, and Y. Horii, "Ultra-wideband band pass filter with built-in notch filter configured by multi-layered CRLH unit cells," *Asia-Pac. Microw. Conf*., pp.1138-1141, Dec. 2010.

K. Song and Q. Xue, "Ultra-wideband (UWB) bandpass filters with multiple notched bands using asymmetric dual-line coupling structure," *Asia-Pac. Microw. Conf*., pp.1055-1058, Dec. 2010.

S. Jung and S.-I. Yang, "Ultra-wideband band-pass filter with controllable arbitrary notched bands using CRLH-TL," *Asia-Pac. Microw. Conf*., pp.1059-1062, Dec.2010.

H.-W. Wu, M.-H. Weng, and C.-Y. Hung, "Ultra wideband bandpass filter with dual notch bands," *Asia-Pac. Microw. Conf*., pp.33-36, Dec. 2010.

J.-E. Lim, et al., "Two-port balanced dual-band bandpass filter based on stepped impedance resonators," *Asia-Pac. Microw. Conf*., pp.1114-1117, Dec.2010.

"UW-MEMS design handbook", version 5.0, the Center for Integrated RF Engineering (CIRFE), University of Waterloo, 2010.

W. Shen, W.Y. Yin, and X.W. Sun, "Compact substrate integrated waveguide transversal filter with microstrip dual-mode resonator," *J. of Electromagn. Waves and Appl*., vol.24, pp.1887-1896, 2010.

F. Wei, L. Chen, Q.-Y. Wu, X.-W. Shi, and C.-J. Gao, "Compact UWB bandpass filter with narrow notch-band and wide stop-band," *J. of Electromagn. Waves and Appl.,* vol.24, pp.911–920, 2010.

P.-Y. Hsiao and R.-M. Weng, "Compact tri-layer ultra-wideband band-pass filter with dual notch bands," *Prog. Electromag. Res*., vol.106, pp.49-60, 2010.

F. Wei, Q. Yi Wu, X. W. Shi, and L. Chen "Compact UWB bandpass filter with dual notched bands based on SCRLH resonator," *IEEE Microw. Wireless Compon Lett.*, vol. 21, no.1, pp.28-30, Jan. 2011.

J. Long, C. Li, W. Chi, J. Huangfu, and L. Ran, "A tunable microstrip bandpass filter with two independently adjustable transmission zeros," *IEEE Microw. Wireless Compon. Lett*., vol.21, no.2, pp.74-76, Feb. 2011.

V. Sakar and K. Entesari, "Miniaturized UWB bandpass filters with notch using slow-wave CPW multiple-mode resonators," *IEEE Microw. Wireless Compon. Lett*, vol.21, no.2, pp.80-82, Feb. 2011.

X. Luo, J.-G. Ma, K. S. Yeo, and E. P. Li, "Compact ultra-wideband (UWB) bandpass filter with ultra-narrow dual- and quad-notched bands," *IEEE Trans. Microw. Theory and Tech*., vol.59, no.6, pp.1509-1519, Jun. 2011.

W. S. Chang and C. Y. Chang, "Analytical design of microstrip short-circuit terminated stepped-impedance resonator dual-band filters," *IEEE Trans. Microw. Theory and Tech*., vol.59, no.7, pp.1730-1739, Jul. 2011.

W. Shen, W.-Y. Yin, and X.-W. Sun, "Miniaturized dual-band substrate integrated waveguide filter with controllable bandwidths," *IEEE Microw. Wireless Compon. Lett*, vol.21, no.8, pp.418-420, Aug. 2011.

M. Vahidpour and K. Sarabandi, "Micromachined J-band rectangular waveguide filter," *General Assembly and Sci. Symp*., pp.1-4, Aug. 2011.

Y. Zheng, M. Sazegar, H. Maune, X. Zhou, J. R. Binder, and R. Jakoby, "Compact substrate integrated waveguide tunable filter based on ferroelectric ceramics," *IEEE Microw. Wireless Compon. Lett*. vol.21, no.9, pp.477-479, Sep. 2011.

F. Wei, L. Chen, X.-W. Shi, and B. Liu, "Compact UWB band-pass filter with tunable notch-band based on folded SIR," *Electronic Lett*., vol.47, no.22, pp.1229-1230, Oct. 2011.

M. Nosrati and M. Daneshmand, "A novel compact dual-wideband band-pass filter using spiral-shaped multi-mode and complementary split ring resonators," *Microw. J*, vol.54, no.11, pp.100-108, Nov. 2011.

Y.C. Chiou and G.M. Rebeiz, "A tunable three-pole 1.5-2.2-GHz bandpass filter with bandwidth and transmission zero control," *IEEE Trans. Microw. Theory and Tech*., vol.59, no.11, pp.2872-2878, Nov. 2011.

O. Glubokov and D. Budimir, "Extraction of generalized coupling coefficients for inline extracted pole filters with nonresonating nodes," *IEEE Trans. Microw. Theory and Tech*., vol.59, no.12, pp.3023-3029, Dec. 2011.

A. Garcia-Lamperez and M. Salazar-Palma, "Single-band to multiband frequency transformation for multiband filters," *IEEE Trans. Microw. Theory and Tech*., vol.59, no.12, pp.3048-3058, Dec. 2011.

J. E. Lim and J. H. Lee, "A novel design method of microstrip dual-band filter using feed line with SIR," *Asia-Pacific Microw. Conf.,* pp.1274-1277, Dec. 2011.

G. F. Zargano, V. V. Zemlyakov, and V. V. Krivopustenko, "Electrodynamic analysis of eigenmodes in a rectangular waveguide with Two L-shaped septa," *Journal of Communications Tech. and Electronics*, vol.56, no.3, pp.259-268, 2011.

F. Farzami, K. Forooraghi, and M. Norooziarab, "Design and modeling of a miniaturized substrate integrated waveguide using embedded SRRs," *IEEE Anten. Wireless. Propag. Lett.,* vol.10, pp.713-716, 2011.

Q.L. Zhang, W.Y. Yin, and S. He, "Evanescent-mode substrate integrated waveguide (SIW) filters implemented with complementary split ring resonators," *Prog. Electromag. Res.,* vol.111, pp.419-432, 2011.

M. Mirzaee, "A novel small ultra-wideband bandpass filter including narrow notched band utilizing folded-T-shaped stepped impedance resonator (SIR)," *Progress In Electromag. Res. C*, vol.22, pp.85-96, 2011.

Y. Dong and T. Itoh, "Miniaturized dual-band substrate integrated waveguide filters using complementary split-ring resonators," *IEEE/MTT-S, Int. Microw. Symp*., 2011.

M. Mokhtaari and J. Bornemann, "Microstrip ultra-wideband filter with flexible notch characteristics," *Int. J. Wireless Engr. and Tech*., vol.3, no.1 pp.12-17, Jan. 2012.

D. E. Senior, X. Cheng, and Y.K. Yoon, "Electrically tunable evanescent mode half-mode substrate-integrated-waveguide resonators," *IEEE Microw. Wireless Compon. Lett*, vol.22, no.3, pp.123-125, Mar. 2012.

Z. Wu, Y. Shim, and M. Rais-Zadeh, "Miniaturized UWB filters integrated with tunable notch filters using a silicon-based integrated passive device technology," *IEEE Trans. Microw. Theory and Tech*., vol.60, no.3, pp.518-527, Mar. 2012.

M. Nosrati and M. Daneshmand, "Compact microstrip UWB double/single notch-band BPF based on wave's cancellation theory," *IET Microw. Antennas Propag*, vol.6, no.8 pp.862-868, Jun. 2012.

D.E. Senior, X. Cheng, and Y.K. Yoon, “Dual-band filters using complementary split-ring resonator and capacitive loaded half-mode substrate-integrated-waveguide,” *IEEE/MTT-S, Int. Microw. Symp*., pp.1-2, Jul. 2012.

F. Wei, L. Chen, X.-W. Shi, and C.-J. Gao, “UWB band-pass filter with one tunable notch-band based on DGS,” *J. of Electromagn. Waves and Appl*., vol.26, no.5-6, pp.673-680, Jul. 2012.

K. Gong, W. Hong, Y. Zhang, P. Chen, and C.J. You, “Substrate integrated waveguide quasi-elliptic filters with controllable electyric and magnetic mixed coupling,” *IEEE Trans. Microw. Theory and Tech*., vol.60, no.10, pp.3071-3077, Oct. 2012.

S. Bastioli and R. V. Snyder, “Broad passband, wide stopband, high power evanescent mode filters using capacitively-loaded ridges,” *Europ. Microw. Conf., (EuMC)*, pp.176-179, Nov. 2012.

X. Shang, M. Ke, Y. Wang, and M. Lancaster, “WR-3 band waveguides and filters fabricated using SU8 photoresist micromachining technology,” *IEEE Tran. THz. Sci. Tech*., vol.2, no.6, pp.629-637, Nov. 2012.

J. Hu, S. Xie and Y. Zhang, “Micromachined terahertz rectangular waveguide bandpass filter on silicon-substrate,” *IEEE Microw. Wireless Compon. Lett*., vol.22, no.12, pp.636-638, Dec. 2012.

S. Bastioli and R. Snyder, “Inline pseudoelliptic TE_{01}-mode dielectric resonator filters using multiple evanescent modes to selectively bypass orthogonal resonators,” *IEEE Trans. Microw. Theory and Tech*., vol.60, no.12, pp.3988-4001, Dec. 2012.

W. J. Feng, W. Q. Che, Y. M. Chang, S. Y. Shi, and Q. Xue, “High selectivity fifth-order wide-band band-pass filters with multiple transmission zeros based on transversal signal-interaction concepts,” *IEEE Trans. Microw. Theory and Tech*., vol.61, no.1, pp.89-97, Jan. 2013.

T. Yang, P.L. Chi, R. Xu, and W. Lin, “Folded substrate integrated waveguide based composite right/left-handed transmission line and its application to partial H-plane filters,” *IEEE Trans. Microw. Theory and Tech*., vol.61, no.2, pp.789-799, Feb. 2013.

Z. Xia and F. Liu, “Dual-band bandpass filters using SIRs with open-stub line and zero-degree feed structure,” *IEEE Int. Wireless Symp. (IWS),* pp.1-4, Apr. 2013.

E. J. Naglich, J. Lee, H. H. Sigmarsson, D. Petroulis, and W. J. Chappell, “Intersecting parallel-plate waveguide loaded cavities for dual-mode and dual-band filters,” *IEEE Trans. Microw. Theory and Tech*., vol.61, no.5, pp.1829-1838, May 2013.

M. Nosrati and M. Daneshmand, “Developing single layer ultra-wide band band-pass filter with multiple (triple and quadruple) notches,” *IET Microw. Antennas Propag*., vol.7, no.8 pp.612-620. Jun. 2013.

M. Nosrati, N. Vahabisani, and M. Daneshmand, “A novel tunable double notch-band UWB BPF using MEMS capacitors,” *IEEE/MTT-S Int. Microw. Symp,* Jun. 2013.

R. Tomassoni and R. Sorrentino, “A new class of pseudoelliptic waveguide filters using dual-post resonators,” *IEEE Trans. Microw. Theory and Tech*., vol.61, no.6, pp. 2332-2339, Jun. 2013.

V. V. Zemlyakov, “The band-pass SIW-filter based on L-ridged rectangular waveguide,” *Prog., Electromag., Res., Symp*., pp.605-609, Aug. 2013.

F. Farzami and M. Norooziarab, “Experimental realization of tunable transmission lines based on single-layer SIWs loaded by embedded SRRs,” *IEEE Trans. Microw. Theory and Tech*., vol.61, no.8, pp.2848-2857, Aug. 2013.

Z. Kordiboroujeni and J. Bornemann, “Designing the width of substrate integrated waveguide structures,” *IEEE Microw. Wireless Compon. Lett*, vol.23, no.10, pp.518-520, Oct. 2013.

S. Yang, L. Lin, J. Chen, K. Deng, and C. H. Liang, “Design of compact dual-band bandpass filter using dual-mode stepped-impedance stub resonators,” *Elect. Lett.*, vol.50, no.8, pp.611-613, Apr. 2014.

P. Chu *et al*., “Wide stopband bandpass filter implemented with spur stepped impedance resonator and substrate integrated coaxial line technology,” *IEEE Microw. Wireless Compon. Lett.*, vol.24, no.4, pp.218-220, Apr. 2014.

L. Gao, X. Y. Zhang, B.-J. Hu, and Q. Xue, “Novel multi-stub loaded resonators and their applications to various bandpass filters,” *IEEE Trans. Microw. Theory and Tech.*, vol.62, no.5, pp.1162-1172, May 2014.

M. Nosrati, N. Vahabisani, and M. Daneshmand, “Compact MEMS-based ultra wideband CPW band-pass filters with single/double tunable notch-bands,” *IEEE Trans. Compon., Pack. Manufac Tech*., vol.4, no.9, pp.1451-1460, Aug. 2014.

R. V. Snyder and S. Bastioli, "Transmission zero generation for wideband high frequency evanescent mode filters," *IEEE/MTT-S, Int. Microw. Symp*., pp.1-4, Jun. 2014.

M. S. Arif and D. Peroulis, "All-silicon technology for high-Q evanescent mode cavity tunable resonators and filters," *Journal of Microelectromechanical Systems*, vol.23, no.3, pp.727-739, Jun. 2014.

S. Bastioli and R. V. Snyder, "Ultra-compact evanescent mode filter using inhomogeneous semi-lumped capacitive elements," *Int. Microw Conf., Radar and Wireless Communication*., pp.1-4, Jun. 2014.

S. Bastioli and R. V. Snyder, "Waveguide evanescent mode filters using high-Q bypassed cavities for extreme close-in rejection," *Europ. Microw. Conf., (EuMC)*, pp.175-178, Oct. 2014.

F. Qiu, L. Z. Zhang, and B. Wu, "High selective dual-band microstrip filter using zero-degree coupled SIR feed lines," *Antennas and Propagation (APCAP), Asia-Pacific Conf.,* pp.731-733, Dec. 2014.

Y. Shen, H. Wang, W. Kang, and W. Wu, "Dual-band SIW differential bandpass filter with improved common-mode suppression," *IEEE Microw. Wireless Compon. Lett*, vol.25, no.2, pp.100-102, Feb. 2015.

L. P. Mospan, S. A. Prikolotin, and A. A. Kirilenko, "Rectangular waveguide section with a pair of antipodal posts; spectral characteristics," *Int. Conf., Antenna Theory and Tech.*, pp.1-3, Apr. 2015.

T. Yan and X.-H. Tang, "Substrate integrated waveguide dual-band bandpass filter with complementary modified split-ring resonators," *IEEE Wireless Symp*., (IWS), pp.1-4, Apr. 2015.

G. Wu, L. Yang, and Q. Xu, "Miniaturised dual-band filter with high selectivity using split ring scheme," *Electronics Lett.*, vol.51, no.7, pp.570-572, Apr. 2015.

S. Xu, K. Ma, F. Meng, and K. S. Yeo, "Novel defected ground structure and two-side loading scheme for miniaturized dual-band SIW bandpass filter designs," *IEEE Microw. Wireless Compon. Lett*, vol.25, no.4, pp.217-219, Apr. 2015.

C. Tomassoni, S. Bastioli, and R. V. Snyder, "Pseudo-elliptic in-line filters with dielectric resonators in propagating waveguide*," IEEE-MTT-S, Int. Microw., Symp*.pp.1-4, May 2015.

J.-X. Zhuang, Z.-C. Hao, and W. Hong, “Silicon micromachined terahertz bandpass filter with elliptic cavities,” *IEEE Tran. THz. Sci. Tech*., vol.5, no.6, pp.1040-1047, Nov. 2015.

A. V. G. Subramanyam, D. Sivareddy, V. V. Krishna, V. V. Srinivasan, and Y. Mehta, “Compact iris-coupled evanescent-mode filter for spacecraft S-band data transmitters,” *IEEE/ MTT, Microw. RF Conf*., *(IMaRC)*, pp.125-127, Dec. 2015.

X. Li, C. J. You, Z. Shao, and Z. He, “A wideband bandpass filter based on stepped impedance stubs and substrate integrated coaxial line,” *Asia-Pacific Microw. Conf.*, pp.1-3, Dec. 2015.

Advanced Design System, ADS 2015.

FCC Code of Federal Register (CFR), Title 47, pt. 15, United States.

Appendix A

This document has been taken from “UW-MEMS DESIGN HANDBOOK”, version 5.0, the University of Waterloo, Ontario, Canada, 2010.

UW-MEMS Fabrication process.

The UW-MEMS microfabrication process uses a 7-mask gold-based process. The process starts by a 0.025” thick Alumina substrate with a relative permittivity of 9.9 and loss tangent of 0.0001.

Layer 1: Titanium tungsten bias lines.

As shown in Figure A.1, a 50 nm TiW layer is sputtered and patterned.

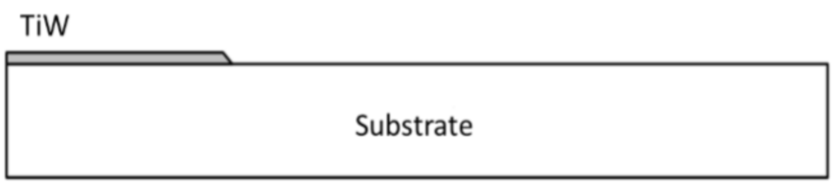

Figure A.1. Sputtering the first layer of 50 nm TiW [A.1].

Layers 2 and 3: First dielectric

As shown in Figure A.2, a 0.7 µm silicon dioxide (SiO_2) is deposited using plasma enhanced chemical vapor deposition (PECVD). The deposited layer is then patterned using reactive ion etching (RIE).

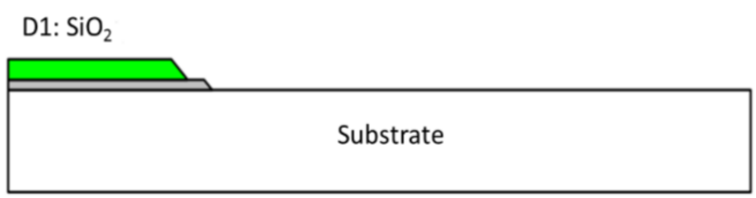

Figure A.2. Deposition of the first dielectric layer [A.1].

Layer 4: First gold layer.

As shown in Figure A.3, a seed layer is deposited using a bilayer 40nm Cr/70nm Au. A negative photoresist (PR) mold is patterned by photolithography using layer “G1”. The both mold and the seed layers are then removed.

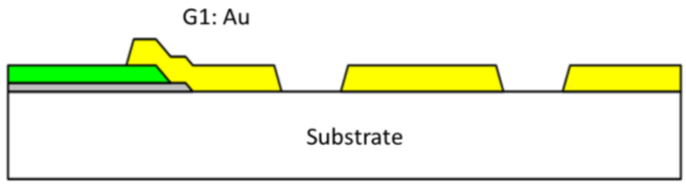

Figure A.3. First gold layer [A.1].

Layer 5: Second dielectric layer.

As shown in Figure A.4, a 30nm layer of TiW is sputtered as an adhesion layer followed by the deposition of 0.7μm silicon dioxide. The SiO_2 and TiW layers are then patterned using "D2" layer.

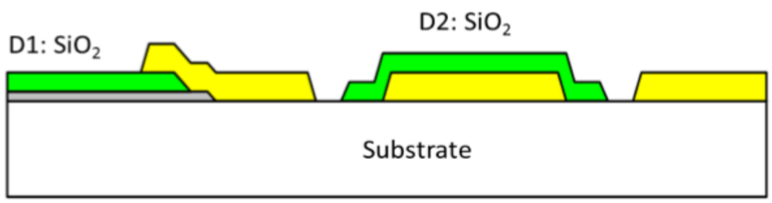

Figure A.4. Second dielectric layer [A.1].

Layer 6: Anchor opening.

As shown in Figure A.5, the sacrificial layer is deposited using spin coated polyimide for the Au structural layer in UWMEMS. The layer is coated to a thickness of 2.5μm and then patterned by "A" layer in RIE. in the polyimide is then etched to realize the anchor holes.

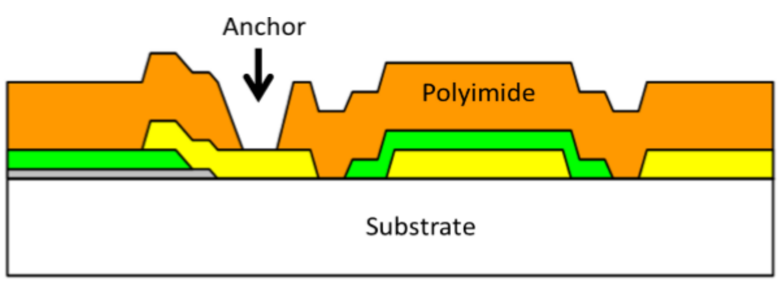

Figure A.5. Anchor opening [A.1].

Layer7: Dimple openings.

As shown in Figure A.6, the dimple openings are similarly performed in polyimide using an RIE etching step. The "D" layer is used to pattern the layer with a depth of 1 μm.

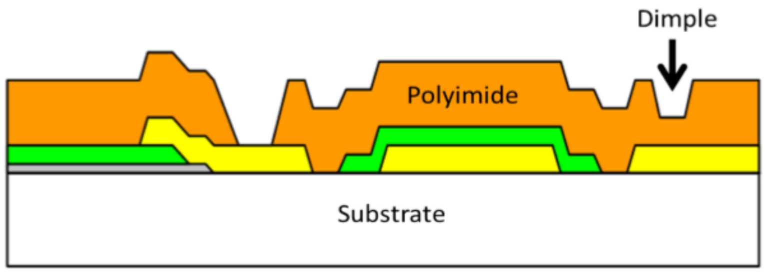

Figure A.6. Dimple openings [A.1].

Layers 8 and 9: The second gold layer.

As shown in Figure A.7, the second 70nm gold layer is sputtered as the seed layer. Then the seed layer is electroplated to be 2µm. This layer is used as the structural layer of all the MEMS devices. The layer is patterned using "G2" layer with a negative PR mold.

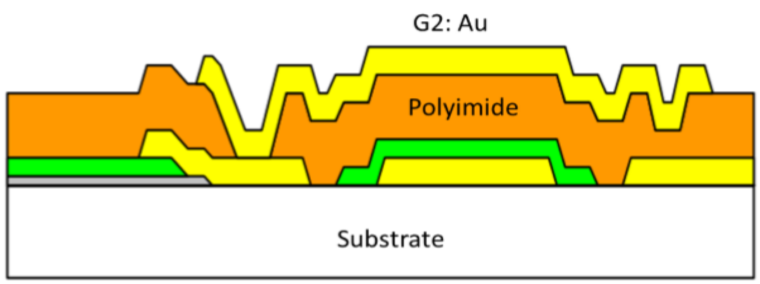

Figure A.7. The second gold layer [A.1].

As shown in Figure A.8, the sacrificial layer is removed using O_2 plasma dry etching in RIE.

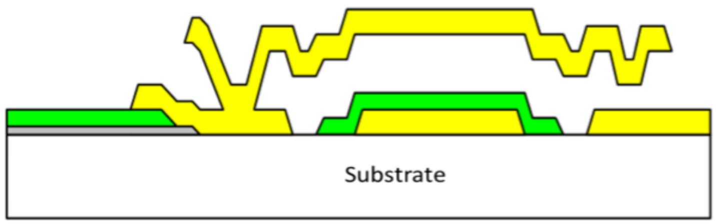

Figure A.8. Release step [A.1].

[A.1] "UW-MEMS DESIGN HANDBOOK", version 5.0, the Center for Integrated RF Engineering (CIRFE), University of Waterloo, 2010.

Appendix B

List of Publications

Journal Papers

[P1] M. Nosrati and M. Daneshmand, “Substrate integrated waveguide L-shaped iris for realization of transmission zero and evanescent-mode pole,” Accepted in *IEEE Trans. Microw. Theory and Tech*., Feb. 2017.

[P2] M. Nosrati, N. Vahabisani, and M. Daneshmand, “Compact MEMS-based ultra wideband CPW band-pass filters with single/double tunable notch-bands,” *IEEE Trans. Compon., Pack. Manufac Tech*., vol.4, no.9, pp.1451-1460, Aug. 2014.

[P3] M. Nosrati and M. Daneshmand, “Developing single layer ultra-wide band band-pass filter with multiple (triple and quadruple) notches,” *IET Microw. Antennas Propag*., vol. 7, no. 8 pp. 612-620. Jun. 2013.

[P4] M. Nosrati and M. Daneshmand, “Compact microstrip UWB double/single notch-band BPF based on wave’s cancellation theory,” *IET Microw. Antennas Propag*., vol.6, no.8, pp 862-868, Jun. 2012.

[P5] M. Nosrati, N. Vahabisani, and M. Daneshmand, “Single/dual-band BPFs using inductively coupled SIW stepped impedance resonator,” Preparing for submission.

Conference Papers

[C1] M. Nosrati, N. Vahabisani, and M. Daneshmand, “Wafer-level waveguide filter realization using simplied 3D fabricaiton process,” *16^{th} Int. Symp. Antenna Tech., Applied Electromag.*, 2014.

[C2] M. Nosrati, N. Vahabisani, and M. Daneshmand, “A novel tunable double notch-band UWB BPF using MEMS capacitors,” *IEEE/MTT-S, Int. Microw. Symp.* Jun. 2013.